UNIVERSITY OF SOUTHAMPTON

FACULTY OF ENGINEERING, SCIENCE & MATHEMATICS

School of Ocean and Earth Science

Electromagnetic investigation of the Lucky Strike Seamount near 37^{o}N, Mid-Atlantic Ridge

by

Neville Barker

This dissertation is submitted for the degree of Doctor of Philosophy

February 2004

To Cheryl

UNIVERSITY OF SOUTHAMPTON

ABSTRACT

FACULTY OF ENGINEERING, SCIENCE & MATHEMATICS
SCHOOL OF OCEAN AND EARTH SCIENCES

Doctor of Philosophy

ELECTROMAGNETIC INVESTIGATION OF THE LUCKY STRIKE SEAMOUNT AT 37°N, MID-ATLANTIC RIDGE

by Neville Davis Barker

In October 1999, a controlled source electromagnetic (CSEM) survey was carried out over the central seamount of the Lucky Strike segment of the Mid-Atlantic Ridge. The summit of this seamount has been a target for biological, geochemical and surface geophysical research since hydrothermal activity was first discovered there in 1992. However, this survey was the first attempt to use geophysical techniques to constrain sub-seafloor crustal properties. This dissertation describes the progress that has been made in analysing the CSEM data.

1-dimensional forward modelling and inversion have proven useful tools in constraining the bulk resistivity of the region, and highlight subsets of the data that are particularly worthy of further study. The data are to first order consistent with a ~700 m-thick layer of 4.4–7.0 Ωm overlaying a crustal resistivity of at least 100 Ωm.

The effect of the Lucky Strike topography was investigated using 2-dimensional forward modelling. Topography was found to have only a minor effect on most of the data. Portions of data that are severely influenced by topographic variations were identified and removed. Subsequent modelling could then be carried out assuming a flat seafloor.

2-D inversion was found to be of little use in constraining lateral resistivity variations: 3-dimensional resistivity anomalies were mapped into the 2-D models, producing large tradeoffs in data residuals. However, good progress was made with pseudoimaging of 1-D residuals, and 3-D forward modelling. A 2 km-wide region with anomalously low resistivities has been identified over the region of known hydrothermal activity. There is also evidence for another region of high resistivities over the north west of the seamount. Co-incident with a small topographic high, this may be due to a hitherto unknown region of hydrothermal activity. Resistivities increase rapidly to the east, over the eastern flank of the seamount.

Evidence for a low resistivity zone within the top 1 km of the crust, 6 km to the north of the seamount summit, along with markedly higher crustal resistivities only 1 km off-axis, suggests that high temperature hydrothermal fluids circulate for a considerable distance along the ridge axis, but not off-axis, only venting onto the the surface in the region of the seamount summit.

Inversion of synthetically-generated datasets has illustrated that the resolution of a crustal mush zone of the extent detected at the Reykjanes Ridge would be well within the capabilities of this dataset. It is therefore concluded that no laterally extensive region of partial melt currently exists at Lucky Strike. However, this does not preclude the existence of a smaller melt body under the axial seamount. Further modelling of the data may be able to resolve such a structure.

These results support models of crustal formation by tectono-magmatic cycling in which the Lucky Strike segment is nearing the end of a magmatically-controlled phase of activity.

Graduate School of the Southampton Oceanography Centre

This PhD dissertation by

Neville Barker

has been produced under the supervision of the following persons

Supervisors

Prof. Martin Sinha
Dr. Lucy MacGregor

Chairs of Advisory Panel

Prof. Bernard Boudreau (Oct 2000 – Sept 2001)
Prof. Kelvin Richards (Sept 2001 – Sept 2002)
Dr. Timothy Minshull (Sept 2002 onwards)

Contents

List of Figures

List of Tables

DECLARATION OF AUTHORSHIP

I, **Neville Barker**, declare that the thesis entitled

Electromagnetic investigation of the Lucky Strike Seamount near 37^{o}N, Mid-Atlantic Ridge

and the work presented in it are my own. I confirm that:

- this work was done wholly or mainly while in candidature for a research degree at this University;
- where any part of this thesis has previously been submitted for a degree of any other qualification at this University or any other institution, this has been clearly stated;
- where I have consulted the published work of others, this is always clearly attributed;
- where I have quoted from the work of others, the source is always given. With the exception of such quotations, this thesis is entirely my own work;
- I have acknowledged all main sources of help;
- where the thesis is based on work done by myself jointly with others, I have made clear exactly what was done by others and what I have contributed myself;
- none of this work have been published before submission.

Signed:

Date:

Acknowledgements

Many thanks to my supervisors Martin Sinha and Lucy MacGregor for teaching me the black art of CSEM modelling, for being available with suggestions and advice when things went awry, for exhaustively proof-reading this thesis, and for the generous offers of employment upon completion of my PhD.

I had the pleasure of experiencing the data acquisition side of CSEM surveying aboard the R/V Thomas G Thompson during the 2001 APPLE cruise that was funded by NSF. My thanks go the officers, crew and scientific staff who ensured everything went (relatively) smoothly.

Amongst the considerable moral support from my fellow researchers at SOC, three people stand out for mention. Simon T always helped with computing and programming issues, even when I'm sure he should have been doing other things; Sarah afforded me lengthy help with my limited understanding of geochemistry; Simon D helped with all things backup-related, amongst other things.

Funding for three years of this project was provided by the NERC. The ISO-3D project was funded under the European Union Mast-III programme. Basic ship time for the MADRIGALS cruise was also funded by the NERC.

Finally I would like to give special thanks to my fiancée, Cheryl, who despite having had a rough time of it over the past year, has repeatedly kept me on the straight and narrow whenever there was no end in sight. Even though she claimed to understand little of the content, she was also an invaluable proof-reader.

Glossary

ADC	Analogue to digital converter
ADCP	Acoustic Doppler current profiler
AMC	Axial magma chamber
AVR	Axial volcanic ridge
CSEM	Controlled source electromagnetic
DASI	Deep-towed active source instrument. The EM transmitter used during the MADRIGALS cruise
(D)GPS	(Differential) Global positioning system
EPR	East Pacific Rise
HED	Horizontal electric dipole
HMD	Horizontal magnetic dipole
HS bounds	Hashin-Shtrikman bounds. These define an upper and lower conductivity (or seismic velocity) in a two phase medium.
JEM	Joint effective medium
LEMUR	Low-frequency electromangetic underwater receiver. The EM receivers used during the MADRIGALS cruise
MADRIGALS	Mid-Atlantic Deep-towed Resisitivity and Induction Geophysics At Lucky Strike. Cruise CD-120, on which the data used in this thesis were collected.
MAR	Mid-Atlantic Ridge
MOMAR	Monitoring on the Mid-Atlantic Ridge. A multi-disciplinary study of the Lucky Strike section of the MAR.
MOR	Mid-ocean ridge
PM	Poloidal magnetic mode, characterised by horizontal current loops
PSD	Power spectral density
SDM	Source dipole moment
SNR	Signal to noise ratio
SVP	Sound velocity profile
SWIR	South West Indian Ridge
TM	Toroidal magnetic mode, characterised by vertical current loops
UTM	Universal transverse Mercator
VED	Vertical electric dipole
VMD	Vertical magnetic dipole
XBT	Expendable bathythermograph

Chapter 1

Introduction

1.1 Mid-ocean ridge overview

The mid-ocean ridge system comprises a global chain of mountains some 60 000 km long where new ocean crust is being formed. Formation rates vary from about 15 cm yr^{-1} full-spreading rate in fast-spreading ridges such as the East Pacific Rise (EPR), to as little as 1.4 cm yr^{-1} on ultra-slow spreading ridges such as the South West Indian Ridge (SWIR). This variation in spreading rate has a marked effect on the thermal regime in the newly-formed ocean crust (Chen & Morgan 1990), which in turn influences the gross morphology of the ridges.

At fast-spreading ridges, the brittle-ductile transition, a mechanical boundary layer constrained by the maximum depth of earthquakes and corresponding to the 700^{o}C isotherm (Wiens & Stein 1983), occurs at a depth of only 2–3 km. The plate is therefore mechanically weak and is found to be in isostatic equilibrium. The ridge axis forms an axial high supported by the hot, buoyant material beneath. At slow-spreading ridges, the crust close to the axis has a longer period to cool and the transition from brittle to ductile behaviour occurs at a depth of 8-10 km, within the upper mantle. Horizontal stresses associated with spreading are then able to locally distort the plate out of isostatic equilibrium. This forms the observed topography of an axial valley, bounded by normal faults (Morgan & Parmentier 1987).

1.1.1 Oceanic crustal structure

An accepted model for old oceanic crust, away from regions of anomalous crustal formation such as hotspots and fracture zones, has been developed from investigations in ophiolites, and seismic and geochemical results (Spudich & Orcutt 1980). This comprises three layers:

Layer 1 consists of sediment cover. This layer generally thickens with crustal age, and may be completely absent over newly-formed crust.

Layer 2 is generally 1–2 km thick, consists of intrusive and extrusive basalt, and is characterised by a steep seismic velocity gradient. The uppermost portion (layer 2a) comprises pillow basalts, lava flows and associated breccia, and has a correspondingly high porosity which decreases with depth as the increasing pressure closes pore spaces. Pillow basalts grade downwards into sheeted dykes, that occupy most of layers 2b/c.

Layer 3 is distinguished from layer 2 by both a higher seismic velocity and a much smaller vertical velocity gradient. This has been interpreted as corresponding to a transition from sheeted dykes to gabbros, although a direct correlation between the seismic results and in-situ lithological properties has never been established. Indeed, interpretation of seismic refraction studies on the Costa Rica Rift by (Detrick et al. 1994) has suggested that the layer 2/3 transition occurs within the sheeted dykes. In this case, the observed layer 3 seismic signature may instead be due to changes in crustal porosity and alteration.

1.1.2 Crustal magma chambers

Several geophysical techniques have been used to identify magma bodies within the crust. Mid-crustal axial magma chambers (AMCs) may be identified with seismic reflection (e.g. Detrick et al. (1987); Kent et al. (1990); Kent et al. (1993)). Deeper within the crust, constraints have started to be placed on melt distributions using tomographic inversions of active source seismic arrivals (e.g. Toomey et al. (1994)), and compliance techniques (Crawford et al. 1991).

It has been found that AMCs are very common, if not ubiquitous, under fast to intermediate spreading ridges. Evidence suggests that they have a typical thickness of 10–100 m, a width of ~500 m, and an along-axis length of >10 km, at a depth of approximately 1.5–2 km below the seafloor (e.g. Detrick et al. (1987); Kent et al. (1990); Collier & Singh (1997); Babcock et al. (1998)).

Numerical modelling of melt bodies under slow spreading ridges suggests that no steady-state AMC can exist: the rate of melt injection is too low to stop conductive and hydrothermal heat loss from freezing thin melt lenses (Henstock et al. 1993, Phipps-Morgan & Chen 1993). To date, only one AMC has been identified under a slow spreading ridge: the RAMESSES experiment targeted a region of the Reykjanes Ridge, Mid-Atlantic Ridge (MAR), which appeared to be undergoing a period of magmatic activity. A seismic reflection survey identified a thin (~100 m), narrow (~4 km) magma body at a depth of 2.5 km beneath the seafloor, overlying a broader zone of partial melt ~8 km in width (Navin et al. 1998). During the same cruise, a co-incident controlled source electromagnetic (CSEM) survey was also able to resolve the deeper region of partial melt (MacGregor et al. 1998). Sinha et al. (1998) calculated that the identified region of melt represents at least 20 000 years of crustal growth, whilst simple thermal arguments suggest that the likely cooling time of this melt body to sub-solidus temperatures is only of the order of 1 500 years. These results therefore support a crustal accretion model based on tectono-magmatic cycling, in which melt bodies are injected into the crust where they cool and solidify. During periods when no magma chamber is present, seafloor spreading continues by amagmatic extension. Studies of seabed bathymetry along the Reykjanes Ridge are able to identify regions that are currently experiencing each of the stages of this tectono-magmatic cycle (Parson et al. 1993).

The varying styles of crustal magma chambers at ridges with different spreading rates is probably also a reflection of the mantle upwelling patterns beneath the crust. At the fast-spreading EPR, 2-dimensional Bouguer anomaly patterns (Madsen et al. 1990), and little along-axis crustal thickness variations (Barth & Mutter 1996) suggest that mantle upwelling is predominantly 2-dimensional. In contrast, at the slow-spreading MAR, a 'bull's eye' pattern of gravity lows at the centre of ridge segments (Kuo & Forsyth 1988) and greater along-axis crustal thickness variations suggests a more 3-dimensional upwelling pattern (e.g. Sinha & Louden (1983), White et al. (1984), Lin et al. (1990)).

1.2 Seafloor hydrothermal systems

The venting of hydrothermal fluids from the seafloor, first observed at the Galapagos Spreading Centre in 1977 (Corliss et al. 1979), is now believed to be a relatively common phenomenon on the world's ridge-crest system. At oceanic ridges, newly emplaced hot crust heats up fluid within the pore spaces of the rocks, causing the fluid to convect. Such transport of heat at and below the seafloor had been predicted (Lister 1972), based upon the 'missing heat' in early models of the thermal evolution of the lithosphere (e.g. McKenzie (1967)). These models assumed hot rock was emplaced at the ocean ridges before being cooled conductively, but consistently predicted more heat flow for younger crust (< 70 Ma) than was observed.

More recent calculations using global seafloor heat flow datasets (Stein & Stein 1994), have shown that 34 % of the global oceanic heat flux (of 32×10^{12} W) is accounted for by hydrothermal discharge. Of this, 30 % occurs on crust < 1 Ma, whilst the rest almost all occurs over crust $< 65\pm10$ Ma. This age, often referred to as the oceanic 'sealing age' is remarkably consistent on all oceanic crust, independent of spreading rate, and is in agreement with the 'missing heat' age predicted by plate cooling models.

Oceanic crustal hydrothermal circulation is important not only because of its relevance to models of plate tectonics, but also for our understanding of oceanic geochemical processes

(Edmond et al. 1979). The global high-temperature hydrothermal water flux is estimated to be about 3×10^{13} kg/yr (Elderfield & Schultz 1996). On this basis, the cycling time of ocean water through the mid-ocean ridge system is of the order of 10 million years, about 1 000 times slower than the water flux for all rivers. However, high temperature hydrothermal fluids rise from the seafloor until they form neutrally buoyant plumes. In the Atlantic Ocean, plume height is well below the top of the rift-valley walls, but in the Pacific, plume anomalies have been recorded as far as 2 000 km off-axis (German et al. 1991). At the height of neutral buoyancy, the entrainment ratio of the hydrothermal fluid is about 10^4. This means that far larger quantities of water pass through plumes, equivalent to an ocean water recycling time of 4 000–8 000 years, and reactions in hydrothermal plumes therefore act as important chemical sinks or sources for many of the trace constituents of seawater (Elderfield & Schultz 1996).

For hydrothermal circulation to occur, (1) conduits in the crust must exist which permit fluid flow and (2) a heat source is needed to cause these fluids to convect. At fast spreading ridges, continuous magmatic intrusion and the associated faulting and fracturing of the crust satisfies both of these requirements. Predictably, evidence of hydrothermal activity has been found along much of the length of fast spreading ridges.

Slow spreading ridges, dominated by discontinuous magma intrusion from localised volcanic centres, and a different style of faulting and fracturing produce a different pattern of hydrothermal activity. The more localised tectonic and magmatic events create larger, more deeply penetrating faults that can provide more long-term sustainable conduits and larger, more mature hydrothermal deposits (Fouquet 1997). Only one third of the energy released by magma chambers is heat of crystallisation; the rest is released as the fossilised magma chamber cools to ambient crustal temperatures (Cannat et al. in prep 2004). An active hydrothermal system at a slow-spreading ridge is not therefore necessarily an indication of a currently molten crustal magma body.

Recent observations at the ultra-slow spreading Gakkel Ridge (Edmonds et al. 2003), and South West Indian Ridge (German et al. 1998) have indicated that hydrothermal activity is not uncommon at these spreading rates. Increased magmatic focussing, or exothermic reactions such as serpentinisation provide possible heat sources for this activity. The Lost City vent field (Kelley et al. 2001), found on a transform fault offset on the MAR in 1.5 Ma old crust, is almost certainly in a region with no magmatic activity. Vent fluid temperatures of 45–75°C and exposed mantle peridotite which has undergone extensive alteration, are consistent with serpentinisation being the heat source required by the hydrothermal system.

1.2.1 Hydrothermal fluids

Hydrothermal venting on the seafloor takes one of three forms. High temperature fluids exit the seabed in focussed flows, usually associated with 'chimney' structures. These vents are sometimes referred to as black smokers as the effusing fluids' metal sulphide load precipitates on contact with ambient seawater, giving them a cloudy appearance. Surface fluid temperatures are greater than about 200°C, but never more than ~400°C. These fluids have penetrated deep into layer 2 of the crust, bringing them in contact with, or near the hydrothermal system's heat source (e.g. Fouquet et al. (1995)). At the high temperatures and pressures experienced by these fluids, phase separation may occur (Von Damm & Bischoff 1987).

Phase separation can take several different forms depending on the temperature and pressure experienced by the fluids, which will affect the concentrations of salts and metals in the effusing fluid (Von Damm 1995). Also, a high-salinity fluid phase may be left in the crust (e.g. MacGregor et al. (2001)).

The mechanisms that control the segregation of the resultant phases, and also limit the maximum temperature of vent fluids, are poorly understood at present. Density contrasts, as well as fluid and vapour phase relative permeability barriers have been proposed for the former (e.g. MacGregor et al. (2001), Fox (1990)). Three mechanisms have been proposed to limit black smoker temperatures (Jupp & Schultz 2000): (1) the ductile nature of high temperature rock may mean that at temperatures over about 500°C it is effectively impermeable (Lister 1974, Fournier 1991); (2) high temperature rocks may become impermeable over time, either by mineral precipitation (Bischoff & Rosenbauer 1985, Lowell et al. 1993), or thermal expansion (Germanovich & Lowell 1992); or (3) the thermodynamic properties of water allow fluids to flow freely within the crust, but limit the temperature of the fluids expelled at the seafloor (Jupp & Schultz 2000).

Although the modelling carried out by Jupp & Schultz (2000) was limited to considering pure seawater, they did find that plumes of a temperature ~400°C formed naturally from any heat source at a temperature greater than ~500°C, at pressures appropriate to seafloor crust. Higher temperature fluids were found to remain near the heat source and only moved laterally, without forming plumes. If this model were correct, then one would expect hot upwelling hydrothermal fluid to be localised in relatively narrow (of the order of hundreds of metres) plumes, with the bulk of the shallow hydrothermal system remaining at near-ambient seawater temperatures.

Low temperature (<200°C) hydrothermal fluids exit from the seabed either as focussed 'white smoker' flow, or in a diffuse fashion, often identified by 'shimmering' due to density contrasts with the surrounding cooler seawater (Von Damm 1995). Geochemical tracers (e.g. Von Damm (1990)) can often be used to identify whether these are higher temperature fluids that have experienced different mixing and residence histories, or that they have never experienced higher temperatures, and originate at a more shallow depth within the crust.

1.2.2 Pore spaces

Porosity, and the interconnectivity of pore spaces are generally considered to be the most fundamental physical parameters that control the form, magnitude and duration of oceanic crustal convection (Anderson & Zoback 1982). Unfortunately, they have also proven to be amongst the hardest parameters to quantify.

Within sedimentary formations, porosity is routinely estimated with resistive (Archie 1942), nuclear (Ellis et al. 1987) and acoustic (Wyllie et al. 1958) techniques. However in crystalline rocks, the different structure of pore spaces, presence of trace elements, and in hydrothermal regions, the wide range of fluid properties, have so far prevented the development of an accurate method for deriving in-situ porosity estimates (Pezard 1990).

Anderson & Zoback (1982) have successfully used a technique called a 'slug test' down ODP hole 504b (on 5.9 Ma ocean crust, about 200 km south of the Costa Rican Rift) to make permeability measurements. In this method, a well at hydrostatic pressure is pressurised by injecting an additional amount of water with a high pressure pump. By sealing the well and monitoring the excess pressure decay over time, the permeability of the rocks surrounding the well may be calculated.

Anderson & Zoback (1982) state that the bulk permeability, along with apparent bulk porosity values (from direct resistivity measurements) obtained are consistent with the vertical zonation of the crust, as known from ophiolite studies: the upper extrusive layer 2A in ODP hole 504b has a higher apparent bulk porosity and permeability, with a sharp decrease measurable between layer 2A and the intrusives of layer 2B.

Unfortunately, drilling through layer 2A of the oceanic crust has proven to be very difficult, and the high cost of such direct porosity measurements limit their usefulness in obtaining a thorough understanding of the oceanic crust (Becker et al. 1989).

It is generally accepted that the future of crustal porosity and pore interconnectivity measurements lie with remote sensing techniques. One solution may come from the integration of two currently available methods: seismic and controlled source electromagnetic (CSEM) studies. Separately, these techniques suffer from a trade-off between the measured rock porosity and the geometry of that porosity. However, as the trade-offs are subtly different in each case, Greer (1999) has shown that it is possible to better constrain the correct solution by developing a joint inversion.

1.3 Electromagnetic methods

The controlled source electromagnetic (CSEM) sounding method, described by (for example) Chave & Cox (1982), is a technique that enables the electrical resistivity structure of oceanic crust to be investigated at a resolution of tens to hundreds of metres vertically, and hundreds of metres horizontally, down to depths of several kilometres.

Prior to the development of CSEM sounding, natural electromagnetic fields had been measured on the seafloor, and used to infer the electrical resistivity of the upper mantle by the magnetotelluric (MT) method (e.g. Cox et al. (1970)). However, the attenuative properties of the oceans limit the measurable range of frequencies to below about 10^{-3} Hz: frequencies which place severe limitations on the resolving power within the crust (see Chapter 2).

The electrical resistivity of rocks within the earth commonly varies over seven orders of magnitude. However, as oceanic crust is mostly made up of basalt, resistivity studies are instead sensitive to secondary properties of the rocks, most notably (1) the porosity and interconnectivity pore spaces; (2) the temperature and salinity of pore fluid; and (3) chemical alteration within the crust. This makes CSEM methods particularly attractive to investigation of ocean ridges, where more traditional seismic techniques, whilst able to accurately constrain sharp lithological boundaries, have difficulty in providing quantitative bounds on fluid fractions and pore fluid interconnectedness.

To date, CSEM experiments have been carried out in a range of oceanic settings (Nobes et al. 1992, Young & Cox 1981, Cox et al. 1986, Evans et al. 1991, Evans et al. 1994, Constable & Cox 1996, MacGregor et al. 1998, MacGregor et al. 2001), and a picture of the broad variation of resistivity with depth in the ocean crust has emerged (Figure 1.1). The upper few hundred metres of the ocean crust are characterised by a steep resistivity gradient that is equated to the decrease in porosity with depth within layer 2A. Seafloor resistivities of $\sim$0.5–5 Ωm, reaching $\sim$7–70 Ωm by a depth of 500 m are typical. By a depth of 2 km, resistivities of as high as 1000 Ωm have been found in mature oceanic crust (Constable & Cox 1996).

As available computing power has increased and techniques have been developed to model EM data in more than one dimension, lateral variations in resistivity within the crust have also been investigated. As described earlier, MacGregor et al. (1998) used 2-D forward modelling to delineate a region of partial melt within the crust at the Reykjanes Ridge. In December 1995, a joint seismic and CSEM study was carried out over the Central Valu Fa Ridge, a back-arc spreading centre of intermediate spreading rate in the Lau Basin, and a site of extensive hydrothermal activity. The CVFR has been a target for geophysical and geochemical studies since the discovery of a 2–3 km wide seismic reflector beneath the ridge,

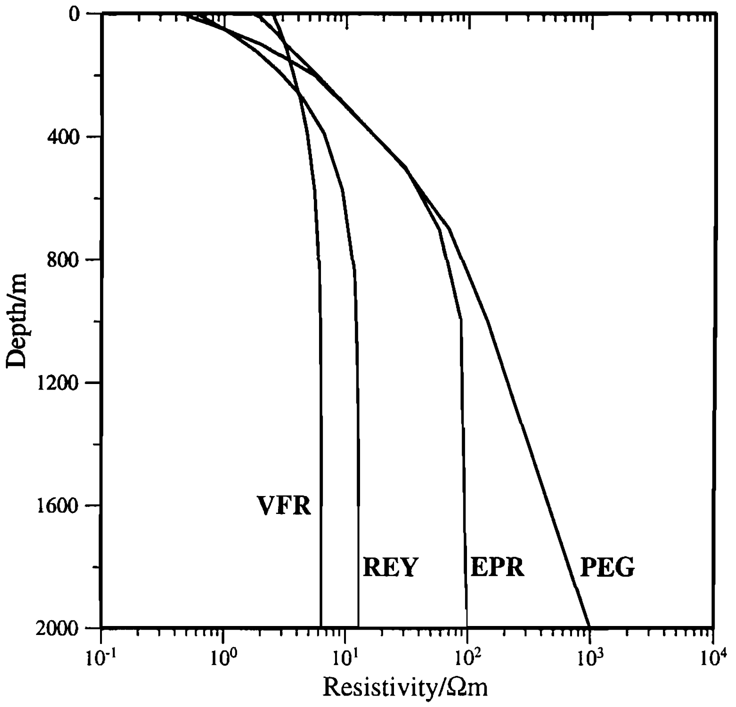

Figure 1.1: Four 1-D resistivity profiles from previous CSEM experiments calculated using the Occam inversion code of Constable et al. (1987) with the 1-D forward code of Chave & Cox (1982). ***PEG***: the Pegasus experiment was carried out over a 40 Ma old section of the Pacific Plate. This site is thought to be a typical example of mature oceanic crust (Constable & Cox 1996). ***EPR***: the results of modelling data obtained over the East Pacific Rise at 13°N. Whilst the EPR is a fast spreading ridge, at 13°N, the ridge appears to be currently in a state of low magmatic activity (Evans et al. 1994). ***REY***: The Reykjanes Ridge, a section of the northern Mid-Atlantic Ridge, currently in a state of high magmatic activity, and underlain by a crustal magma chamber (MacGregor et al. 1998). ***VFR***: The experiment carried out on the Valu Fa Ridge in the Lau basin was centred on the central segment of the spreading ridge. This ridge is in a back-arc environment, forming highly porous rocks due to the high volatile content of the melt, and is both magmatically and hydrothermally active (MacGregor et al. 2001).

interpreted as the top of an axial magma chamber (Morton & Sleep 1985).

The CSEM study did not find evidence for the top surface of the magma chamber. However, it did resolve a region of anomalously low resistivity within seismic layer 2B. This region could not be correlated with any seismic velocity anomaly found by Turner et al. (1999), which would have suggested porosity variation as being the most likely cause. Instead, MacGregor et al. (2001) proposed that the low resistivity anomaly corresponded to hot and/or briney fluids penetrating close to the magma chamber itself.

Modelling has also been carried out to highlight the suitability of CSEM surveying for sub-basalt imaging (MacGregor & Sinha 2000). Imaging sedimentary structure beneath layers such as basalt is of interest to the oil industry in, for example, the Faeroe-Shetland and Rockall areas.

More recently, CSEM surveying techniques have been developed that are particularly sensitive to buried resistive layers, and can therefore be used to detect and delineate buried hydrocarbons (Eidesmo et al. 2002, Ellingsrud et al. 2002).

1.4 ISO-3D project

The ISO-3D research project, a collaboration between 6 institutions in 4 European countries, was funded by the European Commission's MAST-III/Framework IV programme from December 1997 until May 2001.

The specific objectives of the project, as summarized in the technical annexe to the research contract, were:

1. The development of a numerical computer code for modelling the electromagnetic response of a 3-dimensional earth and ocean structure to induction by an arbitrary 3-dimensional source embedded in the ocean.

2. The use of the code in model studies for applications to both physical oceanography and geophysics, including the effects of induction by both natural and artificial sources.

3. The completion of a demonstration 3-dimensional controlled-source electromagnetic sounding (CSEM) experiment on the Mid-Atlantic Ridge south of the Azores, within European waters.

4. The analysis and interpretation of the results of the demonstration CSEM experiment.

1.5 Objectives

The objectives of the PhD outlined in this thesis comprise objective (4) of the ISO-3D project. Specifically, the following subjects are investigated:

1. The MADRIGALS study collected the first CSEM dataset over a region that was expected to have a highly 3-dimensional resistivity structure. How can the currently available 1- and 2-D modelling codes be used to investigate such a large and variable dataset?

2. The Lucky Strike seamount provides the most severe topography sampled to date by a CSEM experiment. How can we quantify the effect that this topography has on the recorded fields, and does the topography influence our ability to resolve resistivity variations within the crust?

3. How can the 3-dimensional numerical code developed under objective (1) of the ISO-3D project, and other imaging techniques, be used to constrain the 3-dimensional crustal resistivity structure at Lucky Strike?

4. What can the crustal resistivity tell us about the Lucky Strike hydrothermal system, and how do these results compare to other constraints on the sub-surface structure of the hydrothermal system at Lucky Strike?

1.6 Outline of dissertation

Chapter 2

Chapter 2 looks at the theory behind the CSEM technique. The concept of electromagnetic skin depth is explained, and a new method of defining field strength in terms of normalised current density is introduced. Simple 1-dimensional resitivity models are used to illustrate the propagation of electromagnetic fields through the earth.

Chapter 3

This chapter deals with the Lucky Strike segment of the Mid-Atlantic Ridge and the CSEM experiment which was carried out there. The geology of the target region is outlined, and the results from surface physical and geochemical studies are discussed with particular emphasis on what they can tell us about the likely crustal structure at Lucky Strike. The summary of the CSEM experiment highlights the data collected during the cruise, and any probems encountered during the acquisition of the dataset.

Chapter 4

Chapter 4 covers the processing and analysis carried out on data from the Lucky Strike CSEM experiment that was necessary before modelling of the EM data could be carried out. The technique used to recover the cruise navigation is explained. The processing of the EM data, including frequency transformation, noise evaluation and error estimation is then discussed.

Chapter 5

This chapter illustrates the uses that 1-dimensional modelling still has when analysing a highly 3-dimensional CSEM dataset. The 'bulk' layer over halfspace resistivity of the region is calculated, and data subsets are chosen for modelling with 1-D inversion. Parts of the data that cannot be adequately explained by a 1-D resistivity profile are also highlighted.

Chapter 6

This chapter covers the 2-dimensional modelling carried out on the EM data. The effect of the Lucky Strike topography on the recorded fields is discussed, and the results of a 2.5-D inversion of a subset of the data are presented.

Chapter 7

Chapter 7 builds on the results obtained from Chapters 5 & 6, and discusses ways of constraining 3-dimensional crustal resistivity variations at Lucky Strike. This includes the first test of the ISIS modelling code with real data, and also illustrates how pseudoimages of the subsurface may be obtained from the residuals from lower-dimensional modelling.

Chapter 8

Finally, Chapter 8 sums up the conclusions from previous chapters, highlights what has been learnt about the target area, and discusses what can be done in the future to improve our understanding of hydrothermal systems such as Lucky Strike with the help of CSEM techniques. Particular emphasis is placed on techniques that allow other crustal properties, such as porosity and fluid temperature, to be investigated.

Chapter 2

Electromagnetic theory

This chapter summarises the physical theory behind the CSEM technique, which has been explained in detail by various authors (e.g. Chave & Cox (1982), Flosadóttir (1990), Everett (1990), Evans et al. (1991), Unsworth (1991) and MacGregor (1997)).

In a CSEM experiment, the horizontal electric field signal resulting from a deep-towed transmitter is recorded by a number of ocean bottom receivers. In order to model and interpret the electric field signals, it is therefore crucial to be able to calculate the propagation of electromagnetic energy through the crust.

An approximate analytical solution for the limited case of a horizontal dipole source overlying a conductive halfspace was provided by Bannister (1984). A more useful scenario consists of a vertical stack of constant-resistivity layers. Chave & Cox (1982) derive exact closed-form expressions for this 1-dimensional situation, as well as providing numerical methods for their evaluation.

The code of Chave & Cox (1982) is used here in order to calculate the propagation of electromagnetic energy through simple crustal structures in terms of a new measure of signal amplitude: the Sinha ratio (Sinha 2003). Electric field attenuation is explained in terms of electromagnetic skin depth, coupled with the inductive and galvanic effects of the two modes of electric field excitation.

2.1 Maxwell's equations

The fundamental equations governing the propagation of electromagnetic fields in a conductor are Maxwell's equations (Maxwell 1891),

$$\nabla \cdot \boldsymbol{E} = \frac{q_{free}}{\varepsilon} \tag{2.1}$$

$$\nabla \cdot \boldsymbol{B} = 0 \tag{2.2}$$

$$\nabla \times \boldsymbol{E} = -\frac{\partial \boldsymbol{B}}{\partial t} \tag{2.3}$$

$$\nabla \times \frac{\boldsymbol{B}}{\mu} = \frac{\boldsymbol{E}}{\rho} + \varepsilon \frac{\partial \boldsymbol{E}}{\partial t} + \boldsymbol{J}_s \tag{2.4}$$

where $\boldsymbol{E}$ is the electric field, $\boldsymbol{B}$ is the magnetic flux density, $\boldsymbol{J}_s$ is the source current density, q_{free} is the free charge density, ρ is the electrical resistivity, ε is the electrical permittivity and μ is the magnetic permeability. The relative permeability values obtained by Keller (1988) for a variety of minerals, illustrate that μ may vary over a factor of two. This contrasts to ρ, which varies over a factor of 10^8 in the earth. It is therefore a reasonable approximation to assume that μ takes its free space value, μ_0, everywhere. These equations can then be rearranged to give

$$-\nabla^2 \boldsymbol{E} + \mu_0 \varepsilon \frac{\partial^2 \boldsymbol{E}}{\partial t^2} + \frac{\mu_0}{\rho} \frac{\partial \boldsymbol{E}}{\partial t} = -\mu_0 \frac{\partial \boldsymbol{J}_s}{\partial t} \tag{2.5}$$

$$-\nabla^2 \boldsymbol{B} + \mu_0 \varepsilon \frac{\partial^2 \boldsymbol{B}}{\partial t^2} + \frac{\mu_0}{\rho} \frac{\partial \boldsymbol{B}}{\partial t} = \mu_0 \nabla \times \boldsymbol{J}_s. \tag{2.6}$$

Assuming both the electric and magnetic fields have a harmonic time variation proportional to $e^{-i\omega t}$ for a signal angular frequency ω, equations 2.5 and 2.6 reduce to

$$-\nabla^2 \boldsymbol{E} + i\omega\mu_0 \left(i\omega\varepsilon + \frac{1}{\rho} \right) \boldsymbol{E} = -\mu_0 \frac{\partial \boldsymbol{J}_s}{\partial t} \tag{2.7}$$

$$-\nabla^2 \boldsymbol{B} + i\omega\mu_0 \left(i\omega\varepsilon + \frac{1}{\rho} \right) \boldsymbol{B} = \mu_0 \nabla \times \boldsymbol{J}_s. \tag{2.8}$$

The first term in brackets corresponds to the radiative part of the field, from the displacement current term, $\varepsilon\frac{\partial \boldsymbol{E}}{\partial t}$ in Equation 2.4. The second term corresponds to the diffusive part of the field. The relative contributions of radiative and diffusive propagation to the total field can be quantified by considering the ratio of these two terms, $\frac{1}{\rho\varepsilon\omega}$. Taking a seawater resistivity of 0.298 Ωm and transmission frequencies of between 0.25 and 9 Hz (as used in the Lucky Strike experiment – see Chapter 3), this ratio varies between 2.4×10^{11} and 6.7×10^9, where ε has its free space value, ε_0. The radiative contribution to the total field is therefore insignificant compared to the diffusive contribution, and can be neglected. Equations 2.7 and 2.8 then become

$$\nabla^2 \boldsymbol{E} - i\frac{\mu_0\omega}{\rho} \boldsymbol{E} = \mu_0 \frac{\partial \boldsymbol{J}_s}{\partial t} \tag{2.9}$$

$$\nabla^2 \boldsymbol{B} - i\frac{\mu_0\omega}{\rho} \boldsymbol{B} = -\mu_0 \nabla \times \boldsymbol{J}_s. \tag{2.10}$$

Closed-form solutions to these equations exist only for 1-dimensional layered resistivity structures, or simple higher dimensional structures such as spheres or cylinders. In more complex situations, numerical solutions are required.

2.1.1 Skin depth

In the simplest case of a plane wave propagating through an homogeneous medium in the absence of source currents, the solutions are of the form

$$B(x) = B_0 e^{-\frac{x}{\delta_s}} e^{i\left(\frac{x}{\delta_s} - \omega t\right)} \tag{2.11}$$

$$E(x) = E_0 e^{-\frac{x}{\delta_s}} e^{i\left(\frac{x}{\delta_s} - \omega t\right)} \tag{2.12}$$

where x is the direction of propagation and

$$\delta_s = \sqrt{\frac{2\rho}{\omega \mu_0}} \tag{2.13}$$

is the skin depth. This is a measure of the rate of attenuation of an electromagnetic signal, and is defined as the distance over which an electromagnetic field decays by a factor e^{-1} and the phase of the signal is shifted by 1 radian. In terms of resistivity and transmission frequency f,

$$\delta_s = \sqrt{\frac{2\rho}{2\pi \mu_0 f}} = \sqrt{\frac{1}{\mu_0 \pi}} \times \sqrt{\frac{\rho}{f}}.$$

As $\sqrt{\frac{1}{\mu_0 \pi}} = 503.3$, to a good approximation

$$\delta_s \approx 500\sqrt{\frac{\rho}{f}}. \tag{2.14}$$

From this, it can be seen that the rate of signal attenuation is proportional to the square root of the resistivity and inversely proportional to the square root of the frequency of transmission. Whilst the source waveform generated during a CSEM experiment is more complex than a simple plane wave and the resistivity structure it is propagating through is not uniform, this quantity is still useful in understanding the attenuation of electromagnetic energy in real situations.

Skin depths for a range of resistivities and transmission frequencies encountered in a CSEM experiment are listed in Table 2.1. These highlight a number of different characteristics of EM sounding :

1. The short skin depth within seawater leads the ocean to act as a lowpass filter. Magneto Telluric (MT) methods use fields generated within the Earth's ionosphere as an

Frequency	Resistivity				
	0.3 Ωm	1 Ωm	10 Ωm	100 Ωm	1000 Ωm
0.25 Hz	551	1006	3182	10062	31820
1 Hz	276	503	1591	5031	15910
9 Hz	92	168	531	1678	12582

Table 2.1: Skin depths in metres for three frequencies used in the MADRIGALS experiment. Seawater resistivity is 0.3 Ωm. The other values are representative of the range of resistivities to be expected in young oceanic crust.

electromagnetic source, to infer the electrical resistivity of the solid earth. However, in deep water the measurable range of frequencies is limited to below about 10^{-3} Hz. As resistivity anomalies of less than a quarter of a skin depth are not generally resolved, this severely limits the usefulness of the technique for resolving structure within the crust.

2. Conversely, the band-limiting nature of the deep oceans makes them an ideal site for CSEM surveys because of the very low background noise levels at these frequencies.

3. Skin depths in the more resistive crust are longer than in the seawater. For this reason, a seabed EM receiver at a range of greater than several seawater skin depths from a transmitter will record a signal which is dominated by energy that has propagated through the more resistive seabed (see Section 2.5). The depth of penetration of this electromagnetic energy will generally increase as the source-receiver separation increases.

4. Deeper crustal penetration may also be attained by using a lower frequency source. However, there will be a corresponding decrease in resolution.

2.2 Seafloor electric field polarisation

An electromagnetic field in a homogenous layered earth may be decomposed into two modes about a vertical axis, z, each of which independently satisfies Maxwell's Equations (Chave & Cox 1982). These modes are referred to as either Transverse Electric and Transverse Magnetic (Chave & Cox 1982), or Poloidal Magnetic and Toroidal Magnetic (Unsworth 1991).

The Poloidal Magnetic (PM) mode is characterised by current loops in the horizontal plane. As loops within neighbouring layers are coupled to each other purely by induction, the PM mode vanishes at the limit of zero frequency.

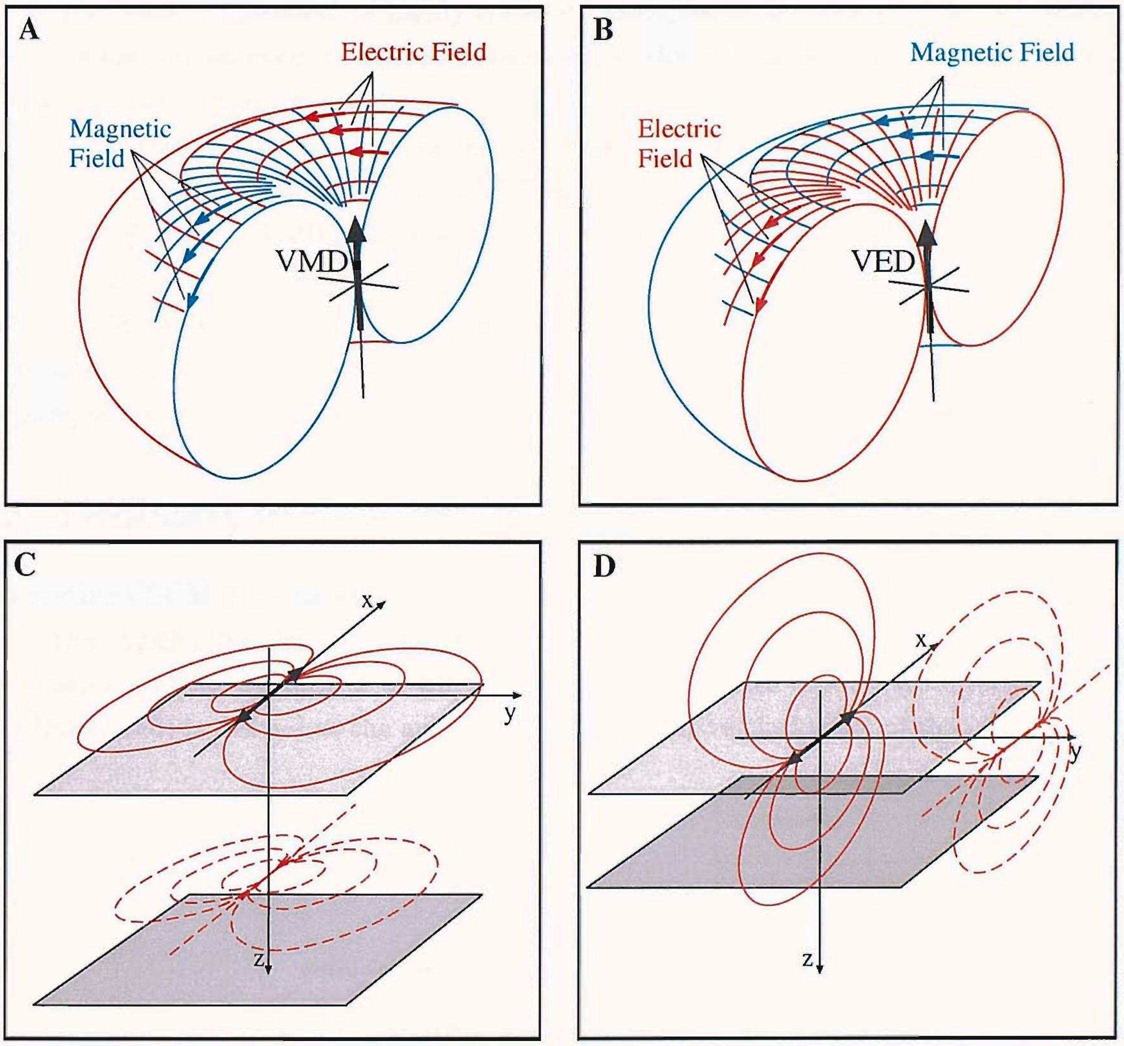

Figure 2.1: Modes of excitation for dipole sources. Plot ***A*** illustrates the PM mode generated by a vertical magnetic dipole (VMD). Plot ***B*** illustrates the TM mode generated by a vertical electric dipole (VED). In Plots ***C*** and ***D***, a horizontal electric dipole (HED) is located above a 1-dimensional layered earth. The horizontal current loops of the PM-dominated mode (Plot ***C***) are therefore predominantly coupled by induction, whilst the vertical current loops of the TM-dominated mode (Plot ***D***) are coupled by a combination of galvanic and inductive effects.

The Toroidal Magnetic (TM) mode is characterised by vertical current loops. As these loops cross resitivity boundaries, they are coupled by a combination of galvanic and inductive effects. At the limit of zero frequency, the TM mode therefore corresponds to direct current.

As the lower atmosphere is highly resistive, ionospheric currents used by MT methods cannot create the galvanic current flow required by the TM mode, and only horizontal PM modes are generated in the earth.

Artificial electromagnetic sources can be subdivided into four categories: horizontal and vertical magnetic dipoles (HMDs and VMDs), and horizontal and vertical electric dipoles (HEDs and VEDs). A VMD generates only PM modes (Plot A, Figure 2.1). A VED generates only TM modes (Plot B, Figure 2.1), as does an HMD (not shown). HEDs generate both PM and TM modes (Plot C & D respectively, Figure 2.1).

In addition to generating both electromagnetic modes, HEDs also offer the most efficient coupling of energy to the crust (Chave & Cox 1982).

2.3 Geometry of a marine CSEM experiment

In a marine CSEM HED experiment, the experimental geometry is described with respect to the source dipole, in polar coordinates (Figure 2.2). Receiver location is defined in terms of the range r and the azimuth ϕ of the receiver from the source dipole. Receiver orientation (not illustrated) is defined as the angle from north (positive clockwise) of the positive end of

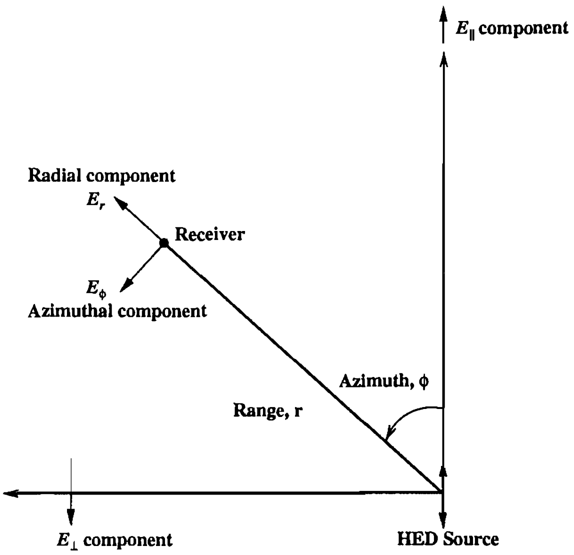

Figure 2.2: A plan view of the geometry associated with an HED source.

the Channel 1 HED. Electric field strength at the receiver is described in terms of a radial component, E_r, which is in line with the direction to the source, and an azimuthal component, E_ϕ, which is orthogonal to the direction to the source.

The E_r and E_ϕ electric field components are of zero magnitude when the receiver is in-line with the source dipole (i.e. $\phi = 0, 180$), or broad-side to the source dipole (i.e. $\phi = 90, 270$) respectively. With an in-line geometry the electric field $E_{\|}$ is therefore equal to E_r. With a broad-side geometry the electric field $E_{\perp}$ is equal to E_ϕ.

The $E_{\|}$ and $E_{\perp}$ electric field components contain contributions from both the PM and TM modes that are dependent upon both the experimental geometry, and crustal resistivity structure.

2.4 Dimensionless amplitudes

It has become customary to normalise the potential gradient E recorded by a seafloor receiver (typically 10^{-6} to 10^{-4} $\mathrm{Vm^{-1}}$) by the source dipole moment (typically 10^4 Am), producing the electric field for a unit dipole E_{norm} (units of $\mathrm{VA^{-1}m^{-2}}$). However, visualisation and interpretation of data in this form can be difficult: subtle electric field variations are often masked by the strong range dependence in the recorded signal. To overcome this, Sinha (2003) has proposed that field strength is defined in terms of normalised current density, or dimensionless amplitude, S.

It is useful to express the amplitudes at the receiver in terms of current, as this is how transmitter amplitudes are specified. The current density J can be obtained from the receiver amplitude E using Ohm's Law (Stratton 1941). As the electric field receivers are located on the seabed within the seawater, taking a seawater resistivity ρ_{sw},

$$J = \frac{E}{\rho_{sw}} \qquad \left(\text{units: } \frac{\mathrm{Vm^{-1}}}{\Omega\mathrm{m}} = \mathrm{Am^{-2}}\right).$$

Receiver current density can then be normalised by the source dipole moment (M), creating a ratio of

$$J_{norm} = \frac{J}{M} \qquad \left(\text{units: } \frac{\mathrm{Am^{-2}}}{\mathrm{Am}} = \mathrm{m^{-3}}\right).$$

Since in the absence of attenuation the amplitude of a potential field from a source dipole decreases with $\frac{1}{r^3}$, this ratio can then be normalised by r^3 to produce dimensionless amplitudes,

$$S = J_{norm} \times r^3,$$

or in terms of normalised electric field strength,

$$S = E_{norm} \times \frac{r^3}{\rho_{sw}}. \tag{2.15}$$

2.5 Diffusion of electromagnetic fields through a uniform earth

The electric field strength as a function of range and receiver azimuth for simple 1-dimensional resistivity structures has been described by various authors (e.g. MacGregor (1997)). However, it is worth revisiting simple halfspace models in order to contrast plots of Sinha amplitudes with the more traditional plots of electric field amplitude normalised by source dipole moment. Figure 2.3 shows the response of uniform halfspace models calculated using the forward code of Chave & Cox (1982). Whilst Plots A & C are dominated by the range-dependent reduction in the electric field, this has been removed in the dimensionless amplitude Plots B & D. The remaining electric field can largely be explained in terms of the differing attenuative effects of the seawater and seabed. At short ranges (less than ~1 km), the signal is dominated by energy that has travelled from the source to the receiver through the conductive seawater. With an in-line geometry (Plot B), the signal is rapidly attenuated with range over this region. However with a broad-side geometry (Plot D), the rate of decay with range is smaller, actually leading to an enhancement in dimensionless amplitudes over this range. At longer ranges, the signal is dominated by energy that has travelled through the more resistive crust. The rate of attenuation is then determined by the resistivity of the crust. At very high crustal resistivities, the signals experience little attenuation with range and the dimensionless amplitude plot is near-horizontal. As the crustal resistivity decreases, the attenuation rate increases. At lower crustal resistivities, the attenuation approaches that predicted for a seawater wholespace.

2.6 Polarisation ellipse parameters

In general, the two components of horizontal electric field recorded during a CSEM experiment neither correspond to $E_{\parallel}$ and $E_{\perp}$, nor E_r and E_{ϕ}. They are instead dependent upon the arbitrary resting orientation of the receiver, and the source-receiver geometry at that time. Grant & West (1965) explain that the locus of the resultant electric field vector is an ellipse if two orthogonal components have different amplitude and phase (Figure 2.4). Smith & Ward (1974) give equations for the tilt α and ellipticity ϵ of a polarisation ellipse, in terms of the

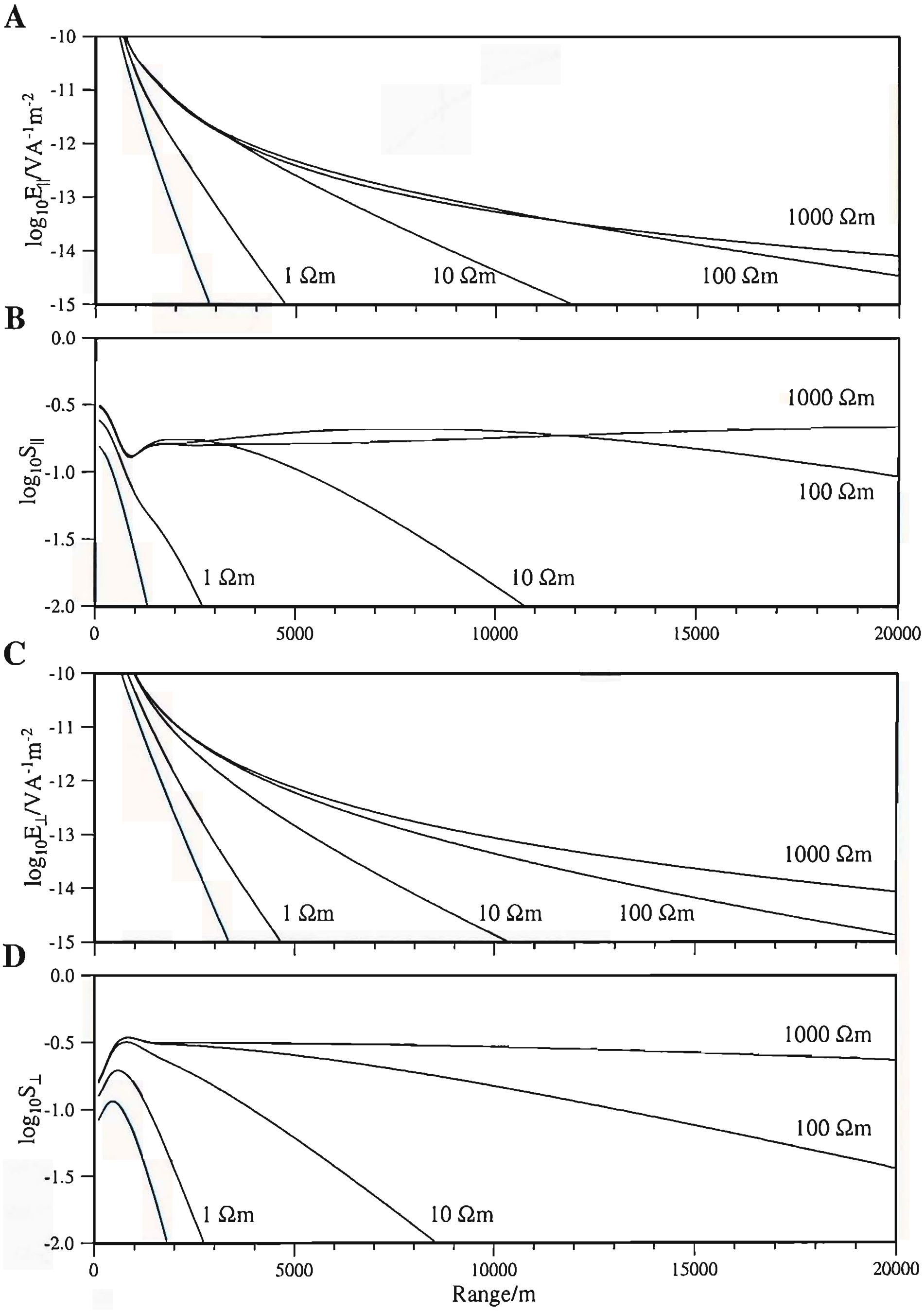

Figure 2.3: Modelled electric field responses for four different halfspace resistivities representing the crust. In each case, the model is overlain by another halfspace of resistivity 0.298 Ωm representing the seawater. Also shown is the modelled electric field for a wholespace with water resistivity (blue lines). Plots *A* and *B* correspond to the in-line geometry. Plots *C* and *D* correspond to the broad-side geometry. Dimensionless amplitude Plots *B* and *D* remove much of the range-dependent decrease in signal amplitudes, allowing more detail to be seen in the calculated fields.

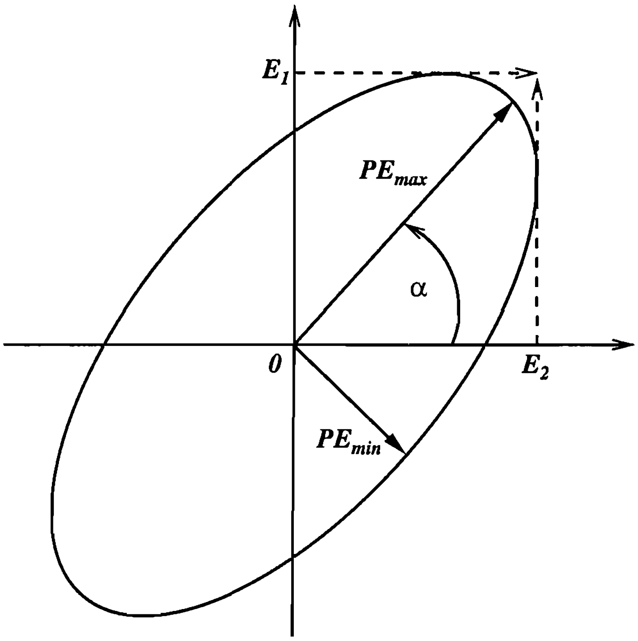

Figure 2.4: Definition of polarisation ellipse parameters.

two orthogonal electric field components E_1 and E_2, and their phases ϕ_1 and ϕ_2:

$$\tan 2\alpha = \pm \frac{2\,(E_2/E_1)\cos\Delta\phi}{1-(E_2/E_1)^2} \tag{2.16}$$

$$\epsilon = \frac{|PE_{min}|}{|PE_{max}|} = \frac{\left|E_2 e^{i\Delta\phi}\cos\alpha - E_1\sin\alpha\right|}{\left|E_2 e^{i\Delta\phi}\sin\alpha + E_1\cos\alpha\right|} \tag{2.17}$$

where $\mathbf{E_1} = E_1 e^{i\phi_1}$, $\mathbf{E_2} = E_2 e^{i\phi_2}$ and $\Delta\phi = \phi_2 - \phi_1$.

If the experimental geometry is well-constrained, E_r and E_ϕ can be calculated using these equations. However, E_r and E_ϕ are highly dependent on receiver orientation and source-receiver azimuth, and therefore small geometric errors can lead to large errors in their apparent amplitudes. The amplitude PE_{max} of the semi-major axis of the polarisation ellipse is far less dependent upon these quantities (see Figure 4.19), and is therefore preferentially used as a more robust estimate of the horizontal electric field amplitude.

2.7 Diffusion of electromagnetic fields through a layered earth

MacGregor (1997) details the effect on normalised electric field of a conductive halfspace overlain by a more resistive layer, and a resistive halfspace overlain by a more conductive

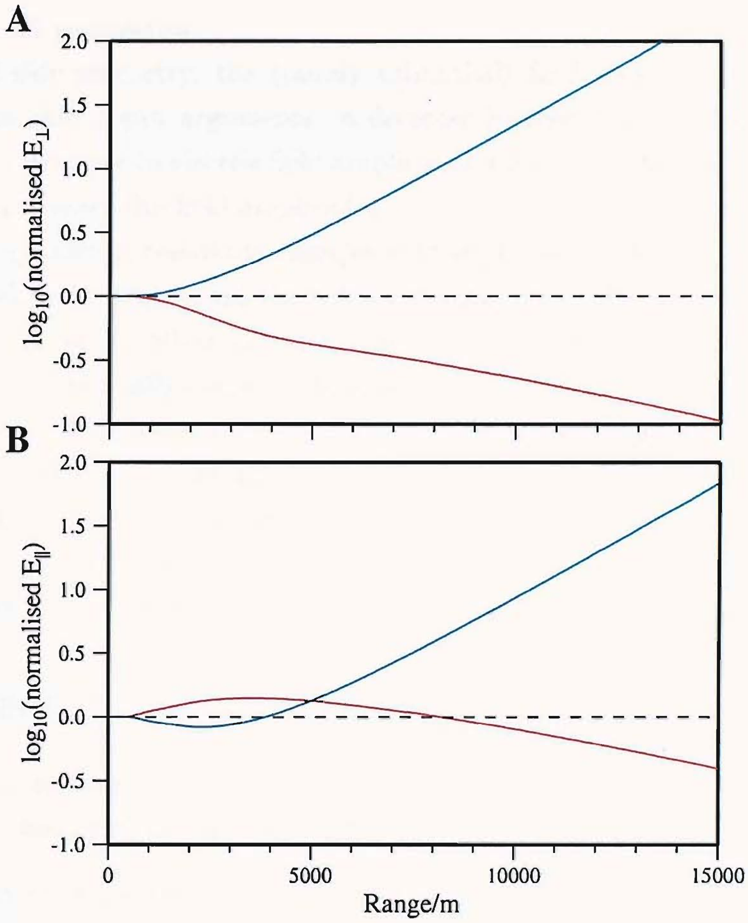

Figure 2.5: Variation of the response with source-receiver azimuth. Plot ***A*** shows the responses calculated in the broad-side geometry from a 1000 Ωm halfspace overlain by 1 km-thick layer of 10 Ωm (blue line), and a 1 Ωm halfspace again overlain by 1 km-thick layer of 10 Ωm (red line). In each case, the response has been normalised by the response calculated from a 10 Ωm halfspace. Plot ***B*** is the same as *A*, but with an in-line geometry. See text for discussion.

layer. Eidesmo et al. (2002) describe the response of a 1-dimensional model comprising a thin buried resistive layer representing a hydrocarbon bearing reservoir, and use the 2.5-dimensional code of Unsworth (1991) (see Chapter 6) to model the 'edge effects' associated with a finite resistive sheet that allow a suitably designed survey to delineate the edges of a hydrocarbon-bearing layer.

Whilst it is often very difficult to directly interpret the electric field produced by more complex resistivity structures, it is instructive to study the effect that an increase in resistivity with depth, and conversely a decrease in resistivity with depth, have on the electric fields recorded at the seafloor. Figure 2.5 illustrates these effects in both the broad-side (Plot *A*) and in-line (Plot B) geometries.

In the broad-side geometry, the (purely azimuthal) field amplitudes behave as would be expected from skin depth arguments: a decrease in resistivity at depth creates higher attenuation and a decrease in electric field amplitudes; an increase in resistivity creates lower attenuation and increases the field amplitudes.

In the in-line geometry, resistivity changes with depth have a more complicated effect on the field amplitudes. At long ranges the fields are again dominated by the attenuative effect of the resistivity. However, when the resistivity decreases with depth, conduction currents, particularly in the galvanically coupled TM mode (which makes a greater contribution to the total field in the in-line geometry), lead to increased electric field amplitudes at short ranges.

The relative attenuation of broad-side fields compared to in-line fields where resistivity decreases with depth is known as the field 'splitting' (or sometimes 'current channeling') effect. Its usefulness in an ocean ridge setting has been illustrated by MacGregor (1997), where it was used to identify a region of partial melt within the crust.

2.8 Summary

1. The physical and mathematical theory behind the CSEM technique is now well understood. A summary of this has been presented here.

2. The concept of electromagnetic skin depth is a useful tool in understanding the propagation of EM fields during a CSEM experiment.

3. By describing electric field strengths in terms of dimensionless amplitudes (Sinha number), the range cubed component of field amplitude decay is removed. This allows more detail to be seen in the signal amplitudes.

4. The amplitude PE_{max} of the semi-major axis of the polarisation ellipse is far less dependent on geometry, and is therefore a more robust estimate of the electric field.

5. The variation of electric field amplitudes with source-receiver azimuth can be used to identify buried conductive anomalies such as an axial magma chamber.

Chapter 3

Lucky Strike: geological setting and data collection

This chapter provides a description of the Lucky Strike ridge segment and a summary of the 1999 MADRIGALS (Mid-Atlantic Deep-towed Resistivity and Induction Geophysics At Lucky Strike) research cruise, on which the EM data used in this thesis were obtained.

3.1 Geological context

The Lucky Strike segment of the Mid-Atlantic Ridge (MAR) is situated between 37°05'–33' N and 32°10'–25'W, at a depth of between 1600 m in the middle of the segment and 3000 m at the segment ends (Figures 3.1 & 3.2). It is on the southern limit of influence of the Azores hotspot, hence the shallow depth and enriched composition of the oceanic crust (Langmuir et al. 1997, Schilling et al. 1983). However, unlike adjacent segments to the north, Lucky Strike exhibits the typical median valley morphology of a slow-spreading ridge.

A summary of the recently completed cruises to the region is shown in Table 3.1. The seabed morphology within the segment has been extensively surveyed. Simrad EM12 swath bathymetry collected during the SIGMA campaign densely covers the overall segment (Detrick et al. 1995). This was the source of the bathymetry data used during the MADRIGALS cruise, and can be seen in Figure 3.3. Two tracks of high resolution TOBI sidescan sonar were obtained during the HEAT experiment (German et al. 1996), with a 6 m resolution over a width of nearly 9 km. More recently, higher resolution swath bathymetry of the summit of the seamount was collected during the LUSTRE'96 cruise (Scheirer et al. (2000) and Figure 3.4), and multibeam bathymetry from Lucky Strike and neighbouring segments were obtained during the Sudaçores cruise (Cannat et al. (1999) and Figure 3.2).

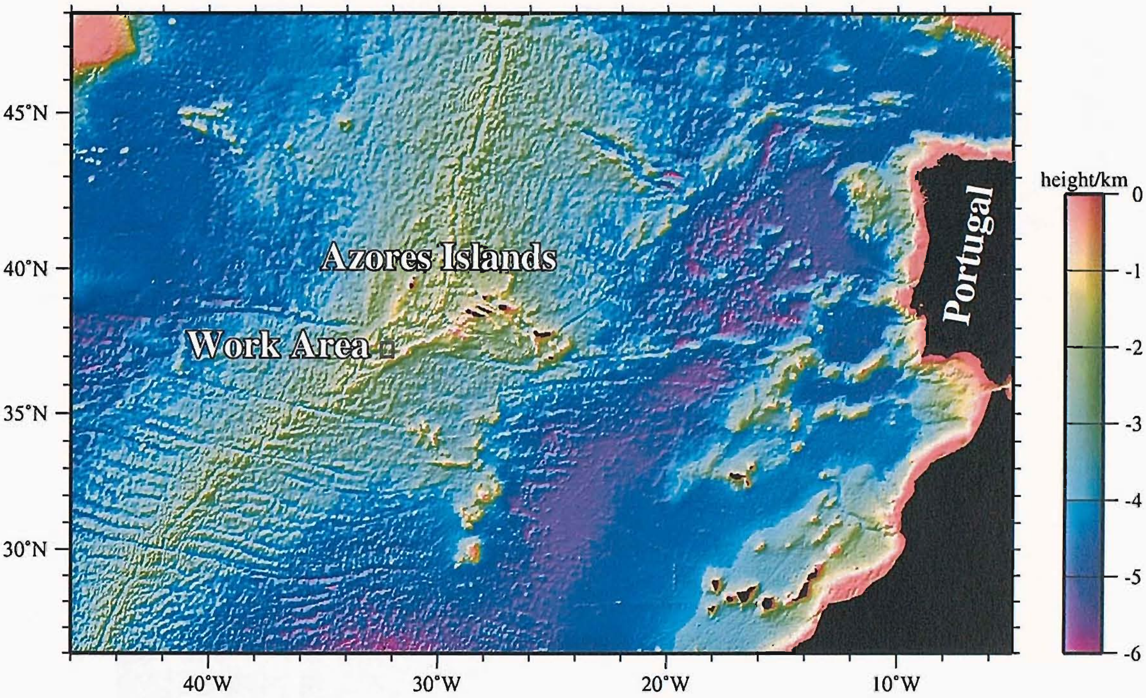

Figure 3.1: The location of the Lucky Strike segment of the Mid-Atlantic Ridge, in the central North Atlantic. The box corresponds to the area covered by Figure 3.3. Bathymetry with a resolution of two minutes from Smith & Sandwell (1997).

A well-defined mantle Bouguer anomaly low over the centre of the segment (Detrick et al. 1995) is consistent with the crustal thickening associated with models of focussed, buoyancy driven magma supply.

The main topographic feature of Lucky Strike is a large (13 km wide and ~430 m high) axial volcanic seamount situated at the middle of the segment. The summit of this seamount comprises a north-south graben, separating a narrow volcanic ridge to the west from three volcanic cones to the east. Most of the surface of these cones is covered by pillow constructs and volcanic breccia. This volcanic breccia, comprising basaltic glass and plagioclase crystals, has become indurated by silica and barite, producing a highly impermeable surface, referred to as 'hydrothermal slab' (Langmuir et al. 1997). The upper surface of the slab is broken into plates ~5 m across, however the slab's thickness is unknown.

The chemical and physical characteristics of basaltic lavas over the region suggest that the Lucky Strike seamount is a composite structure, made up of rocks of variable age (Langmuir et al. 1997). All analysed basalt samples are enriched in incompatible elements relative to MORB, falling into two distinct compositional groups. The older, highly vesicular basalts found on the summits of the cones are particularly enriched in incompatible

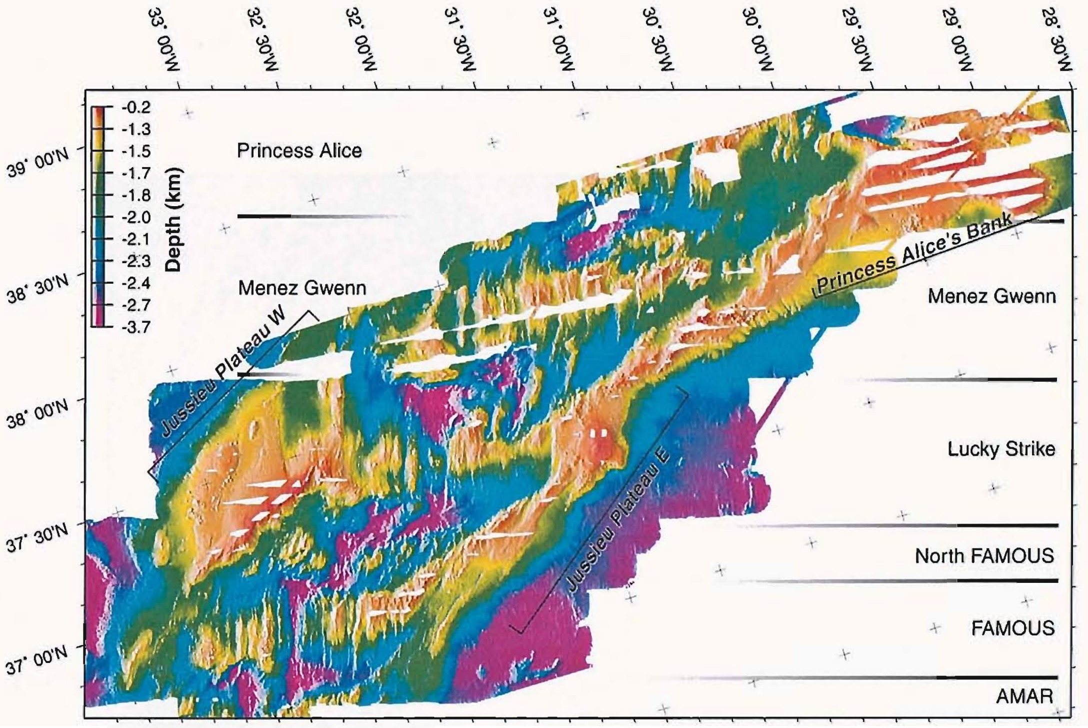

Figure 3.2: The bathymetry of Lucky Strike and adjacent segments, obtained during the Sudaçores cruise. From Escartin et al. (2001).

elements; younger, less vesicular lavas recovered from both the southern cone's north slope and a recently-formed lava lake in the depression between the summit cones, are less enriched.

Although Fouquet et al. (1995) suggest that the summit depression is a caldera, Langmuir et al. (1997) argue that, based on the summit morphology and lava chemistries, the depression is merely a by-product of the late-stage constructive volcanism which formed the cones. Also, there is no evidence of circumferential structures on the summit. Instead, a general N-S tectonic lineation covers much of the area, cutting the seamount flanks and parts of the cones. In places, particularly on the eastern side of the seamount, these lineations are associated with ridges of errupted pillow basalts. This suggests that the faulting structure in the region has influenced the volcanic construction at Lucky Strike (Langmuir et al. 1997).

3.1.1 Hydrothermal activity

Hydrothermal activity at Lucky Strike was first discovered when dredging during the FAZAR cruise in 1992 recovered part of a sulphide chimney, covered in live mussels (Langmuir et al. 1993). A water column survey during the same cruise detected anomalous Mn signals, confirming that the hydrothermal system was currently active.

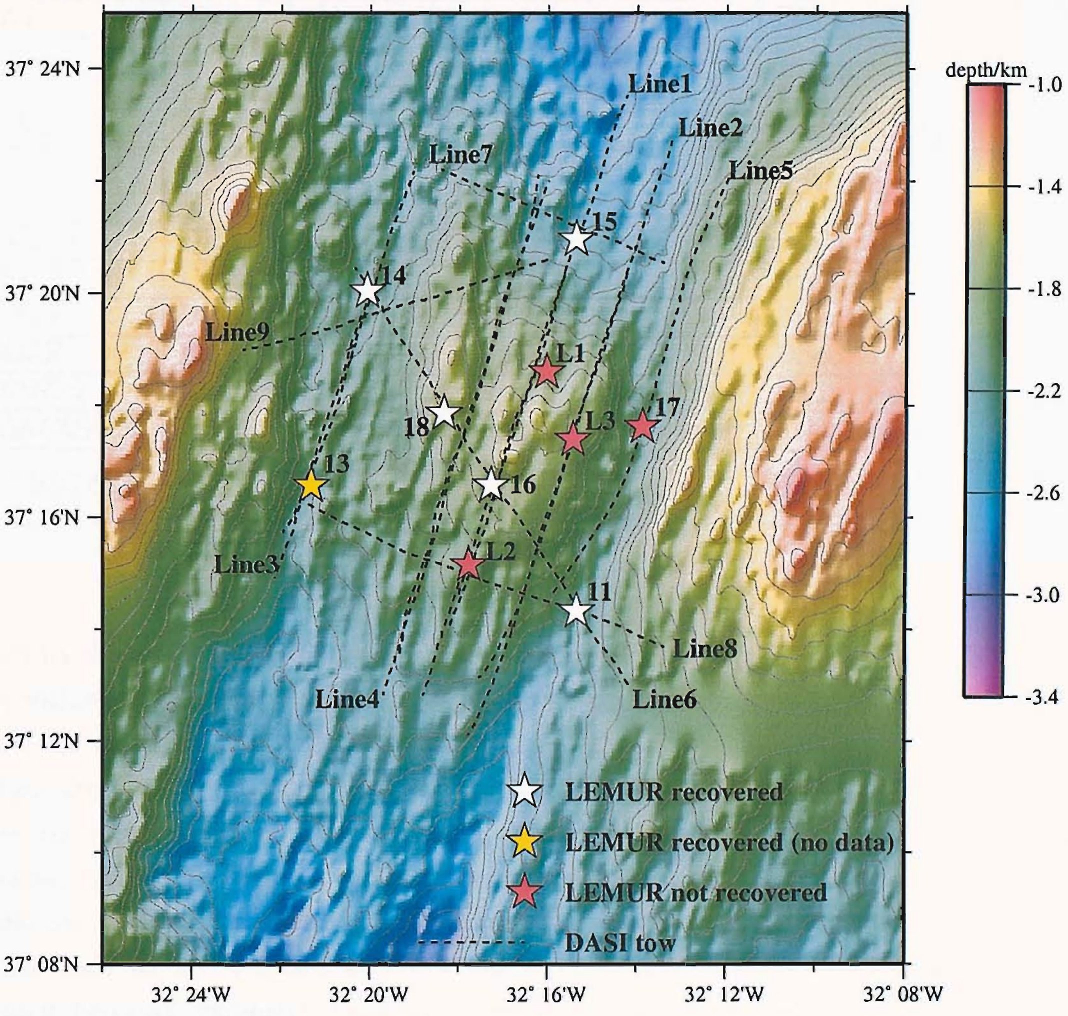

Figure 3.3: Locations of DASI as it was towed along the nine experiment lines and the positions of the LEMUR ocean bottom instruments (deployment positions for the those LEMURs that were not recovered, or were recovered, but were found to contain no data), overlaying a swath bathymetric chart of the Lucky Strike segment of the Mid-Atlantic Ridge (bathymetry from the SIGMA cruise (Detrick et al. 1995)). Contour interval 100 m. See Section 4.1 for further information on instrument location.

Cruise	Brief description	Ship/Equipment	Year
FARA-SIGMA	Multi-beam bathymetry/gravity	Atalante	1992
FAZAR	Basalt and water column sampling	Atlantis II	1992
AII129-6	First Alvin dives on Lucky Strike	Atlantis, Alvin	1993
HEAT	Tobi and side-scan sonar	Discovery	1994
DIVA 1	Hydrothermal site submersible sampling petrology, hydrothermal chemistry	Nadir, Nautile	1994
DIVA 2	Submersible, sampling biology	Nadir, Nautile	1994
LUSTRE	Argo, Jason and AMS-120 surveys of central seamount	R/V Knorr	1996
FLORES	Diffuse hydrothermal fluid sampling	Atalante, Nautile	1997
CRISTA I/II	Collect fish and crustaceans	Arquiplago	1997
LUCKY	Diving and hydrothermal sampling	Atlantis, Alvin	1997
FLAME	Fluxes at AMAR Experiment	Discovery	1997
FLAME-2	Hydrography and sampling	Nadir, Nautile	1998
SUDAÇORES	Gravity, magnetics, bathymetry & dredging	Atalante	1998
MADRIGALS	Mid-Atlantic Deep-towed Resistivity and Induction Geophysics at Lucky Strike	Darwin, DASI	1999

Table 3.1: Previous cruises to Lucky Strike

Whilst there is some evidence for other sites of significant hydrothermal activity further south within the segment (Fouquet et al. 1994), all activity observed to date has been centred around the axial volcano.

High temperature focused and low temperature diffuse flow have both been observed around the summit region of the seamount. Many of the high temperature vents are located in clusters around the central lava lake in the depression between the volcanic cones, or in association with the N-S trending rifts (Figure 3.4). There is evidence that the hydrothermal field has been active for a substantial period of time (Langmuir et al. 1997): hydrothermally cemented breccias, extensive relict sulphides and small relict chimneys cover much of the seamount summit, particularly on its eastern side.

High temperature venting

High temperature vent fluids were first recovered from Lucky Strike by the submersible Alvin in 1993. Samples were taken from seven different vents (Colodner et al. 1993), and were found to lie in two distinct compositional groups. Southern vents, located on hydrothermal slab at a depth of between 1687 and 1708 m, produced fluids at between 297 and 325°C. Northern vents, located in an area of relict sulphides at a shallower depth of between 1618 and 1630 m, produced fluids at between 202 and 212°C. Northern vents were found to have

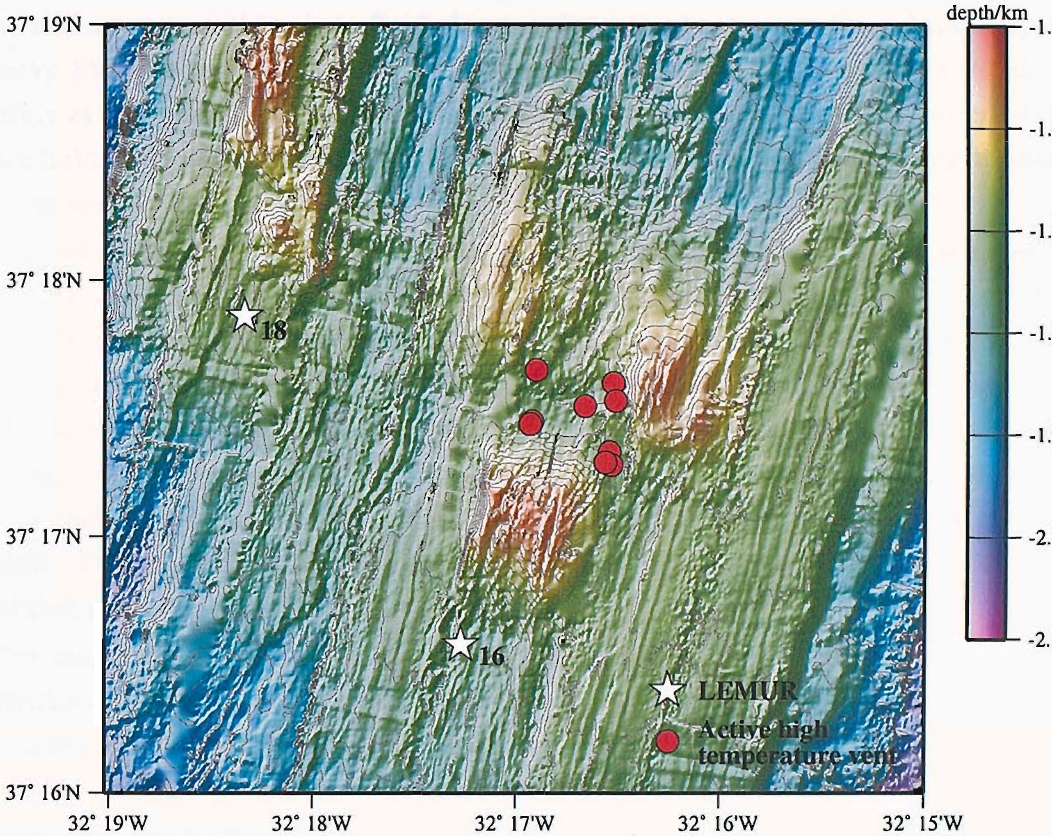

Figure 3.4: Locations of high temperature vents discovered on the summit of the Lucky Strike axial volcano. Two of the CSEM LEMUR receivers are also shown in this plot (see Section 3.2.3). High resolution bathymetry collected during the LUSTRE cruise (Scheirer et al. 2000).

higher concentrations of dissolved Si than most of the southern vents, as well as higher concentrations of Mg.

This distinction between northern and southern vents has remained in the literature, and has led to the suggestion that Lucky Strike high temperature fluids are sourced from two distinct regions (e.g. Langmuir et al. (1997)). However, subsequent dives in 1994 (Fouquet et al. 1994) and 1996 (Fornari et al. 1996) have sampled other high temperature fluids that do not easily fit into this classification scheme. For example, the vent Jason, found to the north west of the lava lake, is at a relatively shallow depth (1644 m) located within sulphide rubble, but produces high temperature fluid (308°C) with a high Mg concentration (7.29 mmol/kg). Also, the silica content of more recently sampled vents does not show a pronounced bimodal distribution (Von Damm et al. 1998).

Chloride levels of 20 % lower than seawater, found in vent fluid particularly to the south of the region suggest that these fluids have undergone phase separation. Phase separation at Lucky Strike is estimated to require temperatures of $\geq 355^oC$ (Von Damm et al. 1998), less than at other MAR hydrothermal fields due to its shallower depth. However, the lower surface fluid temperatures recorded suggest that the vent fluids have cooled prior to sampling, either by conduction, or due to mixing with cooler fluids.

Chloride depletion of only a few percent below seawater, found in other samples, is not sufficient to infer that phase separation has occurred: a small input of water, perhaps from mineral dehydration, or recharge of the hydrothermal system from greater depths (as salinity on the Atlantic decreases with depth) could also explain the measurements (Langmuir et al. 1997). However, as much of the early evidence for two distinct sources of high temperature fluids has been superceded by more recent measurements, a simpler explanation for small levels of chloride depletion would be that these fluids contain a higher proportion of entrained seawater. This mechanism is supported by the higher Mg concentrations of many of the fluids containing higher levels of Cl.

The maximum concentration of Si measured in the samples provides a constraint upon the shallowest depth below the seabed at which the fluids could have originated (Von Damm et al. 1998). At the temperatures measured, quartz should be the phase controlling dissolved Si content. Whilst Si may have precipitated out of solution before reaching the surface, no reasonable mechanism exists to increase Si concentrations above the quartz equilibrium level. For the maximum observed level of Si to be in equilibrium with quartz at the minimum temperature required for phase separation, the fluid must be at a pressure of at least ~300 bar. This pressure corresponds to a minimum formation depth of ~1300 m below the fluid exit point.

Several different models have been put forward to explain the relatively low concentrations of Li, Fe, Mn and rare earth elements, along with the low Sr/Ca ratios measured in the high temperature fluid. Klinkhammer et al. (1995) believe that Lucky Strike reaction zone temperatures are in the region of 350^oC, lower than the 400^oC found in other MOR hydrothermal systems. However, Von Damm et al. (1998) argue that whilst this would explain the rare earth element data, temperatures of 350^oC would not be enough to generate the observed levels of Cu in the fluids (of 10's of μmoles/kg in most samples). Based upon experimental results from Seewald & Seyfried (1990), they argue that temperatures of $\sim 400^oC$ are required.

If a reaction zone temperature of $\sim 400^oC$ exists at Lucky Strike, Von Damm et al. (1998) believe that a more likely cause for the concentrations mentioned above would be reactions between the hydrothermal fluid and a heavily altered, and relatively oxic substrate, at depths $\geq$1300 m below the seafloor.

Low temperature fluids

Low temperature diffuse flow has been recorded over much of the high temperature vent field (Langmuir et al. 1997), and water column studies have also suggested that diffuse flow extends across a wide region, down the flanks of the seamount (Wilson et al. 1996). However to date, the only detailed study of the low temperature flow has been carried out over the region of hydrothermal slab (Cooper et al. 2000), where diffuse flow (with temperatures from 8 to 130°C) discharges from the cracks in the surface of the slab, rather than through the impermeable slab plates.

Lithium concentrations in four of the samples collected were found to be elevated over the background seawater. These samples must therefore contain a proportion of high-temperature fluid (forming at temperatures >150°C); the range of measured fluid temperatures is consistent with the adiabatic mixing of ambient seawater with this hydrothermal fluid (Cooper et al. 2000).

The majority of the samples had concentrations of Li within the errors of seawater, but temperatures higher than expected from the adiabatic mixing relationships. Cooper et al. (2000) infer that the low temperature fluids are dominated by seawater that has been heated conductively by high temperature fluids circulating below the slab, rather than by mixing with these fluids. Furthermore, the lack of any removal of Mg or Li from the samples suggests that the low temperature fluids have a short residence time in the system. Finally, the lack of evidence for silica precipitation (the significant cement which forms the hydrothermal slab) from the diffuse fluids, along with evidence for the reactivation of high temperature vents in the region (Von Damm et al. 1998), suggest that the hydrothermal slab is not currently being formed, and is instead a relic of earlier hydrothermal activity.

Cooper et al. (2000) suggest a '2-layer' model of fluid flow to explain both the high and low temperature hydrothermal fluids observed around the region of the slab (Figure 3.5). High temperature fluids circulate within the seamount, but only vent onto the surface in regions where the hydrothermal slab has been breached. In other areas, smaller-scale low-temperature convective cells exist within the hydrothermal slab, being conductively heated by the high temperature fluids below, and in some areas becoming tainted with the high temperature chemical signature from the localised leakage of this fluid into the slab.

It is not currently known whether off-slab diffuse venting is dominated by fluids with a high temperature origin that have conductively cooled and/or mixed with ambient seawater. However, detailed near-bottom surveys carried out during the LUSTRE cruise has led Humphris et al. (2002) to propose that the permeability barrier created by cementation in the near-surface may be more extensive than previously thought, and not just limited to the visible areas of hydrothermal slab.

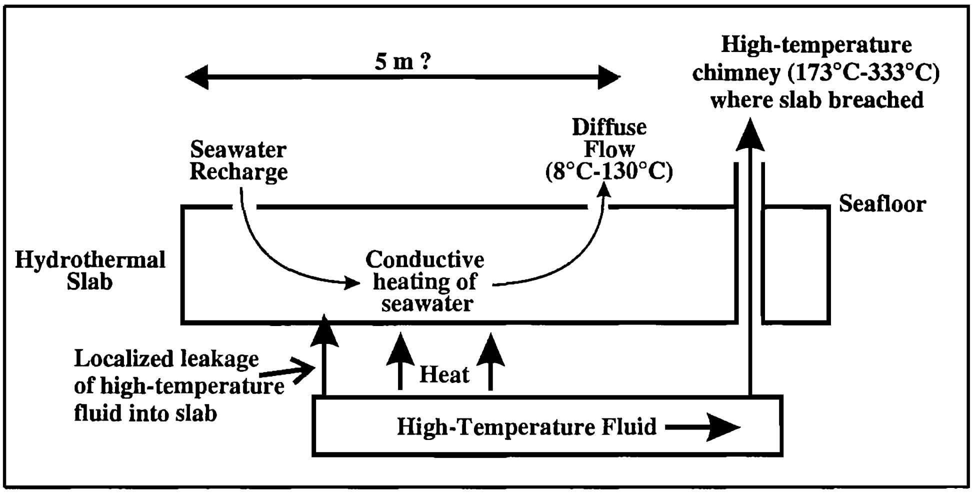

Figure 3.5: Conceptual model for the diffuse flow system at Lucky Strike based on the chemical composition of the diffuse fluids. The hydrothermally-cemented slab creates a permeability barrier through which the high temperature fluids cannot pass. Low temperature diffuse flow effusing from cracks in the slab show that, at least near the surface, the slab is not completely impermeable. Reproduced from Cooper et al. (2000).

3.1.2 Volcanic-tectonic processes at Lucky Strike

Humphris et al. (2002) provide a concise summary of our current understanding of the interrelationship between volcanism, tectonism and hydrothermal activity over the Lucky Strike segment. It is clear from the large-scale faulting in the median valley that the ridge segment as a whole is dominated by amagmatic spreading. However, along-axis melt focussing under the middle of the segment and associated high magma supply rates have provided sufficient thermal energy to sustain hydrothermal activity over a relatively long period of time. It is difficult to calculate an absolute time since the onset of hydrothermal activity at Lucky Strike. However on the basis of spreading rates, the 1 km wide hydrothermal field represents about 45 000 years of spreading. Humphris et al. (2002) therefore suggest that the "operative timescales of hydrothermalism are likely to be hundreds to thousands of years."

Humphris et al. (2002) propose a form of volcano-tectonic cycling to explain the temporal variations in hydrothermal activity observed, as well as to provide a mechanism for repeated focussing of upwelling fluids along the same near-surface fluid flow pathways, as would be required to construct a large hydrothermal deposit within the confines of the summit depression. During periods of amagmatic extension, the active north-south fault zones provide channels for high temperature fluids to exit over a wide area of the seamount summit, producing the extensive hydrothermal deposits and sulphide mounds found. During times of magmatic injection, surface lava flows serve to seal many of the near-surface high temperature conduits, forcing the high temperature fluids to pond below the high permeability barrier, cooling conductively, and exiting the system through more diffuse, low-temperature venting. This cooling fluid also cements the clastic material which it passes through (forming hydrothermal slab), further sealing the system.

Evidence of large-scale relic hydrothermal deposits, extensive sealing of the near-surface by recently-formed lava flows and hydrothermal slab, a seismic swarm with characteristics of magma dike emplacement (Dziak et al. 2003), and the conductive heating of shallow low-temperature convection cells, leads the present-day Lucky Strike seamount to represent this volcanically controlled phase of activity and implies that a magma chamber does currently exist under the centre of the segment.

3.2 The MADRIGALS cruise

On Tuesday 21 September 1999, RRS Charles Darwin sailed from Southampton, UK on the MADRIGALS research cruise (Sinha 1999). This cruise was a collaboration between the University of Cambridge, UK, the Universities of Lisbon and Algarve, Portugal and HALO Ltd, Reykjavik, Iceland. Basic ship time was funded by the UK Natural Environment Research Council (NERC), and all other research costs were funded by the ISO-3D project under the European Union Mast-III programme. The main objective was to carry out a controlled source electromagnetic (CSEM) sounding study of the upper and middle crust beneath the central volcano of the Lucky Strike segment of the Mid-Atlantic Ridge.

3.2.1 The Source

The DASI (Deep-towed Active Source Instrument) transmitter was initially developed at the University of Cambridge (Sinha et al. 1990), where it carried out a number of successful marine electromagnetic surveys (Evans et al. 1991, MacGregor et al. 1998, MacGregor et al. 2001). The ISO-3D project provided funding for further development of the source both in Cambridge and at the Southampton Oceanography Centre.

Capable of operating in water depths of up to 6 km, DASI is a 100 m HED (Figure 3.6) with a dipole moment of $\sim 10^4$ Am. During operation, the transmitter is deep-towed at a forward speed of ~ 0.7 ms^{-1}, within 30–80 m of the seabed to ensure good electromagnetic coupling with the seafloor. DASI is equipped with a pressure gauge and acoustic altimeter to constantly monitor its depth and height above the seafloor. Upcoming topography can be monitored with the ship's echo sounder. With this information, it proved possible to tow

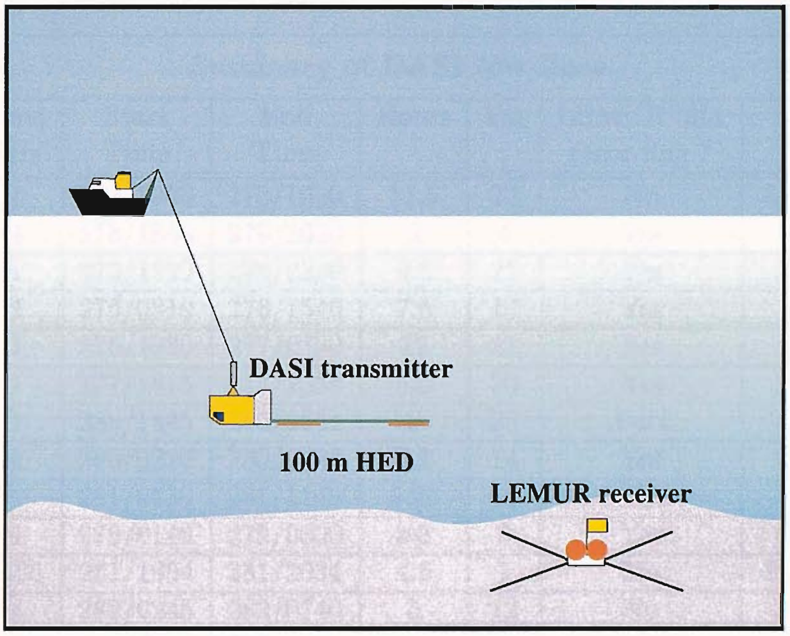

Figure 3.6: A schematic of the DASI transmitter system, and a LEMUR ocean-bottom recorder (not to scale).

DASI close enough to the seafloor during transmission tows, over the most severe topography encountered to date by the DASI transmitter.

3.2.2 Receivers

The LEMUR ocean bottom instruments record two orthogonal components of the horizontal electric field at the seafloor with a pair of 13 m HED arms. Electronics are housed within one of two glass spheres, the other being used for buoyancy. The instruments are deployed attached to a ballasted bottom weight via an accoustic release system, allowing the buoyant instrument to return to the surface at the end of the experiment.

A total of ten LEMURs were deployed during the experiment: four LEMUR '95s, with a recording time of 5 days, incorporated upgrades paid for by the ISO-3D funding; six LEMUR '99s, wholly paid for by ISO-3D funding, were an updated design with disk capacity for over 9.5 days of data. Successful tests on the prototype of the new instruments had been carried out aboard RRS Discovery during July 1998 (Sinha et al. 1998a).

Summary of DASI tow lines

Line No.	Tow No.	Freq /Hz	Start Time	End Time	Hours	km	LEMUR '95s recording ?	Comments
1	1	1	274/2300	275/1030	11.5	22	No	Almost whole line
1	6	1	278/1850	278/2050	2	4	Yes	S end only
2	2	1	275/1720	276/0250	9.5	21	Yes	Whole line
3	3	1	276/0810	276/1540	7.5	17	Yes	Whole line
4	4	1	276/1930	277/0730	12	21	Yes	Whole line
5	5	1	277/1815	277/2355	5.5	20	Yes	Whole line
6	9	1	280/1445	280/2344	9	23	Part	Whole line
7	8	1	280/0220	280/0835	6.2	14	Yes	Whole line
8	10	1	281/0630	281/1145	5.25	15	No	Whole line
9	7	1	279/0140	279/0500	3.3	8	Yes	SW half only
3	11	0.25	281/1604	281/2034	4.5	7	No	From L13 to L14
1	12	4	282/0245	282/0740	5	12	No	Central part
2	13	4	282/0950	282/1550	6	12	No	Central part
4	14	4	282/1900	283/0230	7.5	16	No	Almost whole line

Table 3.2: A summary of completed DASI tow lines. The older LEMUR '95 instruments recorded only part of the experiment.

3.2.3 Experimental geometry

LEMUR instrument locations and DASI tow lines can be seen in Figure 3.3. Experimental geometry was designed to maximise the geometric coverage of the target seamount. Good weather conditions during the cruise led to very few changes being made to the proposed geometry. Tows on some transmission lines were curtailed due to an unfavourable wind direction, but missing sections were repeated when more favourable conditions prevailed (e.g. line 1 at 1 Hz was covered in full by a combination of tows 1 and 6). A summary of completed DASI tows can be seen in Table 3.2.

Of the ten LEMUR instruments deployed, only five were recovered with data. LEMUR13 was found upon recovery to have suffered an ADC malfunction and contained no data; and four instruments were lost, three due to faulty acoustic release cards, and one when its light failed during a night-time recovery.

However, the five recovered instruments still provide good target coverage: two were located on the ridge axis, and four were arranged in a transect across the ridge and axial seamount. Furthermore, LEMURs 16 and 18 were '99 instruments, and therefore recorded all completed transmission tows.

Navigation

Ship positioning was achieved throughout the cruise by differential GPS (DGPS), the experiment area being just within range of the Azores DGPS base station.

A long base line (LBL) navigation system was used to obtain positions for the source during transmission tows. This used six seafloor transponders tethered at a height of 200 m above the seafloor.

Acoustic ranges were taken to all ocean bottom instruments (LEMURs, navigation transponders and current meters) once they had arrived at the seafloor, as the ship was en-route to the next deployment position. Once all instruments had been deployed, the ship spent further time on an acoustic survey of the target area, to ensure enough direct ranges had been obtained to all of the instruments to accurately calculate their position.

For periods when the source was active, a position for DASI was obtained with the aid of a relay transponder attached to the vehicle. In general, the navigation system worked well, with consistent and reliable ranges obtained from the seafloor transponders to slant distances of 12 to 15 km. However, the relay transponder on DASI only partially functioned, with direct ranges to the instrument being obtained only during alternate ranging cycles. Whilst this meant that a real-time fix on DASI was unavailable, all received ranges were recorded for later processing (Section 4.1.2).

The DASI vehicle also carried a pressure meter to determine its depth, and an acoustic altimeter to constantly monitor its height above the seafloor. This provided critical information for the winch controller, to ensure DASI was flown at the optimum height above the seabed. The data received were recorded by DASI's shipboard computer and used to further constrain the location of DASI during post-processing.

3.2.4 Other data collected

A number of other data types were collected during the cruise in addition to the CSEM study. An array of 4 current meters was deployed across the narrowest part of the axial valley and the volcano (Figure 3.7). These instruments, on a 200 m tether, recorded near-bottom water velocity, temperature and electrical conductivity. Two of them (C2 and C4) also carried navigation transponders, augmenting the acoustic navigation array.

Additional data on water column physical properties were obtained by launching a series of expendable bathythermographs (XBTs) at intervals along the current meter profile. At the start of the cruise, a sound velocity meter was also lowered through the water column to within 200 m of the seafloor (Figure 3.7). As well as complementing the XBT and current meter data, the sound velocity profile was essential for accurate calibration and use of the

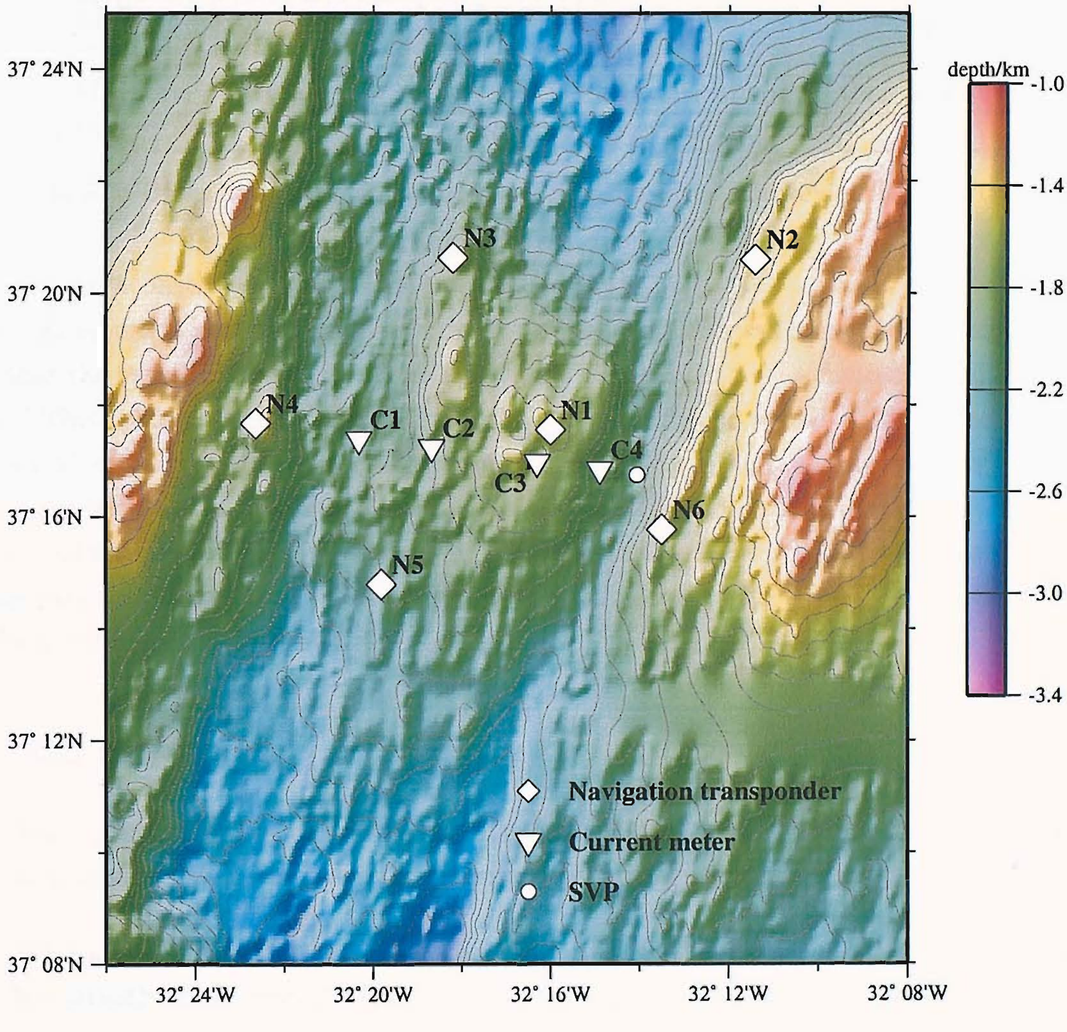

Figure 3.7: The navigation transponders and current meters deployed during the experiment. The position of the single sound velocity profile is also shown.

Data/Instrument type	Times when recorded
DGPS	Whole cruise
Gravity	Whole cruise
10 kHz echo sounding	Most of cruise
ADCP	From leaving Azores until return
XBTs	Eight deployed along line of current meters
Current meters	During time on seabed (Figure 3.7)
Magnetic field	During DASI tows & at some other times
SVP	Single vertical profile (Figure 3.7)

Table 3.3: Other data collected during the cruise. See text for more detailed information.

long baseline acoustic navigation system (Section 4.1).

A hull mounted acoustic Doppler current profiler (ADCP) was run continuously from the time that the vessel departed from the Azores until its return to the Azores at the end of the cruise. Throughout most of the cruise, 10 kHz precision echo sounder data were collected. The vessel was fitted with both a Lacoste and Romberg sea gravimeter, and a total-field proton precision magnetometer. The gravimeter ran throughout the cruise, with base station ties in Southampton at the start and end. The magnetometer was run throughout the DASI towing period, and at other times when the scientific programme permitted. A summary of the data collected can be found in Table 3.3.

3.3 Summary

1. The Lucky Strike segment of the Mid-Atlantic Ridge, to the south of the Azores Islands, is dominated by a large hydrothermally active axial seamount.

2. Whilst much of the segment is undergoing amagmatic extension, the central seamount is currently experiencing a period of active magmatism, or has done so in the recent past.

3. Focussed high-temperature venting at the seamount summit is accompanied by extensive diffuse fluid flow both at the summit, and down the flanks of the seamount.

4. Evidence of extensive relict hydrothermal structures such as silicified slab and extinct hydrothermal chimneys imply that the hydrothermal system has been active for a long period of time. They also may reflect shorter-term episodic variations in the extent of hydrothermal activity.

5. Estimating absolute ages of hydrothermal events at Lucky Strike is difficult. However, based on the size of the hydrothermal field, the operative timescales of hydrothermalism are likely to be hundreds to thousands of years. A maximum possible age of the Lucky Strike vent field is of the order of 45 000 years.

6. A recently-proposed model of volcano-tectonic cycling (Humphris et al. 2002) predicts that hydrothermal deposits, along with recent lava flows, are currently creating a low porosity zone in the crust near the surface over much of the area. This would 'seal' high temperature hydrothermal fluids within the seamount, where they would cool conductively before percolating to the surface as low-temperature diffuse discharge.

7. Whilst the Lucky Strike hydrothermal system has been a site of intense biological, chemical and surface geophysical studies over the past 10 years, no studies prior to 1999 had tried to image the subsurface using geophysical techniques.

8. The MADRIGALS research cruise successfully collected the first 3-dimensional CSEM dataset, over the central portion of the Lucky Strike segment.

9. The DASI transmitter completed transmission tows with a total length of 212 km over a nine day period, with few problems encountered.

10. A long baseline acoustic navigation system should have been capable of providing real-time instrument locations, however a malfunction in the relay transponder in DASI meant that further post-processing of the navigation data was required.

11. A number of LEMUR instruments were lost; a total of five were recovered which had recorded data. These still provide good coverage of the target area.

Chapter 4

Data Processing

This chapter discusses the processing and analysis stages required to recover the experimental geometry, along with processing of the raw time series EM data. Uncertainties and noise levels in the data are also discussed.

4.1 Instrument location

The onboard differential GPS recorded the location of the ship every minute, providing reliable ship locations (with uncertainties of 2–3 m) for the period of the experiment. All cruise navigation was calculated in Universal Transverse Mercator (UTM) coordinates with a central meridian of 33°W. Ship positions were converted using the WGS-84 spheroid and reference frame.

4.1.1 Ocean bottom instruments

During instrument deployment and for a period thereafter, the ship extensively covered the survey area, measuring ranges to ocean bottom instruments in order to ensure that a good geometric spread of acoustic ranges was obtained.

LEMURs and navigational array transponders were located from these ranges using the simulated annealing method described in MacGregor (1997), used by Billings (1994) for the analogous problem of earthquake location. The code used was broadly similar to that of MacGregor (1997), with the exception of the raytracing algorithm. The code of MacGregor (1997) was only capable of tracing rays down through the water column. The new code was written in order to allow arbritrary raypaths through the water, as well as sea surface reflections (as required for DASI location - see Section 4.1.2) to be modelled.

Raypaths through the water column were calculated from the sound velocity meter depth

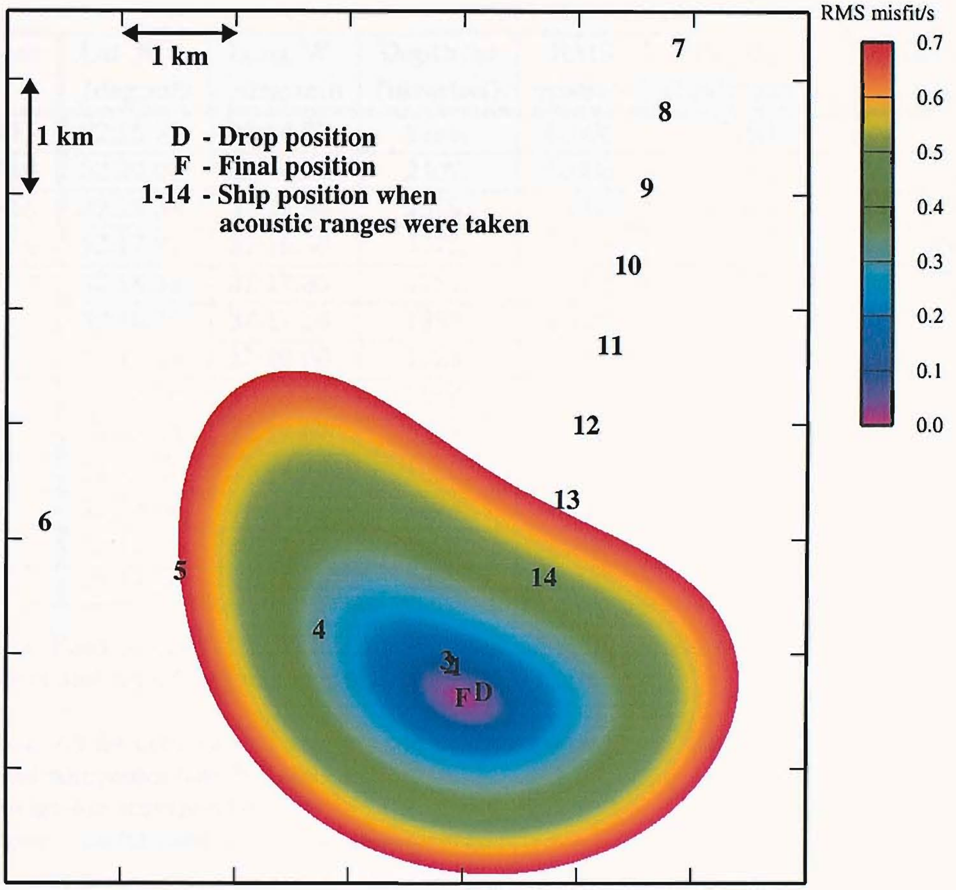

Figure 4.1: A 2-dimensional slice through the misfit function obtained from 3-dimensional acoustic relocation of LEMUR11. The coloured 'bullseye' corresponds to a horizontal slice at the depth of the best-fit instrument location. The instrument has drifted about 100 m laterally from its drop location. Its final location is well-constrained by ranging from two orthogonal ship tracks.

profile using Snell's Law between adjacent velocity layers. An inversion process was then carried out using a simulated annealing algorithm to minimise the mean square misfit between the measured and calculated travel times.

Typically 15 ranges were used to locate each instrument, along orthogonal ship tracks where possible. The inversion algorithm was set to exit when the root mean square (RMS) misfit fell below 0.01 s (about 15 m in seawater).

As the raytracing forward modelling could be completed very quickly (typically, a fraction of a second on a standard PC), it was also possible to investigate the shape of the resulting misfit function, in order to ensure that the acoustic ranges produced a well-behaved global minimum (Figure 4.1).

Instrument	Lat N /deg:min	Long W /deg:min	Depth/m (inverted)	RMS misfit/s	Depth/m (bathymetry)	Orientation[*] /degrees
LEMUR11	32:15.35	37:14.33	2186.	0.005	2193.	012.
LEMUR14	32:20.08	37:20.04	2102.	0.008	2135.	022.
LEMUR15	32:15.38	37:20.96	2369.	0.01	2344.	256.
LEMUR16	32:17.27	37:16.58	1775.	0.006	1776.	258.
LEMUR18	32:18.34	37:17.86	1721.	0.008	1715.	232.
T1[†]	32:16.00	37:17.56	1399.	0.002	1602.	-
T2	32:11.42	37:20.60	1328.	0.004	1543.	-
T3	32:18.20	37:20.64	1586.	0.004	1813.	-
T4	32:22.64	37:17.67	1377.	0.006	1632.	-
T5	32:19.81	37:14.79	1850.	0.005	2093.	-
T6	32:13.50	37:15.77	1474.	0.003	1586.	-
C2[‡]	32:18.67	37:17.24	1926.	0.002	1906.	-
C4	32:14.89	37:16.84	1956.	0.005	1964.	-

Table 4.1: Positions of LEMUR instruments and navigational array transponders. Navigation transponders and curent meters were deployed on 200 m tethers.

---

[*] See Section 2.3 for definition. These are the modelled orientation values, not those obtained from the onboard compasses (see Section 4.4.1).

[†] T# – Navigation transponder.

[‡] C# – Current meter used in the navigation array.

The final instrument locations obtained are listed in Table 4.1. All instruments have been located with an uncertainty of better than 15 m. Discrepancies between the inverted depths and those obtained from the bathymetry can be explained by a combination of the rough topography, and the limited resolution of the available bathymetry.

It is also necessary to obtain the orientation of the dipole arms of the LEMUR instruments. This is achieved by means of an onboard digital compass. However, analysis of orientation data from previous cruises (L. MacGregor pers. comm.) has highlighted the large inaccuracies in the recorded measurements. It has been suggested that the magnetic field associated with the LEMUR alkali batteries (located adjacent to the compass when the instrument is assembled) interferes with the compass. This shall be remedied in future cruises by the use of non-magnetic cells, although in an oceanic setting such as Lucky Strike, comprised of highly magnetic fresh basalt, the compasses may still prove to be of limited use.

In order to obtain the correct instrument orientations for this cruise (Table 4.1), an alternative method utilising simple forward modelling of the recorded EM data was carried out (Section 4.4.1).

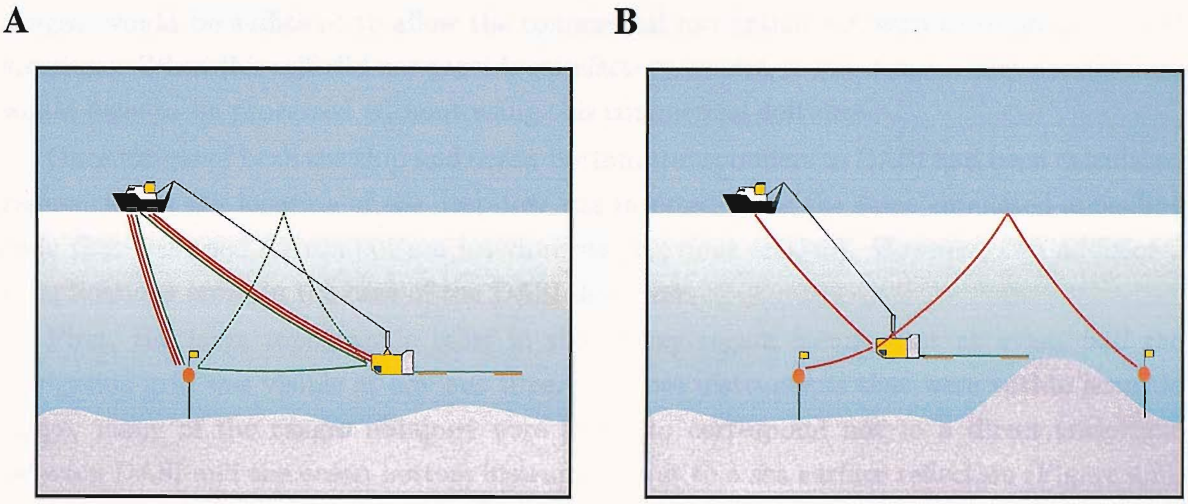

Figure 4.2: A schematic representation of the Long Baseline Acoustic Navigation system used to locate DASI during transmission tows. ***A***: the two transmission cycles. Red raypaths correspond to the direct cycle; green raypaths, to the relay cycle. Note that in areas of rugged topography, it was found that the section of the relay cycle between DASI and a navigation transponder would sometimes consist of a surface reflection (dashed green line). ***B***: DASI ranges obtainable geometrically by the combination of both acoustic cycles. There would need to be ranges to at least three transponders, as well as to the ship, in order to obtain a unique location for the DASI deeptow.

4.1.2 DASI deep tow

An array of six acoustic navigation transponders along with two current meters equipped with acoustic transponders, were deployed within the survey area (see Figure 3.7). The position of the DASI instrument during transmission tows was obtained with two alternating acoustic cycles. In the direct cycle, acoustic ranges were obtained from the ship to all transponders within range, including that on the deep-tow. During the relay cycle, a signal was transmitted from the ship to the relay transponder on DASI. This instrument sent a response that was received by all seafloor navigation transponders within range, which then replied to the ship.

In general, consistent and reliable ranges were obtained from these instruments to slant distances of 12 to 15 km.

By combining the times obtained from each acoustic cycle (Figure 4.2), it was possible to calculate the ranges of both the ship and ocean bottom transponders to DASI. With this information, the associated navigation software should have been able to provide real-time DASI locations. However during the cruise, DASI's relay transponder failed to respond during alternate cycles, meaning that this was not possible. It was hoped that subsequent editing of the datafiles, and replacement of lost ranges with the interpolated value from neighbouring ranges, would be sufficient to allow the commercial navigation software to re-process DASI locations. When this still did not provide satisfactory results, it was decided that the datafiles would have to be processed without using this commercial software.

Once ranges of both the ship and ocean bottom transponders to DASI had been calculated geometrically, the location of the deep-tow was inverted using the same simulated annealing code that was used for sea-bottom instruments (previous section). However, two additional complications arose in the case of the DASI deep tow.

First, the large topographic relief in the survey region meant that at most, half the navigation grid was visible at any one time. Of those instruments that were within acoustic range, many of the ranges obtained were found to correspond not to a direct traveltime between DASI and the ocean bottom instrument, but to a sea surface reflection (Figure 4.2). Once a new raytracing code was written that could handle such reflections, the large number of DASI locations being inverted required a semi-automated method of identifying the reflected traveltimes. This was achieved by inverting all possible combinations of reflected and direct traveltimes for each source location, and choosing the combination that produced the smallest RMS misfit.

It was found that this method correctly identified surface reflections about 95 % of the time. Cases where minimising misfit was not sufficient to identify reflections (when, for example, two incorrectly-identified ranges traded-off against each other, reducing the instrument misfit), could be quickly identified from the the code output, and corrected.

Secondly, the small number of acoustic ranges available at any one DASI location led to a correspondingly larger uncertainty in the inverted location. This produced an inconsistent apparent motion for DASI during transmission tows (the red line on Figure 4.3), that would be unsuitable for use in subsequent EM modelling.

An ideal source navigation code would minimise this problem by not inverting for each source position in isolation, but biasing the inverted position using information such as ship speed and bearing since the last obtained position. A simpler way of obtaining similar results is to remove the high-frequency ‘scatter’ in the DASI tow path obtained. As can be seen in Figure 4.3, it is not sufficient to smooth the source location in each of the three spatial dimensions; this would not guarantee the removal of ‘impossible’ source motion such as doubling-back along transmission tows. Instead, source locations were decomposed into three components related to ship location: vertical distance of the source from the ship (i.e. source depth); horizontal range of the source from the ship; and bearing of the source from the ship. All of these values should vary smoothly during a tow.

Frequency spectra of these three position components have the highest amplitudes at low frequencies, corresponding to real transmission tow variations. At frequencies above

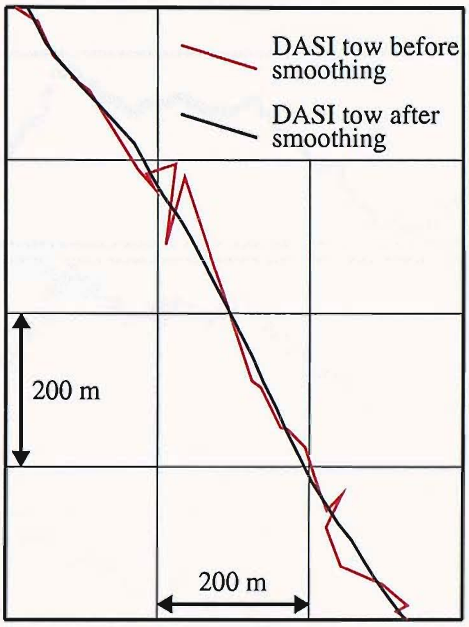

Figure 4.3: A plan view of part of the 1 Hz DASI transmission tow along Line 6, before and after smoothing of DASI locations. The smoothing has removed the apparent 'jumping' of DASI between successive inverted locations.

~0.001 Hz, corresponding to ~600 m of transmission tow, the spectra flatten out. A portion of these higher frequency variations correspond to the scatter in DASI positions that needs to be removed from the data.

High frequency scatter was removed by fitting least-squares best-fit polynomial curves (Press et al. 1992) through successive segments of data. This method was used in preference to a lowpass filter, as successive DASI locations did not occur at equal time intervals (FFTs had to use the average time period between successive positions). It was found that a 5th order polynomial over 25 datapoints produced the most consistent path for DASI through the water (Figure 4.4).

An FFT of the smoothed position components showed that the smoothing had reduced the amplitude of perturbations with a frequency above ~0.0013 Hz, corresponding to 460 m of DASI track, or on average 10 inverted DASI positions.

Estimation of the errors in DASI position is more difficult than for ocean bottom instruments. With fewer acoustic ranges available, the inversion process is not highly overdetermined and RMS misfit cannot be used as a reliable error estimate. Instead, the random errors in DASI positions were investigated by analysing the scatter in unsmoothed components compared to the smoothed data. Taking the smooth path to be the data mean, the standard

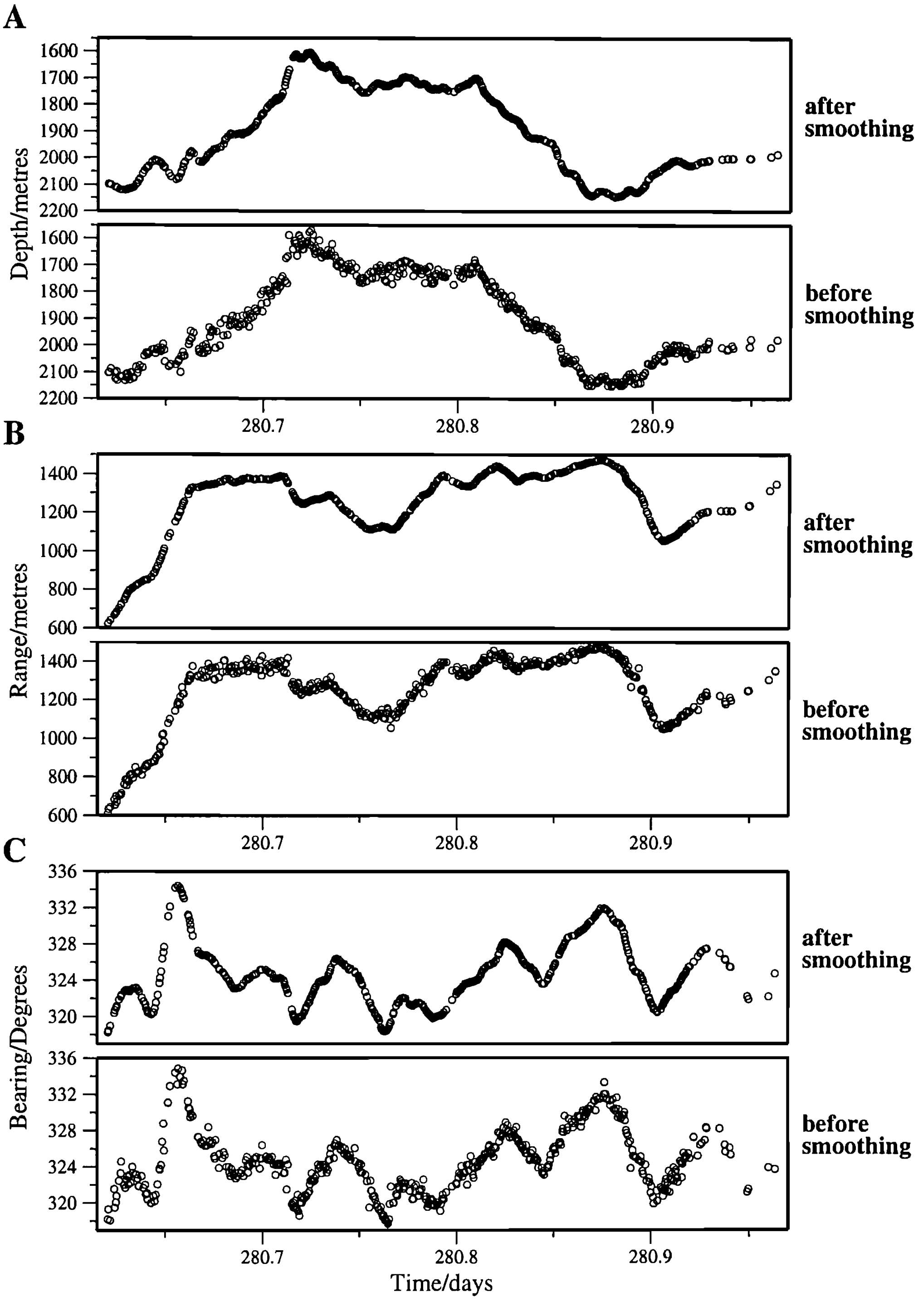

Figure 4.4: Smoothing the three components of DASI's location during the 1 Hz transmission tow along Line 6 (see Figure 3.3). *A* - depth of DASI below the sea surface; *B* - horizontal range from ship to DASI; *C* - bearing of DASI from the ship. The smoothed points were obtained by applying a sliding 5th order polynomial curve to successive datapoints.

deviations in the depth, range and bearing components of the unsmoothed data values were calculated to be 16 m, 16 m and 0.6^o respectively. These correspond to a standard deviation in position of ~26 m. As smoothing effectively averaged the data over ~10 datapoints, the standard deviation in the smoothed DASI positions is estimated to have been reduced to $26 \div \sqrt{10} \simeq 8$ m. This estimate only takes into account the random component of the error during each tow. Possible systematic errors are harder to quantify.

As well as souce position, CSEM modelling also requires the dipole orientation to be known. At the time of the MADRIGALS cruise, the DASI transmitter was not equipped with an acoustic transponder at the far end of its neutrally-buoyant streamer, so no direct measurements of dipole orientation were possible. A first-order estimate of dipole orientation is that it streams behind DASI, following the tow line. A better estimate could be achieved if the water flow pattern over the survey region was known. However, the water velocity data from the four current meters record a complicated tidal flow pattern over the rugged topography of the Lucky Strike seamount (see Appendix B). Any attempt to alter the dipole orientation estimate based on local water flow would therefore probably add as many errors to the orientation as it removed. Final DASI positions were therefore taken to be half-way along the dipole, oriented along the tow line (obtained from the smoothed track).

4.2 Source fields

The DASI transmitter generates a quasi-square wave at the required transmission frequency. A high-voltage 256 Hz sine wave is transmitted to the vehicle via the armoured coaxial towing cable, from the shipboard power supply. This signal is then rectified and its polarity switched each time the required number of zero-crossings have been made.

It is important to accurately evaluate both the source waveform and transmission frequency. Waveform characteristics affect the amount of energy present in each transmission harmonic, whilst the peak in received signal amplitude may be missed if the transmission frequency is not known.

Continuing development of the DASI transmitter led to an improvement in the source performance at Lucky Strike over previous experiments. The source generated a symmetric, stable waveform for the period of the experiment. However source transmission frequencies, whilst improved (during the RAMESSES experiment source frequency drifted and jumped by as much as 0.1 Hz (MacGregor 1997)), were still not accurate enough to rely upon without independent constraints. Since source frequency is derived from the 256 Hz sine wave, it is reliant on the precision of this carrier wave: during the Lucky Strike cruise, the 256 Hz signal was based on a crystal within the PSU, which drifted by several seconds per hour.

4.2.1 Source waveform

The source waveform was evaluated by monitoring the DASI output with an oscilloscope during a deck test both prior and subsequent to deployments, and photographing the results (Plot A, Figure 4.5).

No significant variation in the waveform was detected over the period of the cruise. It can be seen from the photograph that the sharp edges of the rectified 256 Hz carrier wave have been smoothed into a far more sinusoidal waveform at 512 Hz. This is an important observation, as a sinusoidal carrier wave produces a square wave with lower energy levels in each harmonic than the corresponding rectified carrier.

A synthetic version of the waveform was made from the combination of a 512 Hz sinusoid, a square wave at the transmission frequency, and an exponential decay between polarity switches (Plot B, Figure 4.5). An FFT was then carried out on this waveform (Plot C), producing the amplitudes of the required harmonics.

DASI logs from the cruise show that the transmission output current remained stable at 276 A (peak-to-peak) throughout the cruise. With this, and the fractional amplitudes of transmission harmonics, the source dipole moment at each frequency of transmission (Table 4.2) was calculated as follows:

$$\text{SDM} = \text{Output Current} \times \text{Harmonic Fractional Amplitude} \times \text{Dipole Length}. \qquad (4.1)$$

Harmonic	Fractional Amplitude	Source Dipole Moment /Am
1	0.9931	13700.
3	0.3310	4568.
5	0.1986	2741.
7	0.1419	1958.
9	0.1103	1522.

Table 4.2: Source dipole moments up to the ninth harmonic for the source waveform transmitted during the MADRIGALS cruise.

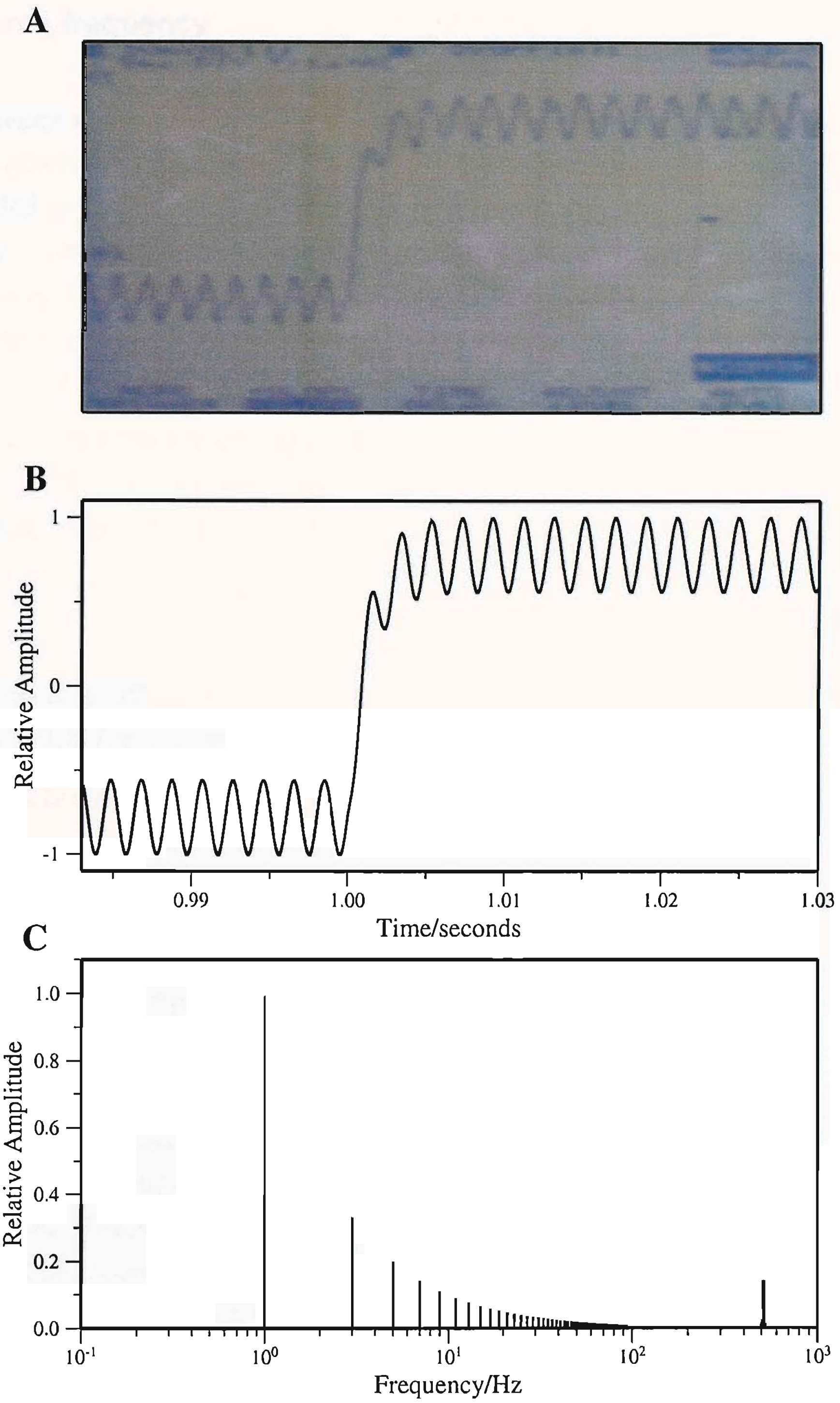

Figure 4.5: Modelling the DASI transmission waveform. Plot *A* is an image of the waveform recorded by an oscilloscope during a DASI deck test. This has been accurately reproduced in Plot *B*. The frequency content of the waveform is shown in Plot *C*: the primary transmission frequency and odd harmonics of the 1 Hz square wave can be seen, along with a spike (and accompanying harmonics) at 512 Hz from the rectified 256 Hz sinusoids.

4.2.2 Source frequency

Source frequency was constrained by analysis of the data recorded on the DASI piggyback logger, and by relative phase data from the LEMUR instruments (Section 4.3.2). The piggy logger recorded useful information intermittently throughout the 1 Hz transmission period of the cruise. The source waveform obtained during these periods, whilst being severely distorted due to the A.C. coupling of the logger, is sufficient to reconstruct the polarity switches in the waveform (Plot A, Figure 4.6) and therefore recover the waveform frequency for the majority of the experiment.

It is probable that the source frequency will not lie exactly on a discrete harmonic returned from a conventional FFT without careful choice of data segment length (MacGregor 1997). For this reason, a least squares fit to the function

$$f(t) = \sum_i a_i \cos(\omega t) + b_i \sin(\omega t) \tag{4.2}$$

was used (Press et al. 1992), where ω is the fundamental transmission frequency ($i = 1$). Odd harmonics ($i = 3, 5, 7, 9 \ldots$), were calculated as required.

In order to obtain the 1 Hz transmission frequency from the reconstructed piggy log data, 64 second data segments were taken. For each of these, fundamental signal amplitudes

$$A_i = \sqrt{a_i^2 + b_i^2}, \qquad i = 1 \tag{4.3}$$

were calculated for all frequencies between 0.99 and 1.01 Hz, with a frequency increment of 10^{-5} Hz. The frequency with the maximum signal amplitude was then taken as the transmission frequency (Plot B, Figure 4.6).

During 1 Hz transmissions, the source initially transmitted at a frequency of 0.997185 Hz, steadily increasing to 0.997245 Hz by day 277.5. This occured during the initial deployment of the instrument. Transmission then stabilised at the latter frequency for the two subsequent deployments. The measured frequency drift in the 1 Hz tows was independently constrained by phase data recorded by the LEMURs (Section 4.3.2 and Figure 4.10).

Without DASI piggy logger data for the 4 Hz and 0.25 Hz transmission tows, the transmission frequency was estimated to be lower than the required frequency by the same amount as the 1 Hz tows. Measurement of the maximum fundamental amplitude recorded by LEMUR instruments during high signal to noise portions of these tows confirmed the accuracy of this estimate.

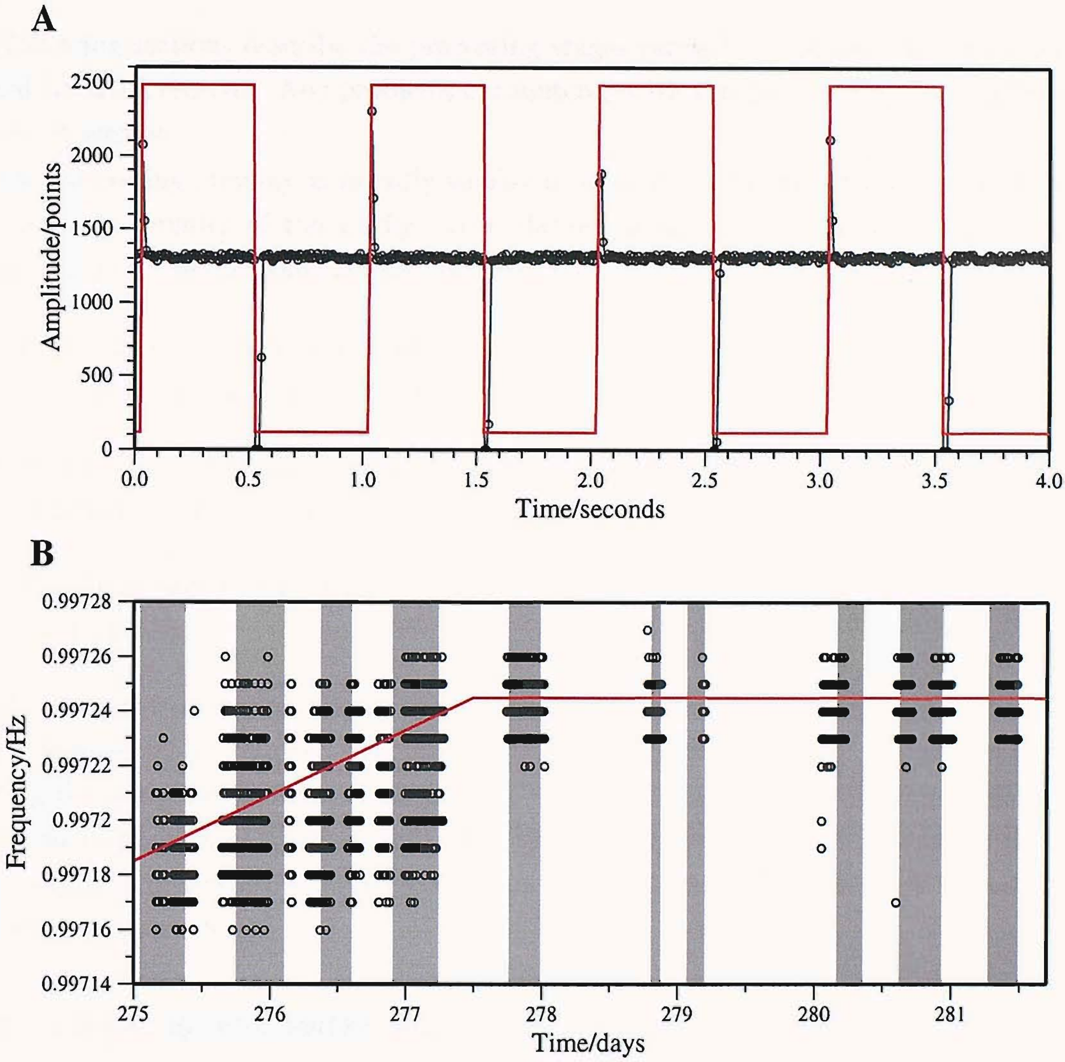

Figure 4.6: Piggy logger frequency reconstruction. Plot ***A*** shows a 4 second portion of the data recorded by the piggy logger during a 1 Hz transmission tow (black circles joined by lines). As the piggy logger was A.C. coupled, only the polarity switches in the source waveform are visible. The square waveform (red line) has been reconstructed from these switches.
The grey regions of Plot ***B*** correspond to times when a DASI transmission signal was being recorded by at least one LEMUR. Each black circle corresponds to the frequency of the maximum signal amplitude in sequential 64 s segments of piggy logger data. Maximum amplitudes were obtained with a search tolerance of 0.00001 Hz (see text), producing the horizontal 'banding' seen. Relative phase data from LEMUR instruments (Section 4.3.2) confirms the steady increase in frequency during the first DASI deployment (up to day 277.5), when there is a high level of scatter in the datapoints from the piggy logger.

4.3 LEMUR data processing

The following sections describe the processing stages carried out on the data recorded by a typical LEMUR receiver. Any problems encountered with the data from specific instruments are also discussed.

The processing strategy is broadly similar to that of MacGregor et al. (2001). However, various characteristics of the Lucky Strike dataset meant that most processing code was changed or rewritten for this dataset. For example:

1. High quality relative phase data provide better constraints on source frequency and clock drift (Sections 4.3.1 & 4.3.2).
2. Accurate orientations for instrument HED arms challenge the orthogonal-arm assumption inherent in previous studies (Section 4.4.1).
3. The large quantity of available data requires more automation of processing stages (Section 4.4).

Also, in previous studies frequency amplitude calculations have generally only been made at the frequencies of interest (usually the transmission frequencies). By calculating and plotting the complete recorded frequency spectrum, characteristics of the dataset as a whole can be more easily seen (Section 4.6). For this reason, two different processing strategies were used, to produce either data spectrogram plots (Figure 4.7), or datasets for subsequent modelling (Figure 4.8).

4.3.1 Obtaining time series data

LEMUR instruments measure electric field at a sampling rate of 128 Hz, until their 2 Mb memory buffer is full (corresponding to about 45 minutes of data). At this point, the internal hard disk is powered up, the data are written to disk in a sequentially numbered file, the disk powers down to save energy and prevent noise contamination, and the instrument continues recording. Each file also contains measurements from a bi-axial tilt meter, fluxgate magnetic compass, and temperature sensor. The disk writing cycle leads to a gap of $\sim$10 s in the recorded data.

The electric field time series from the two channels of a LEMUR is recorded in 3-byte (24-bit) samples. The bits of these samples are individually read by the processing software before reconstructing the complete sample, thus avoiding the need for endian-specific coding for different computer architectures.

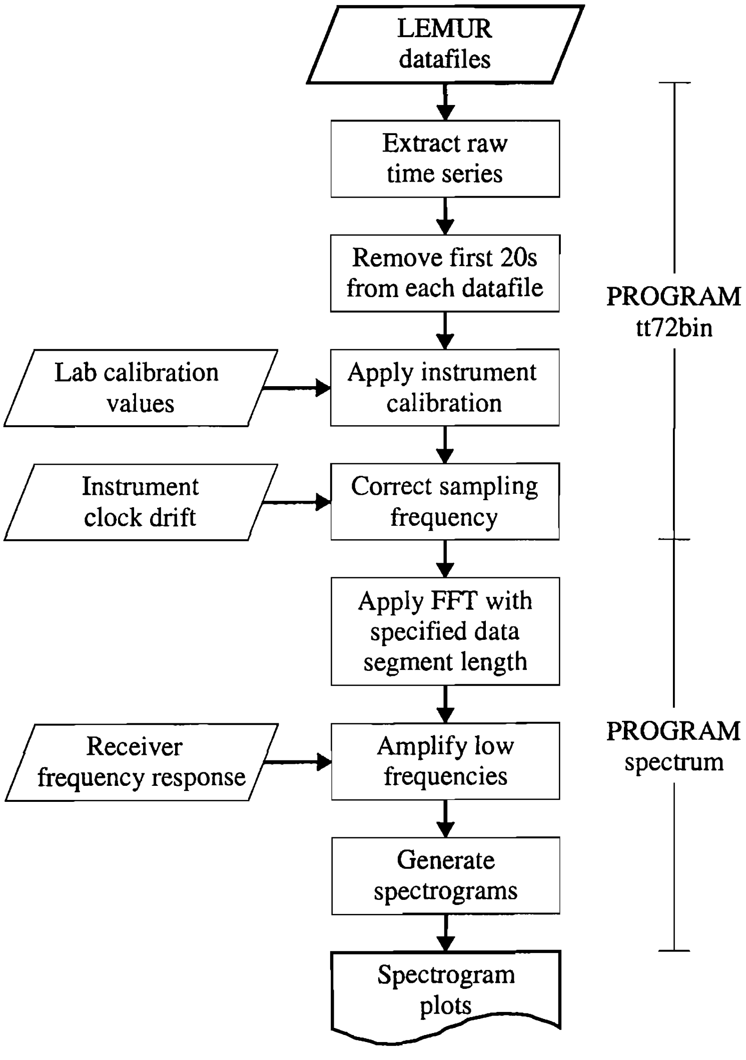

Figure 4.7: Flow diagram illustrating the steps used to generate spectrograms of LEMUR data.

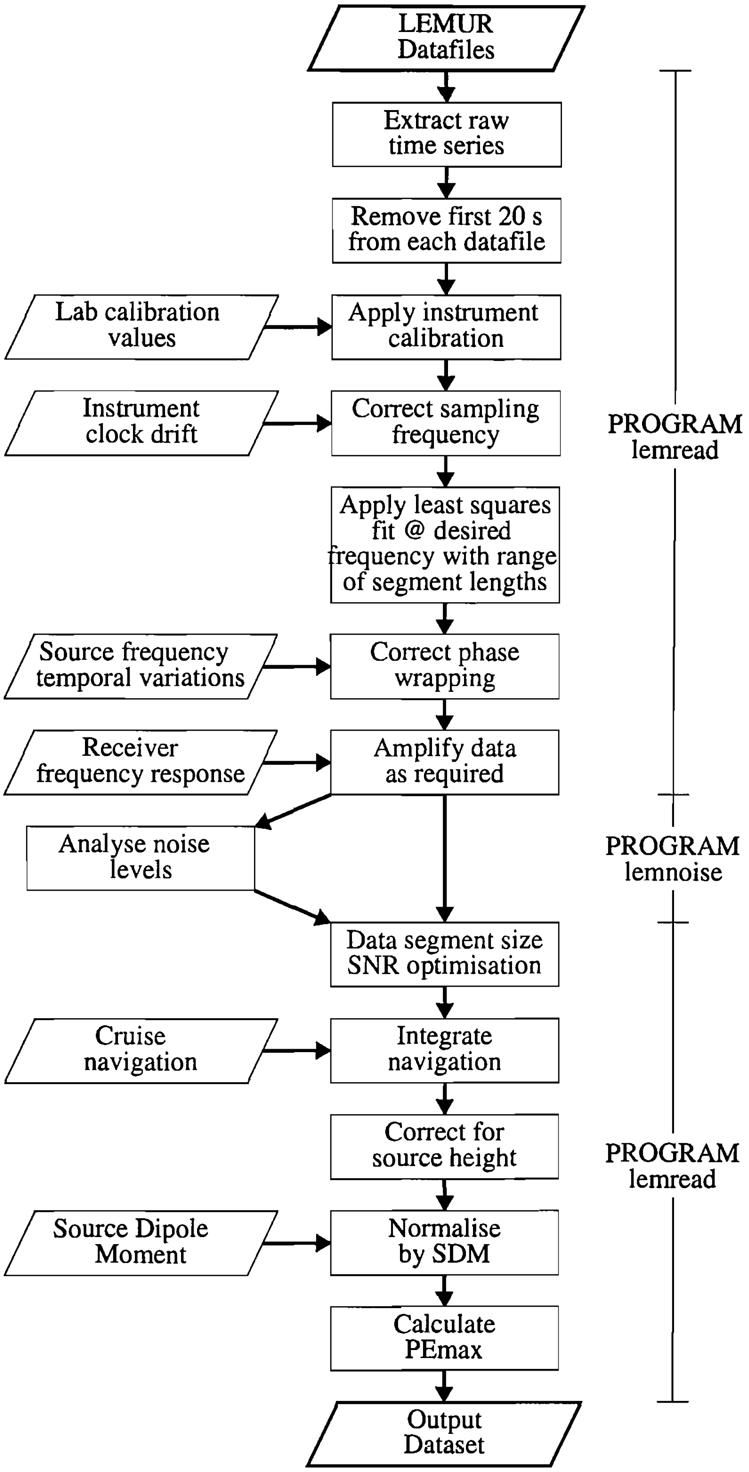

Figure 4.8: Flow diagram illustrating the processing steps used to generate the EM datasets used in subsequent modelling.

Inst	Ch.	Volts/count	Frequency response (multiplier)					
			0.25 Hz	0.75 Hz	1.25 Hz	1 Hz	3 Hz	$\geq$ 5 Hz
11	1	3.7e-12	3.1377	1.4304	1.2256	1.2617	1.0210	1.0
	2	3.83e-12	3.1397	1.4292	1.2252	1.2612	1.0213	1.0
14	1	5.51e-12	2.6961	1.4678	1.2755	1.3137	1.0595	1.0
	2	10.26e-12	3.2712	1.4669	1.2373	1.2807	1.00	1.0
15	1	3.66e-12	3.1037	1.4186	1.4980	1.2549	1.0201	1.0
	2	3.65e-12	2.3787	1.2647	1.1449	1.1689	1.0387	1.0
16	1	1.01e-12	1.4518	1.0505	1.0317	1.0291	1.0048	1.0
	2	1.10e-12	1.4075	1.0434	1.0171	1.0250	1.0040	1.0
18	1	1.05e-12	1.4116	1.0786	1.0295	1.0573	1.0258	1.0
	2	1.11e-12	1.3749	1.0716	1.0253	1.0517	1.0244	1.0

Table 4.3: Calibration values for the LEMUR receivers, derived from the results of lab tests conducted in January 2001.

The first 20 s of readings from each datafile are discarded to ensure the instrument has fully stabilised after each write cycle.

Electric field strength as a function of time is then obtained from these raw data values by multiplying by a calibration factor, and normalising by the receiver dipole length. The instrument- and channel-specific calibration factors for this dataset (Table 4.3) were obtained during lab tests before the cruise and contain the assumption that the instrument has a uniform frequency response. The true instrument frequency response is taken into account after frequency transformation (Section 4.3.2).

Instrument clock drift is evaluated by checking the internal clock against an accurate shipboard clock before deployment and after recovery. Experience from previous experiments suggests that clock drift occurs primarily during the time the instrument is active on the seafloor (L. MacGregor pers. comm.). A uniform clock drift during this time will cause the instrument to record at a slightly different sampling rate to that reported. True sampling rates (S_t) are obtained from the reported sampling rates ($S_r = 128$ samples per second) with

$$S_t = S_r \times \frac{t_a}{t_a - \text{clock drift}}, \tag{4.4}$$

where t_a is the period of time the instrument is active on the seabed.

Cruise data

All recorded datafiles were successfully downloaded from the five functioning LEMURs. However, from datafile numbers 186 to 189, the recording cycle on LEMUR16 appeared to get

LEMUR	Wake Up /Julian day	Shut Down /Julian day	Total /seconds	Drift /seconds
11	275.5	281.75	540,000	+177.439
14	275.5	281.75	540,000	+0.207
15	275.5	281.75	540,000	-0.031
16	274.5	284.25	842,400	-0.384
18	274.5	284.25	842,400	+68.790

Table 4.4: Drifts in the internal clocks of the LEMUR instruments from pre-deployment and post-recovery clock checks. LEMURs 14, 15 and 16 exhibited little clock drift, whilst LEMURs 11 and 18 ran fast by a significant amount. See text for discussion.

jammed, recording the same 2 Mb of data each time. The cause of this is not known, but a significant proportion of the piggy logger data was lost for the same reason. Luckily, only the first few hours of Tow 8, Line 7 occured when LEMUR16 was malfunctioning. From datafile 190, the instrument continued recording as normal.

Instrument clock drifts obtained can be seen in Table 4.4. The drifts of all LEMURs were corrected as above. However, investigation of the relative phase recorded during some transmission tows by LEMURs 11 and 18 showed that their larger clock drifts did not occur uniformly, but were concentrated during periods when data was being written to the internal hard disk, causing the 'jumps' in phase seen in Figure 4.9. This may have been due to a voltage drop in the power supplied to the clock, caused by the hard disk's extra current drain.

If the clock drift had occurred during most or all gaps between datafiles, it could be more accurately compensated for by applying the drift correction uniformly to only data gaps. However, some other transmission tows on the same instrument do not show jumps in relative phase, and no conclusions can be drawn for periods when no transmission tows were recorded.

To estimate the DASI navigation errors due to the jumping clock in LEMUR11, the instrument with the largest clock drift, the scenario where all clock jumps occurred during only half of the experiment was considered (this is the worst-case scenario that is consistent with the phase jumps observed during transmission tows). If a linear clock drift correction was applied, this would lead to a maximum clock error of half the total clock drift: ~90 s, or ~50 m at the average transmission tow speed. In reality, the DASI navigation errors due to clock drift are likely to be considerable smaller than this, and errors from the acoustic location of instruments (Section 4.1) will therefore dominate.

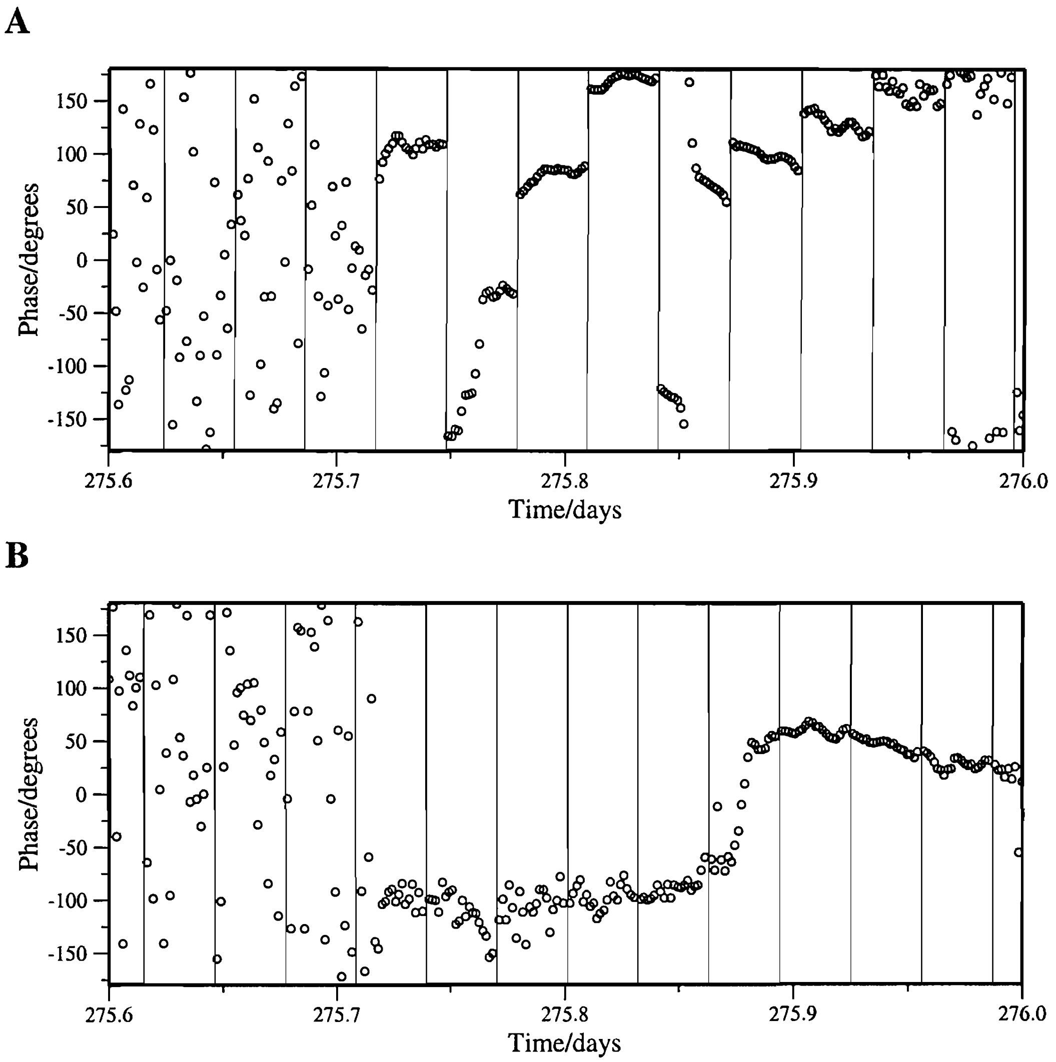

Figure 4.9: LEMUR phase data. Plot *A* shows the jumps in phase that occur between each datafile in a portion of the data recorded by Channel 1 LEMUR11 (vertical lines delineate individual datafiles). Plot *B* shows the same portion of data recorded by Channel 1 LEMUR18, where no such phase jumps are visible. Data segment length: 128 s.

4.3.2 Frequency transformation

Transformation of the electric field time series into the frequency domain is carried out by either an FFT if calculating spectrograms (using the libraries of FFTW (Frigo & Johnson 1998)), or a least squares fit if generating datasets for subsequent modelling.

A least squares fit is even more essential for obtaining signal amplitudes at a particular frequency with LEMUR data than with piggy logger data (Section 4.2.2), as after clock drift corrections, each instrument will have a slightly different sampling rate.

From a least squares fit to the function $f(t)$ in Equation 4.2, the signal amplitude A_i is calculated as Equation 4.3, and the phase ϕ calculated from

$$\phi_i = tan^{-1}\left(\frac{b_i}{a_i}\right). \tag{4.5}$$

After transformation, the data are divided by the instrument frequency response in order to obtain the correct electric field amplitudes at the required frequency. The LEMUR instruments have a flat frequency response above 5 Hz, with their sensitivity decreasing at lower frequencies (Table 4.3). For spectrogram plots, interpolated and extrapolated values are used as estimates of the response at frequencies where no calibration measurements were taken.

Cruise data

No significant differences in received signal amplitudes were found from carrying out least squares fits to the LEMUR data at the lowest and highest 1 Hz transmission frequency (0.997185 and 0.997245 Hz). For this reason, and for simplicity, all least square fits to the 1 Hz transmissions were carried out at the final stable frequency of 0.997245 Hz. Such small differences in frequency do however have a significant effect on the phase of the data obtained.

At the time of the Lucky Strike cruise, the timekeeping of the DASI system was not accurate enough to record the absolute phase of the transmitted signal (required if useful information is to be obtained from modelling the recorded phase). However, the data is of a high enough quality for a coherent relative phase to be detectable during transmission tows.

When applying a least square fit at 0.997245 Hz, the relative phase of early transmission tows (when the source was transmitting at a slightly lower frequency) exhibits 'wrap-around'. The correct relative phase at a time t_1 was reconstructed by applying a phase shift of

$$\text{shift(degrees)} = 360h \int_{t_0}^{t_1} fr(t) - fr(t_1)\, dt \tag{4.6}$$

where: $fr(t)$ is a function defining the variation of primary transmission frequency with time from t_0, the beginning of the experiment; the primary transmission frequency at time t_1 is $fr(t_1)$; and the harmonic being measured is h. The effect of this phase correction can be seen in Figure 4.10.

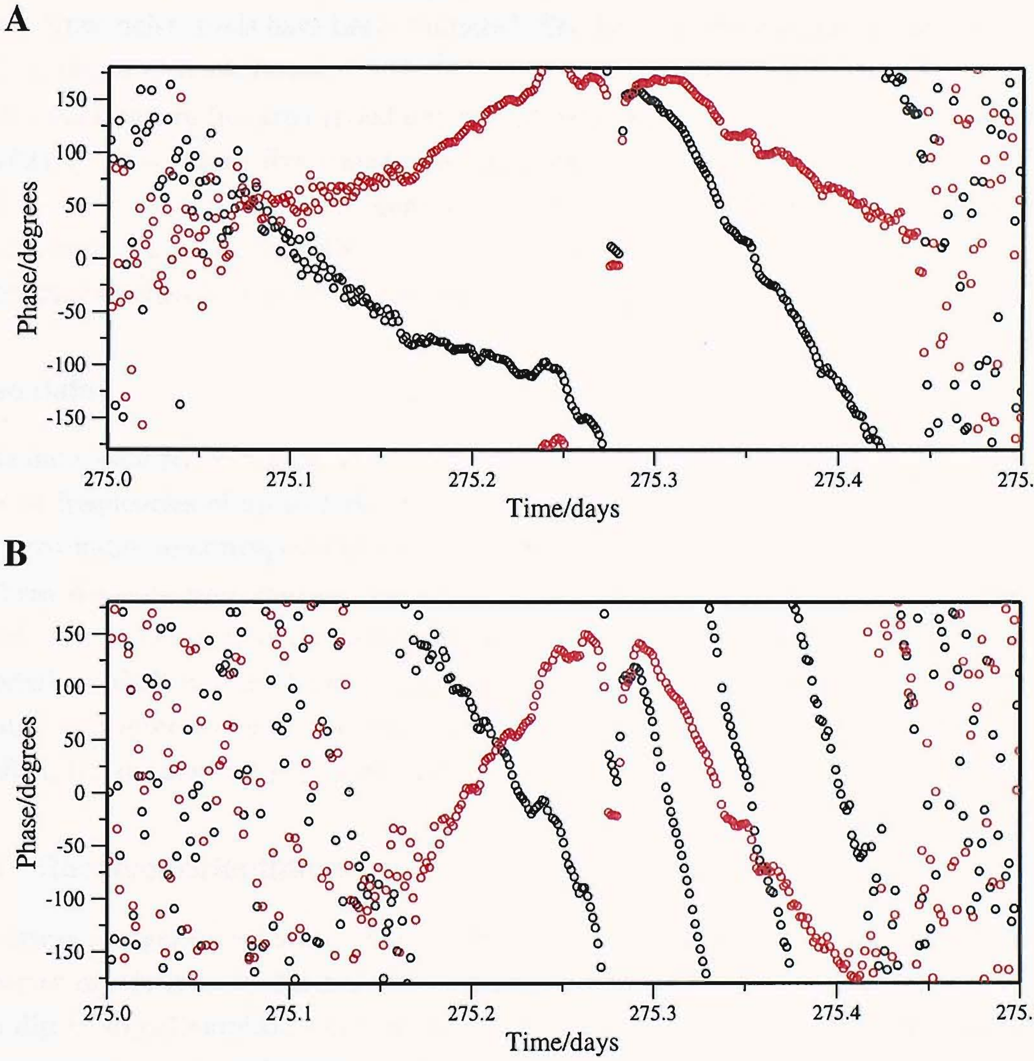

Figure 4.10: Plot A shows the relative phase recorded by LEMUR16, Channel 1 during Line 1, at 1 Hz (black points), and at the correct transmission frequency (red points). This 'wrap around' effect, due to a disparity between the transmission and LSQ fit frequency, becomes more pronounced in higher harmonics (e.g. the 3 Hz harmonic, shown in Plot B). Data segment length: 128 s.

4.4 Least squares segment size optimisation

It is important when choosing an appropriate least squares data segment size to maintain a balance between signal to noise ratio (SNR) and sparsity of datapoints: with an average DASI velocity of 0.7 ms^{-1}, a 64 s window size corresponds to one datapoint every 44 metres; a 1024 s window will have a better signal to noise ratio, but only one datapoint every 717 metres. Once noise levels have been evaluated (Section 4.6), data segment size can be chosen based on signal to noise ratios.

Five least square fits are carried out on the data, with window sizes of 64, 128, 256, 512 and 1024 s. From these five transforms, the smallest window size that reaches a specified signal to noise ratio is chosen (Figure 4.11). At the longest offsets, if none of the window sizes produce a high enough SNR, the 1024 s window is chosen. These noisier long-offset datapoints can then be removed at the modelling stage as required.

Cruise data

Viable data were recovered for almost all source-receiver separations for all recording instruments at frequencies of up to 1 Hz. Data from higher frequencies, with smaller skin depths, were recoverable to correspondingly shorter offsets.

Three datasets were created, with minimum signal to noise ratios of 10, 5 and 2. In general, it was found that the data with an SNR of ≥ 5 produced the best tradeoff for 1-D modelling of all but the longest-range data. In higher dimensional modelling, where the available computer memory and processing power limit the size of datasets which can be modelled, the dataset with the best SNR was used.

4.4.1 Receiver orientation

Once cruise navigation is known, it is possible to simply and accurately model the orientation of receiver dipole arms by finding transmission tows for each receiver channel that exhibit a sharp dip in signal amplitude corresponding to the receiver-HED measuring a minimum in that component of the polarisation ellipse.

Once such sections of data are identified, 1-dimensional forward modelling (as in Chapter 5) is carried out with the same source-receiver geometry, and a crustal halfspace resistivity of 100 Ohm-metres. Receiver orientation is then varied from that recorded by the onboard compass until the amplitude drop-off has been successfully modelled (Figure 4.12). Uncertainties in the calculated orientation are estimated from observing how rapidly the dip in electric field varies with orientation.

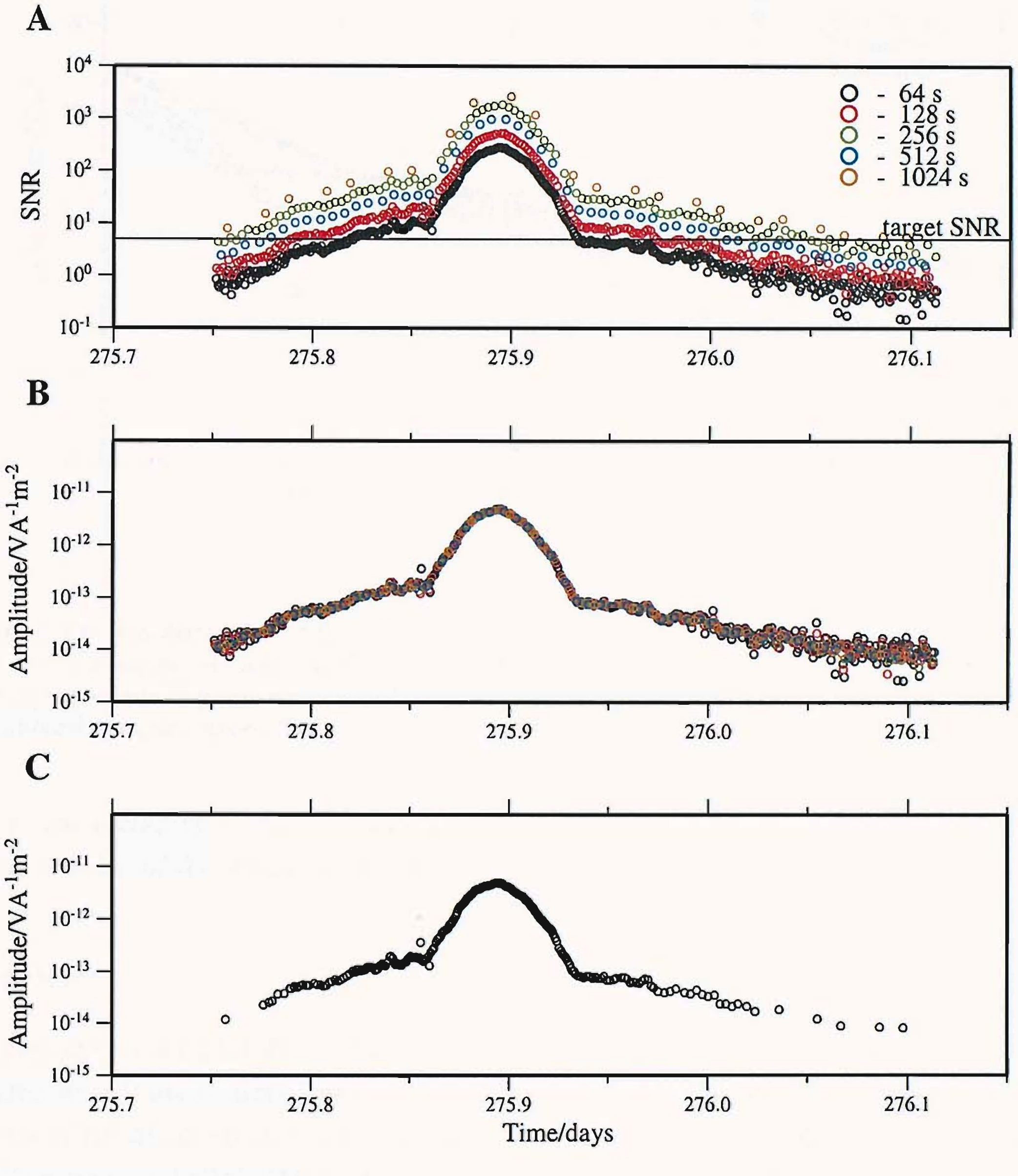

Figure 4.11: Data segment length optimisation based on signal to noise ratio. Plot ***A*** shows the SNR calculated for five different segment lengths in data from LEMUR16 Channel 1, during the 1 Hz transmission along Line 1. SNR can be seen to increase with increasing segment length, with a corresponding increase in data sparsity. The amplitude of these datapoints is plotted in ***B***. Data are automatically chosen from these, based on the target SNR of ≥ 5 (black line in Plot ***A***). Datapoints that pass this selection are shown in Plot ***C***.

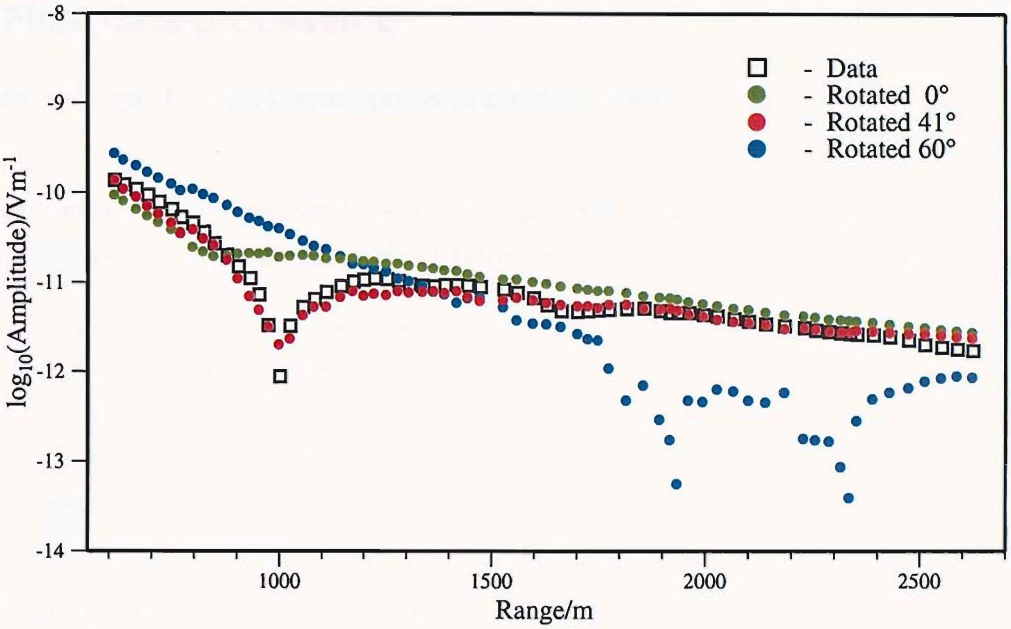

Figure 4.12: A portion of the 1 Hz data recorded by LEMUR15 Channel 1 (black squares), showing the dropoff in amplitude associated with an orthogonal source-receiver geometry. This dropoff is accurately modelled by an arm orientation of 41^o(red dots) relative to the orientation recorded by the onboard compass (green dots).

It is not necessary to have an accurate knowledge of crustal resistivity structure, as the angular position of the dip in amplitude is largely unaffected by different crustal resistivities.

Cruise data

The orientations of LEMURs 11, 14 and 15 were obtained without encountering any difficulties. Orientation uncertainties were estimated to be $\pm 2^o$. An unexpected discovery was that the arms of LEMURs 16 and 18 did not appear to have been resting in an orthogonal geometry. The arms of LEMUR16 were non-orthogonal by 35^o, whilst those of LEMUR18 were out by 20^o. Whilst at first inspection these values seem excessive, it is easy to envisage the 6 metre flexible LEMUR arms coming to rest askew on a rugged, pillow lava-strewn seabed.

Such a non-orthogonal pair of HED receivers would still be able to uniquely measure the horizontal electric field at the seafloor. The two components of the field would simply be expressed in a non-orthogonal coordinate system. It was therefore possible to carry out a coordinate system skew in order to translate the two measured amplitudes into an orthogonal pair (see Appendix A).

4.5 Final data processing

The data undergo these additional processing stages before subsequent modelling is carried out:

1. Data with a source-receiver offset of less than 900 m are removed. The very high signal strengths received over such a short range tend to saturate the LEMUR amplifiers.

2. When the EM data are modelled, it is assumed that the transmitter is located in the water column, directly above the seafloor. Received signal strength is therefore amplified by the required value assuming an exponential attenuation of signal strength in the water column, over the height h above the seafloor measured by DASI's onboard altimeter

   $$E_{corrected} = E_{measured}\, e^{\frac{h}{\delta_s}} \tag{4.7}$$

   where δ_s is the skin depth of the signal in seawater.

3. The signal is normalised by the source dipole moment at the required frequency (Table 4.2).

4. The amplitude of the major axis of the polarisation ellipse is calculated from the two recorded components (see Section 2.6).

4.6 Noise evaluation

In previous studies, plots of amplitudes have generally only been made at the frequencies of interest (usually the transmission frequencies). By plotting the complete recorded frequency spectrum, noise characteristics of both the LEMUR instruments and deployment environment can be more easily seen.

As well as background noise (Section 4.6.1) and the effect of water currents on the instruments (Section 4.6.2), several other types of noise event occur within the dataset, although not significantly effecting noise levels at the DASI transmission frequencies:

1. High levels of noise at very discrete frequencies can be seen throughout the data from each instrument. This noise is probably instrumental in origin as many of the noise bands start at a different frequency when the instrument begins recording, before 'settling down' to a constant frequency (Figures 4.13 & 4.14)

2. Temporally distinct noisy events covering many frequencies (Figures 4.13 & 4.14) are likely to come from any number of environmental sources, e.g. fluid movement due

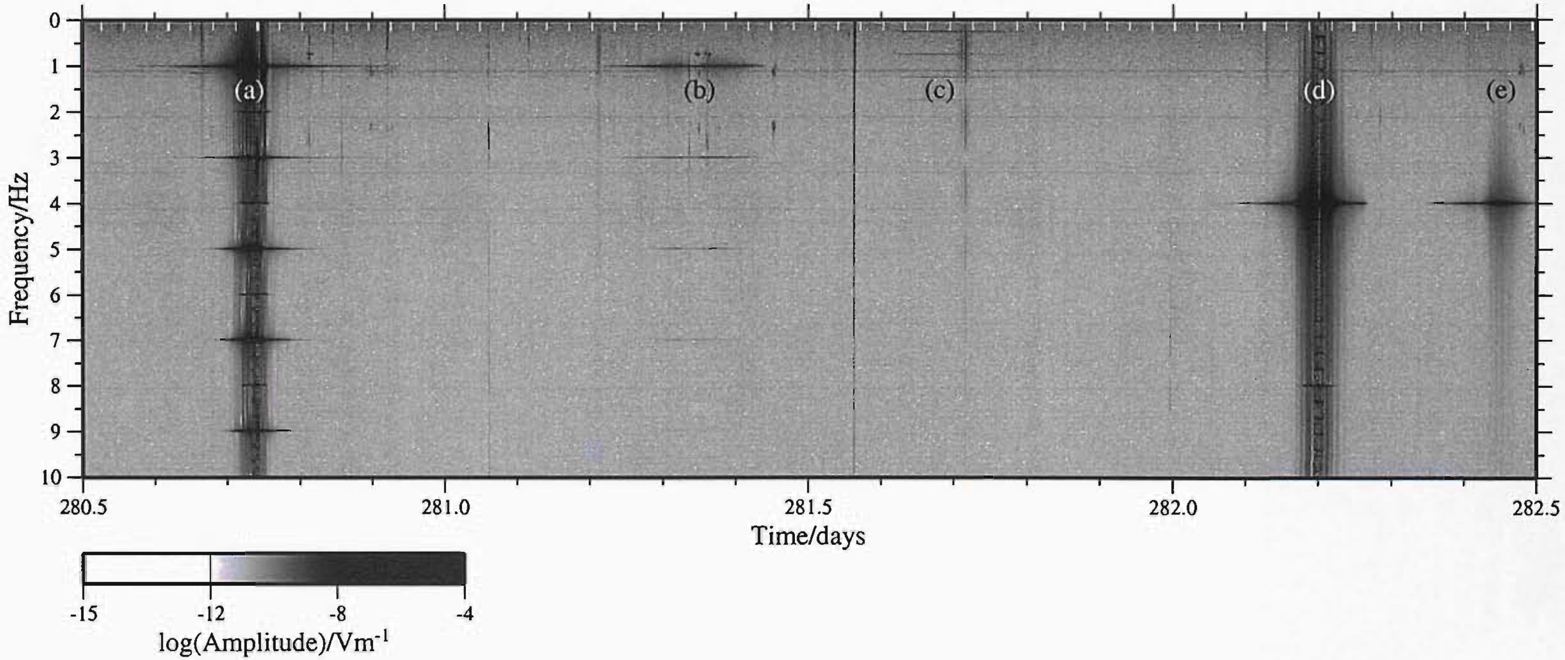

Figure 4.13: A spectrogram of a portion of the data recorded by LEMUR16, Channel 1. FFT segment length: 128 seconds. Small white ticks at the top of the plot correspond to gaps in the data at times when the LEMUR was writing its memory buffer to the internal hard disk. The last available frequency spectrum is copied below these ticks to aid viewing. Five DASI transmission tows are visible: the 1 Hz lines 6 (*a*) & 8 (*b*); the single 0.25 Hz line 3 (*c*); and the 4 Hz lines 1 (*d*) & 2 (*e*). Noisy frequency bands and individual noisy events can also be seen; see Section 4.6 for discussion.

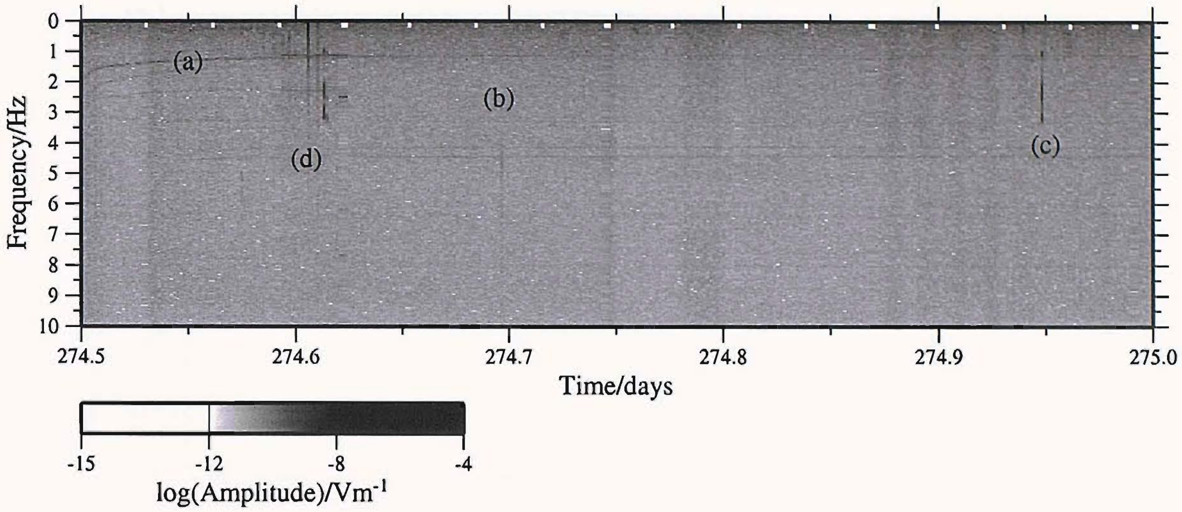

Figure 4.14: The first 12 hours of recorded data from LEMUR16 Channel 1. Discrete noisy frequencies can be seen (e.g., at (*a*) the noise is initially at 2 Hz, settling to ~1.3 Hz within less than an hour); temporally discrete noise events are visible at (*b*) and (*c*); and one instrument 'calibration' cycle occurs at (*d*). FFT data segment length: 128 seconds.

to tectonically generated seismic activity can induce electromagnetic fields (Webb & Cox 1986). Some of these events occur during transmission tows. However, affected data points are obvious outliers, and were removed before modelling was carried out.

3. Each instrument was configured to run a calibration cycle twice during its deployment (Figure 4.14). These 45 minute cycles had been used during previous instrument testing, but were of no use during this experiment. By luck, they did not overlap with any recorded transmission tows.

4.6.1 Background noise levels

There were four periods during the experiment when all LEMURs were recording whilst the transmitter was out of the water. It is during these times (a total of 33.6 hours) that analysis of the background noise levels was carried out. A conventional method of measuring noise levels is the power spectral density (PSD), defined as the RMS noise level normalised to the frequency bandwidth. Power spectral densities of the noise were generated by squaring the stacked amplitudes obtained from FFTs (with a segment length of 128 s), and normalising by the FFT bandwidth.

All instrument channels exhibit a similar noise PSD (Figure 4.15), although the powers vary by up to an order of magnitude between channels. Up to ~3 Hz, noise levels decrease from a maximum at low frequency, before levelling off between ~3 and 53 Hz. This is

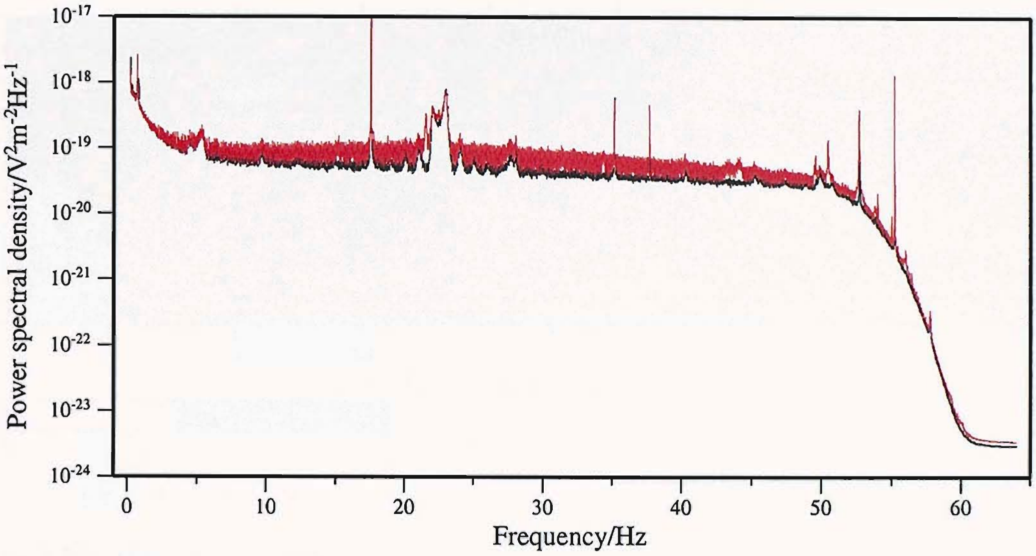

Figure 4.15: A power spectral density plot of the noise on Channels 1 (black) and 2 (red) of LEMUR 11. See text for discussion.

consistent with the noise generated by electrodes in good condition (Webb & Cox 1986). From ~53 Hz up to the Nyquist frequency, noise levels tail off due to the anti-aliasing filter applied by the instrument.

The noise characteristics of this dataset are comparable to those from previous experiments using LEMUR receivers, particularly from the data obtained on the Valu Fa Ridge (MacGregor et al. 2001), an experiment which used the LEMUR '95 instrument design.

4.6.2 Effect of water currents

Intermittent high-amplitude noise in the frequency range 0.75 to 1.0 Hz was observed in the data recovered from the LEMUR '99 testing on the RRS Discovery cruise of July 1998 (Sinha et al. 1998a). Coherence of the noise recorded by two different instruments connected to the same dipoles eliminated the possibility of internal instrument noise. This, and the signal appearing and disappearing over periods of a few hours, led it to be proposed that this noise was due to water currents passing over the instrument.

In the Lucky Strike data, channels on some of the instruments appear to display the same characteristic. This is particularly pronounced on Channel 2 of LEMUR14 (Figure 4.16).

As the amplitude of the noise appears to vary in a cyclic fashion, and to investigate the hypothesis that this noise is tidal in origin, a comparison was made between it and water current data recorded by the current meters.

An amplitude envelope of the noise was constructed by summing the amplitudes of fre-

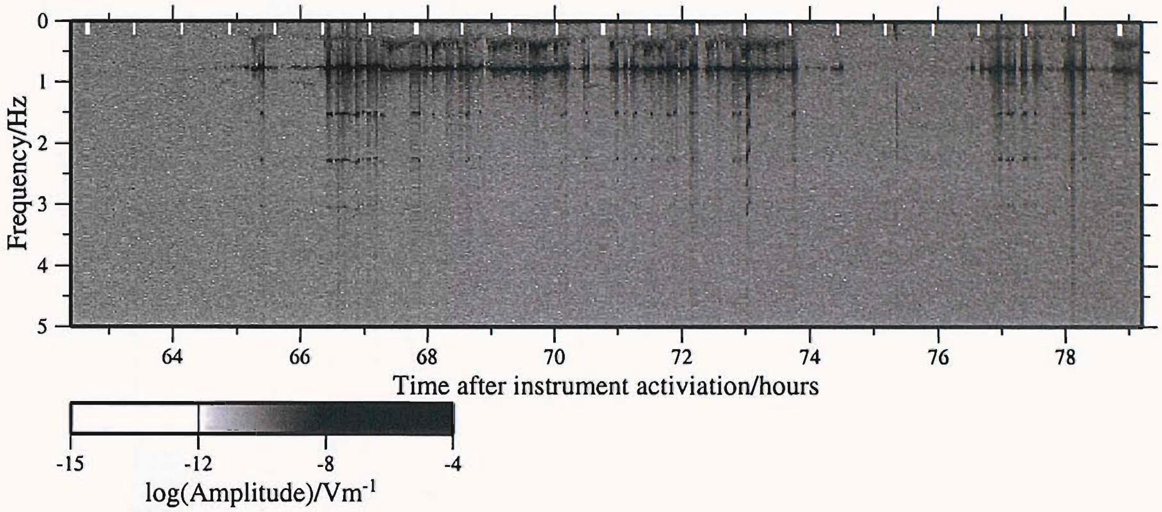

Figure 4.16: Tidal current noise on LEMUR14 Channel 2. The second and third noise harmonics can also be seen in places. FFT data segment length: 128 seconds.

quencies between 0.75 and 0.8 Hz in each FFT window (data segment size: 128 s). This ensured that noisy periods were not missed due to small temporal variations in the frequency content of the noise. A second FFT was then carried out on the resulting amplitude envelope time series (the black line in Figure 4.17). Although the resolution of longer time period variations is limited by the length of data available (in this case 123 hours), it can still be seen that the amplitude of this noise varies strongly with a period of ~12, and to a lesser extent ~6 hours.

The three current meters recorded water current velocity over a period of 255 hours (see Appendix B). Figure 4.17 also shows an FFT of the magnitude of water velocities recorded by instrument C4. This can be seen to contain the same two amplitude peaks as the EM data, strongly supporting the theory that the EM noise is water-current generated, varying with tidal current variations.

The observed EM field variations are probably due to the flexible HED arms of the instrument 'waving' in the water current. This movement would cut the Earth's magnetic field, thereby inducing an EMF in the arms. A rough estimate of the magnitude of movement required can be obtained from Faraday's Law,

$$\varepsilon = -\frac{d\Phi_B}{dt} = -\frac{d(BA)}{dt} \tag{4.8}$$

where ε is the EMF induced, Φ_B is the magnetic flux, B is the magnetic flux density and A is the area swept by the conductor. With a conductor of length l, travelling at a velocity u

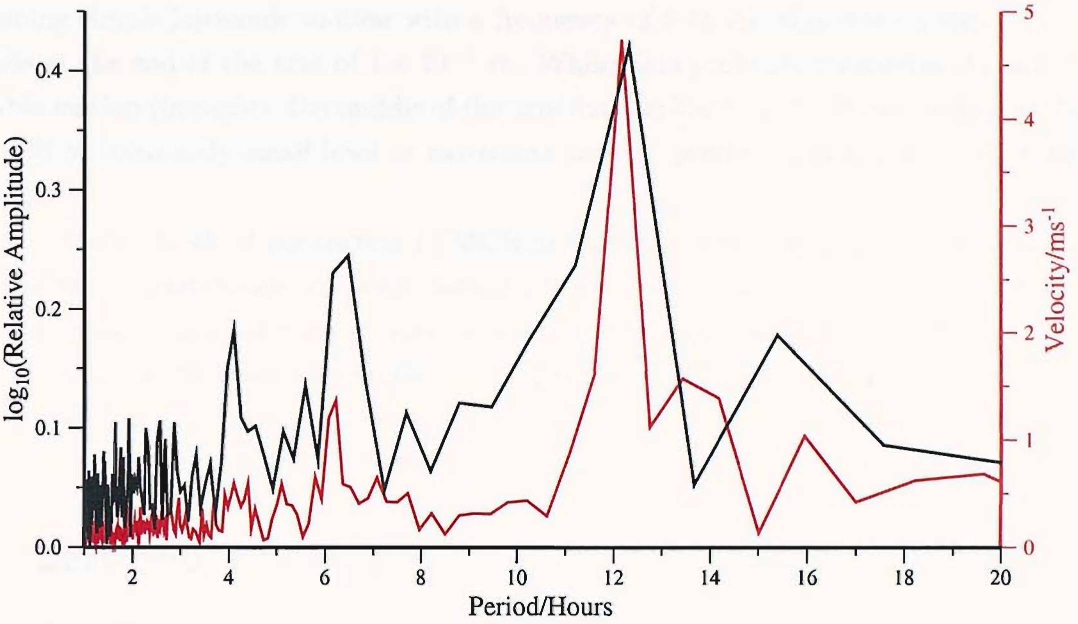

Figure 4.17: The period of variation of 0.75 Hz noise recorded on LEMUR14 Channel 2 (black line), alongside an FFT of the magnitudes of water velocities recorded by current meter C4 (red line).

perpendicular to the magnetic field,

$$lu = \frac{d(A)}{dt} \tag{4.9}$$

$$\Rightarrow \qquad \varepsilon = -Blu. \tag{4.10}$$

Assuming: only one arm is moving (out of the two that form a dipole), perpendicular to the magnetic field, and pivoted at the point at which it enters the main body of the instrument (i.e. arm flexure is neglected); the maximum amplitude of EMF is induced when the arm is travelling at its maximum velocity, in the middle of its oscillation; and the average linear velocity at that time is half the product of the angular velocity and arm length (6 metres). Then, using

$$\text{magnetic field of the earth at } 32^o\text{N} = 4 \times 10^{-5}T; \tag{4.11}$$

$$\text{EMF per unit length,} \quad \frac{\varepsilon}{l} = 10^{-8}\ Vm^{-1}\text{(from Channel 2, LEMUR14)}; \tag{4.12}$$

this produces a maximum velocity at the arm mid-point of

$$V_{max} = 2.5 \times 10^{-4}\ ms^{-1}. \tag{4.13}$$

Assuming simple harmonic motion with a frequency of 0.75 Hz, this corresponds to an amplitude at the end of the arm of 1×10^{-4} m. Whilst this probably represents the minimum possible motion (in reality, the middle of the arm may oscillate, with both ends staying fixed), it is still an extremely small level of movement to have produced such a large effect in the final data.

This characteristic of the current LEMUR instruments will be an important consideration in future instrument design. However, for the purposes of this experiment, the frequency band of water current induced noise is very narrow, varying between 0.75 and 0.8 Hz, and does not therefore interfere with the 1 Hz DASI signal received by the instruments. The short period of 0.25 Hz transmissions recorded by the LEMUR '99 instruments (in which the third harmonic would be within the affected frequency range), is also not obscured by the noise.

4.7 Data error evaluation

Constable & Cox (1996) show that the standard deviations of the real and imaginary components of the noise can be used as normally distributed errors on the data, as long as the following conditions are satisfied:

1. Each component of the noise must follow a zero-mean Gaussian distribution. A Kolmogorov-Smirnov (K-S) test can be used to establish the normality with a known confidence and a Gaussian distribution of N data points with standard deviation σ and mean μ may be assumed to be central if

$$\mu < \frac{2\sigma}{\sqrt{N}}. \tag{4.14}$$

2. If both components follow a normal distribution, amplitudes are distributed as Chi-squared with two degrees of freedom. As long as a signal to noise ratio of about 3 or more is maintained, the Chi-squared distribution will have a sufficiently non-zero mean that the difference between it and a normal distribution will not be significant.

Noise levels at transmission frequencies were calculated using the same least squares fitting procedure as on transmission data, for the same five data segment lengths, and can be seen in Figure 4.18. Phasor diagrams of the real and imaginary noise components were plotted for transmission frequencies, and appeared on visual inspection to be centrally located, without a significant number of outliers.

The majority of receiver channels and transmission frequencies passed the K-S test with a 5 % significance level. Those that failed were generally in the frequency range 0.25–3 Hz, and were on channels particularly affected by the motionally-induced noise discussed above.

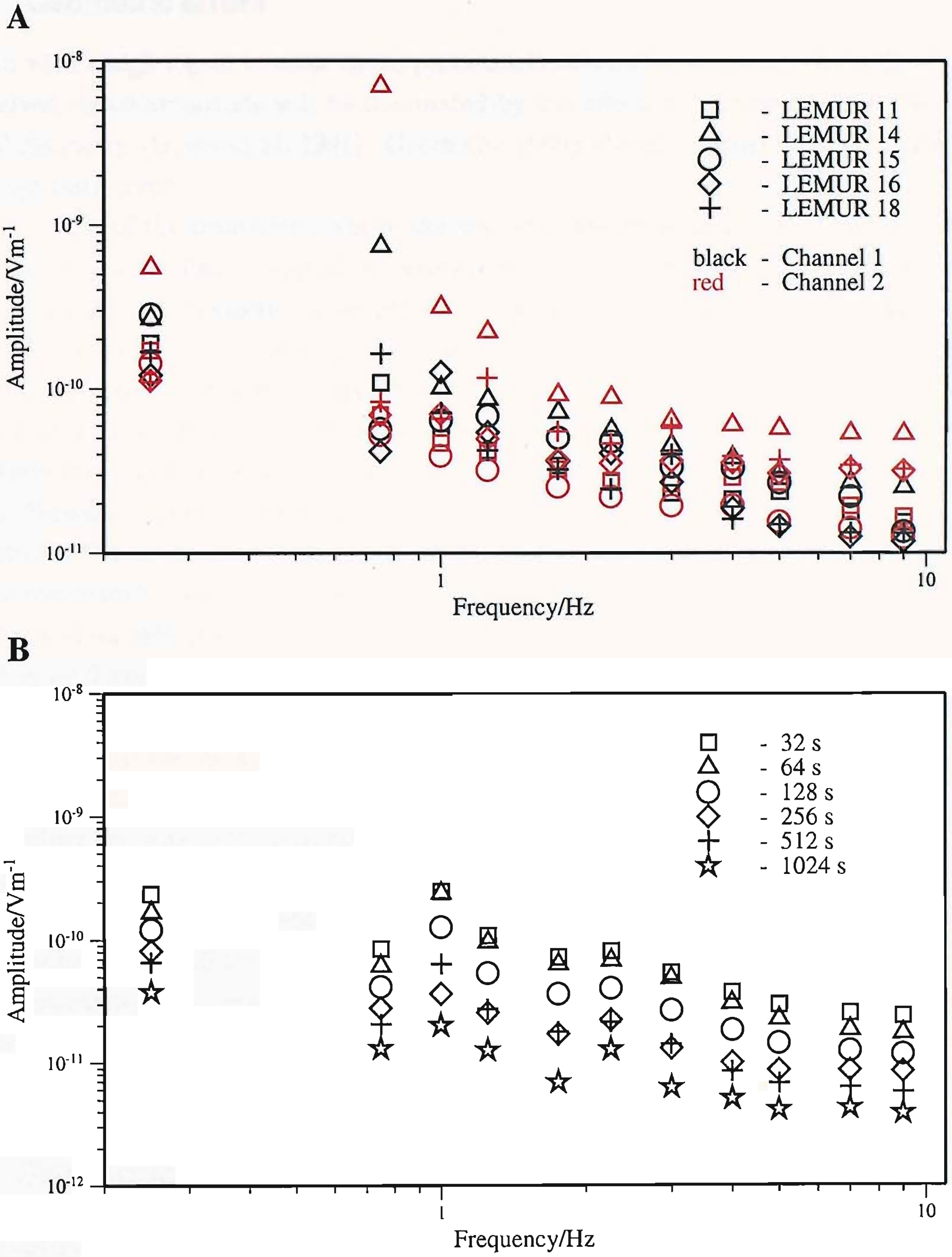

Figure 4.18: LEMUR noise levels. *A*: the noise levels for all LEMUR instruments, defined as the RMS electric field over a bandwidth of ~0.01 Hz (the inverse of the 128 second data segment length). *B*: the noise levels of LEMUR16 Channel 1 for the 5 data segment lengths used in the data processing.

4.7.1 Geometric errors

In data with a high signal to noise ratio, particularly at smaller source-receiver offsets, errors in received signal amplitude will be dominated by the effects of uncertainties in the experimental geometry (Evans et al. 1991). Geometric errors therefore provide an estimate of the minimum data error.

The height of the transmitter above the seabed is known from the altimeter on DASI to an accuracy of 5 m. The magnitude of errors due to this uncertainty is governed by the skin depth in water, and therefore the frequency of transmission. At 0.25 Hz, transmitter height uncertainty generates an error in the received amplitude of 1 %, increasing to 6 % at 9 Hz.

Errors due to uncertainty in the source-receiver separation depend on the seafloor resistivity as well as transmitter frequency. A higher resistivity seafloor leads to a smaller amplitude error, as the geometric uncertainty becomes a smaller proportion of seafloor skin depth. Forward modelling with the code of Chave & Cox (1982) was used to evaluate the magnitude of these errors for various seafloor resistivities and source-receiver separations. With a conservative source-receiver error of 30 m, seafloor resistivity of 10 Ωm, frequency of 0.25 Hz, and an azimuth of 0^o, the error in PE_{max} is $\sim$ 10 % at a range of 1 km, decreasing to $\sim$ 2 % by 5 km. At 9 Hz, the error is $\sim$ 11 % at a range of 1 km, decreasing to $\sim$ 6 % by 5 km.

Errors due to the uncertainty in the source-receiver azimuth are harder to quantify as they are dominated by the uncertainty in source dipole orientation. Their effect is minimised by modelling the maximum amplitude of the polarisation ellipse, which is far less dependent on azimuth than individal electric field components. The effect of azimuth on PE_{max}, as well as on the radial and azimuthal amplitudes for a source-receiver separation of 5 km and seafloor resistivity of 10 Ωm, can be seen in Figure 4.19. In this configuration, errors of 10^o in the azimuth lead to a maximum error in received signal amplitude of $\sim$10 %.

Based on these calculations, minimum signal amplitude errors of 12 % at 1 km, decreasing to 8 % for ranges of 4 km and above was used.

4.8 Frequencies recovered

The quasi-square wave produced by DASI contains the majority of energy in the odd harmonics of the fundamental frequency being transmitted (Section 4.2.1), although some leakage into other frequencies occurs due to distortion of the waveform as it propagates through the earth. Whilst limited modelling has been carried out on higher harmonics obtained from previous experiments (e.g. MacGregor et al. (2001)), it was found that the smaller energy levels in higher harmonics, coupled with a relatively low signal to noise level compared to

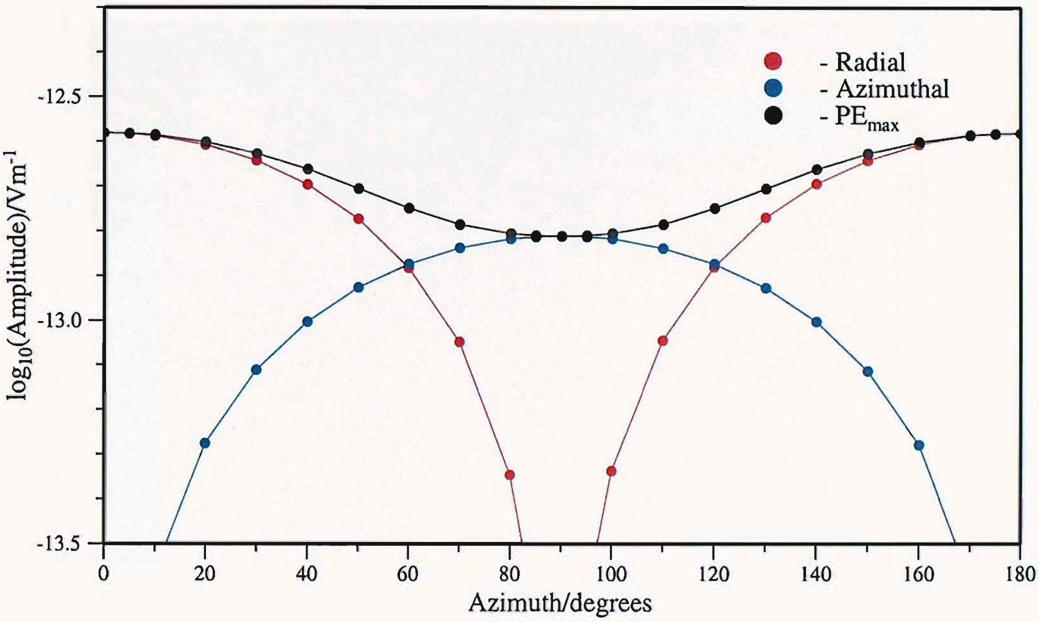

Figure 4.19: The variation of received signal strength by source-receiver azimuth at a source-receiver offset of 5 km over a seafloor resistivity of 10 Ωm. The uncertainty in received signal amplitude caused by an error of 10^o in source azimuth was estimated from the steepest part of the PE$_{\mathrm{max}}$ curve.

the Lucky Strike data, meant that the harmonics were soon lost in the background noise as source-receiver offsets increased.

Viable data can be obtained from the Lucky Strike dataset up to very high harmonics (Figure 4.20). The highest frequency that is modelled here is 9 Hz: the 9th harmonic of the 1 Hz transmission. Higher frequencies were only visible at the shortest offsets, and therefore contained little extra information on crustal resistivity structure. However, future experiment design may make better use of these higher harmonics; these results have shown that it is possible to use a lower fundamental frequency in order to probe deeper into the earth, without necessarily losing information on shallow structure.

4.9 Summary

This chapter deals with the processing of the raw time series EM data, along with cruise navigation. Problems encountered with the LBL navigation during the experiment have been successfully overcome with a combination of simulated annealing acoustic raypath inversion, and careful smoothing of transmitter tows. Receiver locations have been identified to within 15 m, whilst the DASI transmitter has been located at all times during transmission tows to

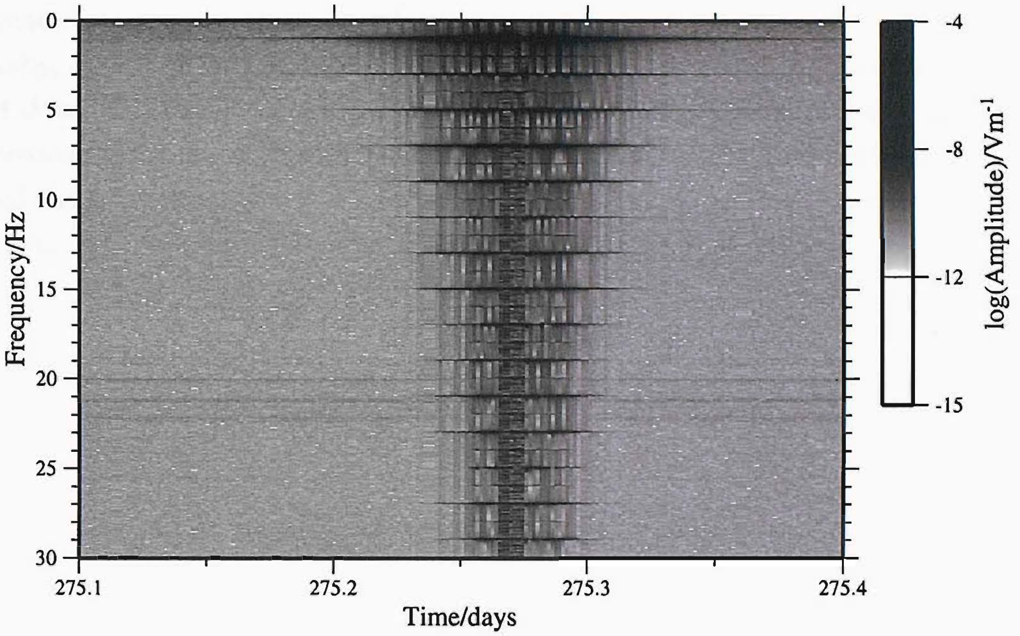

Figure 4.20: A spectrogram of Tow 1, recorded on LEMUR16 Channel 1. The odd harmonics of the 1 Hz square wave are visible up to 29 Hz and beyond. Data segment length: 128 seconds. A longer segment length would allow these higher harmonics to be visible to greater source-receiver offsets.

an uncertainty of approximately 10 m.

Receiver orientations have been calculated by a process of simple 1-D EM forward modelling. Non-orthogonality in the arms of two receivers, detected during this modelling, has been corrected without a significant increase in the noise levels of the corrected channels.

Source waveform characteristics have been constrained with a combination of oscilloscope measurements, and the reconstruction of the signal recorded by the DASI piggy logger. The source waveform was mostly stable during the experiment, with some drift in the transmission frequency during the first deployment of the DASI transmitter.

High levels of noise at 0.75 Hz have been observed in the data from several receivers. Frequency analysis of this and current meter data strongly suggests that this noise is tidal in origin, probably due to small arm oscillations induced by water moving over the instrument. Whilst the noise has not affected the amount or quality of data recovered from the experiment, this characteristic as well as the non-orthogonal orientation of receiver arms, provides compelling reasons for future improvements in the HED receivers on the LEMUR instruments.

A coherent relative phase signal has been recovered from most of the recorded transmission tows. This serves to comfirm the accuracy of the calculated frequency variation of the DASI transmitter.

Finally, compared to previous experiments, the greater signal to noise ratio of the recovered data has allowed far more information to be obtained from higher frequency DASI transmission harmonics. Indeed, the harmonics of the majority 1 Hz transmission tows have rendered the smaller number of 4 Hz tows, recorded by only two instruments, largely superfluous. This has important implications for future experimental design.

Chapter 5

1-D forward modelling and inversion

The 1-dimensional forward modelling and inversion codes used here have now been applied to several CSEM datasets, recorded over various oceanic settings. In some instances, there has been good reason for assuming that the target resistivity is largely 1-dimensional in nature (e.g. the PEGASUS experiment, over mature oceanic crust (Constable & Cox 1996)). However, over higher dimensional targets, 1-dimensional modelling has still been found to be useful in order to give some idea of the possible classes of model which fit the data, and to provide starting models for higher dimensional analysis (e.g. MacGregor (1997) and MacGregor et al. (2001)).

The Lucky Strike seamount provides a target area with both severe 3-dimensional topography, and a focussed hydrothermal system which would be expected to produce a correspondingly 3-dimensional resistivity structure. This chapter therefore investigates the preliminary results that may be obtained from 1-dimensional modelling over such a complex target area.

We begin by discussing the justification for two approximations used in all subsequent modelling: that the seawater is an infinite layer, and that the source can be assumed to be a point dipole. The results of simple 1-D layer over halfspace forward modelling are then presented, and discussed in terms of the 'bulk' resistivity of the target area. The residuals obtained from this modelling can be used to highlight the higher dimensional structure present within the data. Finally, an overview is given of the 1-D Occam inversion code of Constable et al. (1987), and the results of inverting subsets of the data recorded by each instrument are presented and discussed in terms of the regional resistivity structure.

5.0.1 Effect of finite water depth

The signal received by the ocean bottom instruments has two possible routes of travel other than through the ocean crust:

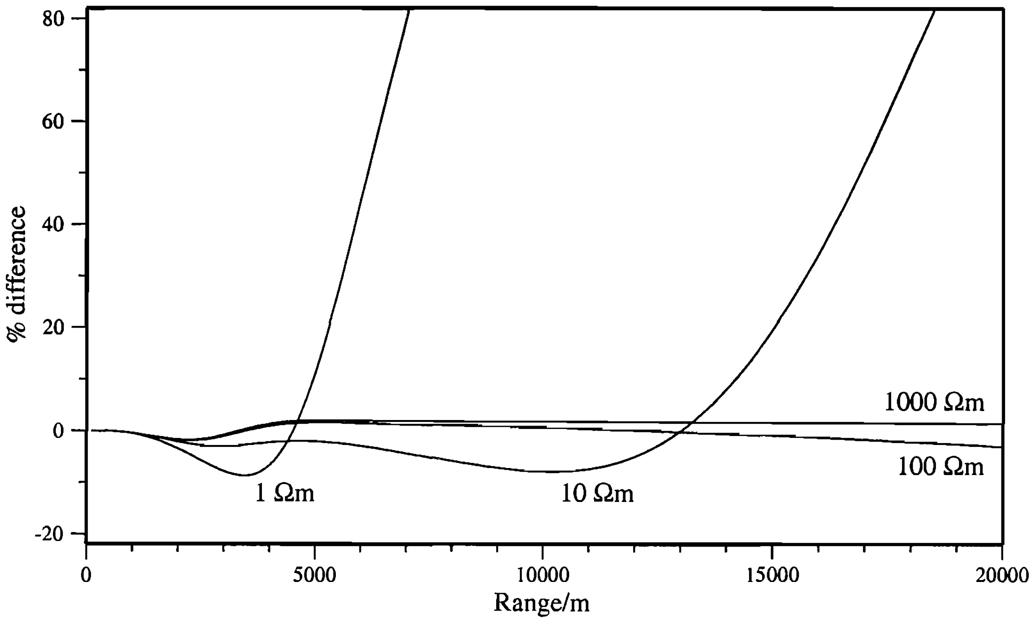

Figure 5.1: The effect of the air wave on modelled responses. The percentage difference in PE_{max} between an infinite water layer and a water layer of thickness 1400 m is shown for four different crustal resistivities at a transmission frequency of 0.25 Hz, and azimuth of 90°. Percentage difference is defined so that an increase in the field above the value for an infinite seawater layer is positive. Oscillations in the percentage difference at shorter ranges are due to the effects of constructive and destructive interference between the crustal and air wave signals (Chave & Cox 1982).

1. It can propagate directly through the water from source to receiver. This contribution will be correctly predicted by the modelling code. However, much of this signal is incidentally removed from the data by limiting the minimum source-receiver offset allowed (Section 4.5).

2. In shallow water depths, the signal can also propagate up through the water column, horizontally through the air, and back through the water to a receiver. This 'up and over' route (known as the 'air wave') is possible because the very high resistivity of air ensures that the signal experiences limited attenuation through this leg of its journey.

During transmission tows at Lucky Strike, neither the source nor any receivers were at a depth of less than 1400 m. Figure 5.1 shows the percentage difference in the electric field between a seawater layer of 1400 m thickness, and an infinite seawater layer, for four crustal resistivities. The modelled frequency is 0.25 Hz, the lowest frequency transmitted during the experiment. As the lowest transmission frequency has the longest skin depth, the air wave will be attenuated the least during its travel through the water column. With a crustal resistivity of 100 Ωm, the difference between a finite and infinite seawater layer is less than

2 % at all ranges that data are available. At a frequency of 1 Hz and a crustal resistivity of 100 Ωm, the difference is less than 1 % at all ranges that data are available. This difference does increase for lower crustal resistivities. However, at a crustal resistivity low enough for the effect of the air wave to be significant, the highly attenuated responses no longer agree with the recorded data.

For this reason, the water depth is considered infinite in all further modelling.

5.0.2 Point dipole approximation

MacGregor (1997) investigated the percentage error introduced in the response by the assumption that the source was a point dipole. The forward modelling code of Chave & Cox (1982) is able to calculate the response of an extended dipole by integrating the effects of point dipoles along its length. It was found that the difference became insignificant at a range equal to approximately four source lengths. This result was largely independent of the crustal resistivity used. With a dipole of length 100 m, and data with a range of less than 900 m being ignored, the source can therefore be assumed to be a point dipole.

5.1 Simple forward modelling results

Figure 5.2 shows a portion of the data recorded by LEMUR18, plotted against the responses predicted by uniform halfspace models. It can be seen that, whilst the data is fully bound by the 2 Ωm and 100 Ωm halfspace lines, they are not adequately predicted by such simple models. It is also clear that short-range data, particularly at source-receiver offsets of less than ~1.5 km, follow lower resistivity halfspace curves than the longer-range data, indicating that the resistivity sampled here generally increases with depth.

In the most simplistic of terms, layer over halfspace 1-D models can be justified geologically in terms of the difference in porosity (and therefore resistivity) expected between the crustal extrusive layer 2A and intrusive layer 2B. Whilst this is undoubtedly a gross oversimplification of the true structure at Lucky Strike, layer-over-halfspace models and their associated misfit functions give some idea of the possible classes of model which will fit the data, as well as quantifying the 'bulk' resistivity structure of the region.

Layer over halfspace model space has only three parameters (layer resistivity, layer thickness and halfspace resistivity) and can therefore be easily explored using the code of Chave & Cox (1982). It was found that the halfspace resistivity was not uniquely constrained by the data. Model misfits suggested that only a lower bound could be placed on it of between 70 and 100 Ωm, a value which was very similar for all five LEMURs. This lack of constraint can be explained using an argument based on the effects of skin depth. As the resistivity of the

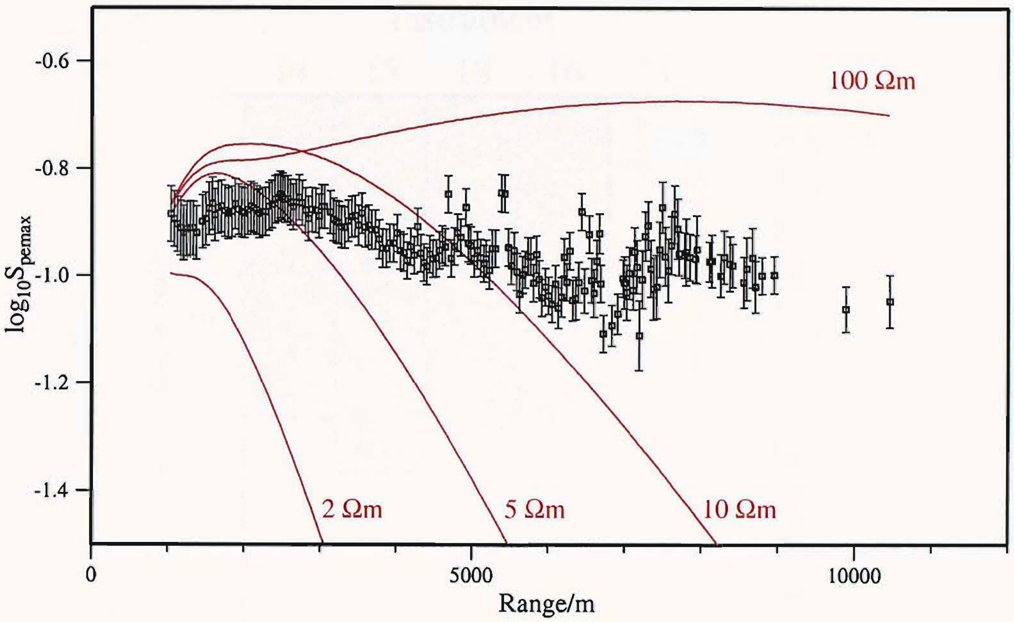

Figure 5.2: Data recorded by LEMUR18, plotted with modelled halfspace responses. The black squares with error bars are the 1 Hz data recorded during transmission along Line 6, when the source was to the east of the receiver (an in-line tow geometry). The five red lines correspond to the predicted response of a uniform halfspace for the resistivities indicated, assuming an in-line geometry. All models shown were overlain by a halfspace of resistivity 0.297 Ωm, representing the seawater.

underlying halfspace increases, the skin depth, or more specifically the number of skin depths covered within the halfspace by energy travelling from source to receiver, decreases. When the halfspace resistivity is at a level where such energy experiences no significant attenuation (corresponding to the lower bound described above), any further increase in resistivity will have little effect on the recorded signal amplitude.

Best-fit models were therefore obtained for each LEMUR (Figure 5.3) by systematically sampling the model parameters of layer resistivity and layer thickness, with a constant half-space resistivity of 100 Ωm. All data at 1 Hz, 3 Hz, 5 Hz and 9 Hz with a signal to noise ratio of 5 or greater were used, along with the small amount of 0.25 Hz data from LEMUR '99 instruments 16 and 18.

The constraint on layer thickness and resistivity provided by the different recorded frequencies can be seen in Figure 5.4. Some tradeoff exists between these parameters at high frequencies, although a well-constrained minimum is still present. The lower frequencies, in contrast, have no well constrained minimum, and exhibit a far greater tradeoff between parameters, reflecting their sensitivity to the integrated vertical resistance, rather than the resistivity of this hypothetical layer.

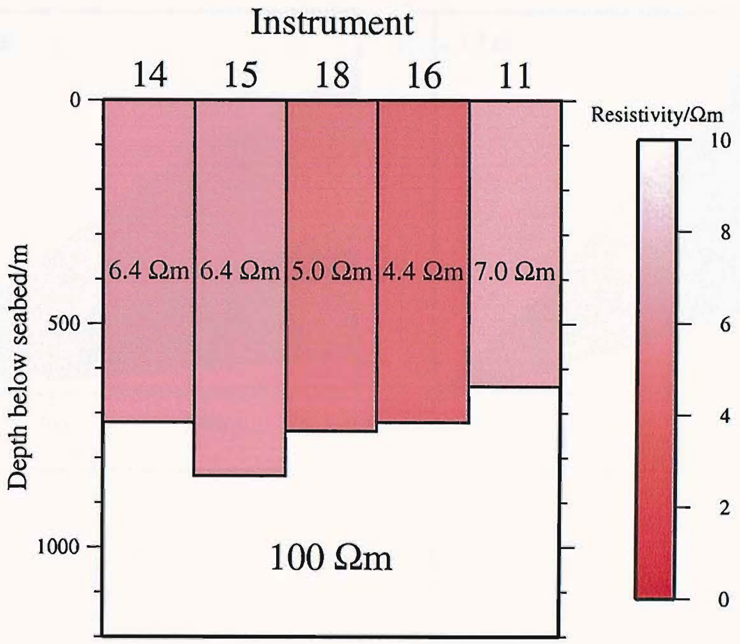

Figure 5.3: Best-fit layer over halfspace resistivity models obtained for each LEMUR. All 1 Hz, 3 Hz, 5 Hz and 9 Hz data with a signal to noise ratio of 5 or greater were used, along with 0.25 Hz data in the case of LEMUR'99 instruments 16 and 18. Best-fit models were obtained by systematically sampling the model parameters of layer resistivity and layer thickness, with a constant halfspace resistivity of 100 Ωm.

5.1.1 Data residuals

Plots of the residuals obtained from best-fit layer over halfspace models make it possible to visualise the higher-dimensional structure present in the EM data (Figures 5.5 & 5.6). They have the effect of highlighting areas where an anomolous electric field strength was recorded, with respect to the model used. The residuals exhibit clear systematic trends:

1. The 1 Hz data from LEMUR16 shows generally negative residuals, balanced by a greater proportion of positive residuals in higher frequencies. The lower frequency may therefore be sensitive to a more conductive region than the higher frequencies, which has the effect of reducing the lower frequency signal amplitudes.

2. Line 5 (down the eastern valley) exhibits consistently higher residuals than the adjacent Line 2. This is particularly visible in the 1 Hz data from LEMURs 11 and 15.

3. In general, there is little difference between the residuals from lines with different source-receiver azimuths at the point at which they cross. Distinct exceptions to this rule are:

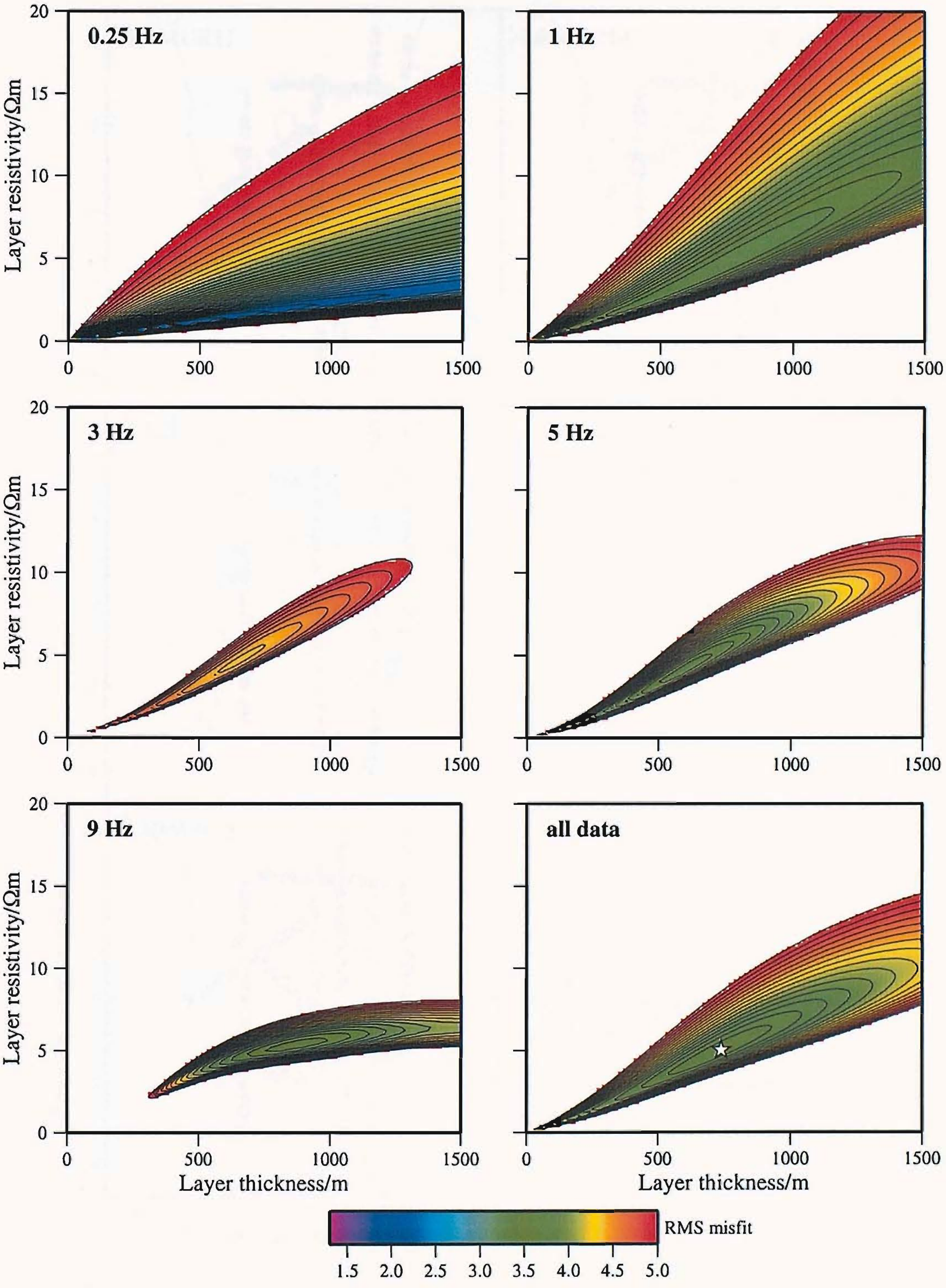

Figure 5.4: Plots of the misfit function obtained from layer over halfspace modelling of data from LEMUR18, for each frequency separately and for all frequencies combined. Areas with an RMS misfit of greater than 5 are plotted in white. The white star corresponds to the location of the best-fit model from all frequencies (Figure 5.3).

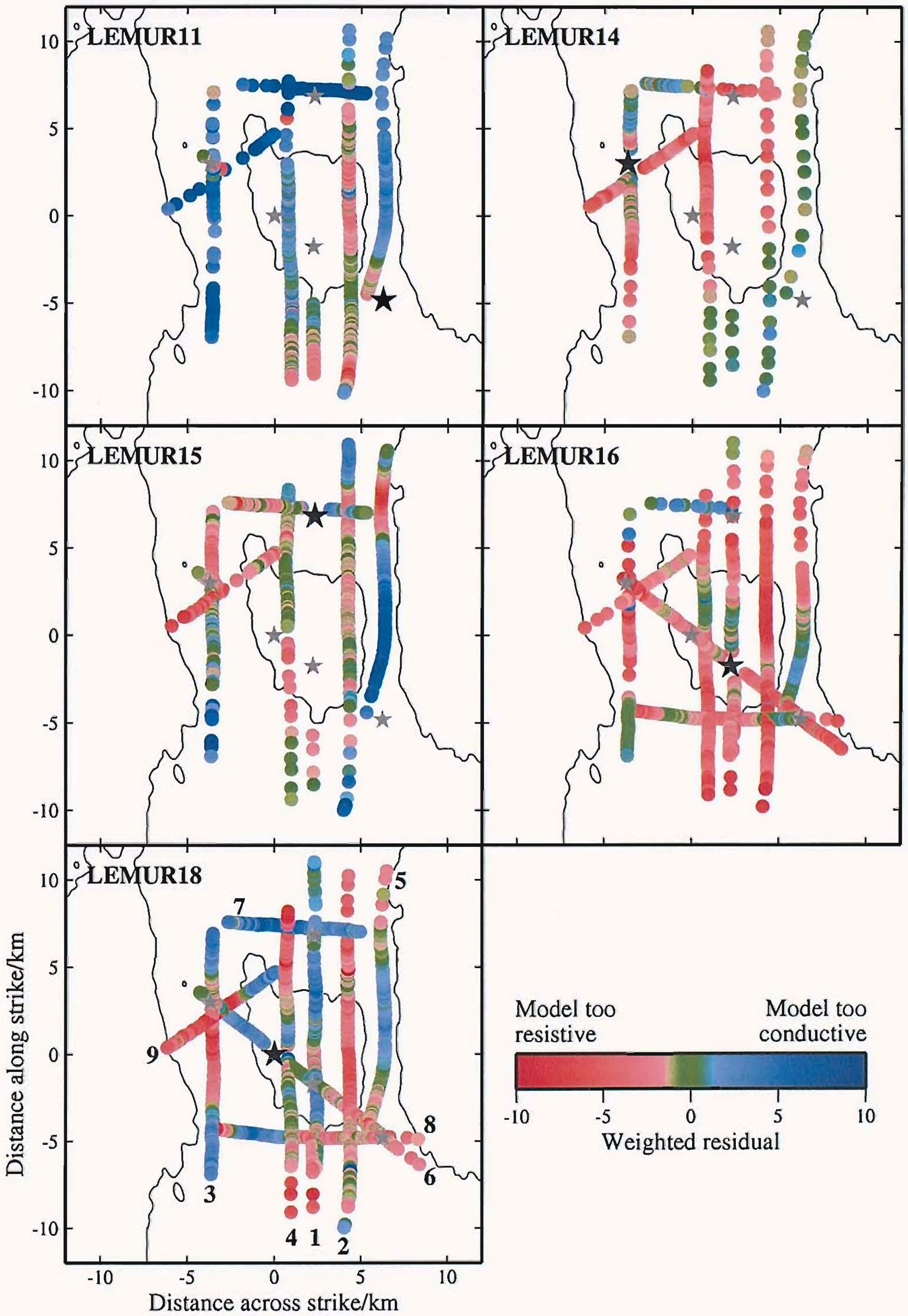

Figure 5.5: Weighted residuals between the 1 Hz data recorded by each instrument, and the modelled response from the best-fit layer over halfspace models shown in Figure 5.3. Data are plotted at source locations. Transmission line numbers are included on the LEMUR18 plot for reference. The map coordinates have been rotated by 18° counterclockwise about an origin at LEMUR18. This has the effect of lining up the ridge axis 'north-south' on the page. Receiver locations for each plot are show as a large black star, whilst other receivers are smaller grey stars. The Lucky Strike seamount and median valley walls are outlined by the 1900 m depth contour.

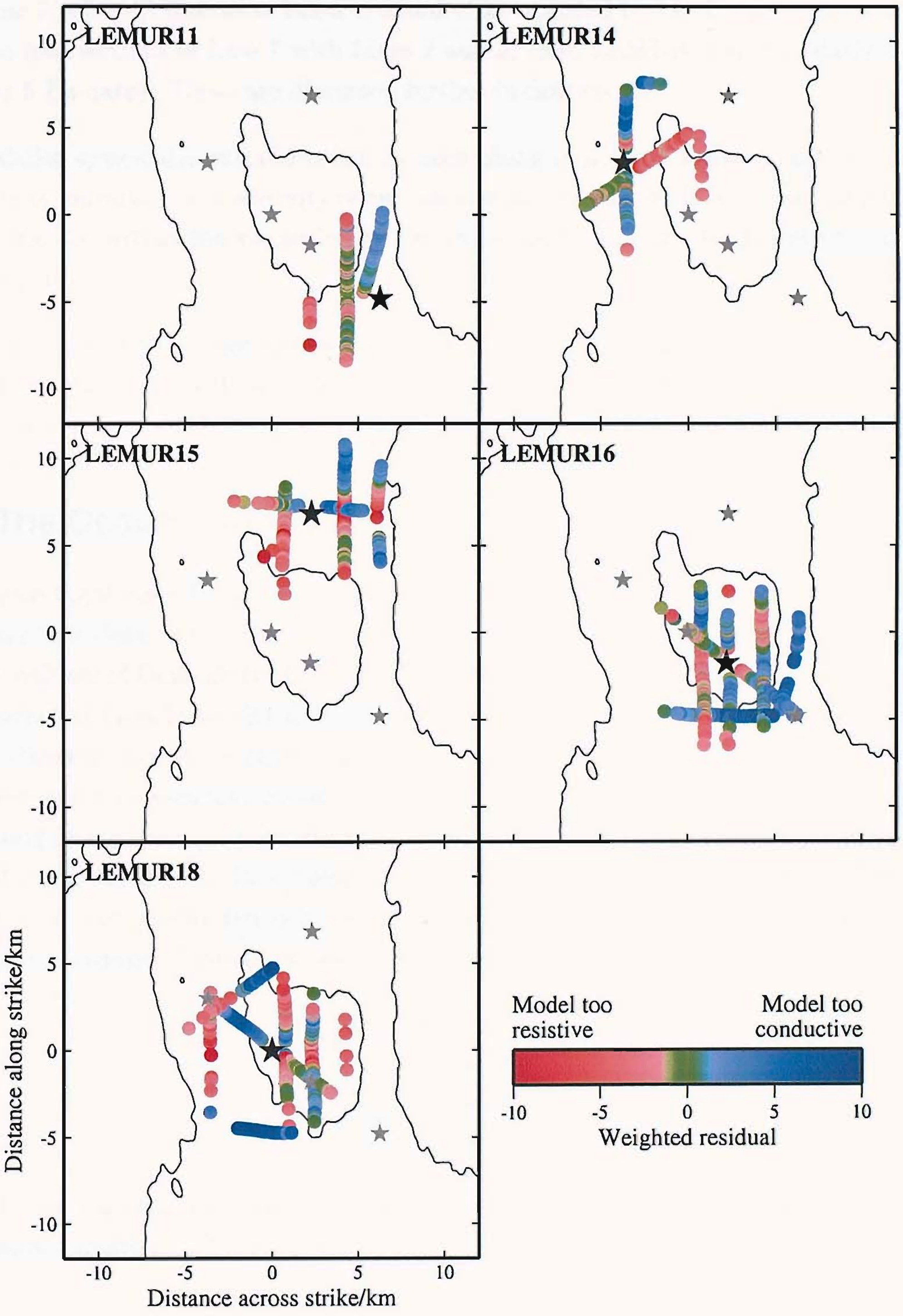

Figure 5.6: Weighted residuals between the 5 Hz data recorded by each instrument, and the modelled response from the best-fit layer over halfspace models shown in Figure 5.3.

Line 7, where it intersects Lines 1, 2 and 4, as recorded by LEMURs 11, 16 and 18; and the intersections of Line 7 with Lines 2 and 5, from LEMUR15 (particularly visible in the 5 Hz data). These are discussed further in Section 5.3.

4. Smaller systematic variations can be seen along individual tows. These are probably due to variations in resistivity structure at scales of hundreds of meters to kilometres, which are within the resolution of the experiment, and not simply short-wavelength scatter.

Whilst some of the above trends have been described here in terms of crustal resistivity variations, topography will also affect received signal amplitudes. This is discussed further in Chapter 6.

5.2 The Occam method of 1-D inversion

The Occam regularised inversion code of Constable et al. (1987) was used for 1-dimensional inversion of the data. Its name refers to 'Occam's Razor', the principle of parsimony championed by William of Ockham (1235-1347). In relation to data modelling, this can be expressed as 'the simplest model that fits the data adequately is the model to be preferred'.

The diffusive nature of electromagnetic fields, which has the effect of smoothing out sharp resistivity boundaries, means that maximising simplicity is thought of in terms of maximising smoothness, or conversely minimising roughness. The model m is expressed in terms of $\log_{10}$(resistivity). Roughness is then defined as the integrated square of the either the first or second partial derivative of the model with respect to depth z, giving rise to two alternative measures of overall model roughness:

$$\begin{aligned} R_1 &= \int \left(\frac{\partial m}{\partial z}\right)^2 \mathrm{d}z \\ R_2 &= \int \left(\frac{\partial^2 m}{\partial z^2}\right)^2 \mathrm{d}z. \end{aligned} \tag{5.1}$$

In the Occam algorithm, the model is defined as a stack of $N-1$ layers, terminated by a halfspace. Equations 5.1 can then be discretised to

$$\begin{aligned} R_1 &= \sum_{i=2}^{N} (m_i - m_{i-1})^2 \\ R_2 &= \sum_{i=2}^{N-1} (m_{i+1} - 2m_i + m_{i-1})^2 . \end{aligned} \tag{5.2}$$

Two forms of model smoothing are available in Occam. R_1 smoothing (known as first derivative smoothing) attempts to minimise the rate of change of resistivity (or $\log_{10}$(resistivity)) with depth. This has the effect of producing a model that is as near to a halfspace as is consistent with the data. R_2 (second derivative) smoothing minimises the variation in the rate of change of resistivity with depth, thereby generating a model that is as close to a steady gradient in resistivity with depth as is consistent with the data.

The number of layers in the model, and layer thicknesses, are user-defined before the inversion begins. A standard way to structure layers is to increase their thickness logarithmically with depth, reflecting the logarithmic decrease in model sensitivity with depth. In this case, model smoothing will be in terms of both logarithmic resistivity, and logarithmic depth.

The model misfit is defined as

$$\chi^2 = \sum_{i=1}^{M} \frac{(d_i - F_i[m])^2}{\sigma_i^2},$$

where there are M datapoints $d_i, (i = 1, M)$ with errors $\sigma_i, (i = 1, M)$; and F is a functional corresponding to the forward algorithm (in this case, Chave & Cox (1982)), such that the response of the model at the ith datapoint, $r_i = F_i[m]$.

If data errors are Gaussian with zero mean, and independent in each of the observations, then for the hypothetical 'true model' we would expect that $\chi^2 = M$. The root mean square (RMS) misfit for the entire model is defined as $\sqrt{\frac{\chi^2}{M}}$, which will then have a value of 1, corresponding to an RMS error between data and model of one standard deviation.

The Occam inversion works by trying to minimise an objective function that contains terms relating to the model roughness and model misfit. The relative importance of these two terms is controlled by a Lagrange multiplier, μ (Smith & Ward 1974): higher values of μ give the roughness term a greater importance, and a smoother model is obtained.

In each iteration, μ is initially chosen so that the misfit of the model is minimised, until the required misfit level is reached. When more than one value of μ produces the required misfit, the highest value (which produces the smoothest model) is chosen. In this way, the inversion generally progresses with a decrease in misfit, obtained at the expense of model roughness. When the required misfit is achieved, the roughness of the model is then reduced. The model is deemed to have converged when the required misfit has been reached, and the change in the model between successive iterations is less than a specified level.

5.2.1 Model bias

In order for the RMS misfit of the 'true model' to be equal to 1, (1) data errors must be accurately known, and (2) the resistivity structure of the earth must be 1-dimensional over the area to which the data are sensitive. In reality both of these are likely to be false to a greater or lesser extent, and so it is unclear what target RMS should be used.

The method used here to obtain the correct final model is described by Constable & Cox (1996). The smoothness criteria used by the Occam code results in a model that overestimates short-range data and underestimates long-range data. This means that a least squares fit to the data residuals against range has a gradient that generally decreases with decreasing RMS. The correct target RMS is then chosen to be the highest RMS at which the slope in the residuals is not significantly different to zero.

MacGregor (1997) applies this method of minimising residual bias by manually trying several likely target RMS misfits, graphing the residual slope versus RMS obtained, and manually selecting the highest RMS that produces zero-bias residuals. This process would be very time consuming for a dataset as large as that analysed here and, as increases in available computing power since 1997 now allow it, an automated process of RMS selection has been developed specifically for the Lucky Strike dataset. Many of the other data selection and processing stages required for 1-dimensional inversions of a large dataset have also been automated. These are detailed in Appendix D.

5.3 Inversion results

Little progress was made with inverting large subsets of the data from each instrument; the models were unstable and seldom converged. This is to be expected from a dataset that exhibits clear higher dimensionality. Instead, smaller subsets of the data were specifically chosen from regions that would be expected to have the most 1-dimensional resistivity structure, or to investigate particular features observed in the data during layer over halfspace modelling. Results from inversion of data from each LEMUR will be discussed in turn, beginning with those instruments furthest from the site of known hydrothermal activity. Unless otherwise stated, inversion was carried out with first derivative smoothing, thereby choosing the final model that was as close to a halfspace as was consistent with the data.

1 Hz, 3 Hz, 5 Hz and 9 Hz data were jointly inverted where this did not produce notable trade-offs between frequencies.

Generally, only data from tows that were within 20^o of pure in-line or broad-side were used to facilitate easier interpretation of the residuals obtained.

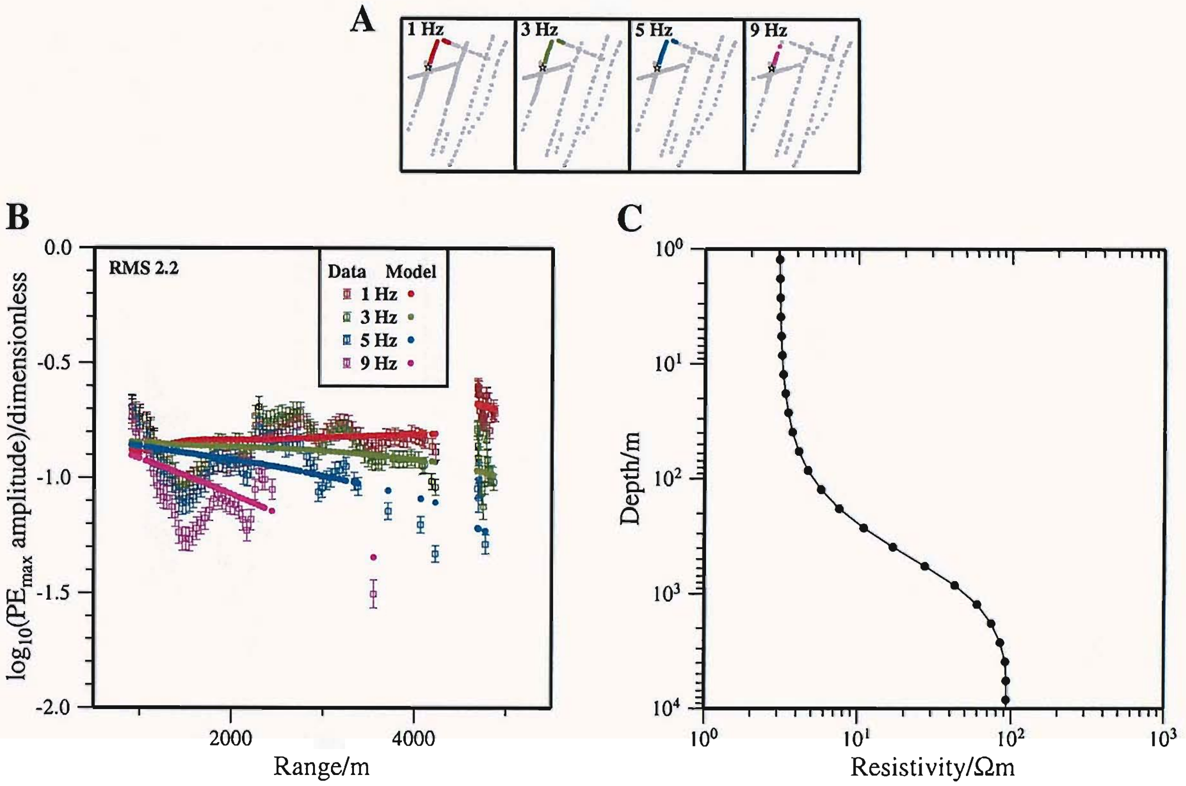

Figure 5.7: Results from 1-D inversion of a subset of the data recorded by LEMUR14. Plot *A* shows the coverage of data used in the inversion. All available data (including that with a low signal to noise ratio) is shown in grey. Data used in the inversion are coloured: in-line data from Line 3, to the north of the instrument, and broad-side data from Line 7, at a source-receiver range of up to 4.8 km. The data (squares with error bars) and modelled amplitudes (circles) are shown in Plot *B*, along with the RMS misfit between the data and model. Whilst these are displayed in terms of normalised current density, all modelling was still carried out in terms of electric field amplitudes, PE_{max}. The final resistivity profile obtained can be seen in Plot *C*: a resistivity of 3 Ωm at the seabed steadily increases to 90 Ωm at depths greater than 3 km.

LEMUR14

From LEMUR14, in-line data from Line 3 and broad-side data from Line 7 were chosen for inversion. These data run parallel to the ridge axis, cover an area with little seafloor topographic variation, and are the furthest away from the topography and possible lateral resistivity variation associated with the Lucky Strike seamount. The final model obtained can be seen in Figure 5.7. Whilst the model is unable to fit the small-scale data variations presumably associated with higher dimensional structures, it provides an adequate average fit to the data at all frequencies.

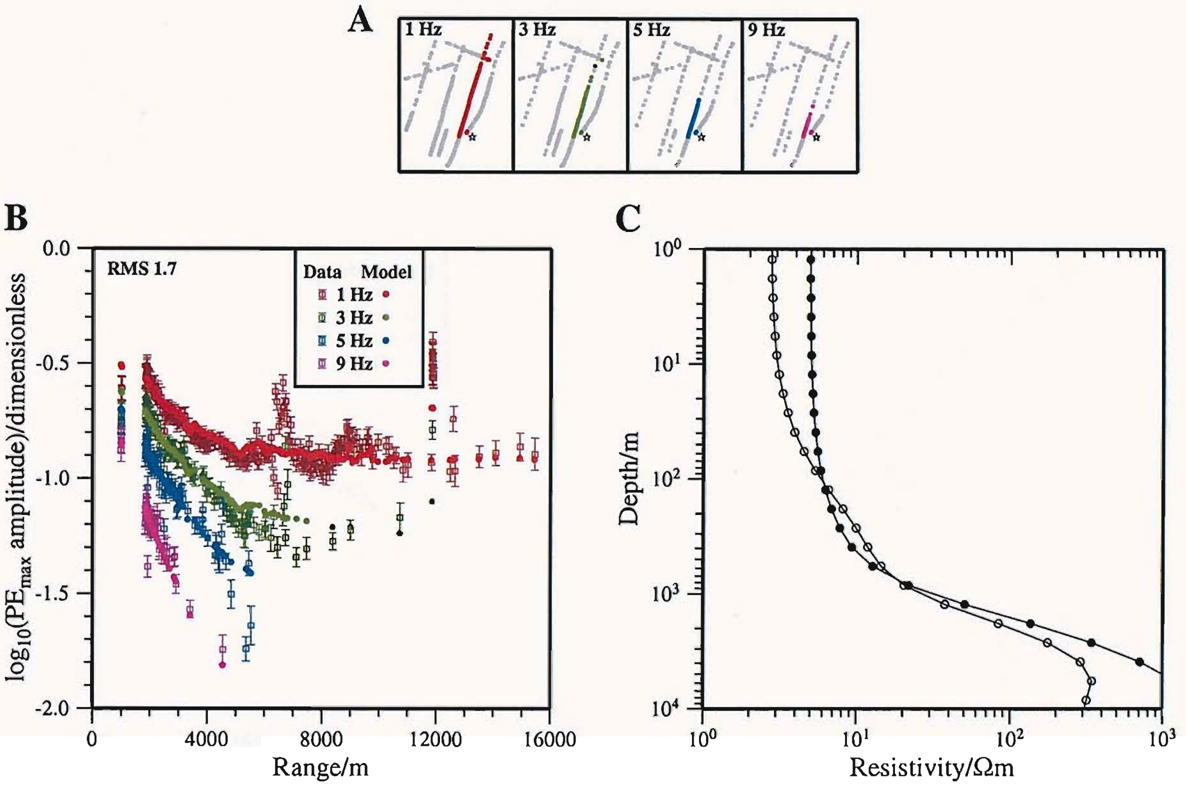

Figure 5.8: Results from 1-D inversion of a subset of the data recorded by LEMUR11. Data are fit to an RMS of 1.7. Whilst there is generally good agreement between data and modelled response in the in-line data, the greater signal strength recorded by the 1 Hz and 3 Hz broad-side data at a range of ~11 km cannot be fully explained by the final model. This model can be seen with filled circles in Plot *C*, and finally reached a maximum resistivity of ~2200 Ωm at depths of 27 km and greater. In an inversion without the long-range broad-side data, the model obtained is shown with open circles. This model fits the data to an RMS of 1.5.

LEMUR11

The radial data from Line 5 to the north of LEMUR11 along the bottom of the eastern valley could not be adequately modelled with a 1-D resistivity structure. Instead, short-range broad-side data from this line, along with broad-side and in-line data from Line 2 and long-range broad-side data from Line 7 were selected for inversion. Whilst these data are predominently parallel to the ridge axis, the effect of topography and resistivity variation associated with the axial seamount do not make it an ideal candidate for 1-dimensional modelling. However, it does allow the enhanced signal amplitudes relative to the layer over halfspace model along Line 7 (see Figure 5.5) to be investigated.

Results of the modelling can be seen in Figure 5.8. The inversion has attempted to fit the

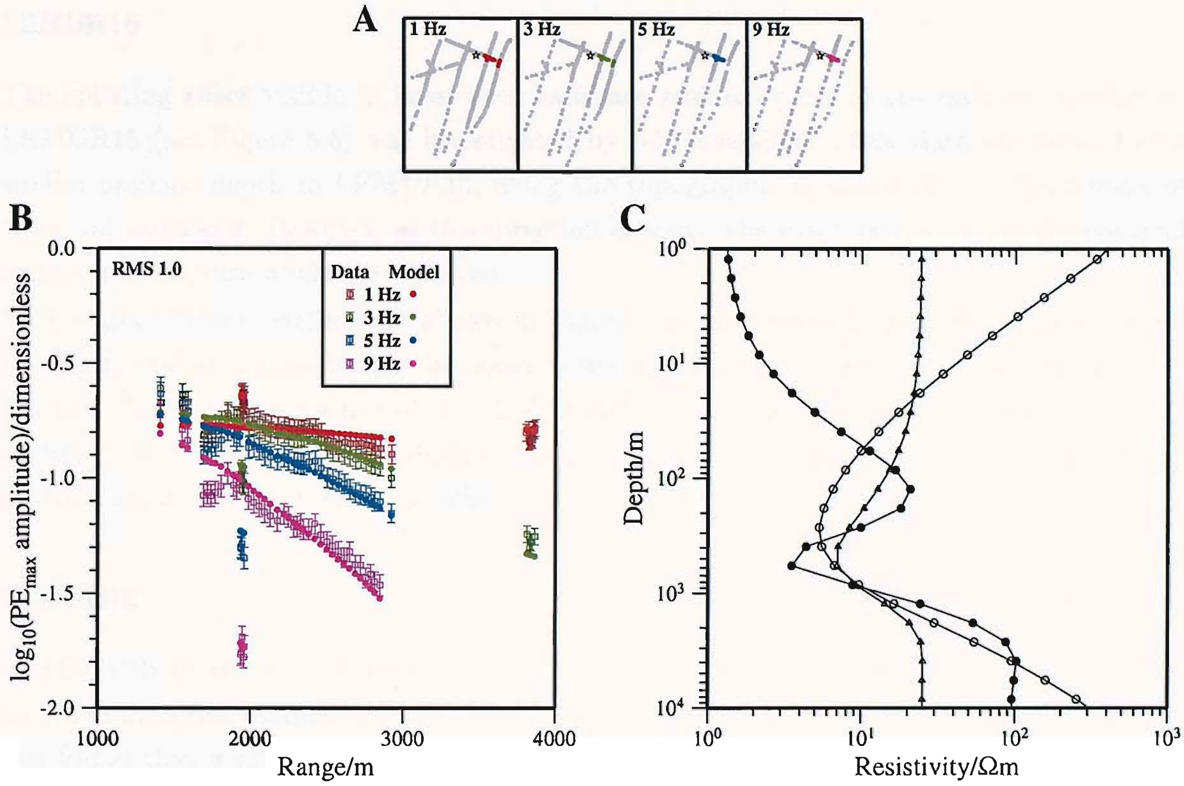

Figure 5.9: Results from 1-D inversion of a subset of the data recorded by LEMUR15. Data are fit to an RMS of 1.0, although some bias between the different frequencies can be seen in the radial data from 2.3–2.9 km. The model obtained from this inversion is shown with filled black circles in Plot *C*. In contrast, the final model obtained from inversion with second derivative smoothing is shown with open circles. This model fitted the data to an RMS of 1.2. The continued presence of the resistivity downturn in a model where it is in direct opposition to the applied smoothing, strongly suggests that it is a requirement of the data, if interpreted in 1-D at this misfit level. However, it is still possible that the resistivity downturn is a result of overfitting the data: the optimum RMS misfits obtained when modelling data from other instruments are generally higher than the 1.0 found here. To eliminate this possibility, the data were inverted with 1st derivative smoothing at an RMS misfit of 1.7 (triangles in Plot *C*). This model shows that changing the RMS effects the tradeoff between shallow resistivity and deep resistivity, but the low resistivity layer is still present.

broad-side data by rapidly increasing the resistivity between depths of 1 km and 27 km. Much of this increase is too deep to have significant effect on the galvanically-channelled energy in the in-line data, as can be seen from the model obtained with long-range broad-side data omitted. But the deep resistive layers are still able to increase the field strength in the inductive broad-side data. However, even this has not produced splitting of the magnitude observed.

LEMUR15

The splitting effect visible in layer over halfspace residual plots of the data to the east of LEMUR15 (see Figure 5.6) was investigated by 1-D inversion. These data are located at a similar seafloor depth to LEMUR15, along the topographic strike of the northern flank of the axial seamount. However, as this direction is across the ridge axis, a higher-dimensional resistivity structure might be expected.

Results of the modelling are shown in Figure 5.9. In general, a good fit to the data has been achieved at all frequencies, although some tradeoff can be seen at ranges greater than 2.3 km. The striking feature of the final model is a dip in resistivity between the depths of 100 m and 2 km. This conductive layer is required in order to explain the significant attenuation in $E_\perp$ observed at an offset of 2 km, particularly at higher frequencies.

LEMUR18

As LEMURs 18 and 16 are located on the axial seamount, it is unlikely that any subset of their recorded data has sampled a predominantly 1-dimensional resistivity structure. However, it was found that a number of subsets from LEMUR18 would converge in Occam modelling. Two of these subsets are described here.

Radial data to the north of LEMUR18 from Line 4, along with broad-side data from Line 7 were chosen in order to investigate the same splitting effect seen in data from LEMUR11. The high-amplitude in-line data from Line 7 has a similar effect on the final model (Figure 5.10). Deep structural resistivity is increased over a model without the broad-side data included, although not to such a degree as found with LEMUR11. It is therefore probable that the greater signal strength from Line 7 recorded by LEMURs 15 and 18 is due to higher-dimensional effects, discussed further in subsequent chapters.

An inversion of data recorded from lines to the south-east of LEMUR18 is shown in Figure 5.11. This subset is chosen in order to compare with results from LEMUR16, below. A good fit to the data has been possible with an increase in resistivity from ~3 Ωm at the seafloor, to ~200 Ωm at a depth of 10 km.

LEMUR16

Data from LEMUR16 proved to be the most difficult to model in 1-D. Inversions generally remained unstable and would not converge. When subsets of data were found which did generate converged models when jointly inverted, significant bias was found in the residuals from different frequencies. This is in agreement with the results from layer over halfspace

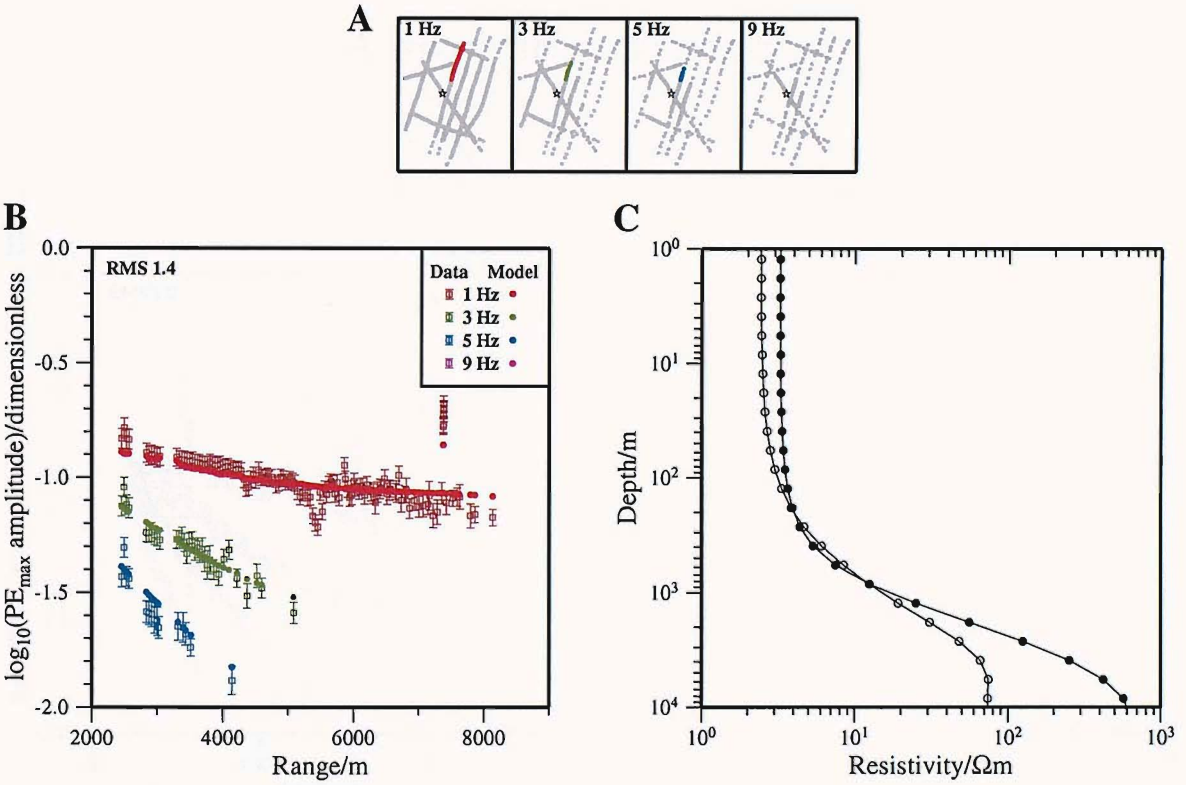

Figure 5.10: Results from 1-D inversion of a subset of the data recorded by LEMUR18. The long-range high-amplitude broad-side data has the same effect on the final resistivity profile obtained, as was found with LEMUR11 (Figure 5.8). The model obtained in the absence of these data is shown with open circles in Plot *C*. This model fitted the data to an RMS of 1.1.

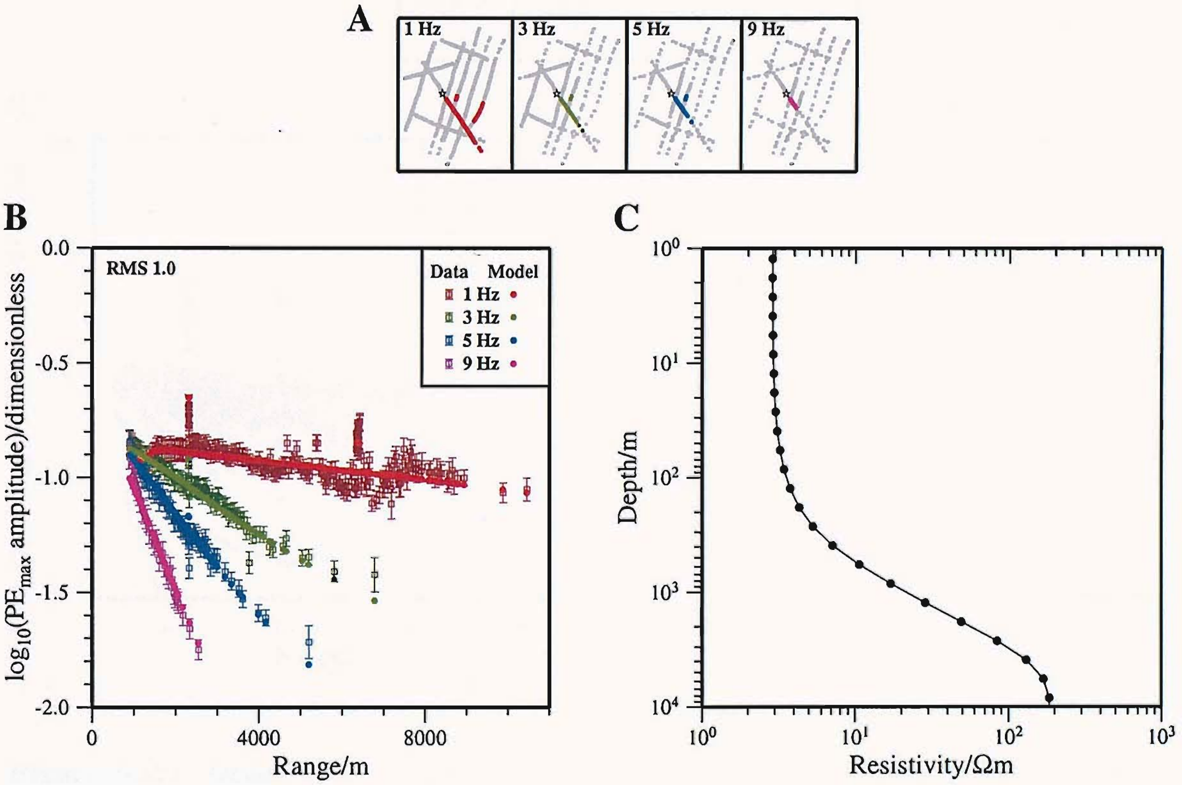

Figure 5.11: More results from 1-D inversion of data recorded by LEMUR18. The data used in this inversion were chosen to be near-coincident to that used from LEMUR16 (Figure 5.12).

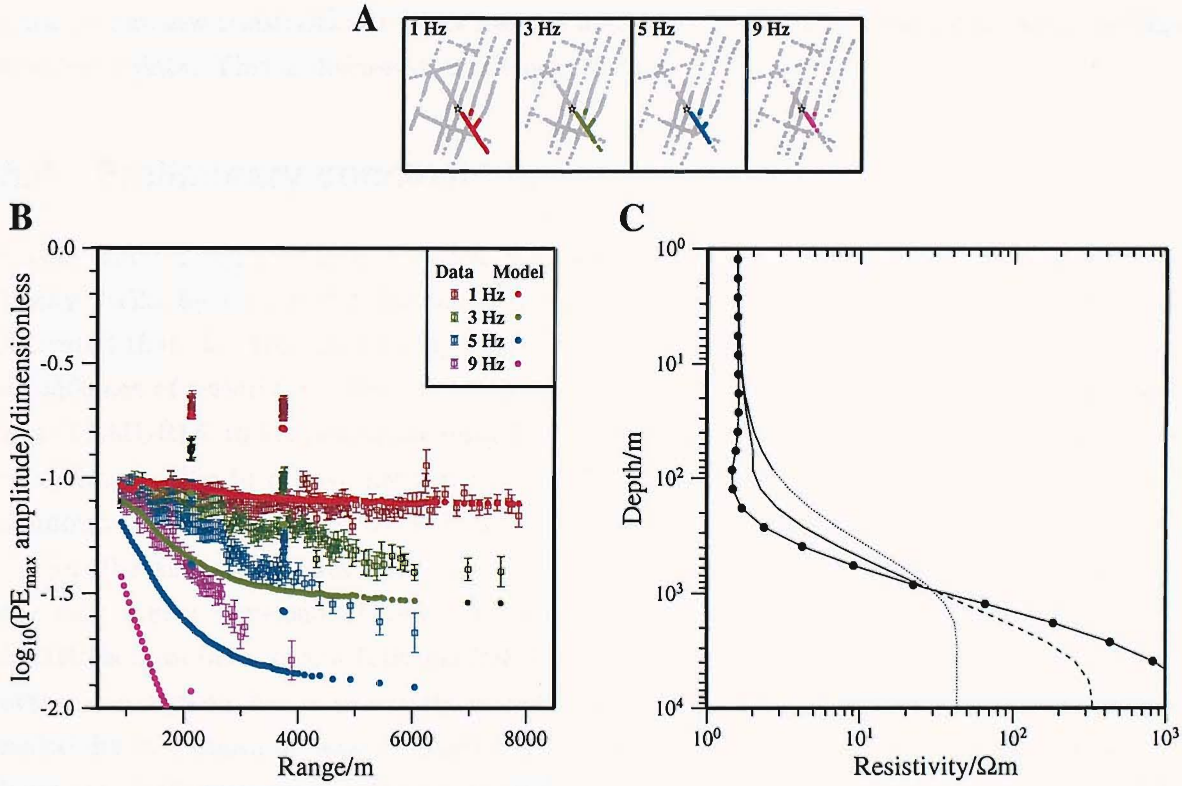

Figure 5.12: Results from a constrained 1-D inversion of a subset of the data recorded by LEMUR16. First, the 9 Hz data were inverted in isolation (RMS misfit: 0.7). The model obtained is shown by the solid and dotted line in Plot *C*. The solid portion of this was used to constrain an inversion of the 3 Hz data, producing the model shown by the solid and dashed line (RMS misfit: 0.9). The solid portion of this line was then used to constrain an inversion of the 1 Hz data, producing the model shown by the filled circles in Plot *C* (RMS misfit: 1.2). Finally, a forward model was carried out using the data from all frequencies, producing the results in Plot *B* (RMS misfit: 7.2). It can be seen that whilst an adequate fit has been obtained to the 1 Hz data, the modelled amplitudes at higher frequencies are consistently underestimated.

modelling, where the best-fit model generated consistently positive residuals in the lower frequencies, and negative residuals in the higher frequencies (Figures 5.5 & 5.6).

The results of constrained inversion of a data subset are shown in Figure 5.12. The residuals obtained from this again illustrate than it is not possible to find a single model that is consistent with the observed data at different frequencies. The models show that the 1 Hz data require low resistivities to be present at a greater depth than is consistent with the high frequency data. This is discussed in the next section.

5.4 Preliminary conclusions

Considerable progress has been made in understanding the crustal resistivity structure at Lucky Strike by means of 1-dimensional modelling. Layer over halfspace modelling has illustrated that the data are broadly consistent with a layer of thickness ~700 m, overlaying a halfspace of resistivity $\geq$100 Ωm. Upper layer resistivities vary from 4.4 Ωm in the data from LEMUR16, to 7.0 Ωm in the data from LEMUR11: it would seem that even this coarse modelling is able to resolve lower resistivities in the region of the seamount summit (which is known to be hydrothermally active) whilst higher resistivities are seen off-axis.

Smaller subsets of data have been selected over regions that may be expected to have the least higher dimensional resistivity structure. In this way, data from all but one of the LEMURs have been successfully modelled using 1-D Occam inversion. The uppermost crust over these regions has a resistivity of between 2 and 4 Ωm. There is a steep increase in resistivity at a depth of between a few hundred metres and one kilometre. In agreement with layer over halfspace results, Occam modelling finds a crustal resistivity of at least 100 Ωm below this depth.

Splitting between the in-line and broad-side fields recorded by LEMUR15, to the east of the instrument, can be explained in 1-D by the presence of a low resistivity zone at depths of between ~500 m and ~1000m in the north east of the survey area. Resistivities are as low as 3 Ωm within this low resistivity zone, whilst the crust directly above this region has resistivities in the order of 20 Ωm. Modelling in the next chapter will investigate whether the topography over this region could also produce the observed field amplitude splitting.

Anomalously high broad-side fields have been highlighted in data recorded by LEMURs 11 and 18 over the northern seamount flank; no 1-D structure could be found that would account for these field strengths.

LEMUR16 data proved to be extremely difficult to invert using Occam 1-D. No 1-D model could be found that simultaneously fit data at different frequencies. Situated near the seamount summit, adjacent to the area of known hydrothermal activity, it would have been surprising if LEMUR16 had sampled a predominantly 1-dimensional resistivity structure.

It is clear that higher dimensional modelling will be needed to constrain the resistivity structure under the central region of the survey area. However, layer over halfspace modelling does suggest that the crustal resistivities sampled by LEMUR16 are higher than in the rest of the survey area.

Chapter 6

2-D forward modelling and inversion

2-D modelling was carried out in order to incrementally improve our understanding of the subsurface resistivity over that obtained from 1-D modelling. Specifically, it was used to address the following questions:

1. What effect does the severe topography at Lucky Strike have on the recorded electric field strength, and can this 3-dimensional effect be adequately modelled in 2-D?
2. Could specific electric field amplitude anomalies highlighted with 1-D modelling and attributed to crustal resistivity variations be instead due to this topographic effect? Namely, (a) can the topography account for the attenuation of $E_\perp$ relative to $E_\parallel$ recorded by LEMUR15, and interpreted as being due to a decrease in resistivity with depth; (b) can it account for the enhancement of $E_\perp$ relative to $E_\parallel$ recorded by LEMURs 11 and 18 on the northern seamount flank; and (c) can it explain why no 1-D model will simultaneously fit different frequencies of data recorded by LEMUR16?
3. Can the topographic effect be adequately quantified in order for the data to be subsequently modelled assuming a flat seafloor (due to the current limitations of 2.5-D inversion and 3-D forward modelling codes)?

The finite element modelling code used here has been described in detail by Unsworth (1991) and Unsworth et al. (1993), with modifications described by MacGregor (1997). The problem is termed 2.5-dimensional, as the resistivity structure is allowed to vary in 2-D, whilst the fields of the point dipole are accurately modelled in three dimensions.

This chapter begins by providing a summary of the 2.5-D modelling technique. Model geometry requirements are discussed, as are strategies for the optimal parameterisation of model space. Topography is included with a method similar to that used by MacGregor

(1997). Limitations in this method have been addressed here in order to allow near-arbitrary topographic model distortion. Methods for verifying the accuracy of the finite element results are discussed, along with a new method for verifying a topographically-distorted mesh. A summary of the 2.5-D inversion implemented by MacGregor (1999) is given. Finally, the results of topographic forward modelling and data inversion are presented, and the answers to the above questions are addressed.

6.1 Finite element modelling

Maxwell's equations (2.1 to 2.4) again govern the total electric and magnetic fields ($\boldsymbol{E}$ and $\boldsymbol{B}$) generated by a specific source current distribution $\boldsymbol{J}_s$. Assuming a harmonic time variation of angular frequency ω, equations 2.3 and 2.4 then become,

$$\nabla \times \boldsymbol{E} = -i\omega\boldsymbol{B} \tag{6.1}$$

$$\nabla \times \boldsymbol{B} = \mu_0\sigma\boldsymbol{E} + \mu_0\boldsymbol{J}_s. \tag{6.2}$$

For the point electromagnetic source, $\boldsymbol{J}_s$ is singular and difficult to represent accurately by a discrete formulation. Unsworth (1991) overcomes this by separating the total field into primary and secondary components, such that

$$\boldsymbol{E}_{total} = \boldsymbol{E}^P + \boldsymbol{E}^S \tag{6.3}$$

and

$$\boldsymbol{B}_{total} = \boldsymbol{B}^P + \boldsymbol{B}^S. \tag{6.4}$$

Both the total, and primary fields are governed by Maxwell's equations, so

$$\nabla \times \boldsymbol{E}_{total} = -i\omega\boldsymbol{B}_{total} \tag{6.5}$$

$$\nabla \times \boldsymbol{B}_{total} = \mu_0\sigma\boldsymbol{E}_{total} + \mu\boldsymbol{J}_s \tag{6.6}$$

for the total fields, and

$$\nabla \times \boldsymbol{E}^P = -i\omega\boldsymbol{B}^P \tag{6.7}$$

$$\nabla \times \boldsymbol{B}^P = \mu_0\sigma\boldsymbol{E}^P + \mu\boldsymbol{J}_s \tag{6.8}$$

for the primary fields. Subtracting one pair of equations from the other leaves the solution to the secondary fields,

$$\nabla \times \boldsymbol{E}^S = -i\omega\boldsymbol{B}^S \tag{6.9}$$

$$\nabla \times \boldsymbol{B}^S - \mu_0 \sigma \boldsymbol{E}^S = \mu_0 \Delta\sigma \boldsymbol{E}^P \tag{6.10}$$

where $\Delta\sigma$ is the difference between the total 2-D conductivity and the conductivity used to calculate the primary fields. Thus if a simple 1-D conductivity structure is used to calculate the primary fields, and $\Delta\sigma = 0$ around the source, the singular source term $\boldsymbol{J}_s$ is replaced for the secondary fields by the non-singular function $\Delta\sigma\boldsymbol{E}^P$.

A cartesian coordinate system is defined with the z-axis vertically upwards, and x-axis in the invariant (along-strike) direction. As the resistivity only varies in 2-dimensions, a Fourier transform can be then carried out in the invarient direction, simplifying the solution still further. The variations of the 3-D source fields are then expressed in the wavenumber, rather than the spatial domain along the x-axis. For all non-zero wavenumbers, a minimum of two field components must be calculated in order to represent the 3-D electromagnetic fields. Unsworth (1991) evaluates $\boldsymbol{E}_x^S$ and $\boldsymbol{B}_x^S$, from which $\boldsymbol{E}_y^S$ is derived in the wavenumber domain. An inverse Fourier transform recovers the solution in the spatial domain, and the primary fields for the 1-dimensional background structure are added to give the components of the total field.

Finite element calculations discretise the model space into elements. Field values are calculated at the corners of each element, called nodes. The fields within each element are then approximated by linear interpolation. If this interpolation is unable to sufficiently represent the true fields, the results obtained will be inaccurate. It is therefore essential to test the accuracy of the model parameterisation chosen. Here, a rectilinear mesh is used to define the model space in the varying directions y and z, along with a discretised wavenumber spectrum in the invarient direction, x.

At the edge of the region defined by the finite element mesh, the solutions for $\boldsymbol{E}_x^S$ and $\boldsymbol{B}_x^S$ must satisfy a boundary condition. Unsworth (1991) applies a derivative boundary in order to satisfy the condition that the electromagnetic fields decay to zero at an infinite distance from the source. This is equivalent to extending the mesh to infinite distance using infinite rectangular elements (Unsworth 1991).

6.1.1 Mesh design

Clearly, accurate results are favoured by a very fine parameterisation of the mesh and wavenumber spectrum. In practice, as computer processing time and memory usage rapidly increase with finer parameterisation, an acceptable tradeoff must be found between parameterisation and accuracy of results. Unsworth (1991) and MacGregor (1997) describe general rules to be followed when parameterising the model: -

1. Generally, a minimum of three mesh elements per skin depth are needed to obtain an

accurate solution. As the mesh is rectilinear, the skin depth must be measured in the least resistive part of the model.

2. In order to accurately represent the exponential decay of fields, finer parameterisation is sometimes needed around the source, especially when the shallow crust has a low resistivity.

3. When node spacing is allowed to vary with position, this spacing should not vary by more than a factor of 2 between adjacent pairs of nodes.

4. The mesh should extend at least 1.5 skin depths from the source, measured in the most resistive part of the model as this controls the long distance diffusion of electromagnetic fields.

5. The minimum and maximum wavenumbers and the resolution of the spectrum must be specified. The minimum and maximum wavevenumbers (k_{min} and k_{max}) control the minimum and maximum along-strike distance from the source (R_{min} and R_{max}) at which the solution is accurate. It can be shown empirically that

   $$R_{min}k_{max} \approx 4. \tag{6.11}$$

   The maximum along-strike wavelength must be at least twice the maximum range required. Therefore

   $$k_{min} < \frac{\pi}{R_{max}}. \tag{6.12}$$

   Spline interpolation is applied between the discrete wavenumber values used. There must therefore be enough wavenumbers to ensure that this interpolation does not introduce significant errors into the calculation. In general, a logarithmic spacing with five wavenumbers per decade is sufficient.

6. The primary resistivity should be close to the true crustal resistivity around the source, otherwise the singularity is not adequately removed from the secondary fields. Conversely, the model may also become unstable if the primary resistivity is so close to the true resistivity that secondary fields are zero over much of the model. This can be avoided by altering the primary resitivity by in the order of 0.1 %.

6.1.2 Inclusion of topography

For some simple topographic situations, it is possible to qualitatively predict the effect that the topography will have on the recorded electric fields. For example, if both the source and receiver are at the bottom of a 'valley', a stronger signal would be expected. This is because the resistive valley walls have replaced a portion of the conductive seawater, reducing the skin-depth controlled attenuation experienced by the fields. Conversely, if both the source and receiver are on a ridge, the 'extra' seawater present down each ridge flank would be expected to reduce the electric field amplitudes. This effect was modelled by Unsworth (1991), who used a non-rectilinear mesh in which the seafloor was allowed to slope away from the axis at angles of between 2.0^o and 10^o. It was found that the electric field strength decreased almost linearly with increasing ridge slope angle. Confronted with the more complicated seafloor topography at the Reykjanes Ridge, MacGregor (1997) distorted a rectilinear mesh to follow the required topography. It is this technique that is used here. An upper and lower level, z_u and z_l are defined, between which the mesh is distorted. The positions of seafloor nodes, z_{sf}, are also specified. New node positions are then calculated so that

$$\frac{z^a_{old}}{z_u} = \frac{z^a_{new} - z_{sf}}{z_u - z_{sf}} \tag{6.13}$$

for rows of nodes above the seafloor, and

$$\frac{z^b_{old}}{z_l} = \frac{z^b_{new} - z_{sf}}{z_l - z_{sf}} \tag{6.14}$$

for rows of nodes below the seafloor, where z^a_{old} and z^b_{old} refer to the undistorted mesh. Topography was incorporated into the existing processing strategy by distorting the mesh input file in this fashion prior to mesh generation. However, it was found that the mesh generator TRIMESH had difficulty functioning with a distorted mesh in some instances. With the Reykjanes Ridge data, it proved necessary to arbitrarily alter the mesh until a distortion was found that would work with TRIMESH (L. MacGregor pers. comm.). This problem is solved here by incorporating the required topography after the mesh has been generated from the startup files (Figure 6.1).

The source must be placed at $z = 0$ in a region of undistorted mesh to ensure that the secondary conductivity is near zero close to the source. There must also be a row of nodes at $z = 0$ to ensure that mesh elements do not straddle the seafloor-seawater boundary, as defined by the 1-dimensional primary structure. These requirements mean that if several sources at different elevations are modelled, they must each have their own mesh files. Results for multiple sources are then combined subsequent to forward modelling.

In the region of mesh distortion there must be enough rows of nodes to ensure that the mesh spacing is not stretched to such an extent that it is unable to accurately represent the fields. In the absence of distortion, the accuracy of the answers obtained can be verified by

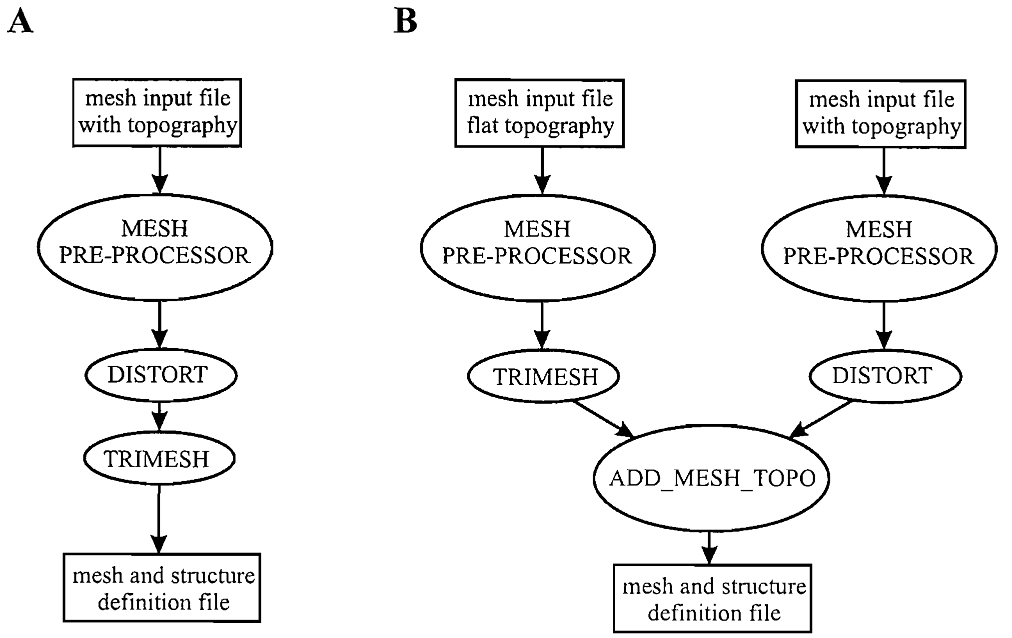

Figure 6.1: The new technique for topographically distorting the 2.5-D mesh. *A*: A flow diagram illustrating the steps required to generate the mesh and structure definition files, developed by MacGregor (1997). *B*: Problems encountered with generating a distorted mesh are overcome here by applying the distortion after the mesh has been generated by TRIMESH, with the new routine ADD_MESH_TOPO.

comparison with the results from the 1-dimensional code of Chave & Cox (1982). However once topography is included, this is no longer possible. MacGregor (1997) verified that the finite element code could produce reliable answers with a distorted mesh by limiting the distortion to the region below the seafloor, thereby allowing direct comparison to the 1-D results. However this does not fully address the validity of the answers obtained from the topographic mesh used. Also, the region close to the seafloor where vertical derivatives of the secondary fields must be calculated is most sensitive to distortion: a region that remains undistorted with this verification technique. The problem is solved here by comparing the results obtained from two different meshes as they are progressively distorted (see Section 6.2.1).

Finally, it is convenient to calculate the total electric field at the seafloor in the wavenumber domain and then perform the inverse Fourier transform, since the primary fields in the spatial domain are more easily calculated at the level $z = 0$. However, this tends to propagate along the invariant spatial dimension the numerical instability associated with the source singularity (L. MacGregor pers. comm.). This problem is also addressed in Section 6.2.1.

6.2 Model geometry

As the fields have to be calculated throughout model space for each HED source, calculation time is greatly reduced by minimising the number of sources in the model. It is also a requirement of the code that sources are located along $x = 0$. In order to accommodate this, the experimental geometry of fixed receivers and a moving source is transformed into a fixed source, and moving receivers. For example, a transmission line along the model invariant direction is reduced to a single point at $x = 0$ and its average position on the y-axis. Fixed receivers then become receiver 'lines' along the invariant direction (e.g. Figure 6.2).

Two near-orthogonal models were constructed in order to investigate the topographic effects of the 3-dimensional seamount, as well as to include as much of the available data as possible given the geometric constraints detailed above. The first model was defined with an invariant direction along the ridge axis. This allowed data from the five north-south transmission tows to be modelled with only five source locations (Plots *A* and *B* in Figures 6.2 and 6.3), as well as allowing the topographic effect of the seamount and median valley walls to be investigated. The second model was defined with a strike direction along the average orientation of lines 7 and 8. These lines could then also be reduced to single sources. In this geometry, the north-south lines have a source dipole which is across the model strike. In order to include data from these lines in the model, sections of each line were selected that could be reasonably modelled with four across-strike source locations (Plots *C* and *D* in Figures 6.2 and 6.3). A model in this orientation encompasses the northern flank of the seamount, the region of steepest topography, and allows comparison with the more gentle slopes on the southern flank. Questions (2a) and (2b) can also be addressed with this geometry.

These two models are now referred to as the across-axis and along-axis models respectively.

Parameterisation

Two rectilinear meshes were created with as fine a parameterisation as processing time and memory requirements would allow. This meant that in each instance, a single set of parameters could be used to study different transmission frequencies. The mesh rules outlined in Section 6.1.1 would suggest that the meshes produced should be capable of modelling frequencies up to at least 3 Hz. Finer meshes capable of modelling higher frequencies, but over a correspondingly smaller region, would likely do little to improve our understanding of the resistivity structure over that already found with 1-D modelling. The across-axis mesh, consisting of 10625 nodes, can be seen in Figure 6.4. The along-axis mesh used a similar parameterisation around source locations, and contained 11815 nodes (not shown).

In order to model data with a maximum offset of 16 km, a minimum wavenumber of less

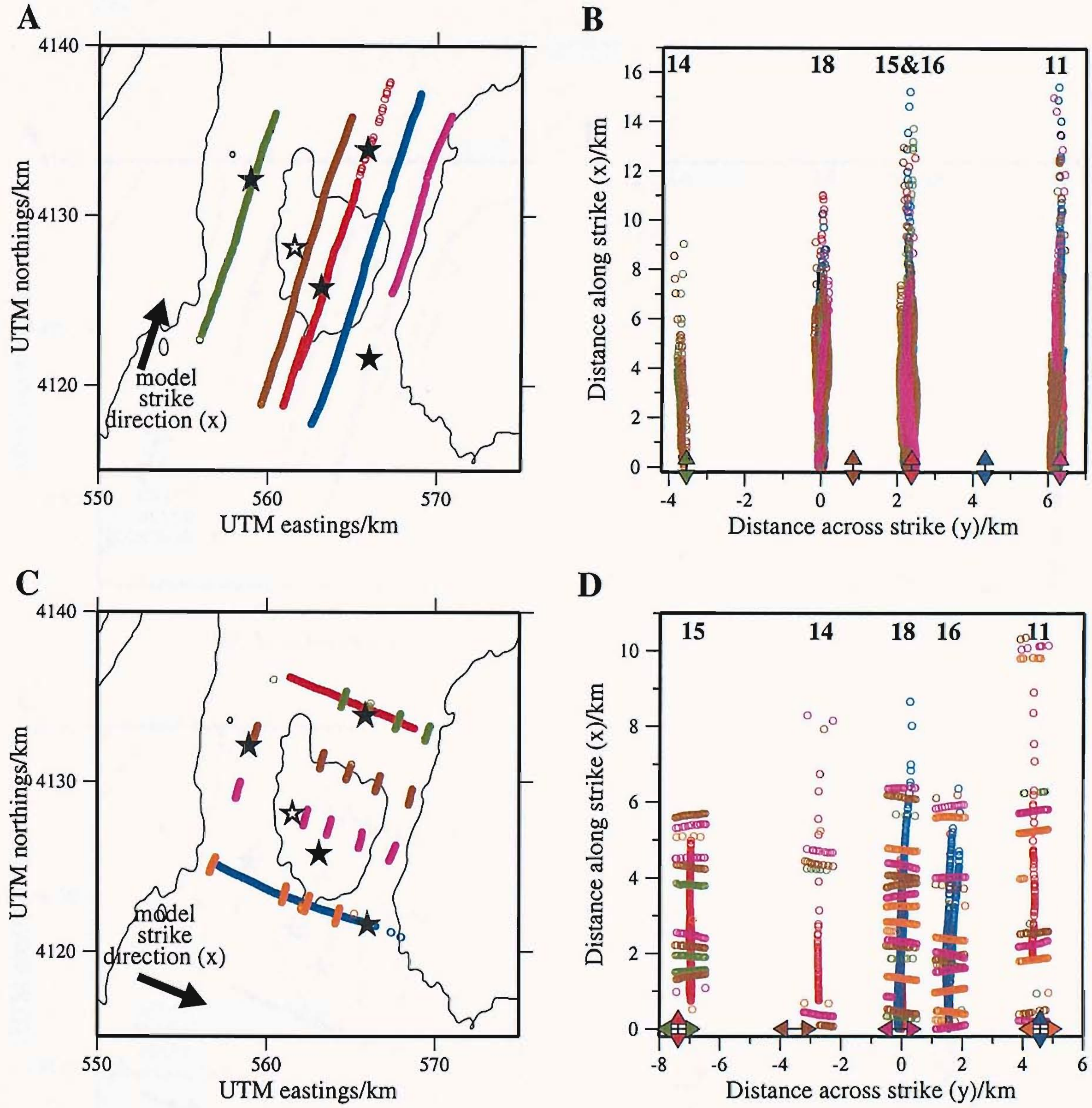

Figure 6.2: 1 Hz data translated into the geometry of the two 2-D models. ***A***: A plan view of the data used in the first 2-D model, with a strike (invariant) direction of 018°, along the ridge axis. Datapoints, plotted at transmitter locations, are coloured according to their source (Red:Line1, Blue:Line2, Green:Line3, Brown:Line4, Purple:Line5). Receiver locations are plotted with stars. LEMUR18, defined as the origin in the model geometry, is plotted with an outlined star. ***B***: A plan view of the same data translated into the model geometry. The five lines are reduced to point sources at $x = 0$ (coloured arrow pairs, reflecting the along-strike dipole orientation), whilst the receivers are elongated into lines. Receiver datapoints are coloured according to which source line was being recorded at the time. LEMUR receiver numbers are shown at the top of the plot. Note that in this model geometry, data from LEMURs 15 and 16 overlap, at the same across-strike location. ***C***: A plan view of the data used in the second 2-D model, with a strike direction of 112°, near-orthogonal to the ridge-axis, and parallel to lines 7 (red datapoints) and 8 (blue datapoints). Transmission lines 1 to 5, which have a dipole orientation across the strike in this geometry, are separated into four source locations (green, brown, purple and orange datapoints). Receivers are plotted as stars, and the origin of the model is again at LEMUR18. ***D***: A plan view of the same data translated into the model geometry.

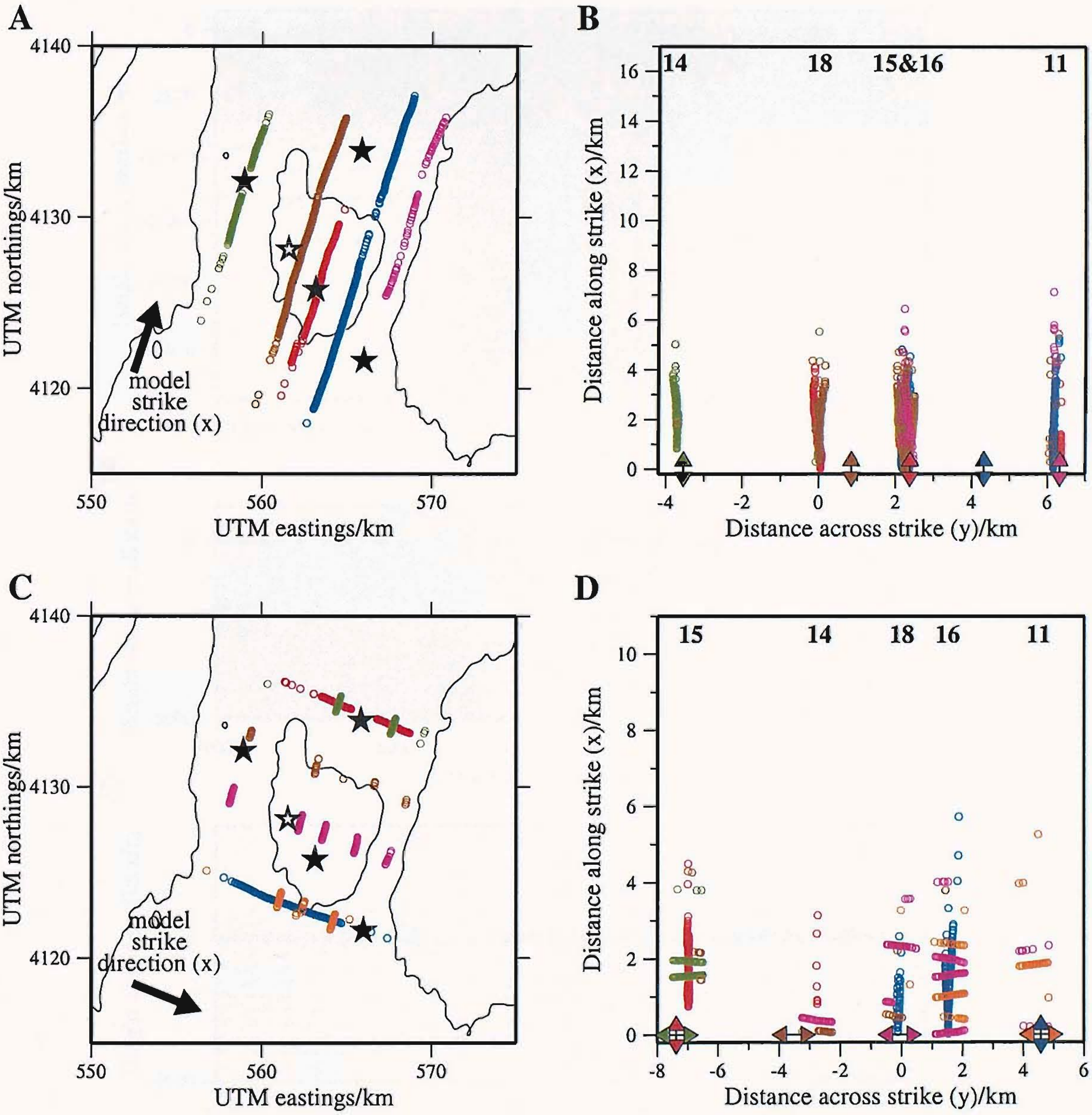

Figure 6.3: 5 Hz data translated into the geometry of the two 2.5-D models. For description, see previous figure caption.

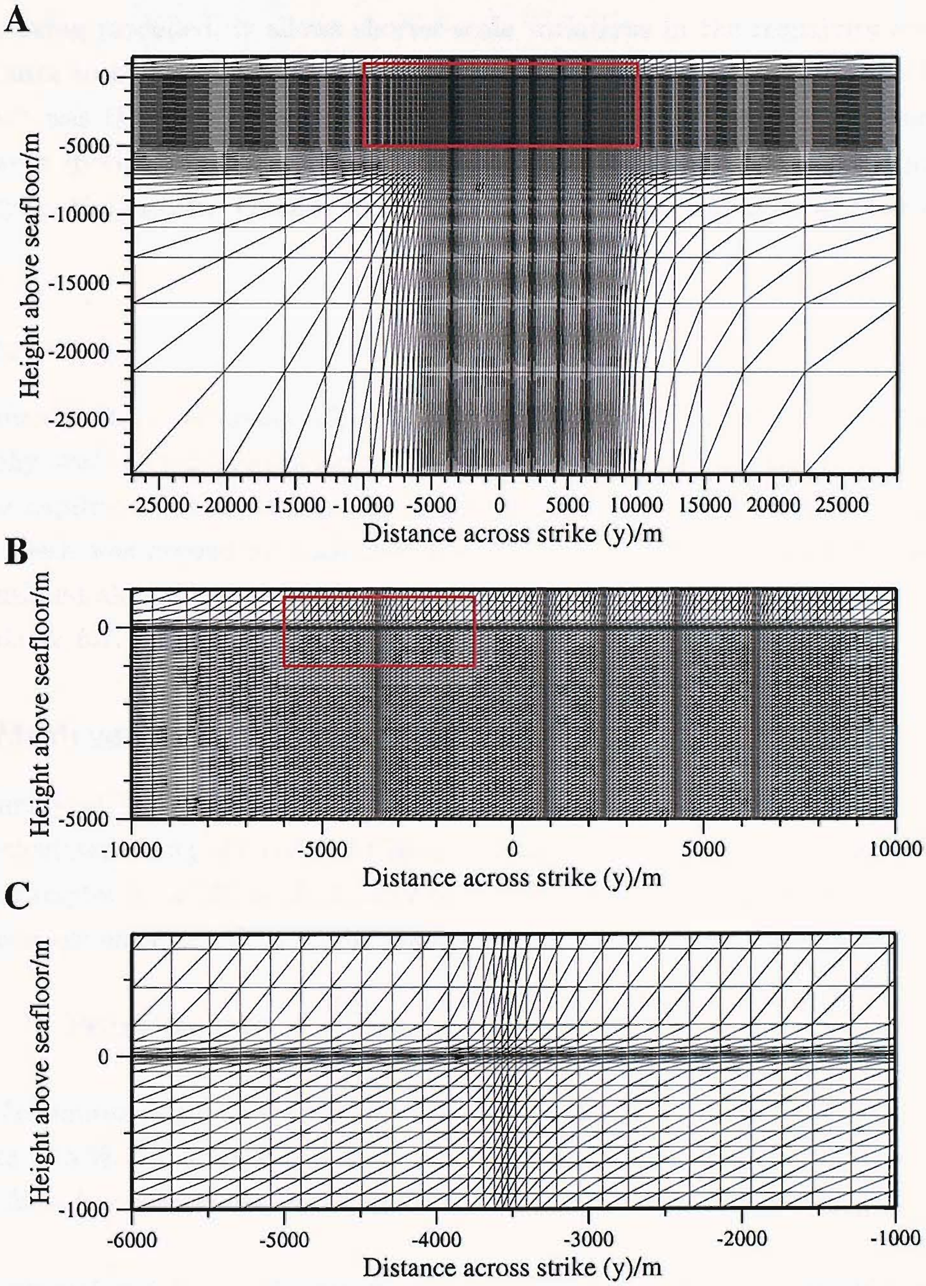

Figure 6.4: The rectilinear mesh used to parameterise the across-axis 2.5-D model. ***A***: the complete mesh, with 10625 nodes. ***B*** and ***C***: successively closer views of a portion of the mesh, outlined by the red box in the previous plot. By ***C***, the fine parameterisation around the seafloor, as well as around source 3 (at -3533 m across-strike) can be seen.

than 2×10^{-5} m^{-1} is required. A maximum wavenumber of 0.0316 m^{-1} should allow accurate modelling to an offset of as little as 130 m. Whilst this is a much shorter offset than any of the data being modelled, it allows shorter-scale variations in the resistivity structure close to the source to be accurately modelled. A wavenumber spectrum between 1×10^{-5} m^{-1} and 0.0316 m^{-1} was therefore chosen. Between 0.0001 m^{-1} and 0.01 m^{-1} ten wavenumbers per decade were specified, as this was the part of the spectrum over which the secondary fields were varying the fastest. Outside this range, a coarser five wavenumbers per decade were used.

Topography

The required 2-D model topography was calculated by averaging the 3-dimensional seafloor topography over the region sampled by the data used in each of the two models (Figure 6.5). The code requirement of a source at zero height, with locally flat topography meant that a different mesh was needed for each source location. These meshes used the same topography, translated along the z-axis as required. Portions of the distorted meshes are shown in Figures 6.6 & 6.7.

6.2.1 Mesh verification

The accuracy of the undistorted meshes were verified externally by comparison with 1-D results calculated using the code of Chave & Cox (1982) for a typical resistivity structure found in Chapter 5: a 700 m thick layer of resistivity 6 Ωm overlying a 100 Ωm halfspace. The percentage error in PE_{max} at the seafloor was calculated such that,

$$\text{Percentage error} = \frac{PE_{max}(\text{finite element}) - PE_{max}(\text{1-D})}{PE_{max}(\text{1-D})} \times 100\%. \qquad (6.15)$$

For a 1 Hz source, errors were obtained of less than 1 % at most data locations, up to a maximum of 3 %. By 5 Hz, errors increased to generally less than 1.5 %, up to a maximum of 3.5 % for a few datapoints. At higher frequencies, the errors increased to an unacceptable level.

The internal stability of the results obtained from the across-axis mesh was verified by comparison with answers from a similar mesh with slightly smaller node spacing, and a total of 12288 nodes. There was no measurable difference between the results from each mesh. Increasing the number of wavenumbers used also had no measurable effect on the results. It was therefore concluded that the undistorted meshes and wavenumber spectra were able to adequately model the fields in the required regions up to a frequency of 5 Hz.

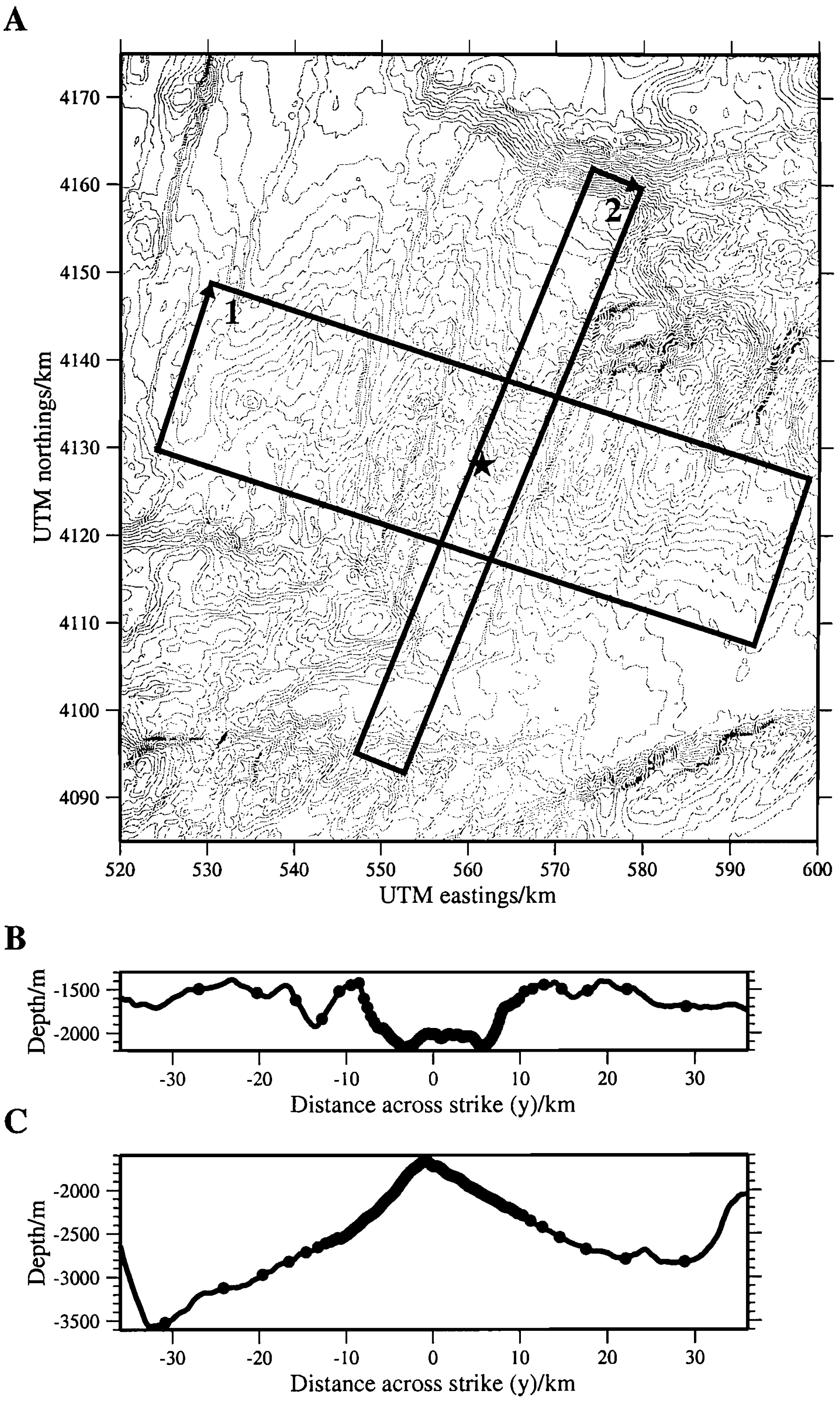

Figure 6.5: Generating the topography for the 2.5-D models. ***A***: for each model, a region of topography is chosen in order to be representative of the topography sampled by the data used. This is the region within each numbered box. The arrows along one side of each box correspond to the models' strike (x) direction. Model origins at the location of LEMUR18 are highlighted by a star. ***B***: The topography for the first, across-axis model, averaged along the invarient direction. Model node positions along this profile are highlighted with circles. ***C***: as ***B***, for the second, along-axis model.

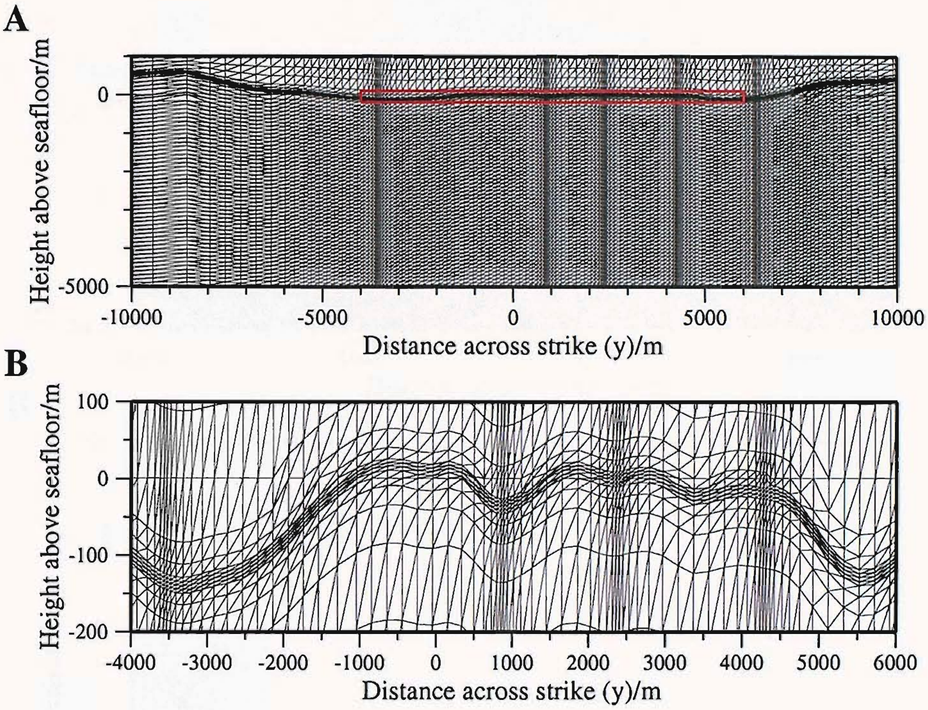

Figure 6.6: Topographic distortion of the across-axis mesh. ***A***: a region of the mesh displayed with no vertical exaggeration. ***B***: The axial seamount, highlighted in ***A*** with a red box, shown with a 10:1 vertical exaggeration. This mesh is for source 1, at 2381 m across-strike. The line of nodes required at z=0 can clearly be seen.

Topographic distortion

There were two clear problems with the topographically-distorted results from the outset. Firstly, the seafloor electric field amplitude appeared to oscillate along the invariant direction. This was found to be due to the resolution of the inverse Fourier transform used at the end of the modelling process. By increasing the number of points at which the transform was calculated from 30 to 300, all visible oscillations were removed. Secondly, some sources oriented along-strike generated a seafloor electric field that became unstable in a line directly along strike from the source. As explained earlier, this is a known consequence of calculating the total field in the wavenumber domain: the source singularity present in the primary fields is propagated along-strike when the inverse Fourier transform is carried out. Examination of the seafloor electric field components showed that this instability was only present in E_y (calculated from E_x and B_x), and not E_x. As the E_y component should decrease to zero along-strike from a source oriented along-strike, this was set to zero within the unstable region.

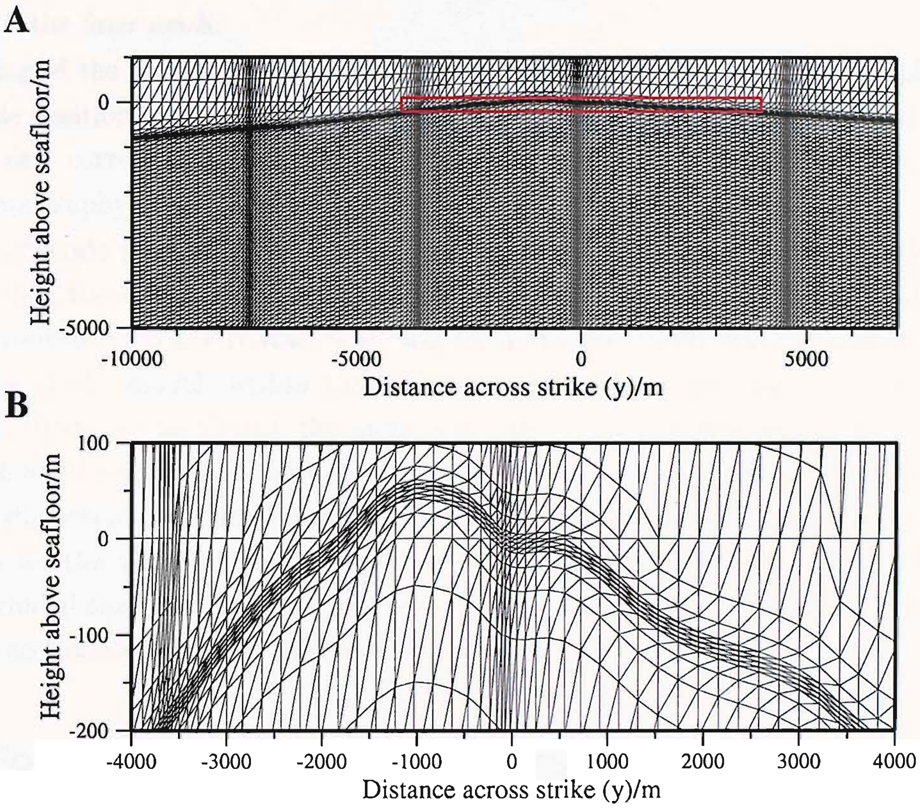

Figure 6.7: Topographic distortion of the along-axis mesh. This mesh is for one of the across-strike sources, at -73 m across-strike. The steep topography on the northern flank of the seamount can be clearly seen in plot ***B***. For further details, see the previous figure caption.

The maximum width of the E_y instability was found to be about 100 m. To estimate the extra error that forcing this to zero would introduce into the calculated seafloor PE_{max} amplitudes, the seafloor fields calculated to verify the undistorted mesh (previous section) were studied. At a range of 1 km along-strike, and 100 m across-strike from the point dipole, setting the E_y field to zero makes a difference of only 0.2 % to the amplitude of PE_{max}. At all ranges and frequencies being modelled, this difference is similarly negligible.

With the two clear errors in the topographic meshes corrected, a method for internal mesh verification was devised. Alternate rows and columns of the mesh being tested were removed, producing a mesh with a quarter of the nodes of the original. In the case of the across-axis model, comparison of this coarse mesh with 1-D results showed that it was still able to model the 1 Hz fields at the seafloor to an accuracy of, at worse, 15 %. However, as this mesh is progressively distorted and the vertical element size increased, one would expect that the results obtained would diverge from the 'true' answer at a lower level of distortion than with the finer mesh.

Scaling of the topography was achieved by multiplying the 'true' topographic height at each node position by a scale factor from 0 to 20: a scale factor of zero creates a flat seafloor; a factor of 1 corresponds to the true topography; higher scale factors generate increasingly severe topography.

At each node position of the coarse mesh, and for each position in the invariant direction calculated in the inverse Fourier transform, the percentage difference between the amplitude of E_x obtained from the coarse mesh and from the fine mesh was calculated. Away from the edges of the model, within the region of interest (in this case, a region bound by -10 km to 10 km across strike), the mean absolute percentage difference was then calculated (Figure 6.8). The difference between the results obtained from each mesh remains constant up to a distortion of at least twice the required level of topography. Similar results were obtained for the along strike mesh, and at a transmission frequency of 5 Hz. Therefore, it was concluded that the distortion of the mesh with the required topography still allowed the mesh to accurately represent the fields being calculated.

6.3 Forward modelling: the topographic effect

In order the investigate the effect of topography on the recorded fields, the cases of a 1 Hz source and a 5 Hz source were studied. Frequencies lower than 1 Hz were not considered, as very little data, recorded by only two instruments, were available from the 0.25 Hz tow.

The topographic percentage shift in PE_{max} was calculated for the two models at the data locations described in Section 6.2, for the 'average' 1-D crustal resistivity (a 700 m thick layer of 6 Ωm overlying a 100 Ωm halfspace). Percentage shift was defined as

$$\text{Percentage shift} = \frac{PE_{max}(\text{topography}) - PE_{max}(\text{flat seafloor})}{PE_{max}(\text{flat seafloor})} \times 100\%, \qquad (6.16)$$

where the signal amplitudes for a flat seafloor were calculated with the undistorted mesh. The results for all instruments from the two topographic models are shown in Figures 6.9 to 6.12 on the following pages.

The most striking feature of these results is that, even with the severe topography over the Lucky Strike seamount, the topography has a relatively small effect on the recorded electric field. For all receivers, most tows at both frequencies show a percentage shift of less than 15 %; of these, the majority of datapoints have a shift of 5 % or less. Areas that experience a greater topographic effect are localised, and can be divided into three groups (these areas are highlighted on the figures):

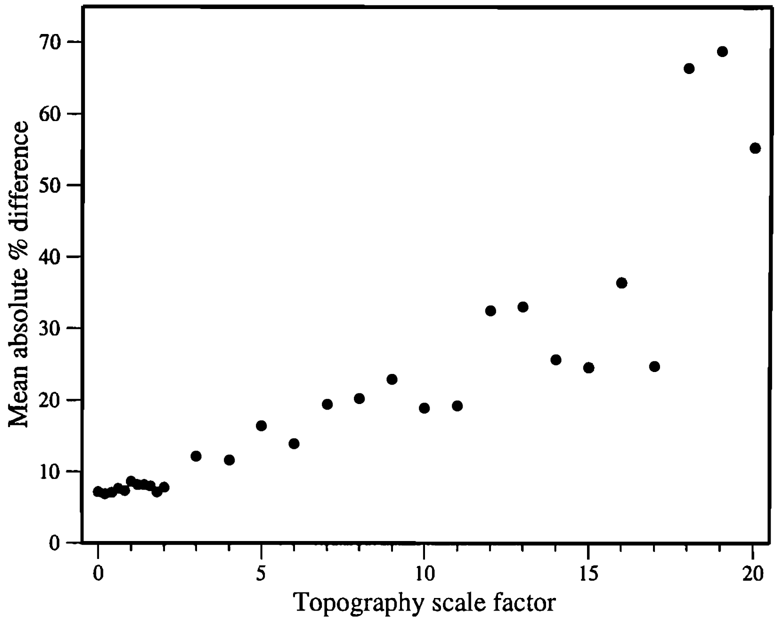

Figure 6.8: Topographic mesh verification. The mean absolute percentage difference in the amplitude of E_x calculated at the seafloor between a coarse and a fine mesh is shown. With a flat seafloor (topography scale factor of zero), this difference is about 7 %. The difference stays constant through a scale factor of 1 (the true topography), up to a scale factor of 2. At scale factors between ~2 and ~17, the results from the two meshes diverge. This is interpreted as being due to the failure of the coarse mesh to accurately represent the fields with topography this severe. Above a scale factor of 17, the percentage difference doubles. This may be the distortion at which the fine mesh also fails.

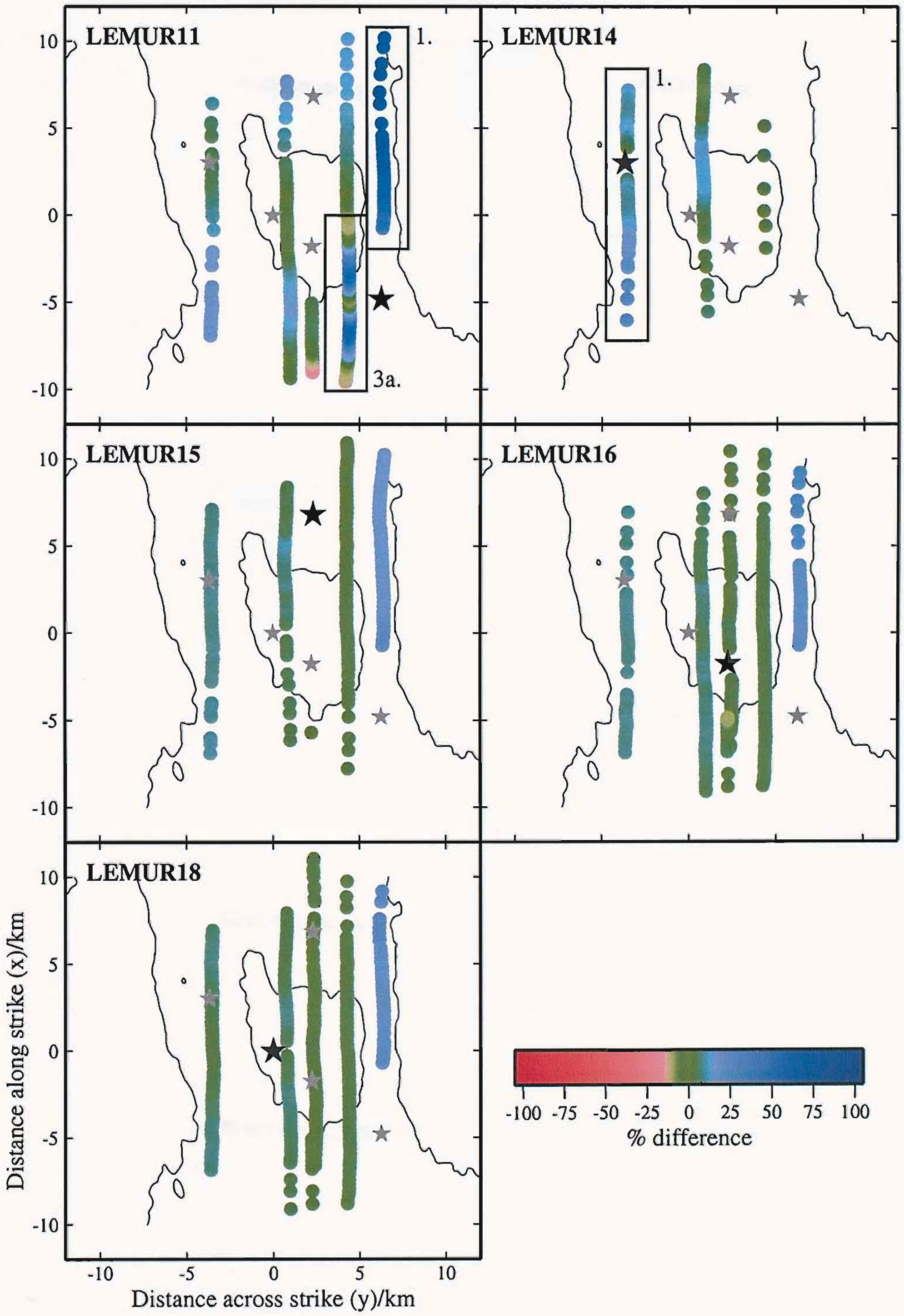

Figure 6.9: The topographic effect of the across-strike model at 1 Hz. Percentage difference calculated in PE_{max} between the topographically-distorted mesh and the undistorted mesh is plotted at source positions, and is defined such that an increase in field strength in the presence of topography is positive. Data have been transformed from the modelled fixed-source geometry into the more recognisable fixed-receiver geometry, keeping the origin and orientation used in the model. Over most of the region, the topography produces less than a 15 % difference in field strength. Portions of lines outlined with numbered boxes are discussed further in the text.

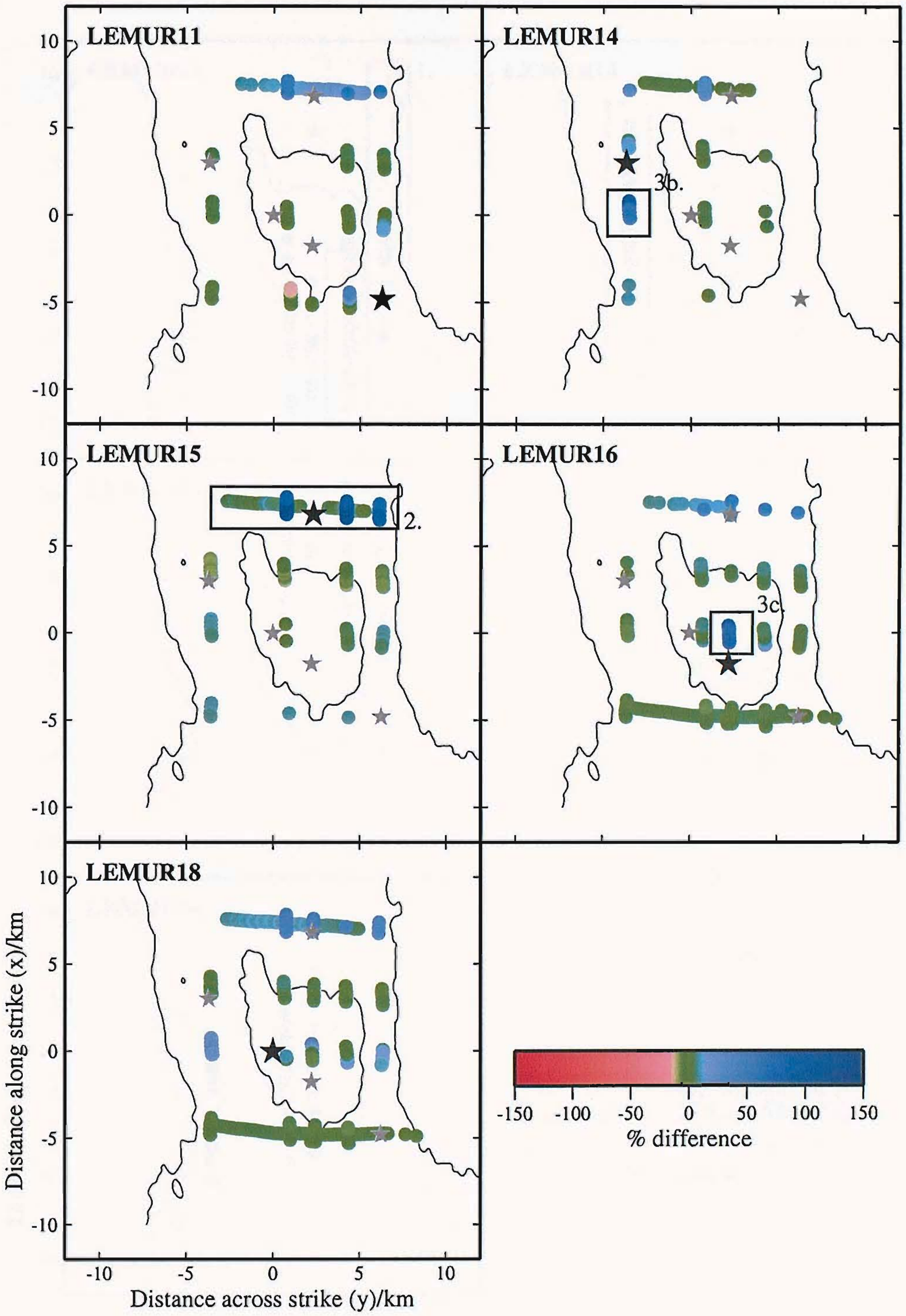

Figure 6.10: The topographic effect of the along-strike model at 1 Hz. In transforming from the fixed-source geometry, the map coordinates have also been rotated into the strike orientation of the across-axis model. This facilitates easier comparison with the previous figure. See the caption of Figure 6.9 for more details.

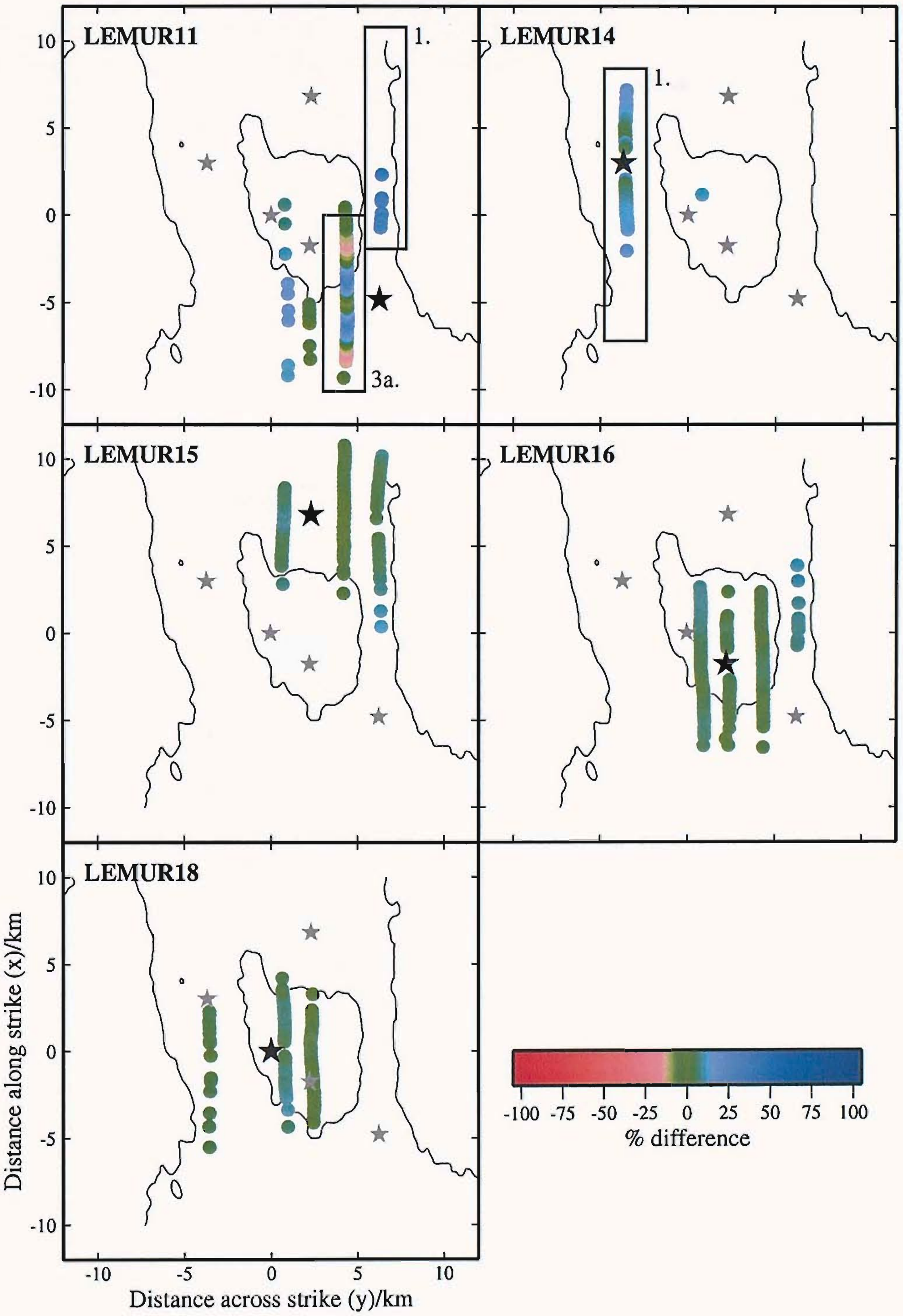

Figure 6.11: The topographic effect of the across-strike model at 5 Hz. See the caption of Figure 6.9 for more details.

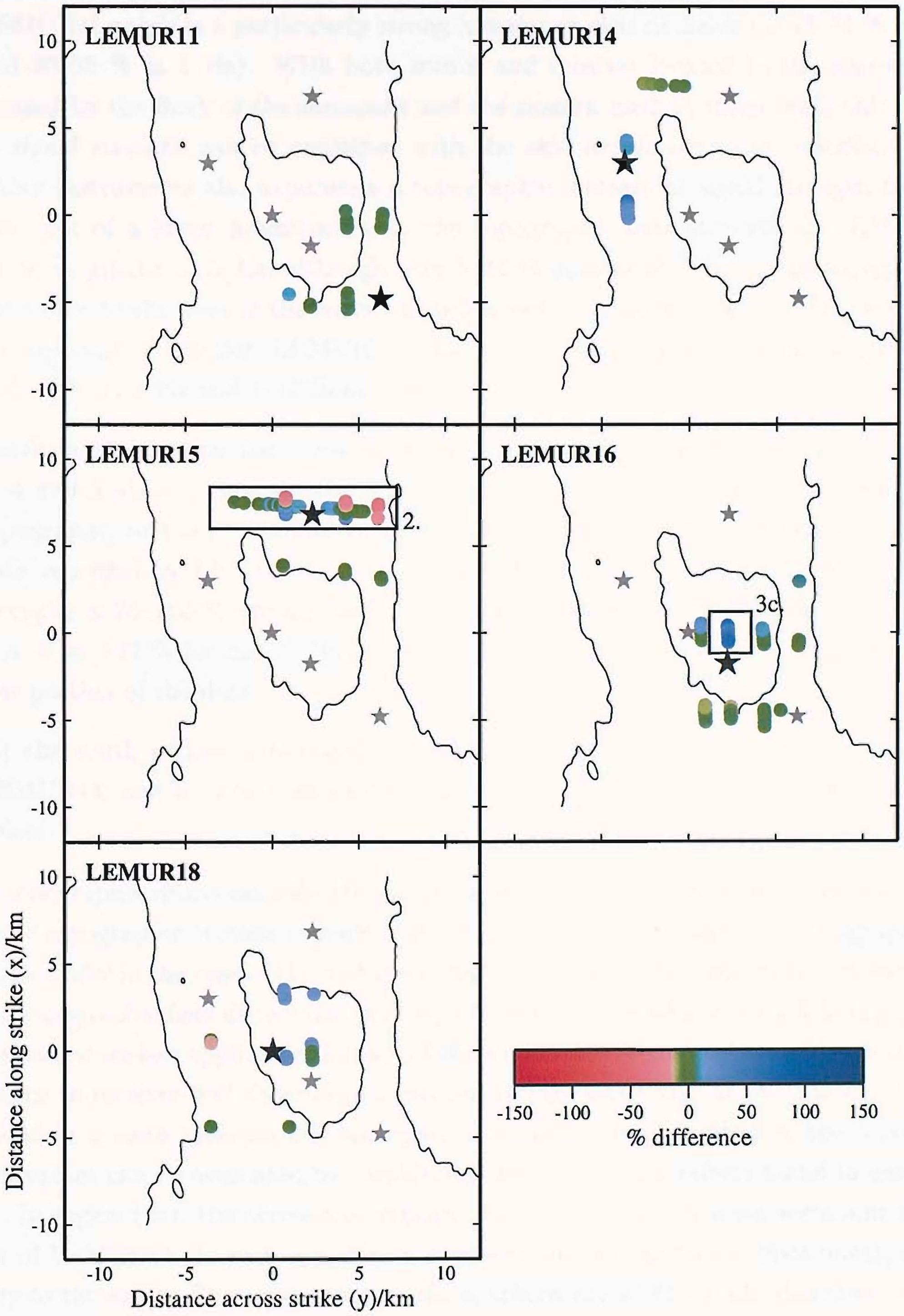

Figure 6.12: The topographic effect of the along-strike model at 5 Hz. See the caption of Figure 6.9 for more details.

1. Lines 3 and 5, along the western and eastern seamount flanks. Line 5, recorded by LEMUR11 exhibits a particularly strong increase in electric fields (of 47–74 % at 1 Hz, and 30–35 % at 5 Hz). With both source and receiver located in the narrow valley created by the flank of the seamount and the eastern median valley wall, this increase in signal strength can be explained with the skin depth argument described earlier. Other instruments also experience a topographic increase in signal strength from this tow, but of a lesser magnitude (e.g. the topographic field strength at LEMUR15 is 23–30 % greater at 1 Hz, although only 5–12 % greater at 5 Hz). The topography in the valley to the west of the seamount is less severe, and the effect on field strength is correspondingly smaller: LEMUR14, also in this valley, experiences the greatest shifts, of 9–25 % at 1 Hz and 1–17 % at 5 Hz.

2. North-south tows on the northern seamount flank. The northern ends of Lines 1, 2, 4 and 5 show a consistently stronger signal strength at 1 Hz than either the flat topography, or the co-incident east-west line 7. This effect is particularly notable in data recorded by LEMUR15, also on the seamount's northern flank: at 1 Hz, field strength is 75–160 % greater with topography for these tows, compared to a shift of just -2 to +12 % for line 7. However, at 5 Hz, there is no strong topographic effect in this portion of the data.

3. (a) the south of line 2 recorded by LEMUR11; (b) line 3 directly to the south of LEMUR14; and (c) line 1 directly to the north of LEMUR16. This group is discussed below.

The topographic effects described in groups (1) and (2) occur in regions where one or other of the 2-D topographic models provide a good approximation to the true topography (the across-axis model in the case of (1), and the along-axis model in the case of (2)). However, the modelled topographic field distortions in group (3) occur in regions where the 2-D topographic approximations are less applicable. In each of these cases, electromagnetic energy propagating from source to receiver will experience a greater average resistivity in the 2-D models than they would in a more accurate 3-D topographic model. The true effect of the topography on these regions can be estimated by considering the topographic effects found in groups (1) and (2). In region (3a), the across-axis topographic model places a steep seamount flank to the west of LEMUR11. In reality, this area is at a similar height to the instrument, dipping gradually to the south. The topography at the southern end of line 2 will therefore probably have little effect on the fields. However, the south-west flank of the seamount is directly to the north-east of the instrument. This portion of line 2 (from an along-strike distance of -0.5 to 0 km on Figure 6.9) would be expected to be affected by the topography. In region (3b), the across-axis model provides a good approximation to the topography down the western flank of the seamount. In contrast, the along-axis model, in which this topographic effect is found, does not provide a good approximation to the true seafloor. This topographic effect should therefore be discarded. Region (3c) is at the very summit of the seamount, where neither model can accurately describe the true topography. Topography is likely to have a strong effect on this portion of line 1 to the north of LEMUR16, although a 3-D topography model would be required to accurately quantify this effect.

6.3.1 A topographic explanation for the 1-D results?

With the topographic effect investigated in both of the 2.5-D models, we are now in a position to investigate whether topography could be the cause of the anomalous electric field amplitudes found during 1-D modelling, highlighted in item (2) of the introduction to this chapter.

(a) Data recorded to the east of LEMUR15 show significant attenuation of $E_\perp$ relative to $E_\parallel$, particularly at higher frequencies (Figure 5.9): at 9 Hz, $E_\perp$ is nearly an order of magnitude weaker than coincident $E_\parallel$ values. In contrast, topographic modelling has shown that the steep slope on the north of the seamount has a strong positive effect on $E_\perp$ recorded by LEMUR15 at 1 Hz. At higher frequencies such as 5 Hz, this effect becomes less pronounced. Therefore, no topographic mechanism has been found which can fit the data. Instead, these results suggest that the topographic effect may be acting to mask splitting that might otherwise be visible at lower frequencies.

(b) Data recorded by LEMURs 11 and 18 on the northern seamount flank show attenuation of $E_\parallel$ relative to $E_\perp$ (see Figures 5.8 & 5.10). However, the addition of topography has increased $E_\parallel$ relative to $E_\perp$ over this region. This is again in direct contrast to the data, and provides convincing evidence that the data splitting is not caused by seamount topography.

(c) The best-fit 1-D model obtained from a subset of LEMUR16 data, whilst providing an acceptable fit at 1 Hz, underestimated the 5 Hz electric field strength by up to half an order of magnitude (Figure 5.12). Whilst topography has been found to have a markedly different effect on fields depending on the frequency of transmission, no topographic modelling for any instrument has identified a shift of field strength of this magnitude, and we must again conclude that this effect is due to crustal resistivity variations, and not seamount topography.

6.3.2 Minimising the topographic effect

Neither the 2.5-D inversion code nor the 3-D forward modelling code used in Chapter 7 are currently capable of easily modelling varying topography. If these codes are to be used in the modelling and interpretation of the Lucky Strike dataset, it is therefore essential that the effect topography has on the dataset is removed, or minimised. One possible way would be to normalise the dataset by the topographic effect quantified above. However, ignoring the errors this would introduce due to the 2-D topographic approximation, this would only remove the topographic effect of the modelled crustal resistivity (in this case, an average layer over halfspace); different crustal resistivities would generate a topogoraphic effect with a different amplitude.

On the other hand, the overall regions affected by the topography vary little with different crustal resistivity models because the predominant factor affecting their position is the contrast in resistivity between the seawater and crust. As topographically-affected regions in the Lucky Strike dataset are localised, and limited to roughly 20 % of the total data, it is possible to remove these without adversely affecting the data coverage over the seamount.

A topographically-minimised subset of the 1 Hz and 5 Hz data were therefore created by removing all data that had been found to exhibit a 15 % or greater shift in amplitudes due to topography. As this excludes all 1 Hz data along line 5, a second subset was created with line 5 included for all instruments except LEMUR11. The remaining data along this line have an estimated topographic error of up to 30 %.

6.4 Inversion

The Occam inversion algorithm of Constable et al. (1987), implemented in 2-dimensions for magnetotelluric data by de Groot-Hedlin & Constable (1990), was combined with the 2.5-D CSEM forward code of Unsworth (1991) by MacGregor (1999). A brief summary of this code is given below, the process of data binning applied to the data is discussed, and the final 2-D model obtained is presented.

6.4.1 Code outline

In order to accurately model the electromagnetic field with a finite element mesh, a large number of elements are needed, particularly around the source. If this mesh is used as the regularisation mesh for the inversion, the memory and time requirements soon become too great for the available computing power. Instead, a regularisation mesh is defined which consists of a subset of the finite element mesh. The resistivity within each region of this regularisation mesh is kept uniform. In general, the finest regularisation mesh is used that does not require a prohibitive amount of computing time and memory.

As in the 1-D implementation (Section 5.2), the algorithm attempts to find the smoothest model that fits the data to a pre-defined misfit level. Model roughness R is defined in terms of the first derivative of 2-dimensional model parameters with respect to position,

$$R = \left\| \underline{\underline{\partial}}_y \boldsymbol{m} \right\|^2 + \left\| \underline{\underline{\partial}}_z \boldsymbol{m} \right\|^2 , \tag{6.17}$$

where $\boldsymbol{m}$ is the vector of model parameters, $\underline{\underline{\partial}}_y$ is a regularisation matrix which differences the model parameters of laterally adjacent regions in the regularisation mesh, and $\underline{\underline{\partial}}_z$ is a matrix which differences the model parameters of vertically adjacent regions. Elements in the regularisation mesh should be kept as similar in size as possible over the region of highest sensitivity to ensure that R is also a good measure of spatial roughness.

Finding the best final misfit using an automatic method of minimising residual bias such as that described in Section 5.2.1 would take too long with the more computing-intensive 2-D inversion. Instead, the suitability of a target RMS misfit must be decided upon by studying the residuals and increasing or decreasing the required RMS as necessary.

6.4.2 Data binning

Data for a 2.5-D inversion need to be arranged into along-strike bins in order to meet the geometric requirements of the code, as well as the memory and processing capabilities of the computer.

Data along the five transmission tows to be modelled were taken from the set with the highest minimum signal to noise ratio of 10. Portions of data from regions with a high topographic effect were removed, as were data with an SNR of less than 10. LEMUR15 data was not used, as this would overlap with LEMUR16 data in a geometry with a strike direction along the ridge axis.

Amplitudes were converted into normalised current density for binning. Transformed into the "fixed source, moving receiver" geometry, the datapoints were moved across-strike to bring them into line with the average across-strike positions for each receiver. This inevitably altered the range of each datapoint by up to several tens of metres. In some instances at short ranges, this corresponded to a significant percentage difference in the source-receiver range. However, the error in signal amplitude associated with this was significantly reduced by working with normalised current density, in which much of the range-dependence of the fields is removed.

Data from each receiver were then grouped into along-strike bins, each 250 m in length.

This bin size was found to provide the best tradeoff between number of datapoints and size of inversion. The average amplitude of the n datapoints within each bin for each transmission tow was then calculated using a weighted average $\overline{S}_w$, based on the percentage error σ_{pe} on each datapoint

$$\overline{S}_w = \frac{\sum_{i=1}^{n} \frac{S_i}{\sigma_{s_i}}}{\sum_{i=1}^{n} \frac{1}{\sigma_{s_i}}} \quad \text{where} \quad \sigma_{s_i} = \frac{\sigma_{pe_i}}{100} \times S_i. \tag{6.18}$$

The average data error $\overline{\sigma}_s$ was taken as the RMS of the individual data errors,

$$\overline{\sigma}_s = \sqrt{\frac{\sum_{i=1}^{n} \sigma_{s_i}{}^2}{n}}. \tag{6.19}$$

The average along-strike location within each bin was taken as the arithmetic mean of the along-strike data locations.

Finally, binned data were converted from dimensionless amplitudes to normalised electric field using the source-receiver range at the binned location (Figures 6.13 & 6.14).

6.4.3 Results

Combined inversion of 1 Hz and 5 Hz data used 5.1 Gb of memory, taking about 1 week, and 35 iterations to run to convergence on a single processor of an IRIX64 machine, depending on the target RMS misfit chosen. Three converged models at target misfits of 4.0, 3.5 and 3.1 can be seen in Figure 6.15. These will be discussed in the following sections.

Inversion stability

It was found that within about 10 iterations, the models reached a form similar to the final converged model. Subsequent iterations slowly reduced the model roughness and iteration stepsize. However, in some instances, particularly at low target misfits, the smoothness constraints were unable to remove rough features in the model that did not appear to be required by the data. For example, initially a best-fit layer over halfspace model was used as the starting model for the inversion. This was replaced with a double halfspace when instabilities at the depth of the layer-halfspace interface persisted in later iterations and produced problems with model convergence. All models shown here started as a double halfspace of seawater resistivity and 6 Ωm crust.

Other less severe but persistent rough features developed as inversion progressed. An example can be seen in Figure 6.16, which formed during inversion to a target RMS of 3.5.

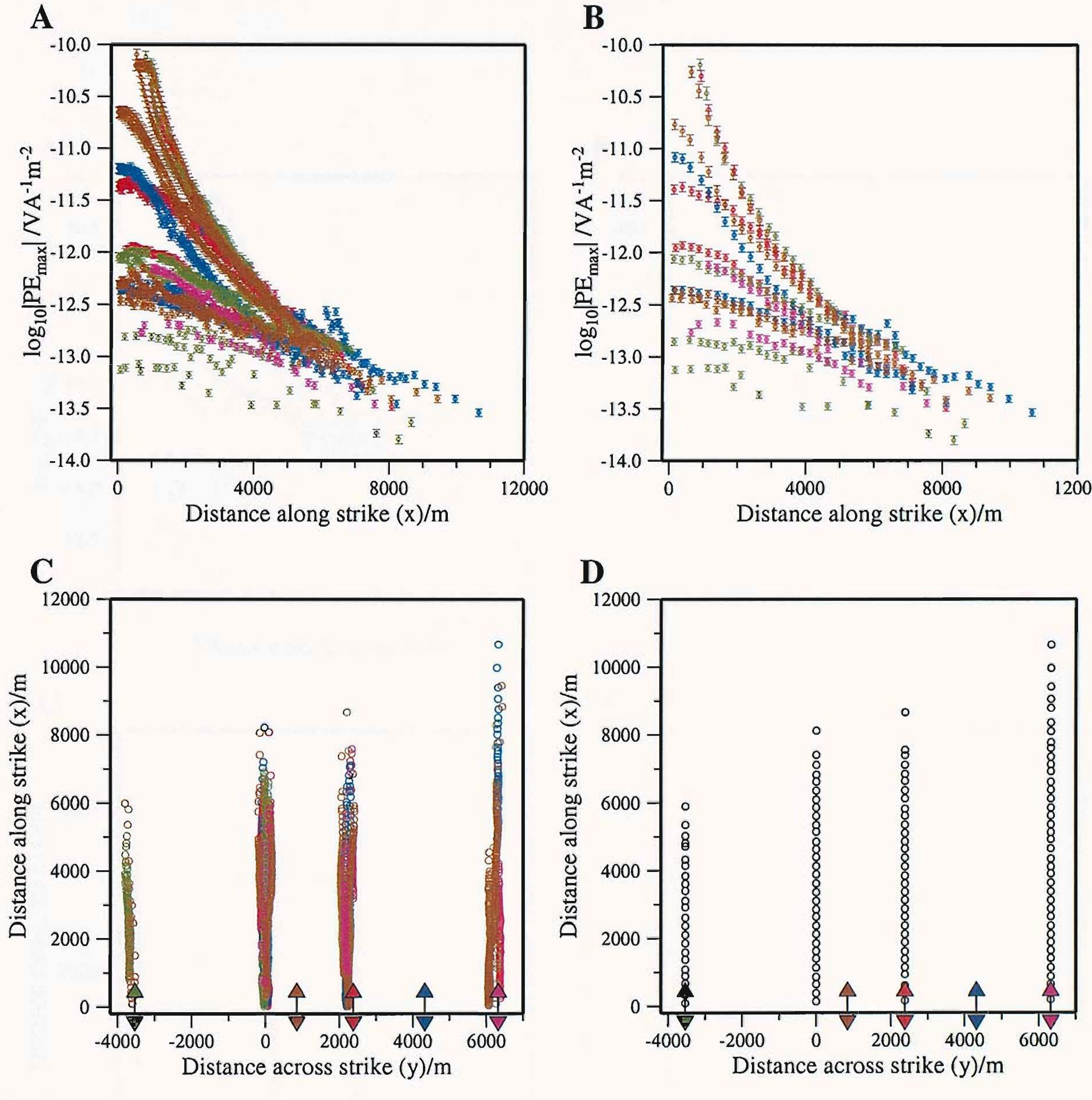

Figure 6.13: 2.5-D 1 Hz data binning. Plots *A* & *C* show the data selected from the five transmission tows to be modelled. Data are taken from the highest signal to noise ratio dataset. Points with an SNR lower than 10 have been removed, as have data from areas with a strong topographic effect. Points are coloured according to their transmission tow (line1:black, line2:red, line3:green, line4:blue, line5:purple). Source dipoles are plotted as coloured arrow pairs on the plan view, *C*, whilst the four tracks on this plot correspond to the four LEMURs (from left to right) 14, 18, 16 and 11. Data from LEMUR15 has not been used, as this overlaps LEMUR16 data in this geometry. Plots *B* & *D* show the data after they have been arranged and averaged into 250 m bins. As data from different transmission tows overlap in the binned plan view, all datapoints are plotted in black.

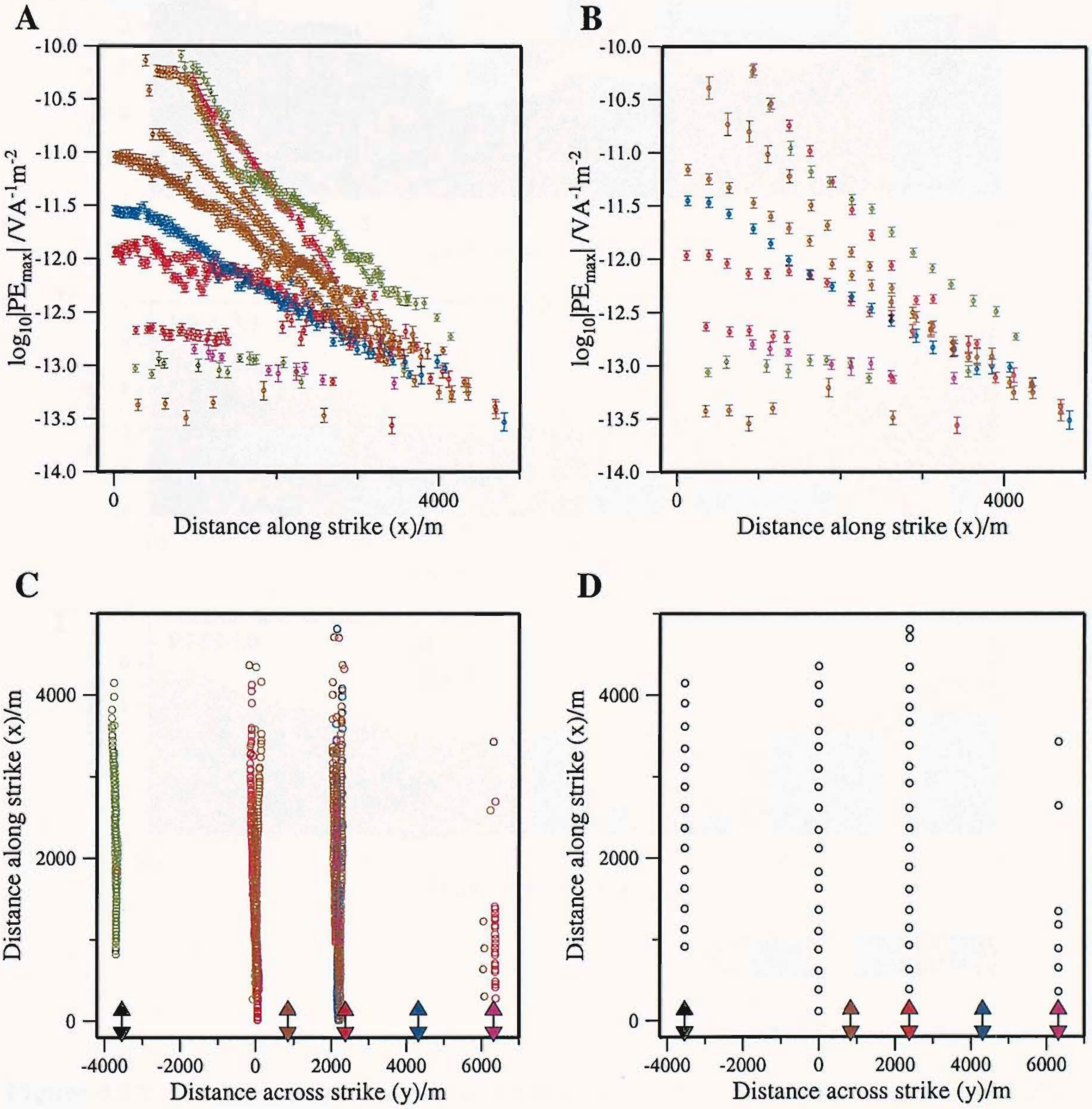

Figure 6.14: 2.5-D 5 Hz data binning. See previous figure caption for description.

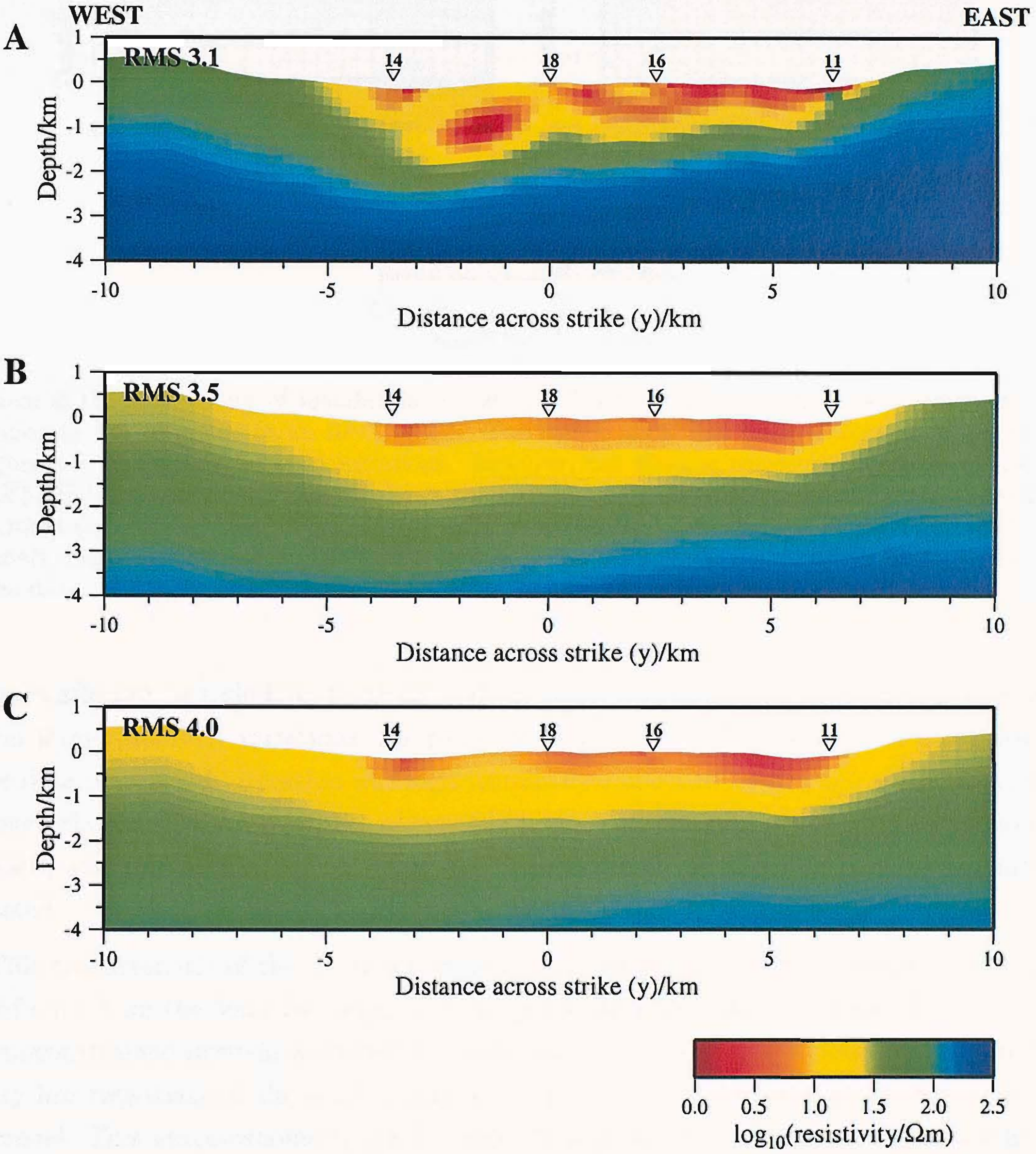

Figure 6.15: Three converged models from 2.5-D inversion of the data, fit to progressively higher RMS misfits. At RMS misfits around 3.1 (Plot ***A***), the model appears overfit, and resistivity structures are highly misfit-dependent. At RMS misfits of about 3.5 and higher (Plots ***B*** & ***C***), a smoother, less misfit-dependent model is produced. LEMUR instrument locations, mapped into the model geometry are also shown on the models. See text for further discussion.

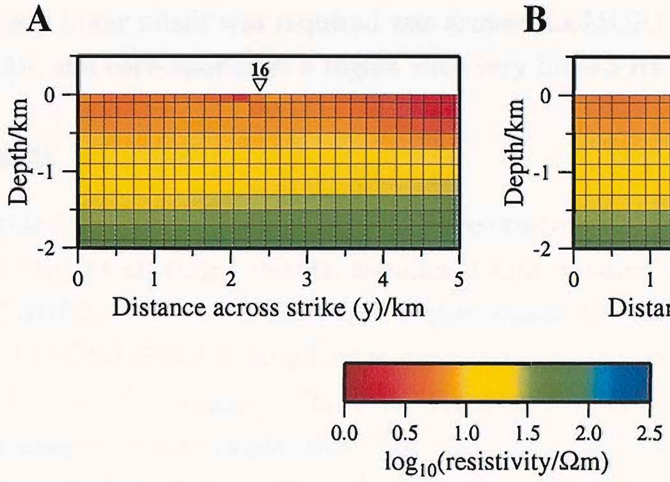

Figure 6.16: Smoothing of instabilities in the 2.5-D inversion. Plot ***A*** shows a portion of an iteration in the inversion to an RMS of 3.5. The target misfit has been reached, and the model roughness is decreasing between iterations. However, the shallow resistivity anomaly to the left of LEMUR16 is persistent. Plot ***B*** shows the same part of the inversion mesh after it has been smoothed (see text). This model fits the data to a slightly lower RMS of 3.494. The resistivity anomaly does not reappear in subsequent iterations, and is therefore unlikely to be a requirement of the data.

The area affected, at a shallow depth around the summit of the seamount, may be expected to exhibit large resistivity variations. So, to investigate whether this feature was a requirement of the data, the 'rough' iteration was logarithmically smoothed by averaging a 3×3 square of inversion elements, centred on each element in turn. This actually produced a slight decrease in misfit, and the feature did not reappear in subsequent iterations once the inversion was restarted.

This characteristic of the 2.5-D inversion code has been encountered before, during analysis of data from the Valu Fa Ridge (MacGregor et al. (2001) & pers. comm.). They found that unconstrained inversions tended to remain unstable, producing models with a thin layer of very low resistivity at the seafloor, and correspondingly higher resistivity over the rest of the model. This was overcome by prejudicing the top 800 m of their model to converge to a pseudo-2-D model derived from several 1-D inversions of high frequency data. It is possible that the problem with the Valu Fa data was more severe than found here because they were jointly inverting only 0.25 Hz and 1 Hz data in their 2.5-D model: analysis of 1-D layer over halfspace misfit functions produced from the Lucky Strike data (Section 5.1) found that these frequencies contained a significant tradeoff between layer thickness and resistivity. By including the 5 Hz data in the 2.5-D modelling, this tradeoff will have been reduced here. Interestingly, one region of the model that was prone to developing a highly conductive upper layer when a lower misfit was required was around LEMUR11. This can be seen in Plot A of Figure 6.15, and corresponds to a region with very little 5 Hz data to constrain the resistivity.

Data misfits

The weighted residuals obtained from the three converged models can be seen in Figure 6.17. It is clear that at all target misfits, significant bias remains within the data. For example at 1 Hz, LEMUR11 data has consistently higher amplitudes than the model; much of the data recorded by LEMUR16 has amplitudes lower than the model. There are also clear differences between the two frequencies. These are greatest in data that could not be adequately fit with 1-D models. For example, the 5 Hz data recorded by LEMUR16 generally have higher weighted residuals than the 1 Hz data.

Whilst decreasing the target RMS to 3.1 does improve the fit to some parts of the data, such considerable bias remains that it is not possible to justify the increase in structure that this decrease in misfit requires (Figure 6.15): features in this model, such as the low resistivity area between LEMURs 14 and 18 at a depth of 1 km, are highly misfit-dependent. However, increasing the RMS above 3.5 makes little difference to the salient features of the model.

An RMS of 3.5 is therefore considered to provide the best fit to the inverted data. Its features, as well as the residual bias that remains, are discussed further in Section 6.4.4.

Model sensitivity

In order to quantify the sensitivity of different parts of their final model to changes in resistivity, MacGregor et al. (2001) carried out a linearised sensitivity analysis around the model, calculating the derivative of the response with respect to small changes in the model parameters. The same technique has been applied here to the best-fit (RMS 3.5) model shown previously. Figure 6.18 shows the modulus of the sensitivity, S_j, in the final model, defined as

$$S_j = \frac{1}{A_j} \sum |J_{ij}| \tag{6.20}$$

and

$$J_{ij} = \frac{\partial d_i}{\partial m_j}, \tag{6.21}$$

where J_{ij} is the sensitivity of the ith datum, d_i, to small changes in the jth model parameter, m_j. In this case m is $\log_{10}$(conductivity), and the sensitivity is normalised by the area of each region A_j (MacGregor et al. 2001).

It can be seen that, whilst data are most sensitive to the regions directly beneath the sources and receivers (to a depth of ~1 km), there are no pronounced gaps in sensitivity over

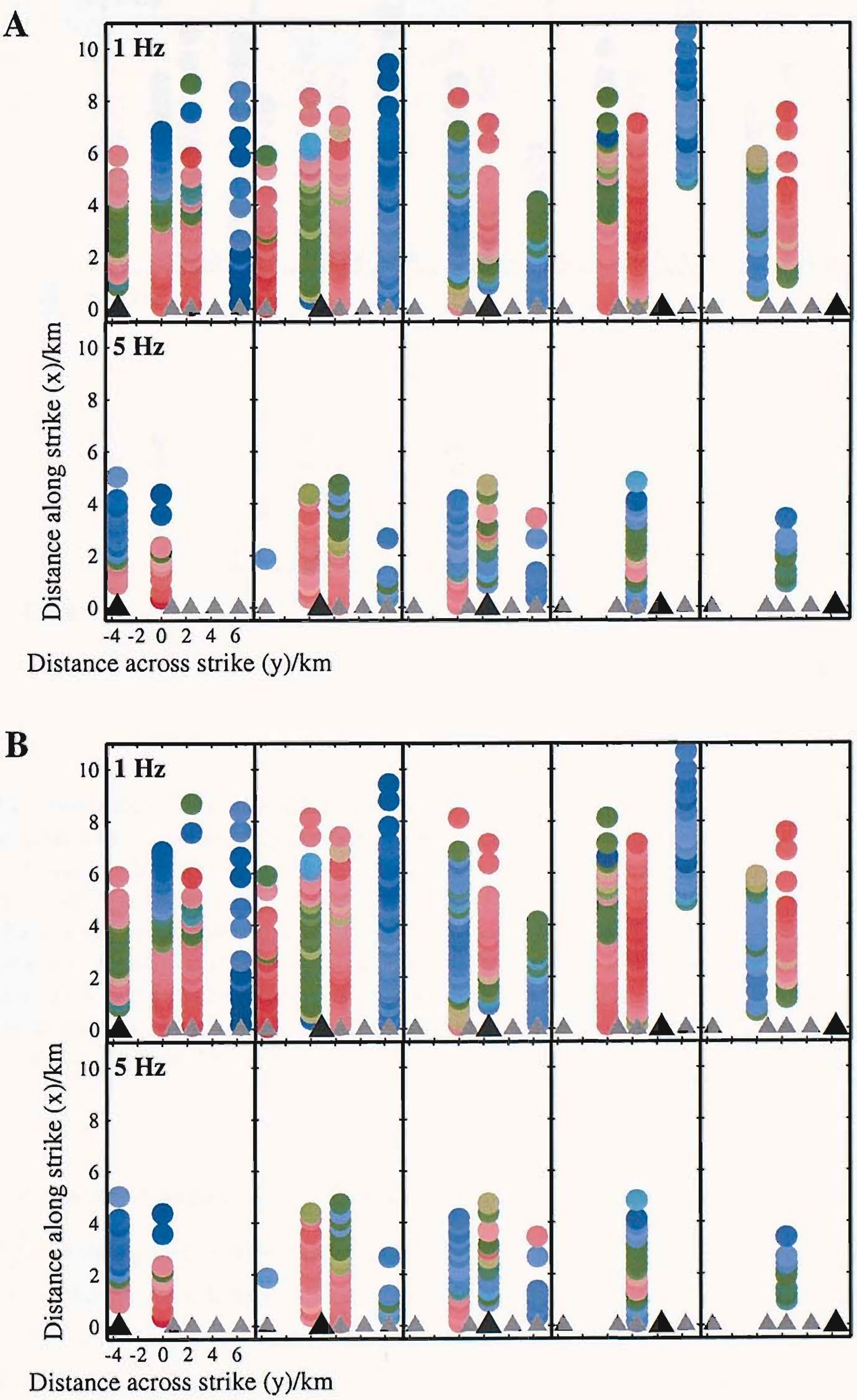

Figure 6.17: (continued on next page)

C

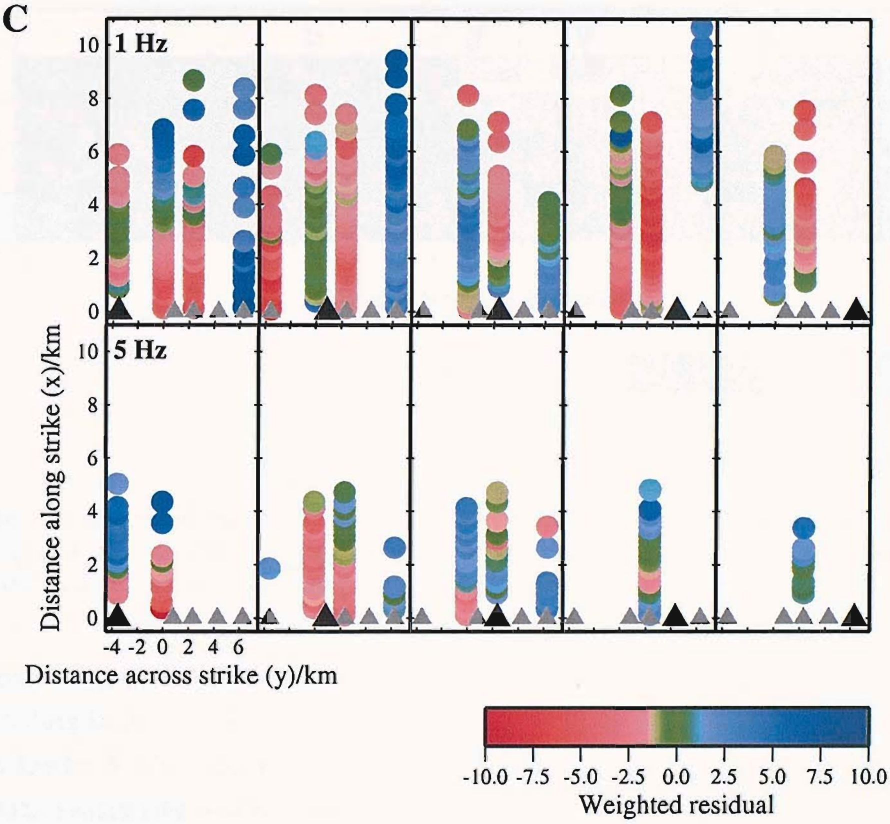

Figure 6.17: Residuals from the 2.5-D inversions. Plots *A* to *C* show the weighted residuals between the data and modelled responses for the corresponding models shown in Plots *A* to *C* of Figure 6.15. Data are plotted in a plan view at the receiver location in the model geometry: the four receiver 'lines' from left to right correcpond to LEMURS14, 18, 16 and 11. Residuals from 1 Hz and 5 Hz are shown in the top and bottom rows respectively of each plot. Residuals from each source location are shown separately in each column. The source location in each case is shown by a black triangle; other sources are plotted as grey triangles. From left to right, the sources correspond to experimental lines 3, 4, 1, 2 and 5. Positive residuals (corresponding to the recorded PE_{max} being greater than the modelled PE_{max}) are shown in blue, negative residuals in red. See text for discussion.

the region such as were found by MacGregor et al. (2001) in their dataset.

Short of identifying regions of particularly low or high data sensitivity, the usefulness of this form of data analysis is limited: a relative measure of the sensitivity of a region to model changes is given that clearly illustrates sensitivity decreases with depth, without quantifying the significance of the effect. Also, it is unable to address the tradeoffs that exist within the data: whilst a change in one part of the model may worsen the model fit, it is often possible to alter another part of the model to counteract this. These problems are usually addressed with a combination of forward modelling and constrained inversion to investigate

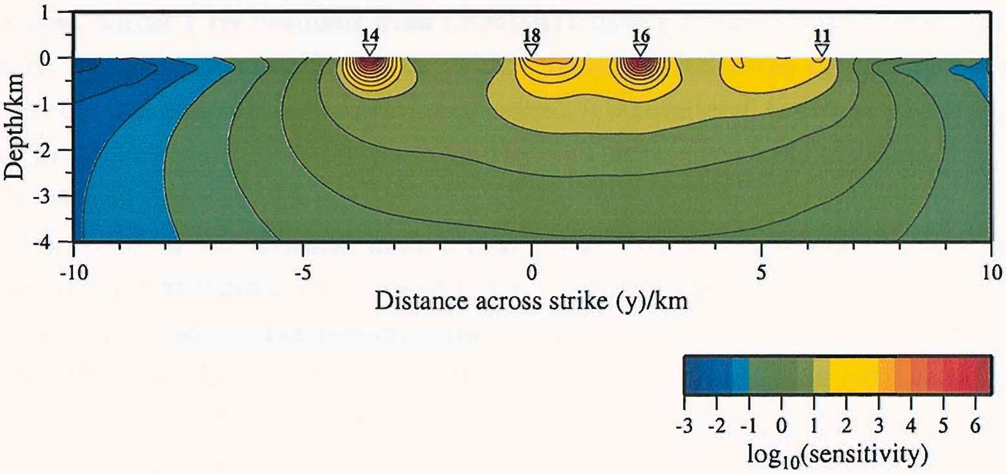

Figure 6.18: Magnitude of the survey sensitivity, as defined in Equation 6.20 for the model shown in Plot *B*, Figure 6.15. The data are most sensitive in the top 1 km of the crust, particularly around receivers (locations shown) and sources (locations not shown).

which features of the model are requirements of the data (MacGregor et al. 2001). This kind of modelling in 2-D is likely to do little to improve our understanding of the resistivity structure at Lucky Strike, where even the best-fit 2-D model leaves considerable bias within the data. Data sensitivity will therefore be revisited in the following chapter.

6.4.4 Discussion

In general, the final 2.5-D model is consistent with our understanding of the resistivity structure obtained from 1-D forward modelling and inversion. The upper 700 m of the crust exhibits resistivities of less than 10 Ωm. Below this level, resistivities increase, reaching 100 Ωm by a depth of 3 km. To the left and right sides of the model (at across-strike distances of less than -5 km and more than 7 km), the shallow crust reaches resistivities of 50 Ωm. This is outside the region of high model sensitivity, and has formed due to the smoothness constraints applied to the inversion.

Within the upper conductive layer there are at least three regions of lower resistivity. The most striking area lies between LEMURs16 and 11, with resistivities varying from 4 Ωm at a depth of 500 m, to 1 Ωm at the seafloor. This is an unexpected result, as this lies under the eastern flank of the seamount, several kilometres to the east of the region of active hydrothermal venting at the seafloor. However, data residuals show that this area of the model has a particularly bad fit to the data. The source corresponding to Line 2 (the second furthest source to the east in this model) is directly over this region. Whilst there is an adequate fit the the 5 Hz data recorded by LEMUR16, the 1 Hz data residuals have a strong negative bias, whilst 1 Hz residuals from LEMUR11 have a strong positive bias.

Clearly, the data are sampling lateral variations in the resistivity structure of about the upper 1 km of crust over the region. However, with 2.5-D inversion, these resistivity variations are being inadequately mapped into the 2-dimensional resistivity model, creating the observed tradeoffs between different sources and different receivers.

One feature of all the inversion models that is not obviously due to inadequate mapping of 3-D resistivity structures is the increase in the vertical gradient of resistivity from the west to the east of the region. For instance, the resistivity at 2.5 km depth is much higher at y=+5 km (100 Ωm) than y=-5 km (54 Ωm). The significance of this asymmetry remains unclear. However, MacGregor et al. (2001) also found a distinct asymmetry in their final 2-D model across the axis of the Valu Fa Ridge. This may have been partially due to the effect of the active Tofua Island arc, although they concluded that the mechanism was as yet unknown.

6.5 Summary

1 A good understanding of the effect of topography on the recorded electric fields at Lucky Strike can be gained with 2-D topographic modelling. Regions where the 2-D approximation break down may be interpreted in light of other results obtained. In general, the 3-D topography over the Lucky Strike seamount and median valley walls has a relatively small effect on the electric field recorded. However, there are localised regions where the effect of topography is more pronounced. These regions have been adequately delineated with the 2-D modelling presented here.

2 (a) Topographic effects cannot explain the attenuation of $E_\perp$ relative to $E_\parallel$ recorded by LEMUR15. In fact, they provide a mechanism for the 'masking' of this splitting at lower frequencies. It is therefore still likely that data from LEMUR15 are sampling a decrease in resistivity at depth.

  (b) Likewise, the addition of topography cannot explain the attenuation of $E_\parallel$ relative to $E_\perp$ recorded by LEMURs 11 and 18 on the northern flank of the seamount.

  (c) Whilst the effect of topography has been shown to be different at different transmission frequencies, it is unlikely that this disparity alone is enough to explain why no 1-D model will simultaneously fit different frequencies of data recorded by LEMUR16. A more likely explanation is that this is due to higher-dimensional resistivity variations in the crust.

3 Data with a greater topographic influence can be removed without sacrificing overall

data coverage. Topography will have, at most, a second-order effect on the remaining data.

4 Results from inversion of data in the across-strike model are generally consistent with the 1-D results obtained in the previous chapter.

5 However, data residuals from the best-fit model show considerable bias both between different receivers, between the two modelled frequencies and along strike. This reflects the fact that the Lucky Strike data cannot be approximated to 2-dimensional.

6 The clear 3-dimensionality of the data means that considerable caution should be taken when relating specific features of the 2-D model to the true resistivity structure below the seamount.

7 One feature that has remained consistent throughout 2.5-D modelling of the data is an increase in vertical resistivity gradient from the west to the east of the region, although the reason for this asymmetry remains unclear.

Chapter 7

3-D forward modelling and pseudoimaging

In this chapter, the results from 1- and 2-dimensional modelling are used to investigate the 3-dimensional resistivity structure beneath the Lucky Strike seamount. Pseudoimaging of the residuals from modelling the 'average' 1-D resistivity profile is used to map lateral resistivity variations. These images are then used to guide 3-dimensional forward modelling with the ISIS (Induction Sources In the Sea) code of Flosadóttir & MacGregor (2004), to find a resistivity structure over the region that is consistent with the data.

7.1 ISIS code outline

Until recently, no suitable code has been available for modelling the electric dipole response when the resistivity of the earth is allowed to vary in more than two dimensions. As part of the ISO-3D project, Flosadóttir & MacGregor (2004) used the 3-D magnetotelluric code of Mackie & Madden (1993) & Mackie et al. (1994), to develop a numerical code for modelling electromagnetic fields generated by arbitrarily distributed induction sources embedded in a 3-dimensional resistivity structure.

The problem is discretised on a staggered finite element grid, with a constant resistivity within each grid element. The solution is initially obtained for the magnetic field, along the edges of the grid elements. The electric field through each face of an element is then calculated from these. This generates a staggered grid of E_x, E_y, and E_z electric field components. Polarisation ellipse parameters may then be calculated by linearly interpolating E_x and E_y to common locations.

Several options are available for defining model boundary conditions. By default, magnetic fields are set to zero on the sides and top of the model, and use the boundary conditions of Mackie & Madden (1993) on the bottom edge. Alternatively, a 'buffer' zone containing a specified resistivity may be defined, surrounding the sides and bottom of the model. A low resistivity buffer leads to the component of the electric field tangential to the boundary being approximately zero. By comparing the results from these two situations, it is possible to assess over how much of the model the boundary may safely be ignored (Flosadóttir & MacGregor 2004).

7.1.1 Mesh design

Empirical observations of the numerical behaviour of ISIS has led Flosadóttir & MacGregor (2004) to provide a series of guidelines on model parameterisation that are broadly similar to those discussed previously for 2.5-D modelling:

- The computational domain should extend at least 1.5 to 2 skin depths beyond the region over which accurate field results are required.
- The ratio of adjacent cell sizes should be no greater than two, and the cell aspect ratio should never be greater than about 100:1.
- About four cells per skin depth are needed. Finer parameterisation around the ocean/ seafloor boundary is needed to allow modelling of the sharp resistivity contrast. Doubling the grid resolution around the source significantly improves near-source errors in the calculated fields. However, increasing the resolution further in this region can introduce errors associated with the large aspect ratio cells near the edge of the modelled region.

Flosadóttir & MacGregor (2004) used a parameterisation comprising 117×117×90 cells to test the performance of ISIS in modelling a resistivity structure that was broadly similar to preliminary results from the Lucky Strike data. It is this parameterisation that is used here (Figure 7.1). The ability of the mesh and ISIS code to handle vertical variations in resistivity was verified by Flosadóttir & MacGregor (2004) by comparison with the quasi-analytic solution of Chave & Cox (1982), over the range of primary transmission frequencies used at Lucky Strike (0.25 Hz to 4 Hz). They found that the mean differences in both components of horizontal electric field strength at the seafloor were calculated between -10 km and 10 km in the x and y directions, and were found to be no greater than 1.6 %. Errors were largest close to the source, at source-receiver ranges that have been removed from the Lucky Strike data.

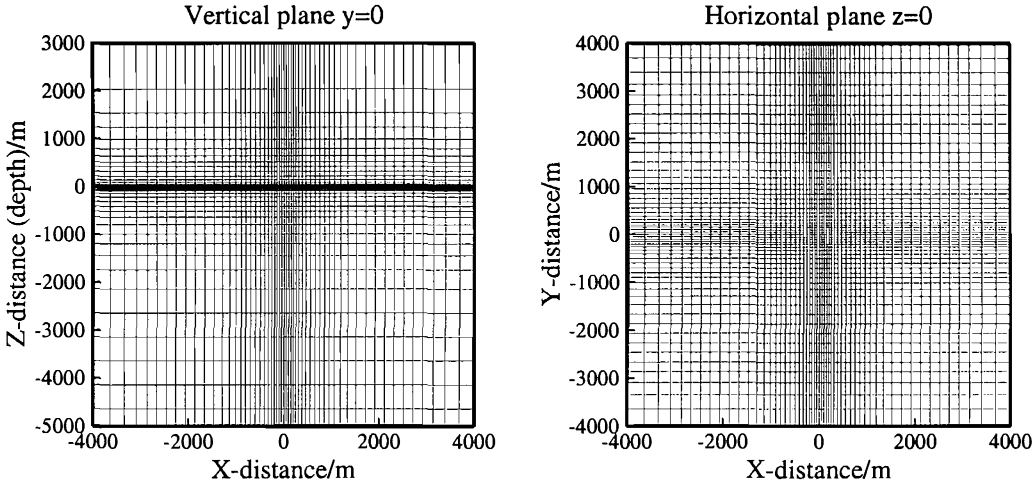

Figure 7.1: The central portion of the finite difference mesh used in the 3-D forward modelling. The HED source is located at the origin, and the seafloor boundary is at a depth of 0 m: the extra parameterisation around both of these features can be seen in the plots. The full 117×117×90 mesh extends from -75 km to 75 km in both horizontal directions, and from 5 km above the seafloor to 68 km below the seafloor. This mesh was first used by Flosadóttir & MacGregor (2004) for intercomparison with the modelling codes of Chave & Cox (1982) and Unsworth et al. (1993), and to calculate the response from a simple 'box' resistivity model based upon preliminary results from the Lucky Strike dataset.

Flosadóttir & MacGregor (2004) also tested the effect on the modelled response of lateral variations in resistivity by comparison with the 2.5-D finite element code of Unsworth et al. (1993), and found an agreement of better than 2 % in amplitude and phase between the codes, apart from close to the source and near the edge of the computational domain. The internal stability of the results obtained were then verified by varying grid cell graduation, the size of the computational domain, and the modelling convergence criteria.

Whilst I have not repeated the full range of mesh tests carried out by Flosadóttir & MacGregor (2004), I have re-tested the mesh against the code of Chave & Cox (1982), this time using the 'average' 1-D resistivity profile at Lucky Strike, described in the next section. At 1 Hz, over a region between -15 km and 15 km in the x and y directions, the mean absolute difference in PE_{max} at the seafloor was 2.2 %. At 5 Hz, over the smaller region between -7 km and 7 km in the x and y directions (reflecting the shorter maximum range in the 5 Hz data), this difference was 2.7 %. Although greater than at lower frequencies, this is still an acceptable error, especially as the largest differences are again close to the source.

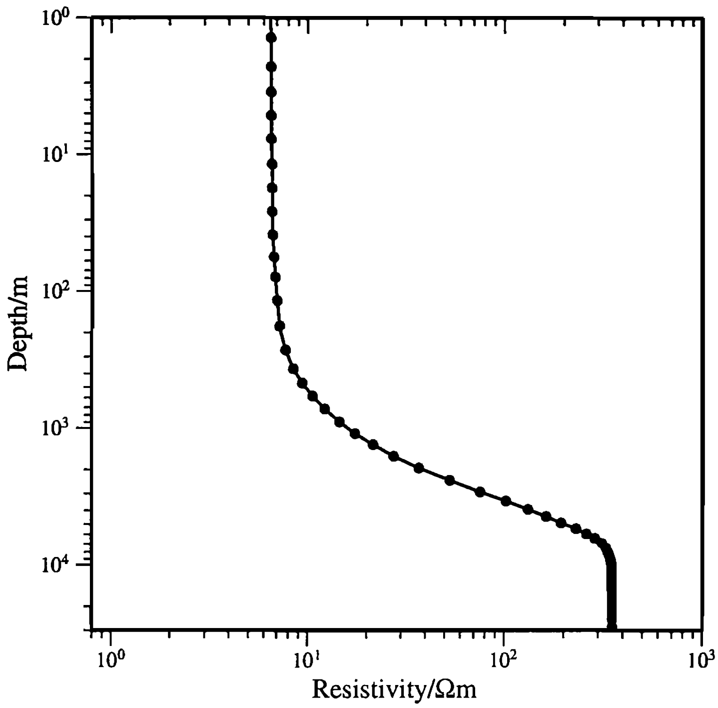

Figure 7.2: The 1-D resistivity profile obtained from averaging the final 2-D model (Figure 6.15) between -7 km and 5 km across strike. The curve has been linearly interpolated between the midpoints of the layers in the 2-D model, and resampled to fit the layers in the 3-D model (filled black circles).

7.2 Model design

In order to investigate the higher-dimensional resistivity features at Lucky Strike, a 1-D resistivity profile was generated from the 2.5-D inversion results by averaging the final 2-D model obtained (Figure 6.15), between -7 km and 5 km across strike. This 1-D profile can be seen in Figure 7.2.

In the ISIS code's current form, the model resistivity structure is specified by inserting rectangular prisms of a uniform resistivity into a background halfspace. If prism edges do not correspond to an edge of a model element, the closest element boundary is used; if a prism lies wholly within a single element in any of the dimensions, it is ignored. There is no practical limit to the number of prisms that may be specified; as prisms are inserted into the structure sequentially, regions of overlap contain the last resistivity specified in that region.

One limitation to the model generation is that the resistivity of a prism is specified by an integer value, which corresponds to a position in a table of required resistivities. With the 1-D resistivity profile used here, and as distortions are applied to this profile, the list of resitivities quickly becomes large, and cross-referencing unwieldy. Instead, a fixed resistivity table was generated with 1000 entries, evenly spaced logarithmically over four orders of magnitude between 0.1 and 1000 Ωm. This provides ample resistivity resolution; a resistivity can be converted to its nearest integer record number with the simple equation

$$\text{record number} = \text{nint}\left(\left(\log_{10}(\text{resistivity}) + 1\right) \times 1000/4\right).$$

7.2.1 Source locations

In the 2.5-D case, multiple source locations along the model invariant direction were calculated at a single source location and multiple receiver locations (see previous chapter). However, once the resistivity is allowed to vary in three dimensions, this transformation is no longer possible. Furthermore, the greater memory requirement of 3-D modelling means that a 3-D mesh with multiple source locations (and a correspondingly finer grid) quickly becomes too large to model.

Therefore, in order to model data from Lucky Strike, ISIS was run separately for each required source position. The experimental geometry and resistivity structure being modelled were then translated as appropriate in order to position the source at the origin of the mesh. Translating the resistivity structure in this way inevitably leads to small changes in the structure being modelled at different source locations, as the required structure is fit to the static model grid. However, over the region being modelled, the maximum horizontal grid size is 200 m. This would lead to a maximum possible difference in the position of resistivity structures being modelled of 100 m between different source locations. This is considerably smaller than the size of resitivity anomalies that will be modelled here.

The locations of source positions tested are shown in Figure 7.3. The recorded field strength at each of these locations was calculated by averaging data recorded when the source was in the correct orientation, and within 100 m of the modelled source location. The average amplitude and data error of these points was then calculated as for the 2.5-D inversion (Equations 6.18 & 6.19). Data were taken from the dataset with SNR ≥ 5; data with an SNR below 5 were discarded.

7.3 Pseudoimaging

Figures 7.4 & 7.5 show the residuals obtained from modelling all the 1 Hz and 5 Hz data with a SNR greater than 5, against the 1-D resistivity profile described above. It is a non-trivial task to translate these residuals into deviations in resistivity from the 1-D background model used. Residuals are plotted at the source location, whilst in practice they are a misfit

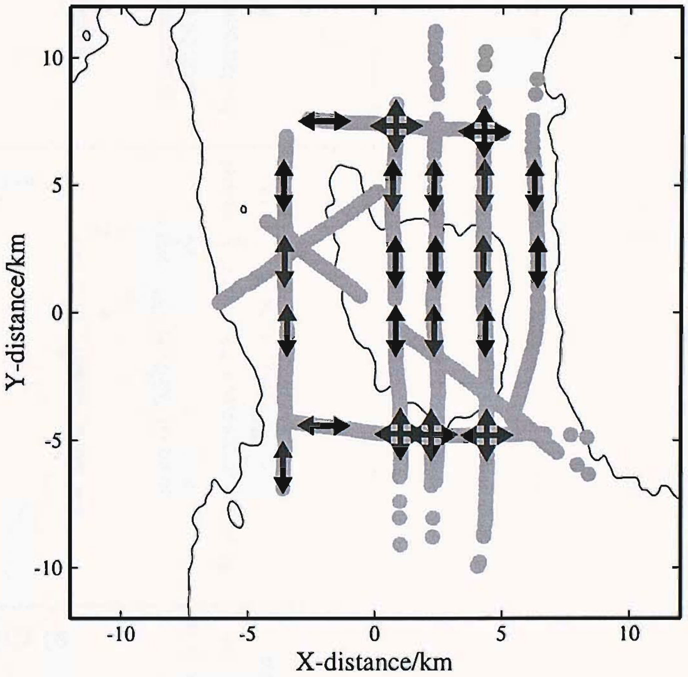

Figure 7.3: The 27 source locations used to model the data in 3-D. The experimental geometry has been rotated by 18^o counterclockwise about an origin at LEMUR18. Source dipoles were in the same orientation as the double arrows; in some instances, where x- and y-oriented tows were co-incident, both source orientation were modelled. For reference, the grey filled circles correspond to 1 Hz source locations when data were recorded by LEMUR18 (from the SNR $\geq$5 dataset). The 1800 m depth contour is also shown.

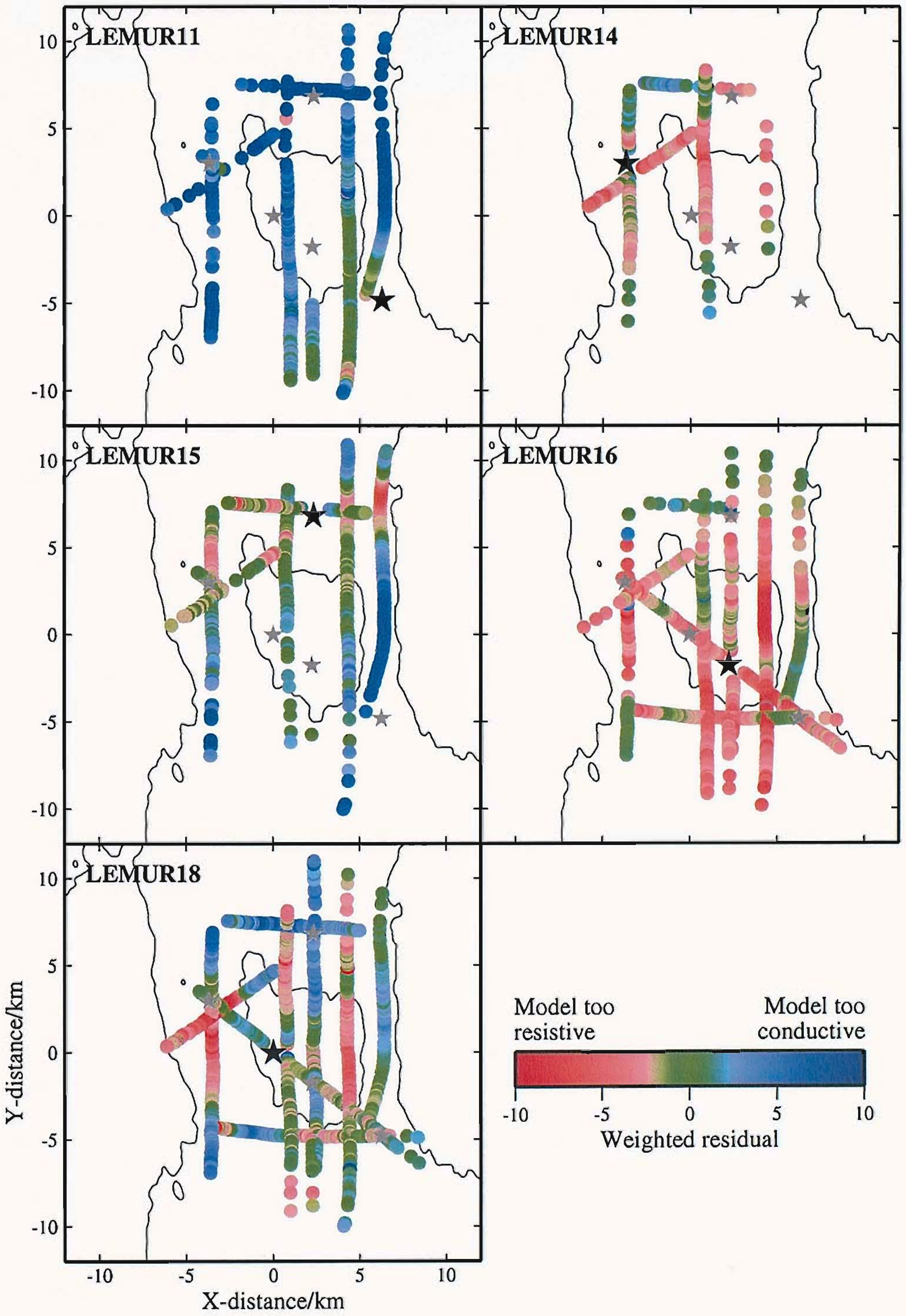

Figure 7.4: Residuals between the 1 Hz data, and the 1-D modelled response using the average 1-D profile shown in Figure 7.2.

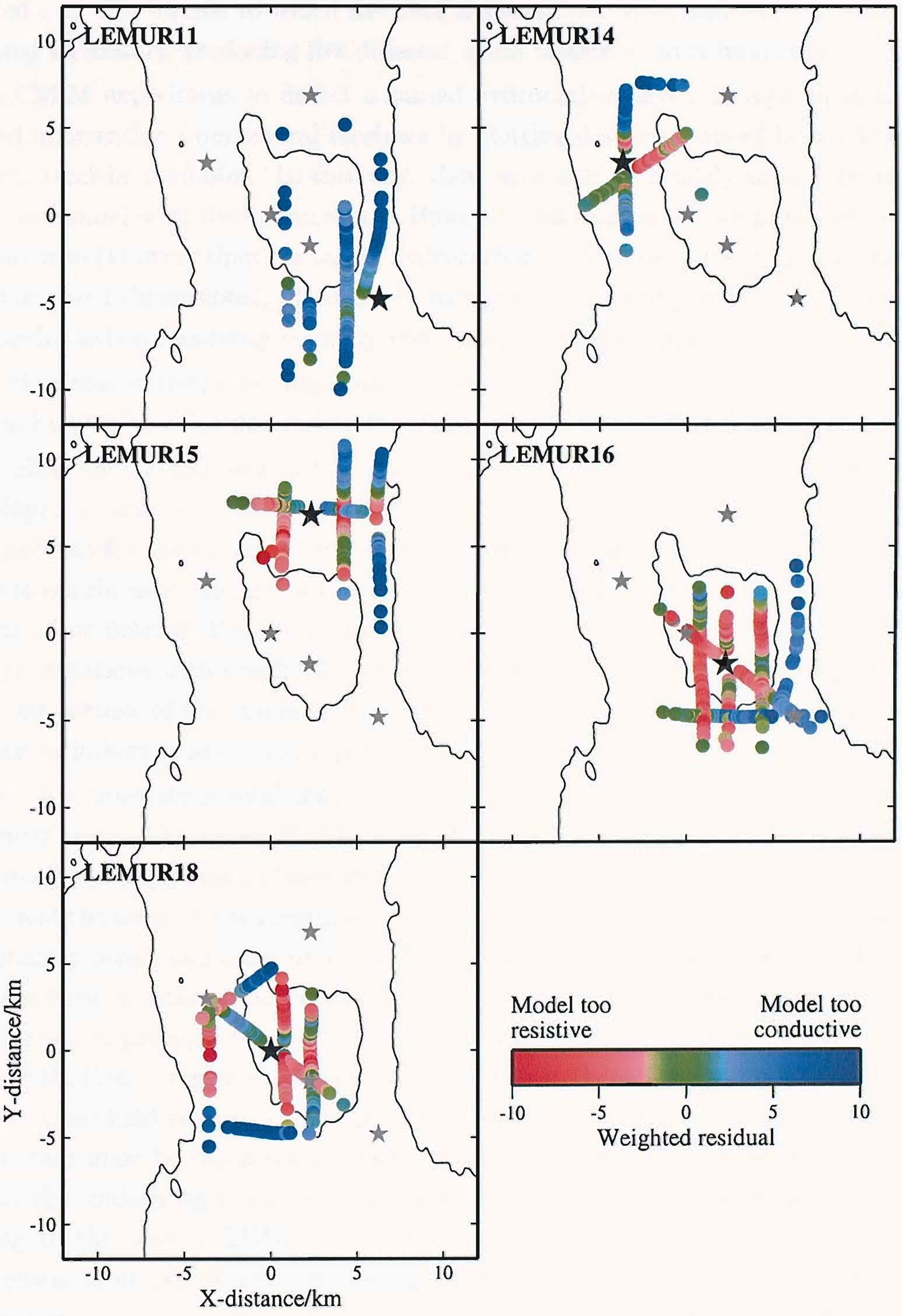

Figure 7.5: Residuals between the 5 Hz data, and the 1-D modelled response using the average 1-D profile shown in Figure 7.2.

integrated over the volume to which the data are sensitive. Also, results from each receiver are plotted separately, producing five different misfit images at each frequency.

In a CSEM experiment to detect a buried hydrocarbon layer, Ellingsrud et al. (2002) combined information from several receivers by plotting data normalised by a 1-D model at the source-receiver midpoint. In this way, they were able to crudely image the resistivity anomaly assocated with the hydrocarbon. However, this technique only produced acceptable results because (1) other than the target hydrocarbon, the survey resistivity was expected to approximate to 1-dimensional, (2) this 1-D background resistivity was well constrained and (3) the hydrocarbon resistivity anomaly was limited to a single depth.

It is clear that in the more complicated resistivity structure at Lucky Strike, the residuals plotted in Figures 7.4 & 7.5 do not directly relate to anomalies at the source-receiver midpoint.

It is likely that in the near future, tomographic or other related imaging techniques will be developed to map anomalous resistivities from data residuals. Such a technique would need to account for the volume of space to which the data were sensitive. However, it is still possible to obtain useful images with the simple approximation that data are sensitive to all points in a line between the source and receiver. Whilst this clearly does not account for resistivity variations with depth, the results from 1-D and 2-D modelling suggest that the greatest proportion of the residuals from the 1-D model used here should relate to lateral resistivity variations in about the top 1 km of the crust.

Figure 7.6 shows the results obtained from applying this approach to the 1 Hz residuals. The sources and receivers are arranged into a grid of evenly-spaced bins. The residuals from each source location are then placed into each bin that lies on a line between the source and receiver, and the mean of the residuals within each bin is plotted. Predominantly in-line and predominantly broad-side data are plotted separately (Plots A and B respectively), as they will be sensitive to different aspects of the resistivity anomaly. Many of the features of the data discussed in previous chapters can be seen in these plots, including low field strengths around LEMUR16, a region of attenuated broad-side fields to the east of LEMUR15, and a region of higher field strengths over the east of the region, particularly around LEMUR11. However, care must be taken when interpreting these plots, as certain features are unlikely to reflect the underlying resistivity structure. For example, the strong positive residuals extending to the west of LEMUR11 on the broad-side plot are probably a result of the oversimplistic assumptions used: in this region, there is no data from other instruments, and therefore nothing to counteract the large positive residuals recorded by LEMUR11, which probably correspond to an anomaly closer to the instrument. Plots of data density (i.e. the number of data within each bin) do little to reflect the accuracy of these images. Instead, Plots C and D show the number of receivers that have contributed to each data bin.

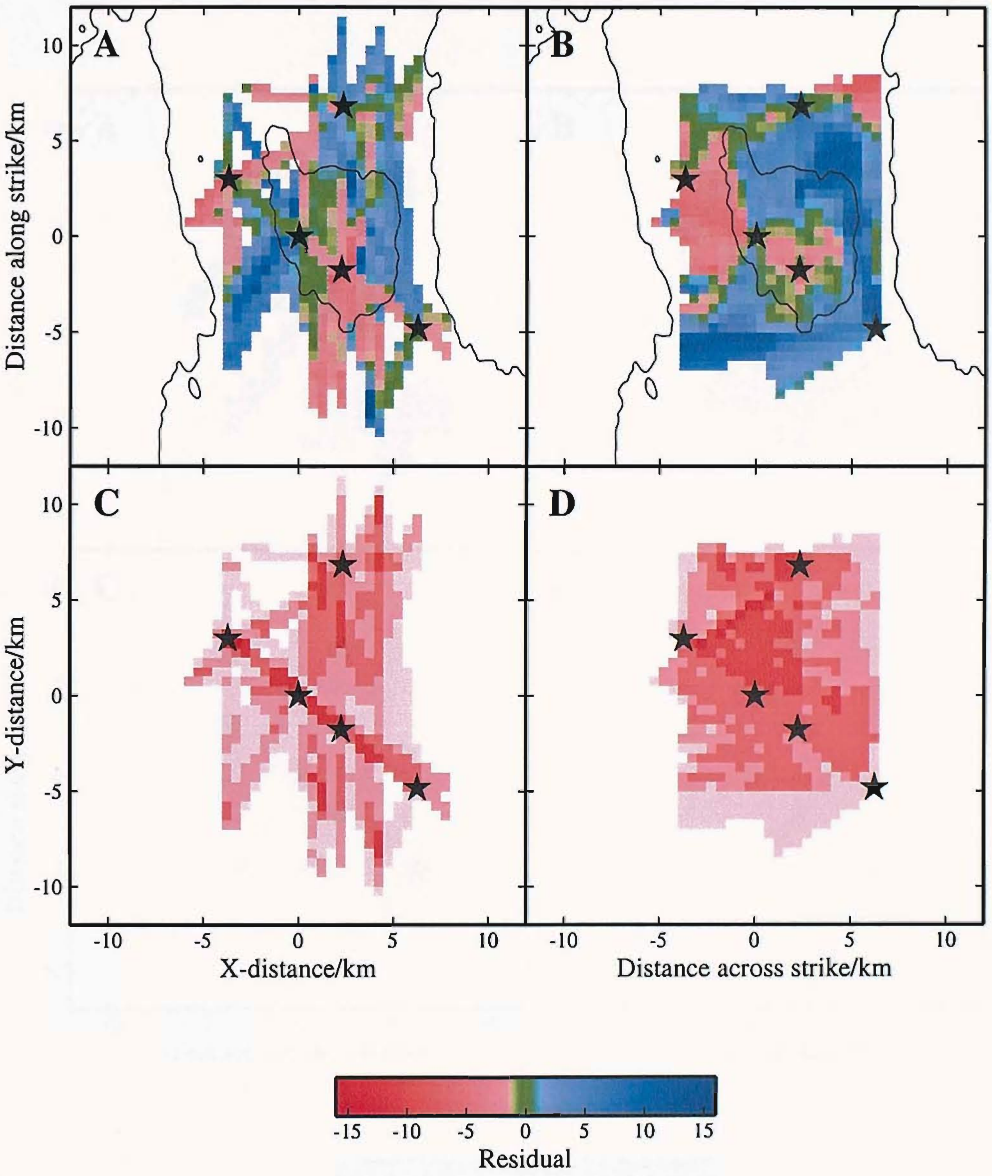

Figure 7.6: Pseudoimages of the 1 Hz data. Plot ***A*** shows the image obtained from the near-in-line data residuals of Figure 7.4. The bins have 500 m sides. See the text for further imformation on how the image is generated. Plot ***B*** shows the image obtained from the near-broad-side data. The intensity of colour in Plots *C* and *D* illustrates the number of instruments that contributed to the data in each of the bins of Plots *A* and *B* respectively: empty bins are plotted in white, whilst bins which contain data from all five LEMURs are dark red. Such bins may be qualitatively considered to give a more reliable result.

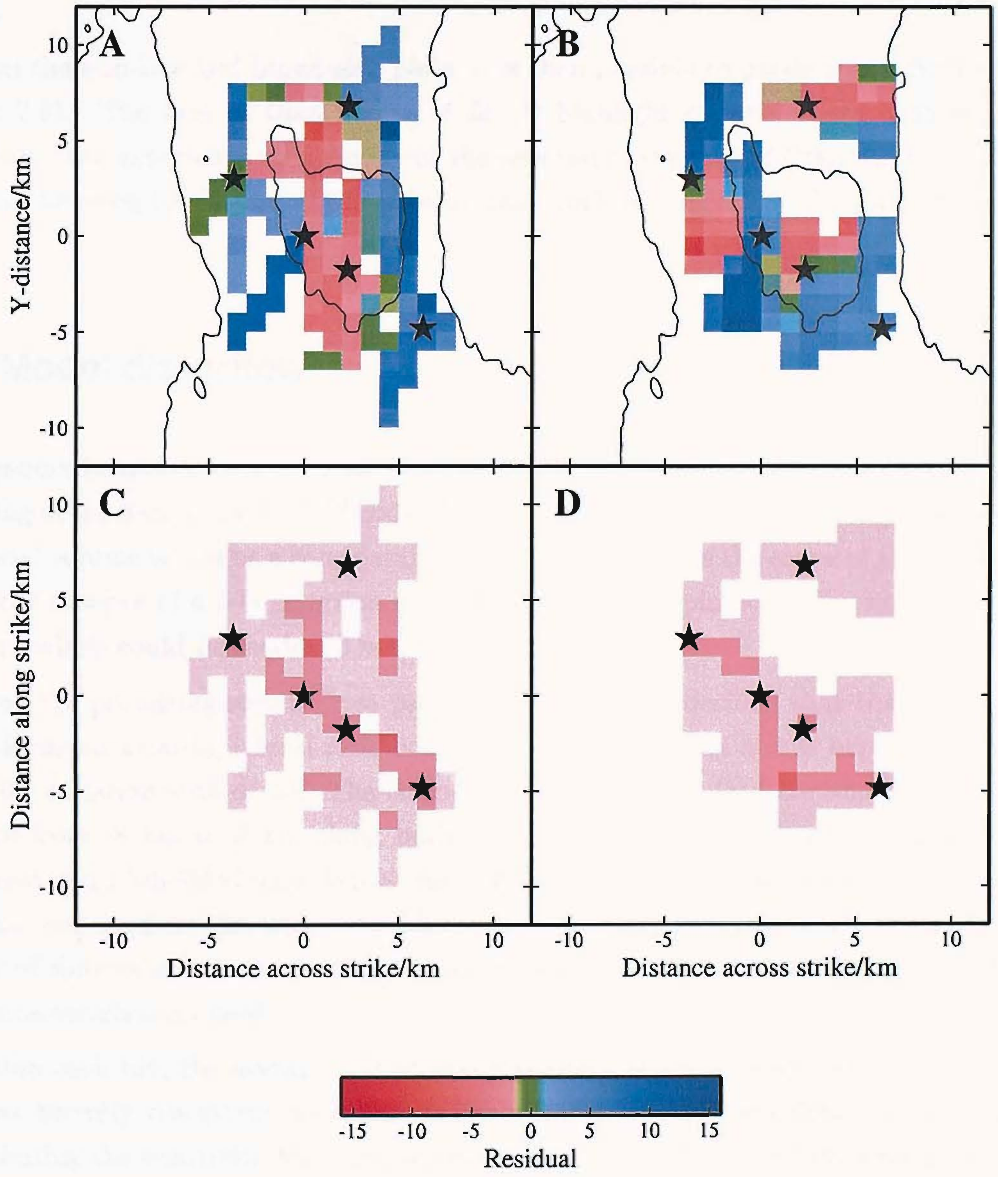

Figure 7.7: As Figure 7.6, with the 5 Hz data. As less data are available at this frequency, 1 km-sided bins are used to improve the coverage of the image.

The 5 Hz data (Figure 7.7) are less well suited to this form of imaging: the more limited range of high SNR data at this frequency means that there is little overlap between data from different instruments. However, the general pattern remains consistent with the 1 Hz images.

From these in-line and broad-side plots, it is then possible to produce two further images (Figure 7.8). The first of these (Plots *A* & *C*) highlight regions where both in-line and broad-side data experience an anomaly of the same sign; the second (Plots *B* & *D*) show the difference between the in-line and broad-side data, highlighting areas of amplitude 'splitting'.

7.4 Model distortion

These pseudoimages were used as a reference to guide a process of manual iterative forward modelling of the data with the ISIS code. As an exhaustive forward modelling investigation of the crustal volume would be a considerable undertaking, outside the scope of this dissertation, and in the absence of a 3-D inversion code, limitations were placed on the type of resistivity structure which could be modelled within the crustal volume.

Given the promising results from pseudoimaging, it was decided that the 3-D modelling should focus on locating lateral resistivity anomalies, somewhat at the expense of resolving resistivity variation with depth. The lateral area to which the data are sensitive, comprising a square from -8 km to 8 km along both axes of the geometry shown in Figure 7.3, was discretised into 1 km-sided bins. Whilst the full dataset would have a greater lateral resolution than this over much of the area, 1 km bins were considered to be adequate given the limited number of sources to be modelled in 3-D, along with the coarse (up to 200 m laterally) 3-D mesh parameterisation used.

Within each bin, the average 1-D crustal resistivity profile was allowed to vary in a way that was broadly consistent with the results obtained from lower-dimensional modelling, redistributing the resistivity variation across all depths to which the data were sensitive (see section 7.6). The distortion d of the average 1-D crustal resistivity profile $\rho(z)$ was defined such that at a depth z,

$$\log_{10}(\rho_m(z)) = \log_{10}(\rho(z)) + (\log_{10}(\rho_{\max}) - \log_{10}(\rho(z)) \times d), \tag{7.1}$$

where $\rho_m(z)$ is the modelled resistivity and $\rho_{\max}$ is the maximum resistivity in the profile. The effect of this can be more clearly seen in Figure 7.9.

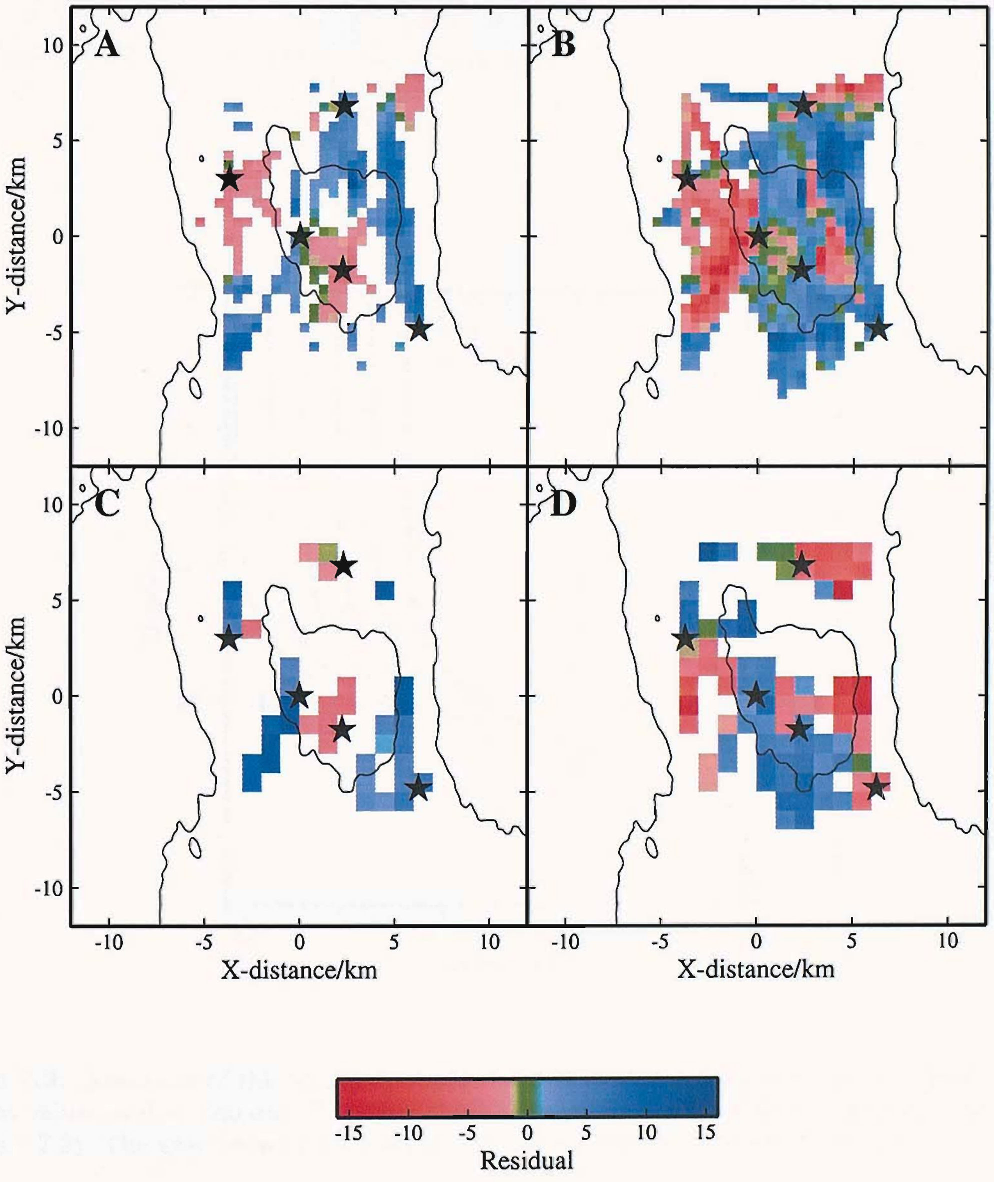

Figure 7.8: Further pseudoimages of the data. Plots *A* and *B* are generated from 1 Hz data; plots *C* and *D* are generated from 5 Hz data. Plots *A* and *C* highlight bins where both in-line and broad-side data experience an anomaly of the same sign. In these cases, the plotted value is the mean of the two anomalies. Plots *B* and *D* highlight the differences between the anomalies in the in-line and broad-side data. In bins where both in-line and broad-side data are available, the plotted value is the broad-side anomaly minus the in-line anomaly.

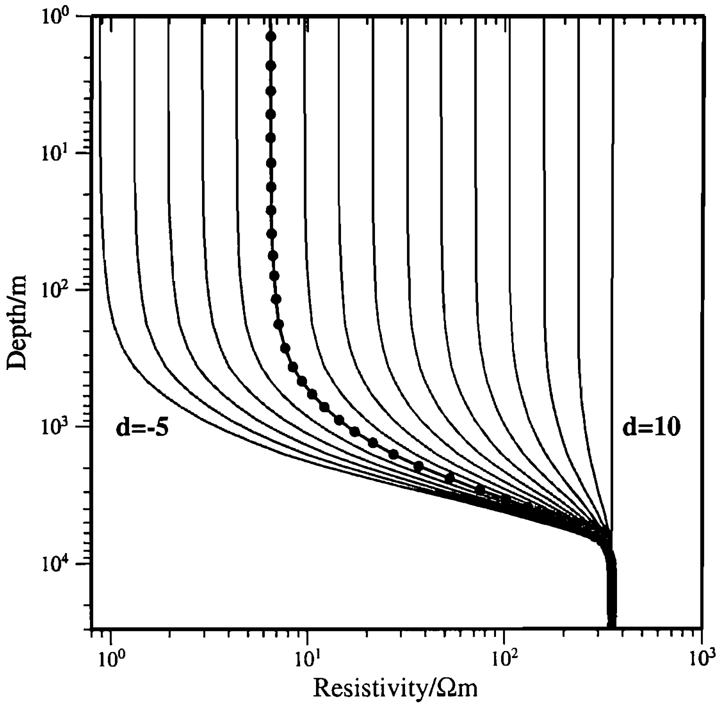

Figure 7.9: Distortion of the resistivity profile for 3-D modelling. The grey curves illustrate how different values of *d* in Equation 7.1 affect the 1-D resistivity profile (black line with filled circles, as Figure 7.2). The grey curves shown are for integer values of *d* between -5 and 10.

7.5 Forward modelling results

The undistorted 1-D resistivity profile was found to fit the 1 Hz data at the 27 source locations to an RMS misfit of 4.3 (Figure 7.10). After a process of iterative forward modelling, the resistivity structure shown in Figures 7.12 & 7.13 reduced this misfit to 3.13. The residuals obtained from this model can be seen in Figure 7.11. These illustrate that the relatively small decrease in misfit belies a major improvement in the fit to the data: much of the large-scale structure has been removed from the residuals, which are now far less systematically and geographically biassed. The most striking features of the model are:

1 A localised region of low resistivities (down to 3.3 Ωm in the shallow crust) to the north-east of LEMUR16 (x=2 to 4 km, y=-2 to 1 km). This region is required in order to provide a fit to the low field strengths recorded by LEMUR16, and provides a good correlation with the known area of active high temperature hydrothermal discharge (see Figure 3.4). The elongation of this region to the south is a requirement of the data recorded by LEMUR16 to the south of the instrument. A more extensive region with a correspondingly higher resistivity is unable to sufficiently fit data recorded by the other instruments particularly LEMURs 15 and 18.

2 High resistivities, reaching 208 Ωm in the shallow crust, over the east of the region (x >5 km). These reduce the large positive residuals in the LEMUR11 data (RMS reduced from 7.04 to 4.88), although a significant negative bias is still present. They also provide a better fit to data recorded by LEMURs 15, 16 and 18 over this region. The sharp increase in resistivities from the seamount summit to this eastern flank region is also well constrained by this data.

3 The high resistivity region from x=-5 to -1 km and from y=-7 to -2 km is needed to explain the high field strengths recorded by LEMURs 15 and 18 over this area. The high resistivities to the west of here (x <-5 km) are not a requirement of the data (no transmission tows were made over this area), but have been included in light of the high resistivities on the opposite flank of the AVR, described in (2).

4 A broader region of lower resistivities (down to 3.3 Ωm in the shallow crust) between LEMURs 14 and 15 (x=-3 to 1 km, y=4 to 7 km). This area is required in order to reduce the positive residuals in the data to the east of LEMUR14, and to the west of LEMUR15. This feature may be associated with the topographic high located on the north west flank of the axial seamount (see Figures 7.12).

In the 5 Hz data, which is more sensitive to shallow structure (Section 7.6), the overall misfit has increased from 5.79 (Figure 7.14) to 7.83 (Figure 7.15). Whilst there has been

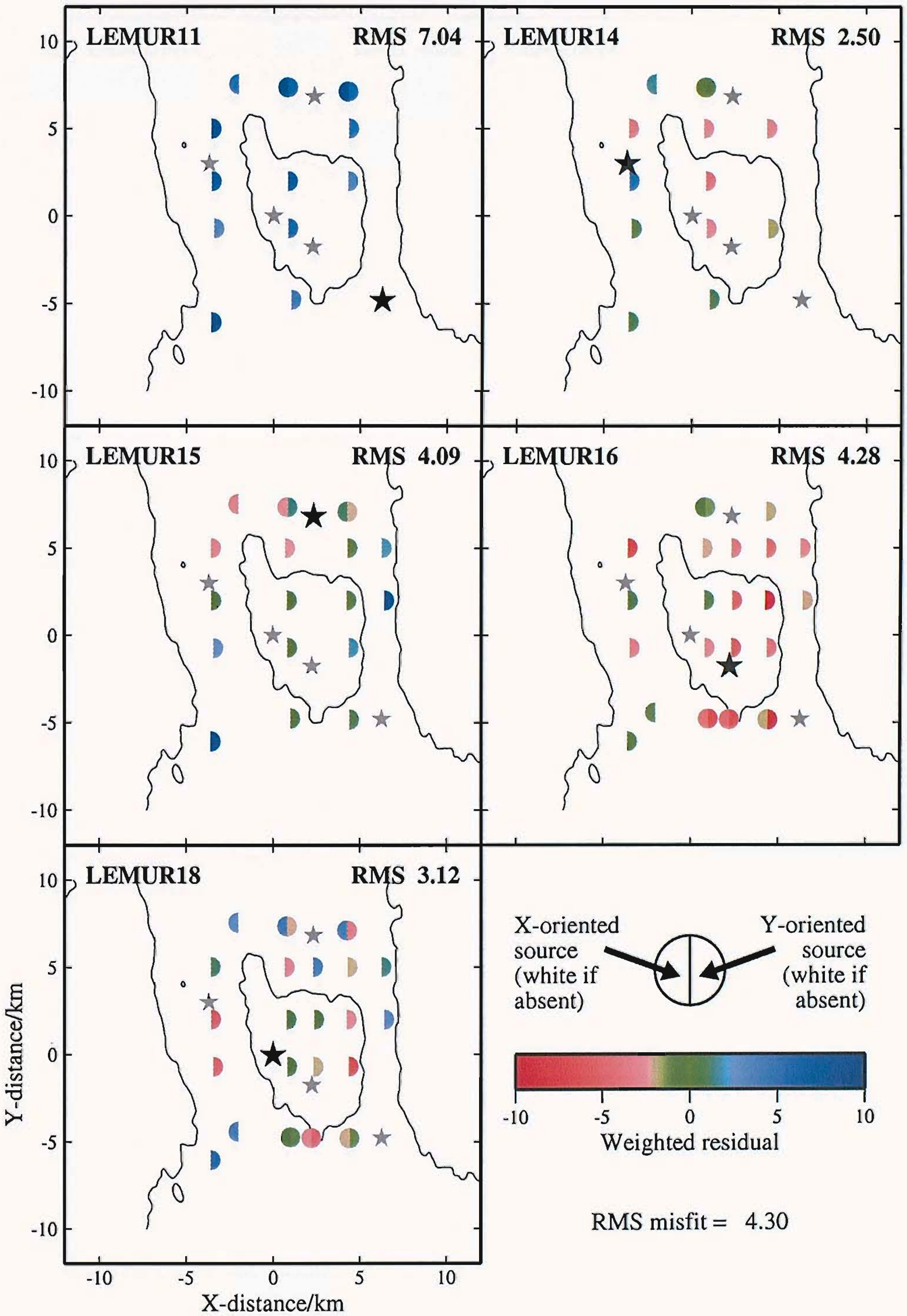

Figure 7.10: 1 Hz residuals at the 27 source locations modelled in 3-D with the 1-D resistivity profile shown in Figure 7.2. Residuals are plotted as semi-circles to allow residuals from co-incident x-oriented and y-oriented sources to be viewed in the same plot. The RMS misfit from each receiver is also shown, along with the overall misfit (bottom right).

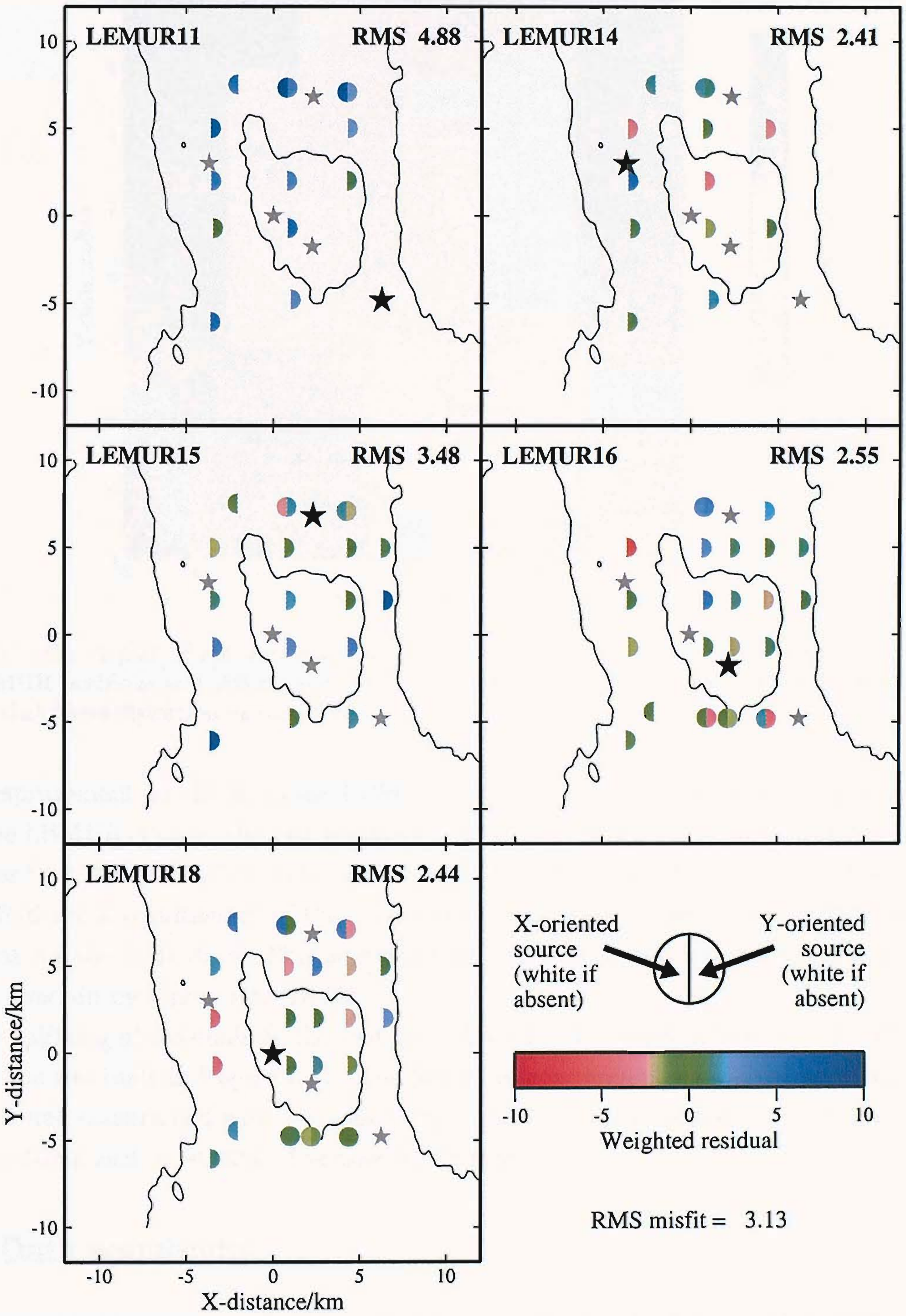

Figure 7.11: Residuals obtained at 1 Hz from modelling of the final 3-D resistivity structure, shown in Figures 7.12 & 7.13. See text for discussion.

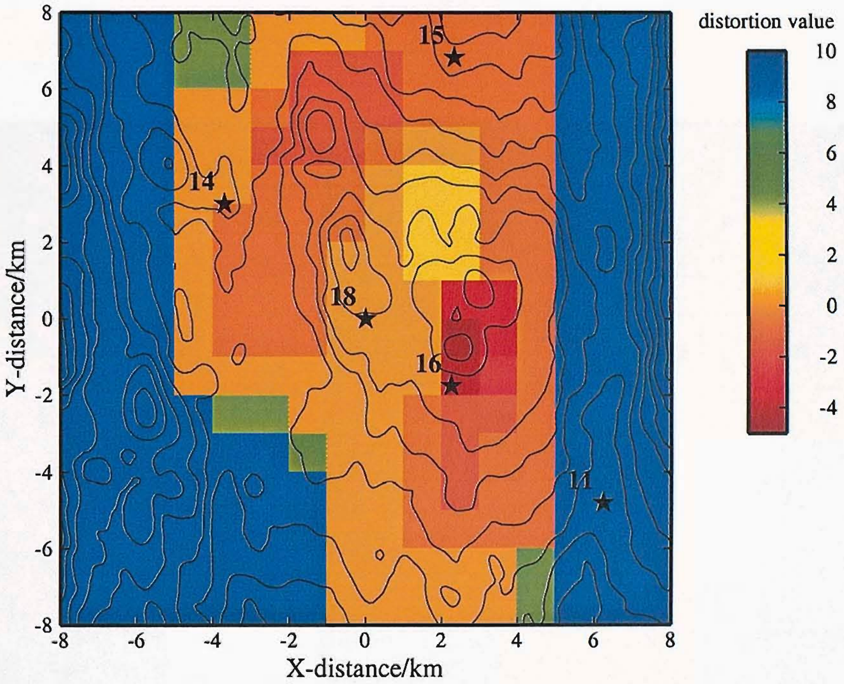

Figure 7.12: A plot of the distortion (*d*) values used in the final 3-D resistivity model overlain by LEMUR positions and 100 m depth contours. See Figure 7.13 for slices through the resistivity model that these distortion values produce.

some improvement on the fit to the LEMUR11, 15 and 18 data, and some worsening of the fit to the LEMUR14 data, the vast majority of this increase is due to LEMUR16 (RMS misfit increases from 3.96 to 11.70). It is clear that whilst the low resistivities to the north east of LEMUR16 are a requirement of the 1 Hz data, the increase in shallow resistivity has been too great for the 5 Hz data. This suggests that these lower resistivities must be at greater depths, overlain by higher resistivities.

The splitting of residuals to the east of LEMUR15, discussed in Section 5.3, can also be seen in the residuals in Figure 7.15. The low resistivity anomaly required to fit these data has been well constrained with 1-D modelling, but cannot be included in this 3-D model due to the self-imposed constraints described in Section 7.4.

7.6 Data sensitivity

As discussed in the previous chapter, the sensitivity of the CSEM technique is highly dependent on the target resistivity structure. Accordingly, without having carried out exhaustive 3-D modelling of the data, it is not possible to provide a definitive answer to such questions as ‘does an axial magma chamber exist beneath the Lucky Strike seamount?’. However,

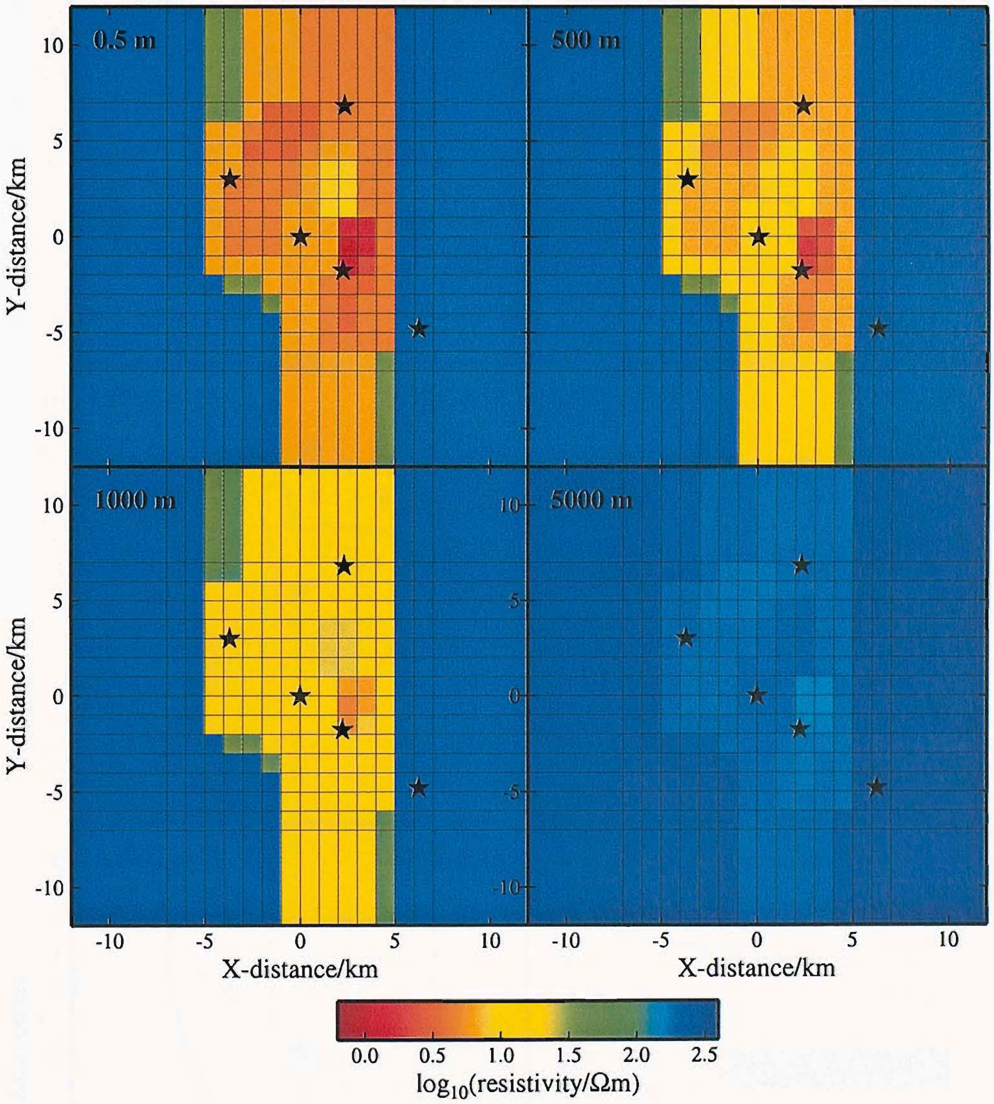

Figure 7.13: Four slices through the final 3-D resistivity structure obtained by a process of iterative forward modelling, guided by the pseudoimages obtained previously. The vertical resistivity profile within each plotted element was defined by the distortion value d (see Equation 7.1 and Figure 7.9) shown in Figure 7.12. Resistivity elements have 1 km sides, except at the edge of the 16 km×16 km region, where they are extended to fill the model space. Receiver locations in this geometry are plotted with stars.

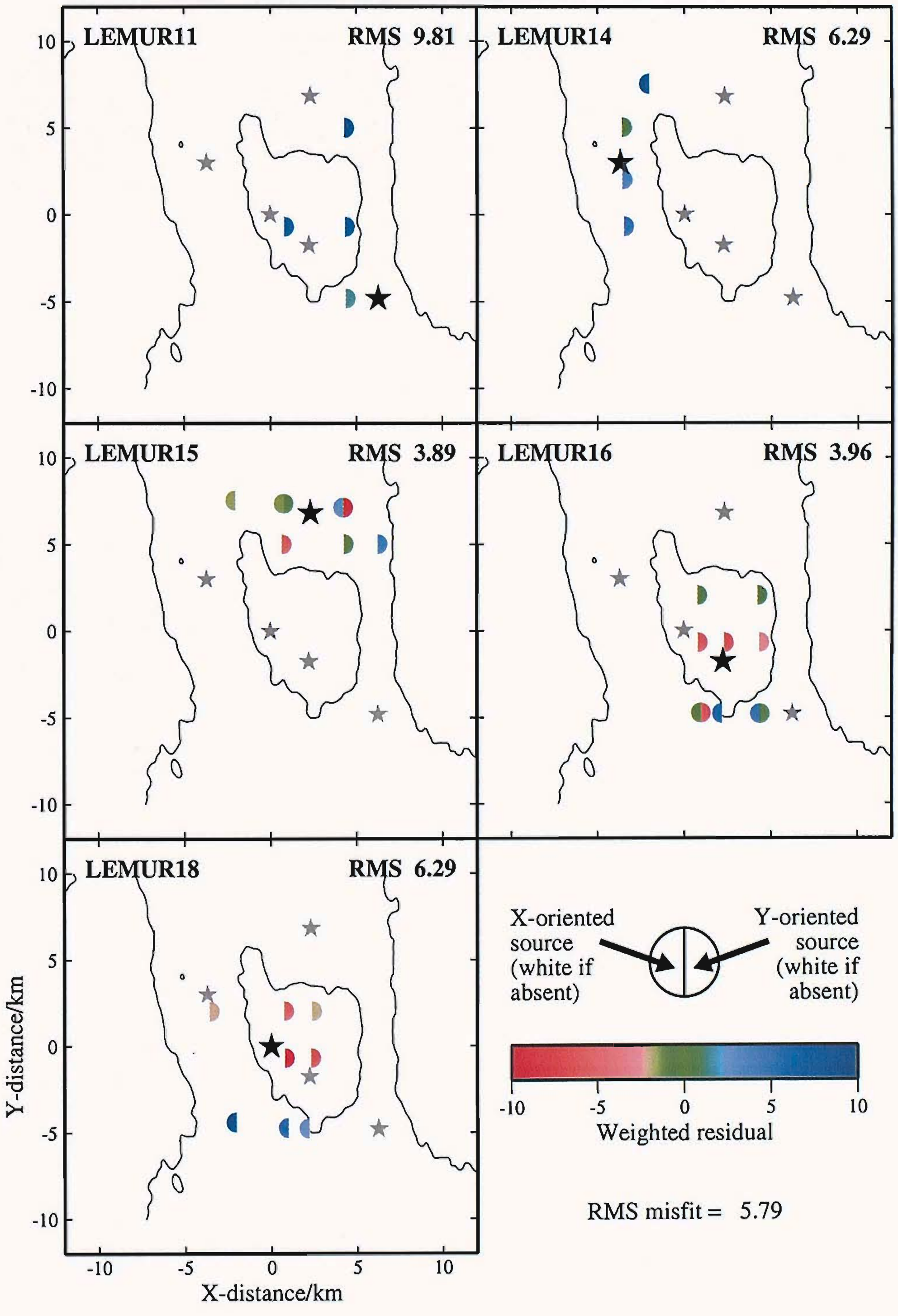

Figure 7.14: 5 Hz residuals at the 27 source locations modelled in 3-D with the 1-D resistivity profile shown in Figure 7.2. See the caption of Figure 7.10 for more information.

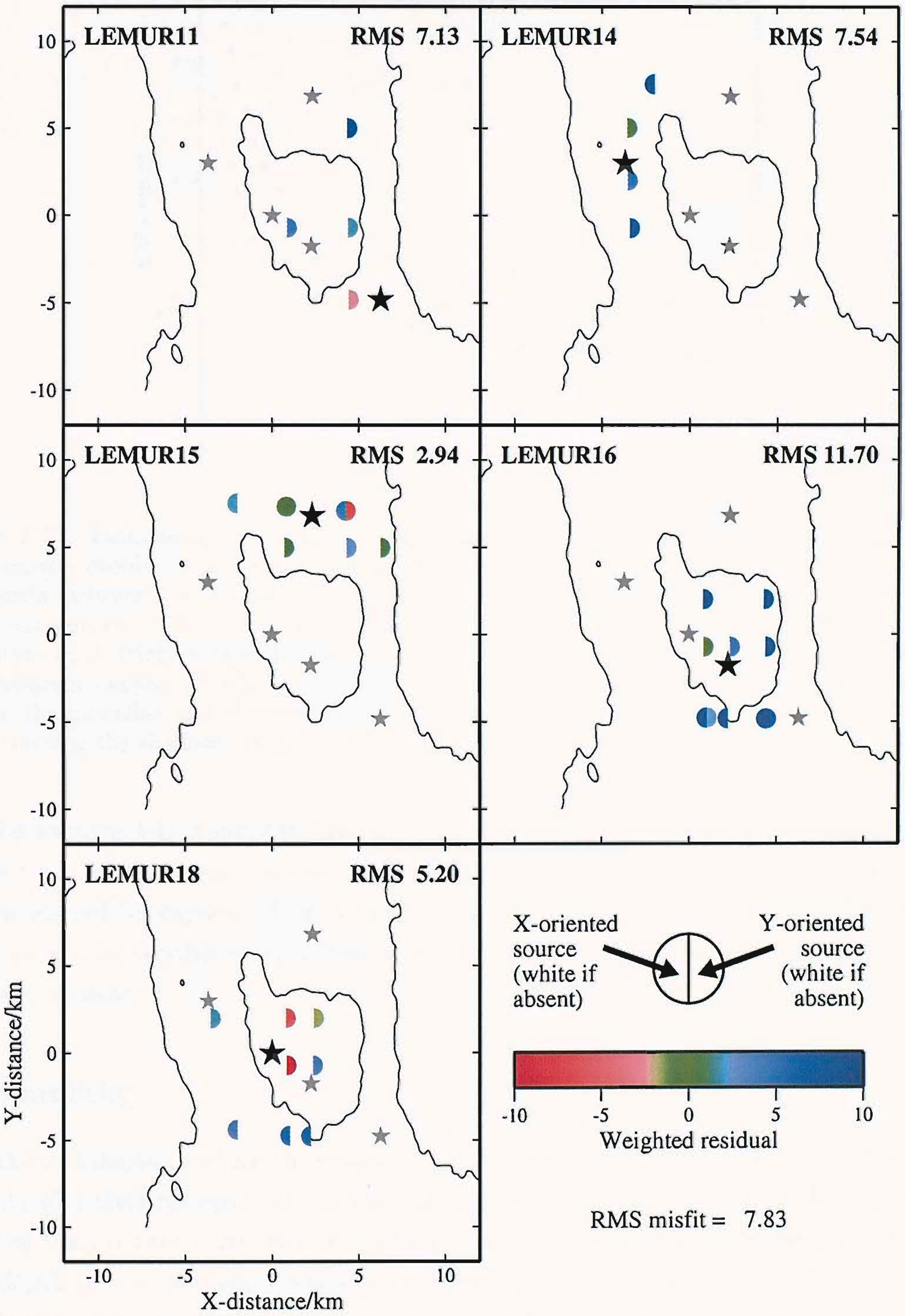

Figure 7.15: Residuals obtained at 5 Hz from modelling of the 3-D resistivity structure illustrated in Figure 7.13. See text for discussion.

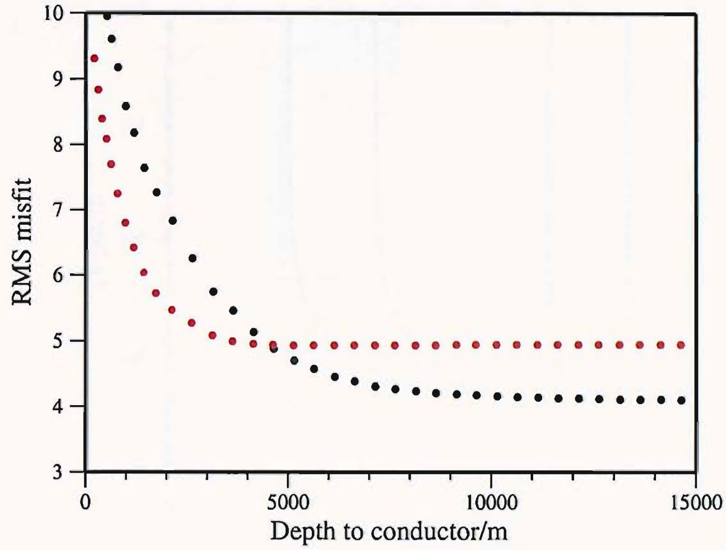

Figure 7.16: Estimating the depth of sensitivity of the data from 1-D modelling. The average 1-D resistivity profile was underlain by a low-resistivity (0.1 Ωm) halfspace at different depths. The RMS misfit between the response calculated from these models and the observed data is plotted at two frequencies: 1 Hz (black dots) and 5 Hz data (red dots). When the conductor is placed at a large depth (right side of the plot), it has little effect on the misfit. When the conductor is at shallower depths, its effect on the modelled response can be seen by the increase in misfit between the modelled and observed data. This increase occurs at shallower depths for the 5 Hz data, reflecting the shallower sensitivity of this higher frequency.

given the average 1-D resistivity profile over the region, obtained from 2-D inversion, it is possible to investigate the class of resistivity anomalies that the Lucky Strike CSEM experiment should be capable of detecting. This highlights questions that the Lucky Strike dataset should be capable of answering when 3-D CSEM modelling techniques have become sufficiently advanced.

Depth sensitivity

The maximum depth to which the data are sensitive was investigated in 1-D by placing a low-resistivity (0.1 Ωm) halfspace at the base of the average resistivity profile. The RMS misfit in the residuals between the observed data and modelled 1-D responses was then calculated as the depth to this conductor was decreased (Figure 7.16). From this, it can be seen that the 1 Hz data are sensitive to a greater depth than the 5 Hz data (as skin depth arguments would suggest).

Taking a significant change in misfit to be ≥5 %, the 1 Hz and 5 Hz data have an average maximum depth sensitivity of ~7.5 km and ~3 km respectively.

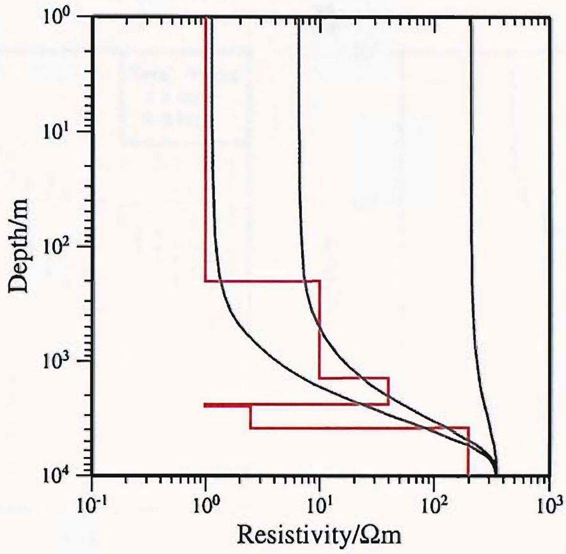

Figure 7.17: Comparison of Lucky Strike resistivities with the resistivity profile obtained at the Reykjanes Ridge. The red line corresponds to the on-axis resistivity profile obtained at the Reykjanes Ridge by MacGregor et al. (1998). The grey curves correspond to the minimum, average and maximum resistivity profiles calculated from 3-D modelling of the Lucky Strike data. See text for discussion.

Sensitivity to the presence of an AMC

A thin axial magma lens (of the order of 100 m thick) at a depth of several kilometers is not within the resolution of this CSEM survey (e.g. MacGregor et al. (1998)). However, MacGregor et al. (1998) were able to resolve the larger mush zone present beneath the AMC at the Reykjanes Ridge.

The final on-axis resistivity profile obtained by MacGregor et al. (1998) can be seen in Figure 7.17, along with the range of resistivity profiles calculated from 3-D modelling of the Lucky Strike data. It can be seen that particularly the lower resistivity profiles, obtained over the summit of the seamount, are in the same range as the Reykjanes model, with the exception of the low resistivity zone corresponding to the region of partial melt at a depth of 2.5 km.

In order to investigate whether the Lucky Strike dataset would be able to detect a resistivity structure similar to the Reykjanes model, synthetic 1 Hz and 5 Hz data were generated from the red profile in Figure 7.17. Both $E_{\parallel}$ and $E_{\perp}$ responses were computed, up to ranges similar to those obtained at Lucky Strike. These synthetic data were then contaminated with centrally distributed Gaussian noise, with an amplitude of 3.6×10^{-15} $\mathrm{VA^{-1}m^{-2}}$ (comparable to the noise levels obtained from 256 s segments of the Lucky Strike data). At short ranges, this underestimates the true uncertainty in the observed data, due to factors such as navigation

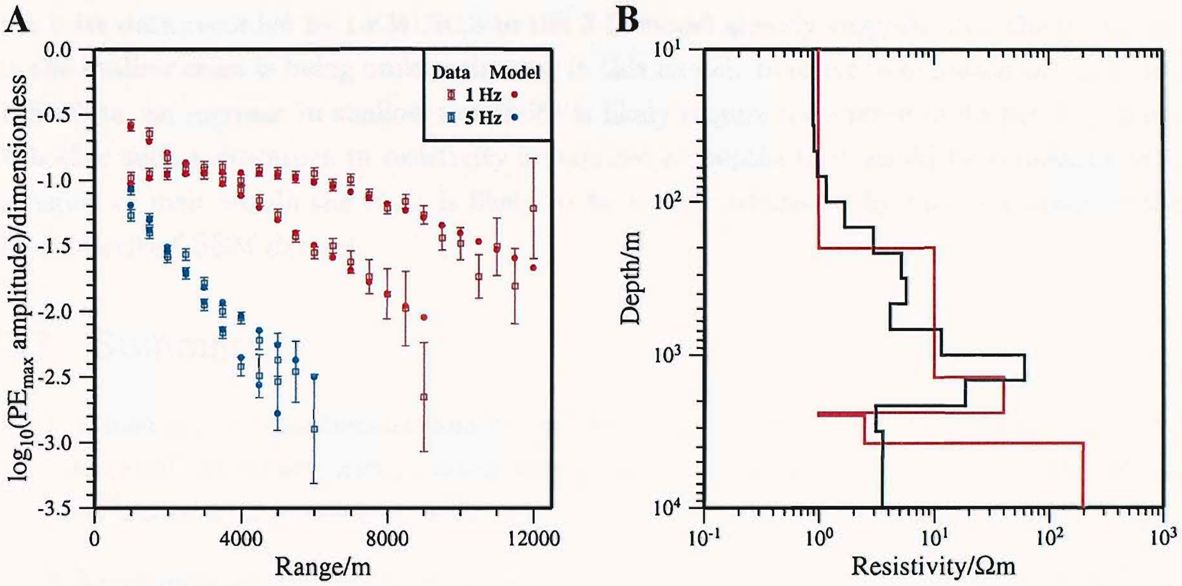

Figure 7.18: 1-D modelling of synthetic data with a low-resistivity mush zone. The on-axis resistivity profile obtained at the Reykjanes Ridge by MacGregor et al. (1998) (red line in Plot ***B***) was used to generate synthetic $E_{\parallel}$ and $E_{\perp}$ data at 1 Hz and 5 Hz with similar noise characteristics, and over a similar range to the Lucky Strike dataset (see text, and data with errorbars in Plot ***A***). The model obtained from a 1-D inversion of the data to and RMS of 1.0 with first derivative smoothing is shown by the black line in ***B***, and the calculated response from this model is shown by the filled circles in ***A***. The downturn in resistivity representing the top of the mush zone has been accurately recovered, to the nearest inverted layer.

errors (see Chapter 4). Therefore, a minimum level of 10 % Gaussian noise was applied to these datapoints.

The results obtained from carrying out a 1-D Occam inversion on the synthetic data, to an RMS misfit of 1.0 can be seen in Figure 7.18. The method of RMS searching based on model bias (Section 5.2.1) was not required here, as the noise in the data was known to be Gaussian.

The inversion has managed to recover convincing evidence for the downturn in resistivity associated with the melt body, even with a very conservative representation of the data coverage available from Lucky Strike.

This strongly suggests that if a laterally extensive melt body existed beneath this region of the Lucky Strike segment, 1- and 2-dimensional modelling would have been able to clearly detect it. It is therefore likely that no such body exists. However, over the region of the central seamount, lower dimensional modelling is not applicable, and the 3-D modelling carried out to date has done little to constrain the vertical resistivity profile. It is therefore conceivable that a less laterally extensive region of melt exists within this volume. Indeed, the bad fit of the 5 Hz data recorded by LEMUR16 to the 3-D model already suggests that the resistivity in the shallow crust is being underestimated in this model. In order to maintain the fit to the 1 Hz data, an increase in shallow resistivity is likely require a decrease in deeper resistivity. Whether such a downturn in resistivity is required at depths that would be consistent with a region of melt within the crust is likely to be a topic addressed by future analysis of the Lucky Strike CSEM dataset.

7.7 Summary

1 Whilst a full 3-dimensional analysis of the Lucky Strike dataset has fallen outside the scope of this dissertation, considerable progress has been made in constraining lateral variations in the resistivity structure.

2 A new method of pseudoimaging residuals from 1-D modelling has been used to highlight lateral resistivity anomalies.

3 These anomalies have been investigated with the 3-D ISIS modelling code.

4 Twenty-seven source locations have been modelled with a single-source model mesh by translating a coarse resistivity structure to locate each source in turn at the model origin.

5 A localised (~2 km in diameter) region of low resistivities exists to the north east of LEMUR16, co-incident with the area of known hydrothermal activity.

6 The high electric field strength recorded by LEMUR16 at 5 Hz over this region requires that shallow crustal resistivities be higher than those at a depth detectable by the 1 Hz data, although further modelling is requred to constrain this resistivity profile.

7 A second region of low resistivities is a requirement of LEMUR14 and 15 data, on the north west flank of the seamount. This is co-incident with a local topographic high. Future cruises to Lucky Strike may wish to study this feature for evidence of hydrothermal activity.

8 Considerably higher crustal resistivities are required by the data off-axis, particularly over the east of the region.

9 1-D inversion has been carried out on synthetic data based on the resistivity profile found on-axis at the Reykjanes Ridge (MacGregor et al. 1998). This illustrates that the Lucky Strike dataset would be able to detect a similar region of partial melt within

the crust. The fact that no such structure has been found during 1- and 2-D modelling strongly suggests that no laterally extensive melt body such as this exists at Lucky Strike. However, the lack of constraint on the vertical resistivity structure under the central region of the seamount means that results obtained to date are not inconsistent with there being a smaller volume of melt in this region.

10 Further 3-dimensional modelling of this dataset should be able to constrain crustal resistivities over the central seamount region to a depth of several kilometers, and may provide evidence for a smaller mush zone.

Chapter 8

Summary, conclusions and suggestions for further work

8.1 Summary and conclusions

The aim of this project was to analyse and interpret the results of the CSEM survey carried out in the region of the Lucky Strike seamount. Specifically, the following subjects were investigated:

1 The MADRIGALS study collected the first CSEM dataset over a region that was expected to have a highly 3-dimensional resistivity structure. How can the currently available 1- and 2-D modelling codes be used to investigate such a large and variable dataset?

2 The Lucky Strike seamount provides the most severe topography sampled to date by a CSEM experiment. How can we quantify the effect that this topography has on the recorded fields, and does the topography influence our ability to resolve resistivity variations within the crust?

3 How can the ISIS 3-dimensional numerical code, and other imaging techniques, be used to constrain the 3-dimensional crustal resistivity structure at Lucky Strike?

4 What can the crustal resistivity tell us about the Lucky Strike hydrothermal system, and how do these results compare to other constraints on the sub-surface structure of the hydrothermal system at Lucky Strike?

Broadly speaking, items 1 to 3 are methodological, whilst item 4 is geological. These two categories are addresses separately below, after a brief summary of the processing applied to the cruise navigation and EM dataset before analysis and interpretation of the data could be carried out.

8.1.1 Data Processing

Due to a malfunction of the acoustic transponder on DASI, existing long baseline navigation software was unable to recover locations for the transmitter during the survey. Recovering an accurate experimental geometry therefore required considerable processing effort, including inversion of the raw acoustic travel times. Processing of the CSEM data progressed in a broadly similar manner to previous datasets, with three notable exceptions. (1) High quality relative phase data provided better constraints on the source transmission frequency, and receiver clock drift. (2) Modelling of the orientation of receiver arms identified two receivers that had non-orthogonal arms when lying on the seabed; recorded signal amplitudes on these instruments were translated into an orthogonal coordinate system. (3) The size of this dataset required that the process of choosing optimum data segment size for frequency transformation, based on signal to noise ratio, was automated, recovering viable data to greater offsets, and with a greater density of datapoints than would have been otherwise possible.

8.1.2 Methodological conclusions

Significant progress was made towards interpreting the Lucky Strike data with the use of 1-D forward modelling and inversion. Even simple best-fit layer over halfspace models illustrated that each receiver had sampled a significantly different resistivity structure in the upper 1 km of the crust. Simple models such as these were also useful in quantifying the 'average' resistivity structure over the region, and suggested that the data can be regarded as showing local shallow variability over a constant deeper resistivity. Such modelling was harder to carry out with the 1-D Occam inversion, as the models fail to converge if an adequate fit to the data is impossible in 1-dimension. Instead, code was developed that allowed smaller subsets of data to be selected for modelling quickly and easily, and the technique of inverted RMS misfit selection based on model bias was fully automated. In this way, converged models could be generated and interpreted in terms of more localised (and therefore more 1-dimensional) resistivity variations.

In the absence of 2-D inversion and 3-D forward modelling codes capable of modelling topography, it was important to quantify the effect that the topography would have on the measured electric fields. This was achieved with the use of 2.5-D forward modelling, where the model mesh could be distorted to follow an average topography for the region. It was found that two orthogonal 2-D topographic models of the seamount were sufficient to delineate most areas of the seafloor where the topography had a strong effect. Regions where the 2-D approximations broke down could be interpreted in light of these results.

It was found that the seamount topography only had a large effect (with respect to other data errors) on about 20 % of the dataset. These portions could be removed without sacrificing overall data coverage, allowing further modelling to be carried out assuming a flat seafloor.

2.5-D forward modelling and inversions were less successful in constraining the resistivity structure of the region. The average resistivity profile from 2.5-D inversion was consistent with the 1-D inversion results; the inversion results also illustrated that the data were sensitive to large lateral resistivity variations in at least the upper 1 km of the crust. However, tradeoffs in the data residuals from the modelling showed that these resistivity anomalies were being inadequately mapped into the 2-dimensional resistivity model. This is illustrated in Figure 8.1, where the 2.5-D inversion results are compared with the final 3-D model (discussed below), averaged along the 2.5-D invariant direction. In conclusion, whilst excellent 2.5-D inversion results were obtained by MacGregor et al. (2001) from data recorded over the (more 2-dimensional) Valu Fa Ridge, it is clear that over resistivity structures as 3-dimensional as the Lucky Strike seamount their use is limited.

Methods of delineating lateral resistivity variations by creating images from the residuals of 1-dimensional forward modelling have also been investigated. Most plots of residuals in this thesis have the data residuals plotted at the source location (e.g. Figure 5.5). This was found to be the most convenient way of quickly identifying the relative fit of portions of the data to the model. However, these plots are of far less use in identifying regions of anomalous resistivity in the crust (with respect to the model used). This is because (1) the calculated residual is really an integrated residual over the region to which the datum is sensitive, and (2) each receiver being modelled requires a separate residual plot (a problem that would have been even worse if all ten receivers had been recovered from the Lucky Strike cruise). Instead, residual 'pseudoimages' were generated, using the simplistic assumption that the data were sensitive to all points in a line between the source and receiver. With the Lucky Strike dataset, this assumption was adequate because much of the variations in the data could be explained by lateral variations in the top 1 km of the crust. However, with a resistivity structure such as that found at the Reykjanes Ridge, where data had sampled lateral resistivity variations over a much greater range of depths, a more accurate measure of data sensitivity would likely be required.

3-D forward modelling was also used to investigate lateral variations in the crustal resistivity structure. The average resistivity profile, obtained from the final 2.5-D resistivity model, was allowed to vary uniformly within 1 km-sided bins over the target area, in a way

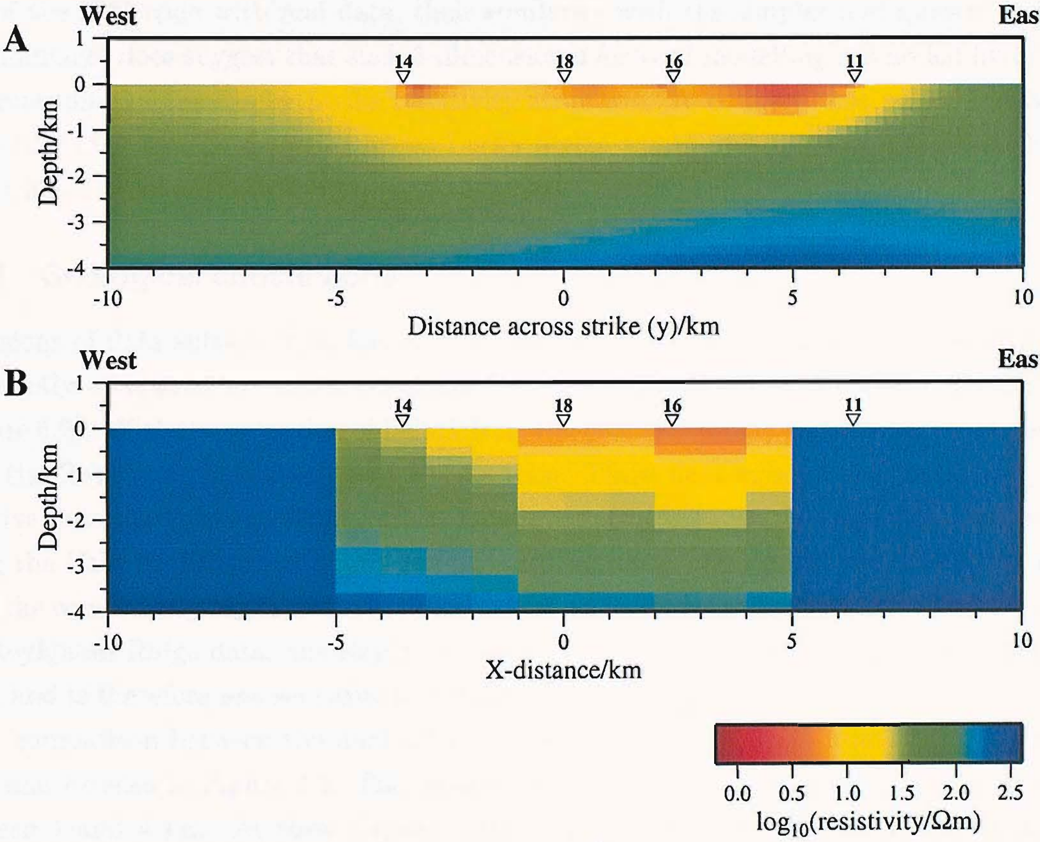

Figure 8.1: A comparison of th 2.5-D inversion results, with an average of the final 3-D model. Plot *A* shows the final 2.5-D inversion model (as Figure 6.15) without subsequent topographic mesh distortion. The model invariant direction is approximately north-south, along the ridge axis. Plot *B* shows a section through the final 3-D model (see section 7.5) to the same scale as *A*. model resistivities have been logarithmically averaged along the 2.5-D invariant direction. This highlights that resistivity anomalies such as the one found around LEMUR16 in *B* are not simply mapped into their along-strike position when modelled in 2.5-D: this anomaly has been incorrectly positioned at y=5 km in *A* due to large tradeoffs in the model residuals.

that was consistent with the 1-D inversion results. A process of iterative forward modelling, guided by the pseudoimages obtained previously, created a resistivity model that significantly reduced the misfit between the 1 Hz data and responses, and removed much of the large-scale structure and the systematic and geographic biasses in the residuals.

Whilst interesting results were obtained from this modelling, and they were the first test of the ISIS code with real data, their similarity with the simpler and quicker to obtain pseudoimages does suggest that such 3-dimensional forward modelling has added little to our understanding of the Lucky Strike resistivity structure. It is likely that an exhaustive 3-D modelling analysis of a dataset such as Lucky Strike would provide more useful results at a time when 3-D inversion codes are available.

8.1.3 Geological conclusions

Inversions of data subsets from four of the receivers generated resistivity profiles that could be directly compared to results obtained from previous CSEM surveys over oceanic crust (Figure 8.2). With the exception of LEMUR15, the profiles broadly lie between those obtained from the Reykjanes Ridge and East Pacific Rise. These data subsets are consistently more resistive than the Valu Fa Ridge profile. This is not surprising, as the andesitic rocks erupted along the Valu Fa Ridge are highly porous and fractured. No significance should be drawn from the consistently higher resistivities obtained at depths greater than 700 m, compared to the Reykjanes Ridge data: the Reykjanes Ridge curve was calculated from higher frequency data, and is therefore less sensitive to the deeper resistivity structure.

A comparison between the final 2.5-D inversion models obtained from Lucky Strike and VFR can be seen in Figure 8.3. The most striking difference in the models are at depths of between 1 and 4 km. At these depths, particularly near the ridge axis, the crust at VFR still has resistivities as low as 4 Ωm. In contrast, the resistivities at the same depth at Lucky Strike are an order of magnitude higher. With the aid of porosity constraints provided by a co-incident seismic study, these high mid-crustal resistivities have been interpreted by MacGregor et al. (2001) as being due to a hot, briney water created during phase separation of the hydrothermal fluids.

Results from geochemical studies of the high temperature hydrothermal discharge at Lucky Strike imply that phase separation is also occurring here, at a depth of at least 1300 m below the seabed (see Chapter 3). At these depths, no on-axis resistivity anomaly has been detected by the Lucky Strike 2.5-D inversion, suggesting that any hot, briney phase present within the crust covers a far smaller lateral extent than observed at the VFR. This is consistent with a more localised hydrothermal heat source, as discussed at the end of the previous chapter.

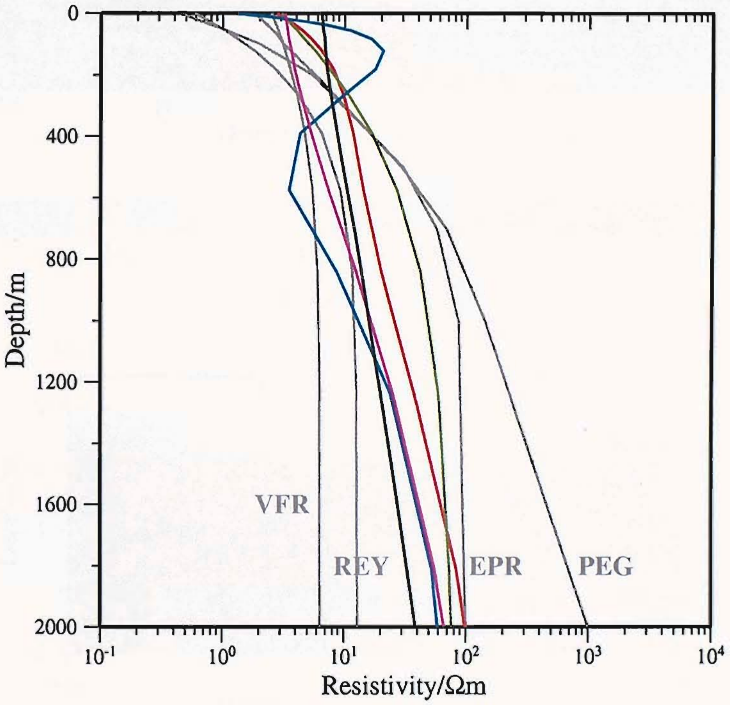

Figure 8.2: Comparison of 1-D inversion results obtained here with those from previous CSEM experiments over oceanic crust. The grey lines are as Figure 1.1. The black line corresponds to the resistivity profile obtained from averaging the 2.5-D inversion results (see Section 7.2). The coloured curves correspond to the results obtained from 1-D inversions of subsets of the Lucky Strike data, as described in Section 5.3. Red: LEMUR11 (as Figure 5.8). Green: LEMUR14 (as Figure 5.7). Blue: LEMUR15 (as Figure 5.9). Purple: LEMUR18 (as Figure 5.10). See text for discussion.

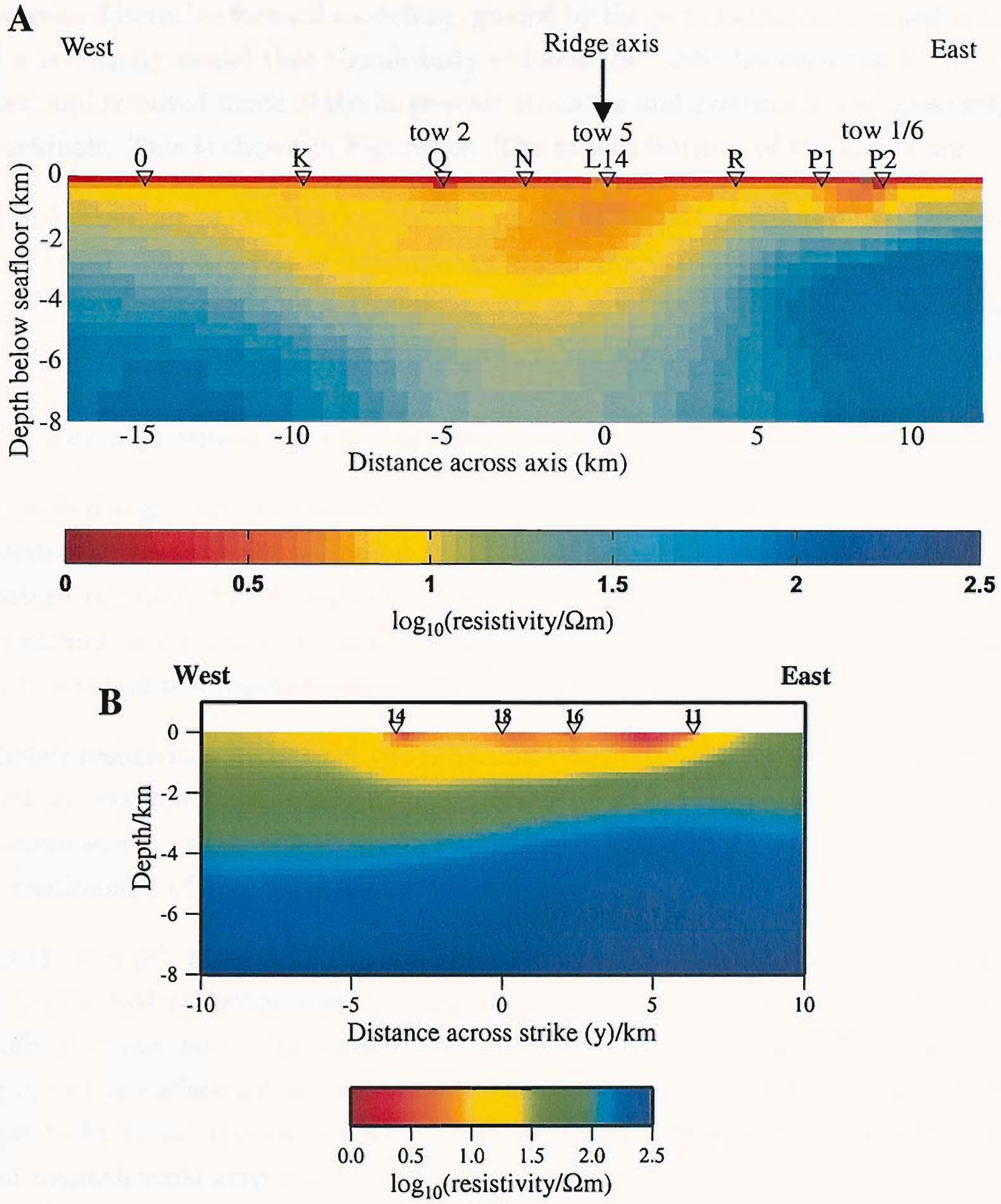

Figure 8.3: Comparison of the 2.5-D model results obtained here with those calculated from the Valu Fa Ridge dataset. ***A***: the result of inverting 1 Hz and 0.25 Hz data from the Valu Fa Ridge to a misfit of RMS 1.9, with no vertical exaggeration, from MacGregor et al. (2001). The model is invariant perpendicular to the page (parallel to the ridge axis). Label positions mark the positions of the tow lines and receivers (see MacGregor et al. (2001)). The top 800 m of the model were prejudiced to converge to a 1-D model derived from inversion of 8 and 24 Hz data, which were more sensitive to the shallow structure. ***B***: The results of inverting 1 and 5 Hz data from Lucky Strike to an RMS misfit of 3.5 (from the same inversion as Plot *B*, Figure 6.15, but without the subsequent topographic distortion of the mesh). The model invariant direction is again parallel to the ridge axis, and the plot is to the same scale as *A*. Note that the colour palettes are similar, but not identical. See text for discussion.

A process of iterative forward modelling, guided by the pseudoimages obtained previously, created a resistivity model that significantly reduced the misfit between the 1 Hz data and responses, and removed much of the large-scale structure and systematic and geographic bias in the residuals. This is shown in Figure 8.4. The salient features of the model are:

1 A region of anomalously low resistivities under the seamount summit (x=2 to 4 km, y=-2 to 1 km). There is a good constraint on this feature at the modelled resolution (1 km-sided elements), as it lies within the centre of the survey area: data from LEMUR16 require there to be a low resistivity region, whilst data from other instruments limit its possible lateral extent. There is good correlation between this feature and the locations of known high temperature hydrothermal venting.

2 A second region of low resistivities co-incident with a small topographic high on the north west flank of the seamount (x=-5 to -1 km and from y=-7 to -2 km). As this feature lies more to the edge of the survey area, modelling to date has provided less constraint on its precise location and lateral extent. However, a low resistivity anomaly in this region is a requirement of data from both LEMURs 14 and 15.

3 Higher resistivities away from the ridge axis. Although there is little constraint on the extreme east and west of the model, the sharp off-axis increase in resistivity around the eastern seamount flank, and the high resistivities to the south west of the seamount are a requirement of data from several receivers.

Features (1) and (3), along with the low resistivity zone identified 7 km along axis from the area of known hydrothermal venting, suggests that high temperature hydrothermal fluids potentially circulate for a considerable distance along the ridge axis, but not off-axis, only venting onto the surface in the region of the seamount summit. Feature (2) is worthy of investigation by future cruises to Lucky Strike, as it may correspond to a hitherto unknown region of hydrothermal activity.

The 5 Hz data, with a greater sensitivity to shallow crustal resisitivities, cannot be fit well with this modelling strategy. In particular the area of low resistivities in the central seamount region required by the 1 Hz data, increases the misfit at 5 Hz, which requires higher shallow resistivities. This anomalously low resistivity is therefore likely to be at a greater depth than the resistivity profiles used in 3-D modelling will allow.

Finally, 1-D inversion of synthetic data investigated the sensitivity of the Lucky Strike dataset to the presence of a region of melt within the crust. It was concluded that the lack of evidence for the presence of such a structure in 1- and 2-D modelling precludes there being a region of melt under the Lucky Strike segment, comparable in size to that found at the

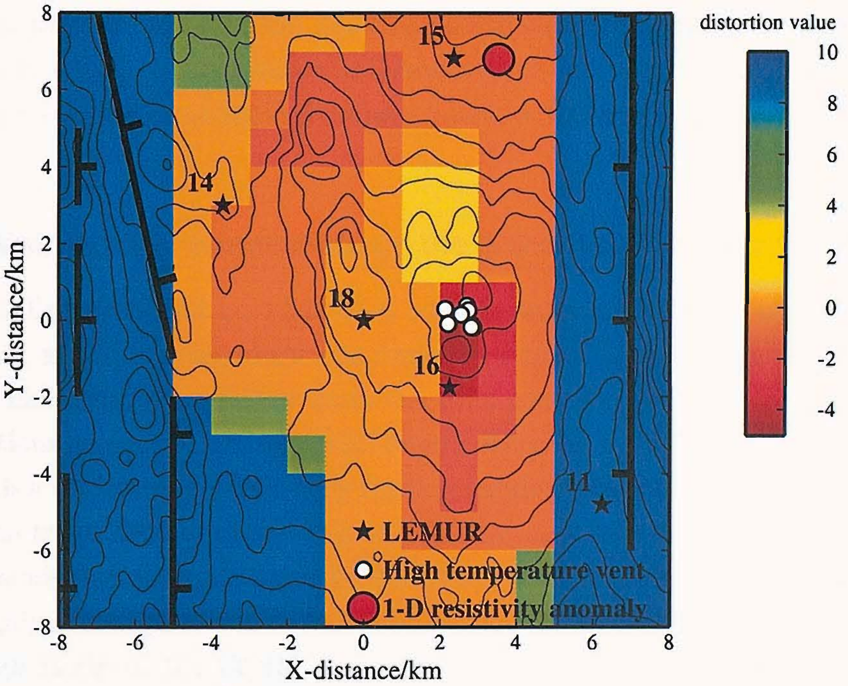

Figure 8.4: The final 3-D resistivity anomaly obtained, defined in terms of a level of distortion *d* from the average 1-D resistivity profile (as Figure 7.12). Also plotted are: locations of LEMUR receivers; the location of the low resistivity zone identified from 1-D inversion (see Figure 5.9); locations of known high temperature hydrothermal venting; and 100 m bathymetry contours, along with an estimate of the positions of the median valley normal faults from this bathymetry. See text for discussion.

Reykjanes Ridge (MacGregor 1999). However, the lack of depth constraint on the resistivity structure under the seamount summit area means that a smaller region of melt may still be detectable with further modelling.

8.2 Further work

It is clear that there is still much work to be done on the Lucky Strike CSEM dataset. Whilst the available data and processing techniques currently allow some of this to be carried out whenever time permits, much of the possible information that could be obtained from the dataset requires either supplementary information, or improved modelling techniques, or both. It is therefore useful to highlight where I believe the greatest opportunities for future work lie.

8.2.1 Obtaining better constraints on the 3-D crustal resistivity structure

The 3-D modelling presented here has been used in order to constrain lateral variations in the ocean crust, at the expense of vertical resolution. In some regions, such as the seamount summit, it is clear that a far better fit to the data could be obtained by investigating the effect of variations in crustal resistivity with depth, using the 3-D ISIS code. However, forward modelling such a volume would be a very time consuming process. This would be made more difficult by the tradeoffs that often exist with CSEM data (such as high resistivities in one region of the model being counteracted by low resistivities in another region) that would have to be thoroughly investigated.

A thorough study of the CSEM data with 3-D modelling will therefore probably not be possible until 3-D inversion codes are available. At the present time, the ISIS code is too slow, and requires too much computer memory for it to be used as the basis for a 3-D inversion code. However, there is still much scope for optimising this code (Flosadóttir & MacGregor 2004), and with future increases in computing power, an ISIS-based inversion code may be feasible in only a few years' time.

Unfortunately, even a 3-D inversion code would, in the forseeable future, only be able to consider a tiny fraction of a dataset the size of the one considered here. This will severely limit the possible resolution of the technique. It seems likely that imaging, rather than modelling, techniques may go some way to solving this problem: the imaging results discussed in Chapter 7 use very simplistic assumptions about the region of data sensitivity, and yet are able to generate useful images of a complicated resistivity structure in seconds.

It is likely that CSEM survey design will have to be re-evaluated in light of new data imaging techniques. In particular, an evenly-spaced array of many ocean bottom receivers, used in conjunction with a uniform grid of tow lines would maximise the number of locations where co-incident data of different source-receiver azimuths would be available.

8.2.2 Relating the resistivity structure to other crustal properties

It is clear that a well-constrained image of the 3-D resistivity structure is not an end in itself: we must be able to relate these resistivity variations to other crustal properties if we are to improve our understanding of crustal formation and the role played by hydrothermal systems. As was discussed in the introduction, the most important properties that need to be constrained are porosity and the interconnectedness of pore spaces, permeability, temperature, hydrothermal fluid salinity, and, where melt is present in the crust, the melt fraction.

MacGregor (1997) showed that where a region of low resistivity is detected that is interpreted as a region of partial melt, considerable progress can be made towards constraining the melt fraction present.

The Hashin-Shtrikman (HS) bounds describe an upper and lower limit on the resistivity of an isotropic two phase medium (Schmeling 1986). In the case of a medium consisting of a liquid phase and a solid phase of much higher resistivity, the upper HS bound (HS^+) describes the case where the liquid forms a fully connected network. Using HS^+, and experimentally determined basaltic melt conductivities, Shankland & Waff (1977) calculated curves of constant effective resistivity for varying melt fraction and temperature. By using these curves in conjunction with the solidus and liquidus temperatures of basalt, determined experimentally by Presnall et al. (1972), MacGregor (1997) calculated a minimum value for the melt fraction of 20–30 %.

In a hydrothermal system, tradeoffs in rock and crustal properties calculated from resistivity alone are far harder to overcome. Considerable progress in this direction has been made by Greer (2001) by combining the results from co-incident seismic and CSEM studies with a joint effective medium (JEM) approach. This technique models fluid inclusions as prolate and oblate spheroids within a resistive groundmass. This allows both porosity and pore interconnectedness, and pore fluid properties such as temperature and salinity to be investigated.

A seismic survey of the Lucky Strike seamount is planned for later in 2004, as part of the MOMAR (MOnitoring the Mid-Atlantic Ridge) research programme. Joint analysis of data from this cruise, in conjunction with a known 3-D crustal resistivity structure, would provide an excellent opportunity for further development of the JEM technique. Funding for a joint PhD studentship between IGPG Paris and the SOC to tackle this subject has recently been granted by the European Union FP6 programme.

Appendix A

Translating from a non-orthogonal linear coordinate system

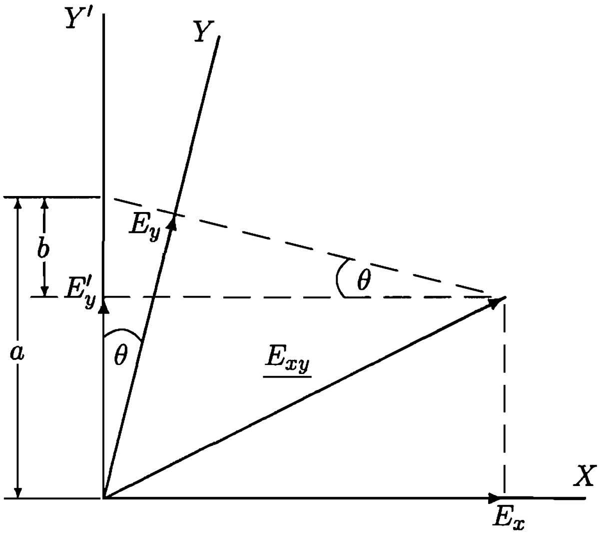

With the two receiver arms oriented an angle θ from orthogonal, along the axes X and Y respectively, a horizontal electric field vector $(\underline{E_{xy}})$ will be recorded as the two amplitudes (E_x, E_y). The transformation of the amplitude E_y into the correct orthogonal amplitude E'_y is equivalent to a coordinate skew along the X-axis of angle $-\theta$. This can be obtained geometrically as follows: –

$$E'_y = a - b \tag{A.1}$$

$$a = \frac{E_y}{cos(\theta)} \tag{A.2}$$

$$b = E_x tan(\theta) \tag{A.3}$$

$$\Rightarrow \qquad E'_y = \frac{E_y - E_x sin(\theta)}{cos(\theta)}. \tag{A.4}$$

Appendix B

MADRIGALS current meter data

The figure on the following page shows a four-day section of the current speeds and directions recorded by the four current meters deployed in a transect across the Lucky Strike survey area (see Figure 3.7 for instrument locations). The frequency content of the current speed data recorded by instrument C4 has been discussed in Section 4.6.2.

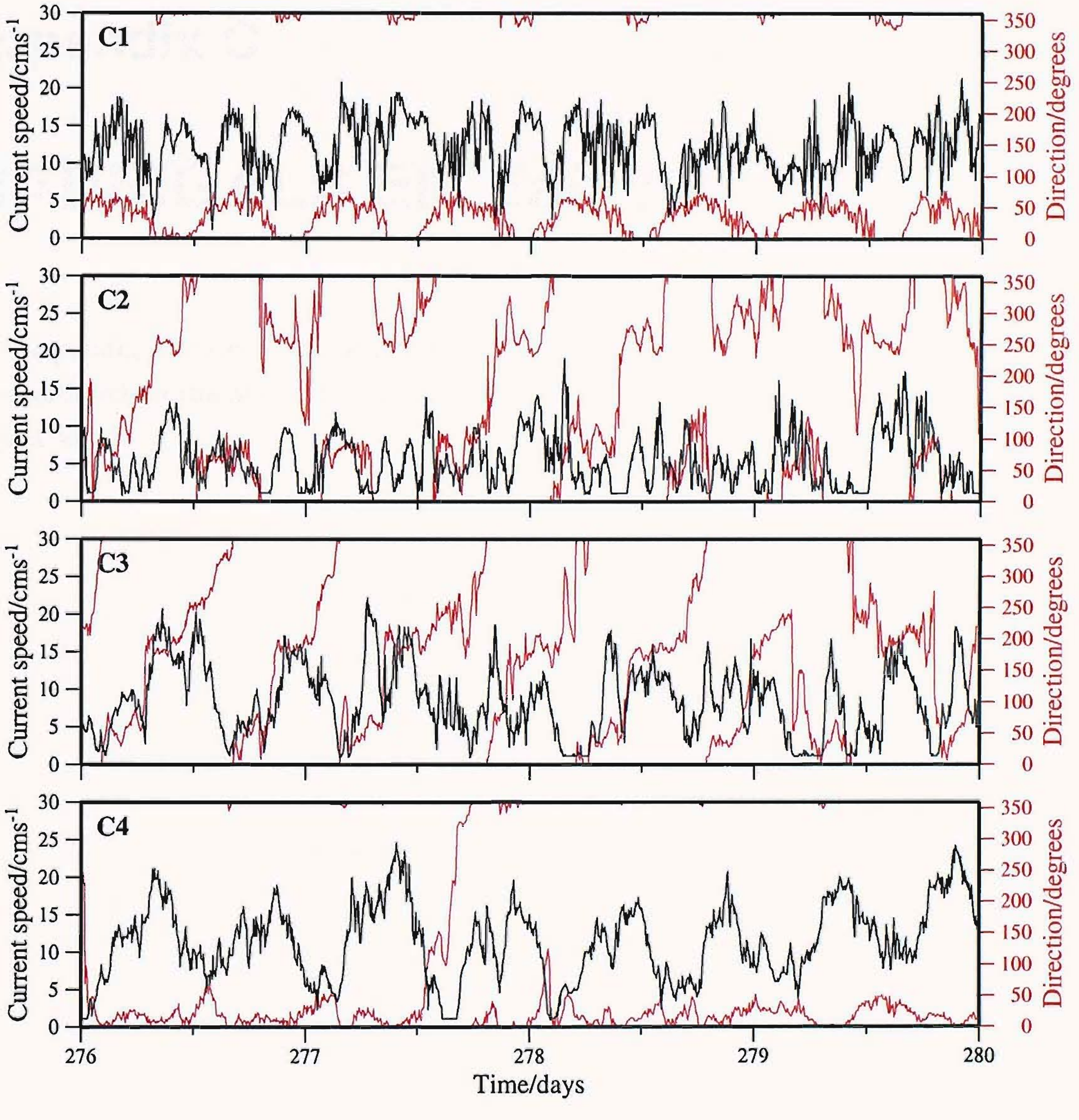

Figure B.1: Data recorded by the four current meters (see previous page for more information).

Appendix C

MADRIGALS EM dataset

This appendix contains plots of the one of the three final processed datasets created from data collected on the MADRIGALS cruise. The target minimum signal to noise ratio of this dataset was 5.

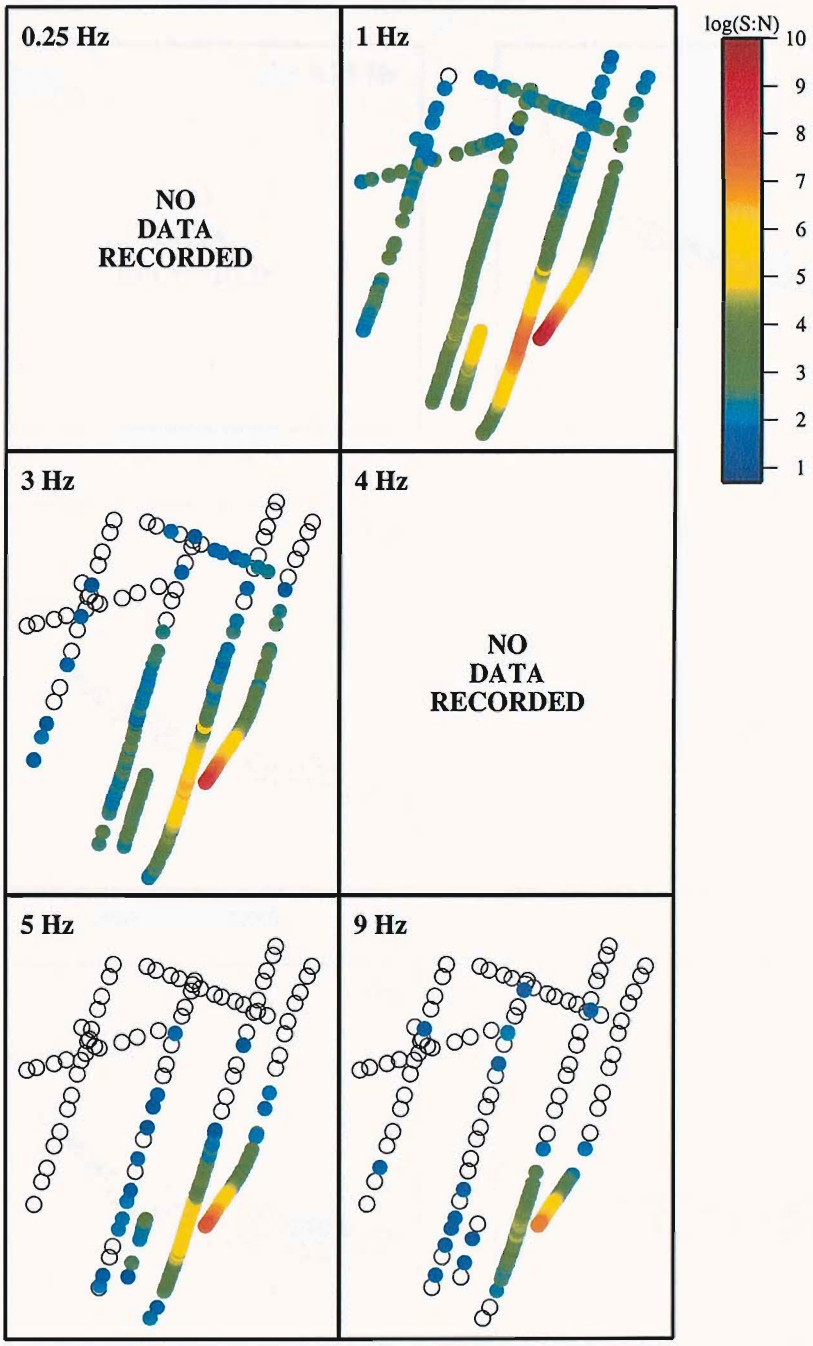

Figure C.1: A plan view of the data coverage obtained by LEMUR11. Data points for the three fundamental transmission frequencies, 0.25 Hz, 1 Hz and 4 Hz, as well as the third, fifth and ninth harmonic of the 1 Hz transmission are plotted at the correct source positions. The dataset with a target signal to noise ratio of 5 or better was used. Data with a greater signal to noise ratio than 5 are plotted with the appropriate colour (see scale). Data with a lower ratio are represented by a black circle. This data was generally removed before modelling was carried out. As LEMUR11 was a LEMUR'95 instrument, it had ceased recording before the 0.25 Hz and 4 Hz transmission tows. Plot region: 32°23'W to 32°11'W and 37°11.5'N to 37°24'N.

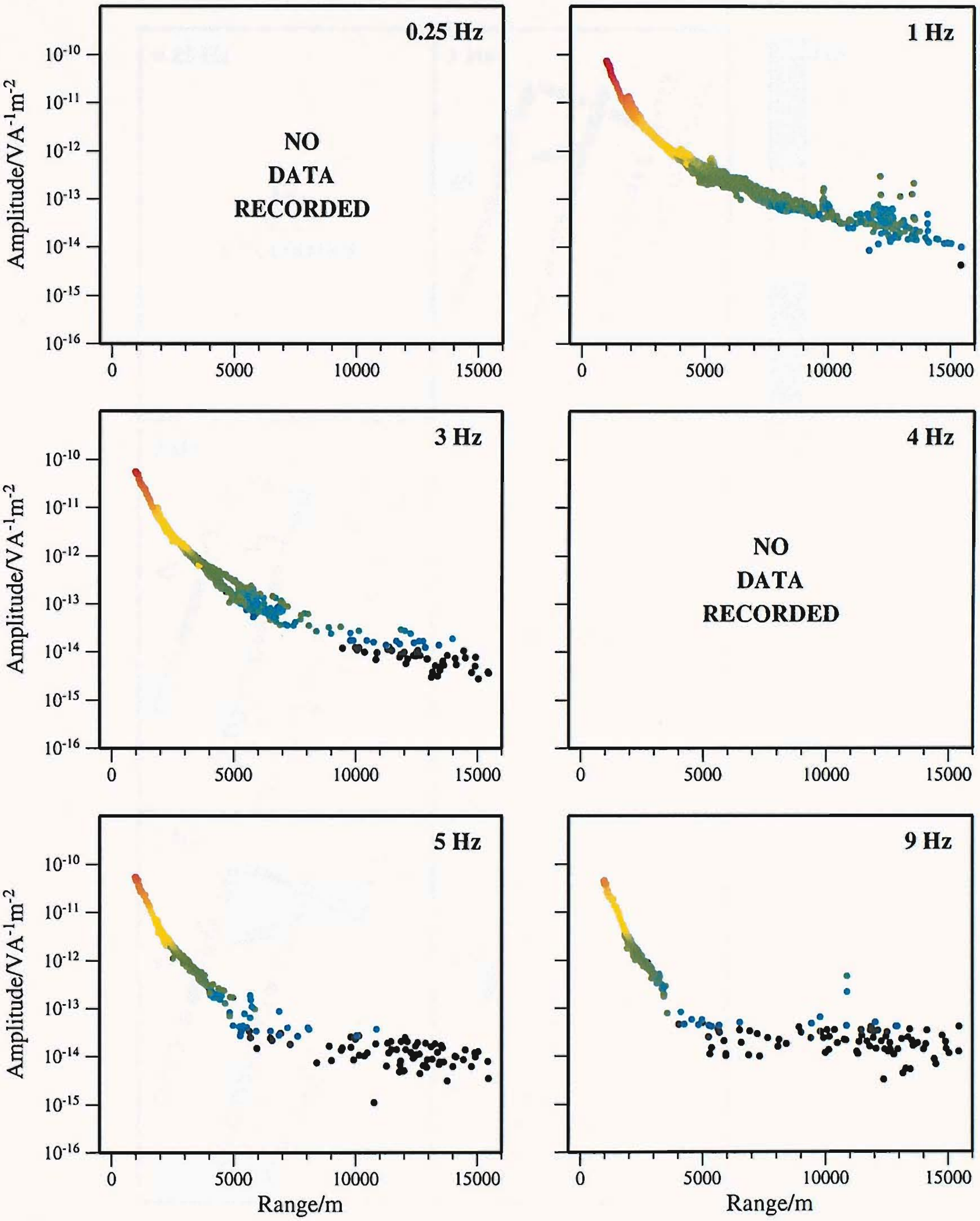

Figure C.2: Plots of PE_{max}amplitude against range for all data in Figure C.1. Data with a signal to noise ratio lower than 5 are plotted in black.

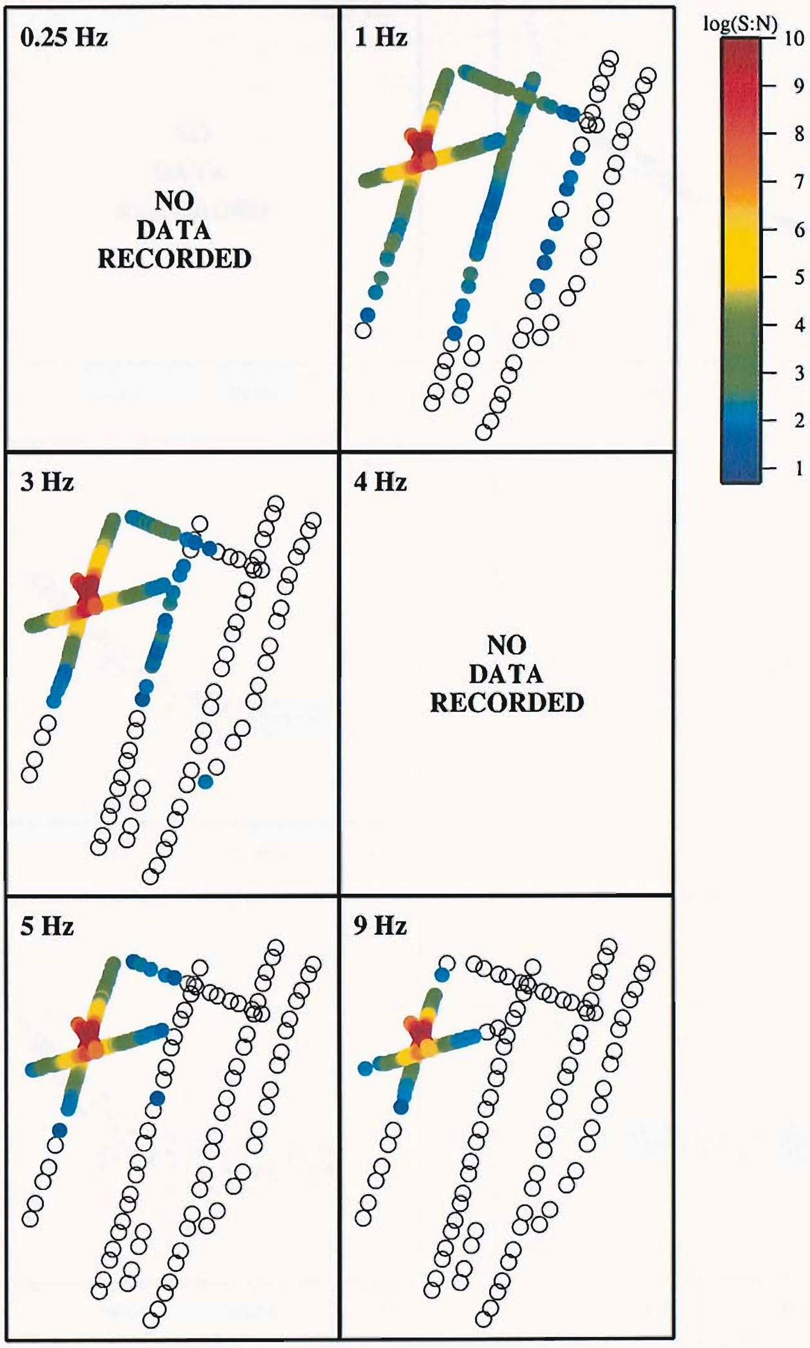

Figure C.3: A plan view of the data coverage obtained by LEMUR14. See the caption of Figure C.1 for more information. Plot region: 32°23'W to 32°11'W and 37°11.5'N to 37°24'N.

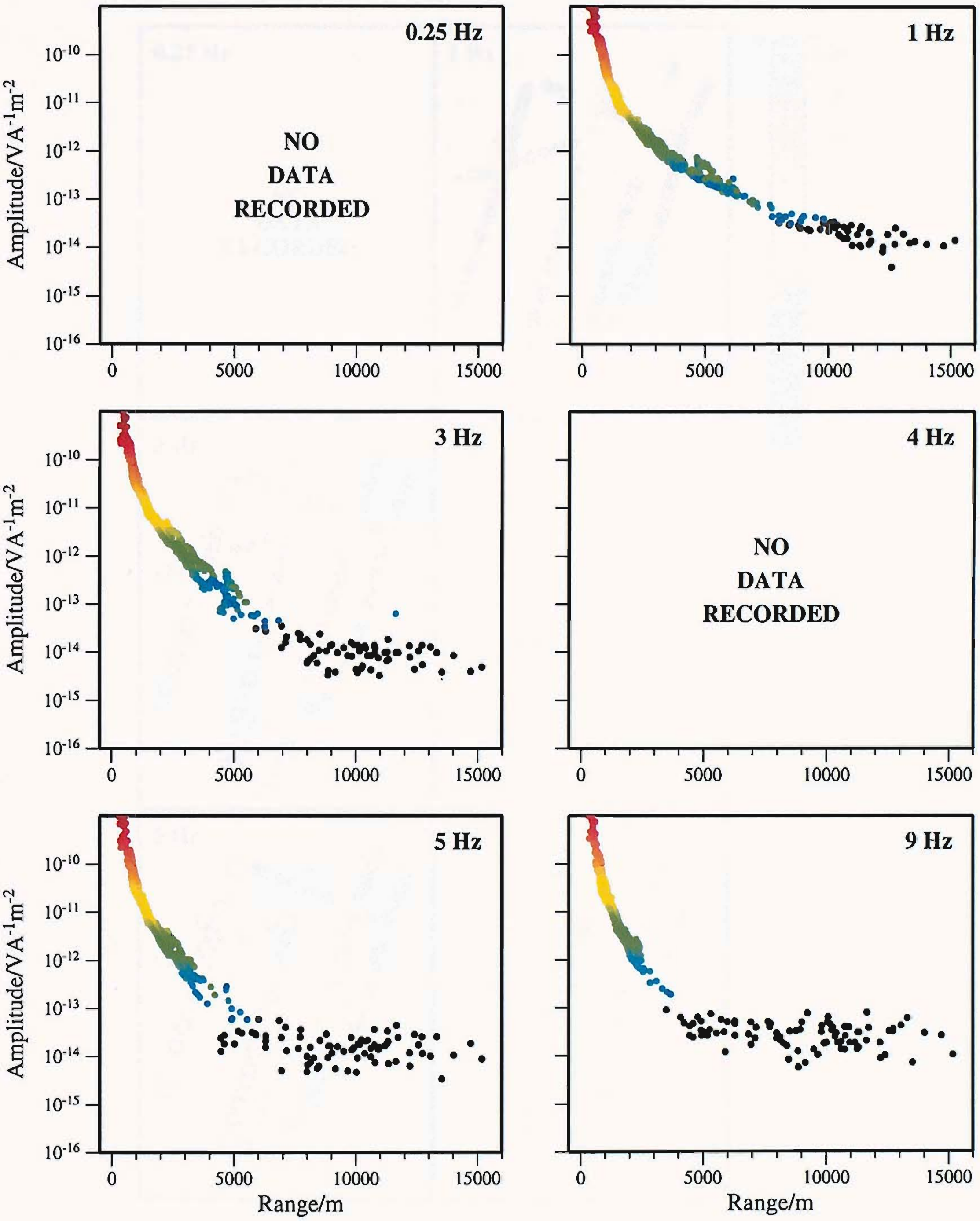

Figure C.4: Plots of PE_{max}amplitude against range for all data in Figure C.3. Data with a signal to noise ratio lower than 5 are plotted in black.

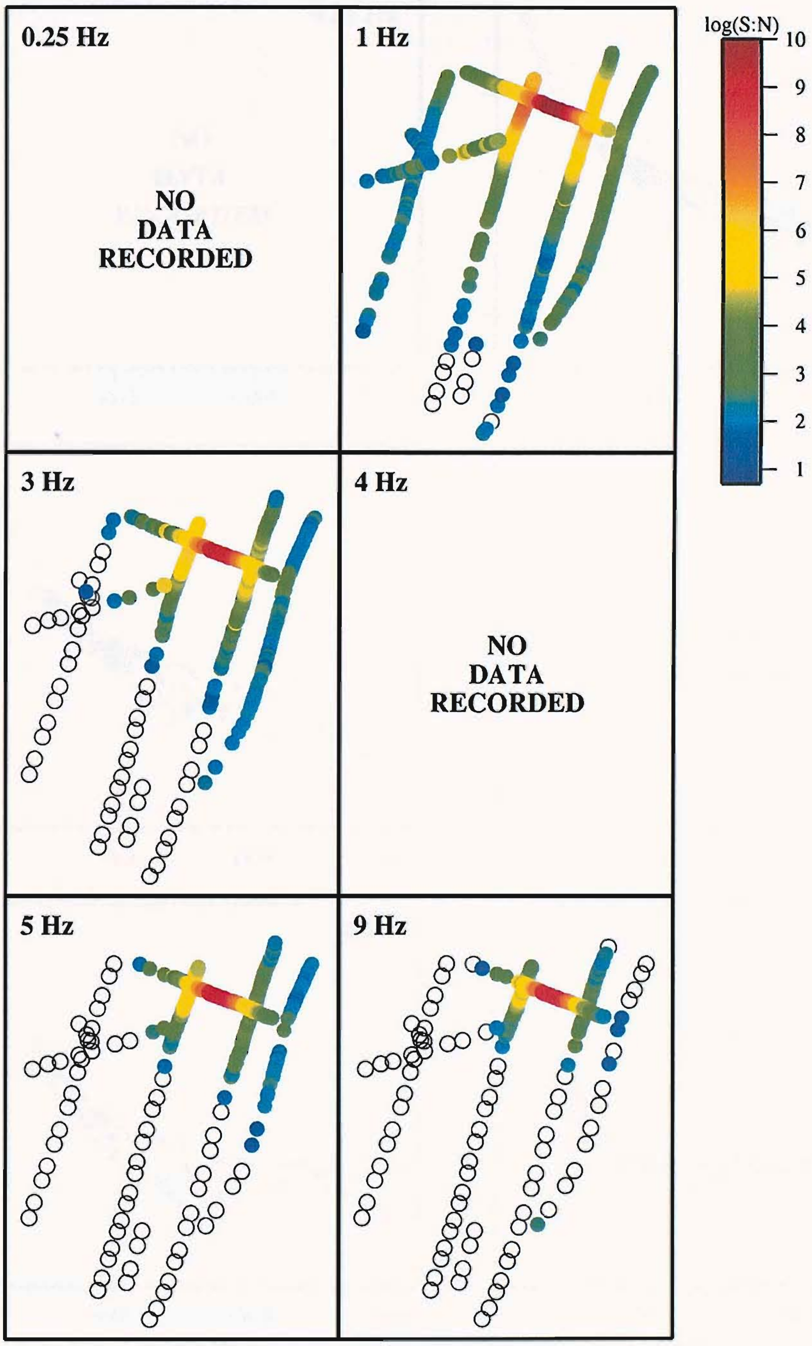

Figure C.5: A plan view of the data coverage obtained by LEMUR15. See the caption of Figure C.1 for more information. Plot region: 32°23'W to 32°11'W and 37°11.5'N to 37°24'N.

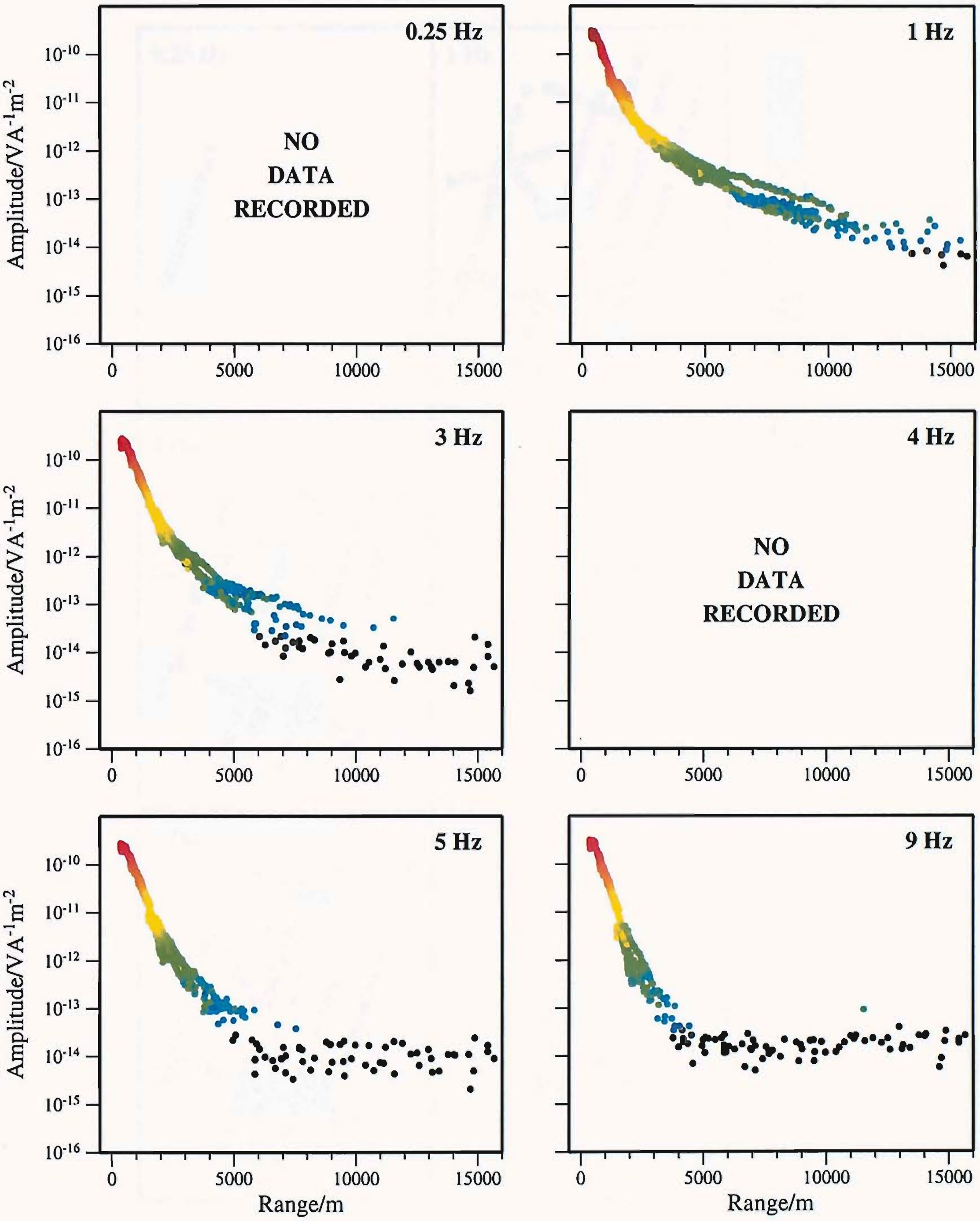

Figure C.6: Plots of PE_{max}amplitude against range for all data in Figure C.5. Data with a signal to noise ratio lower than 5 are plotted in black.

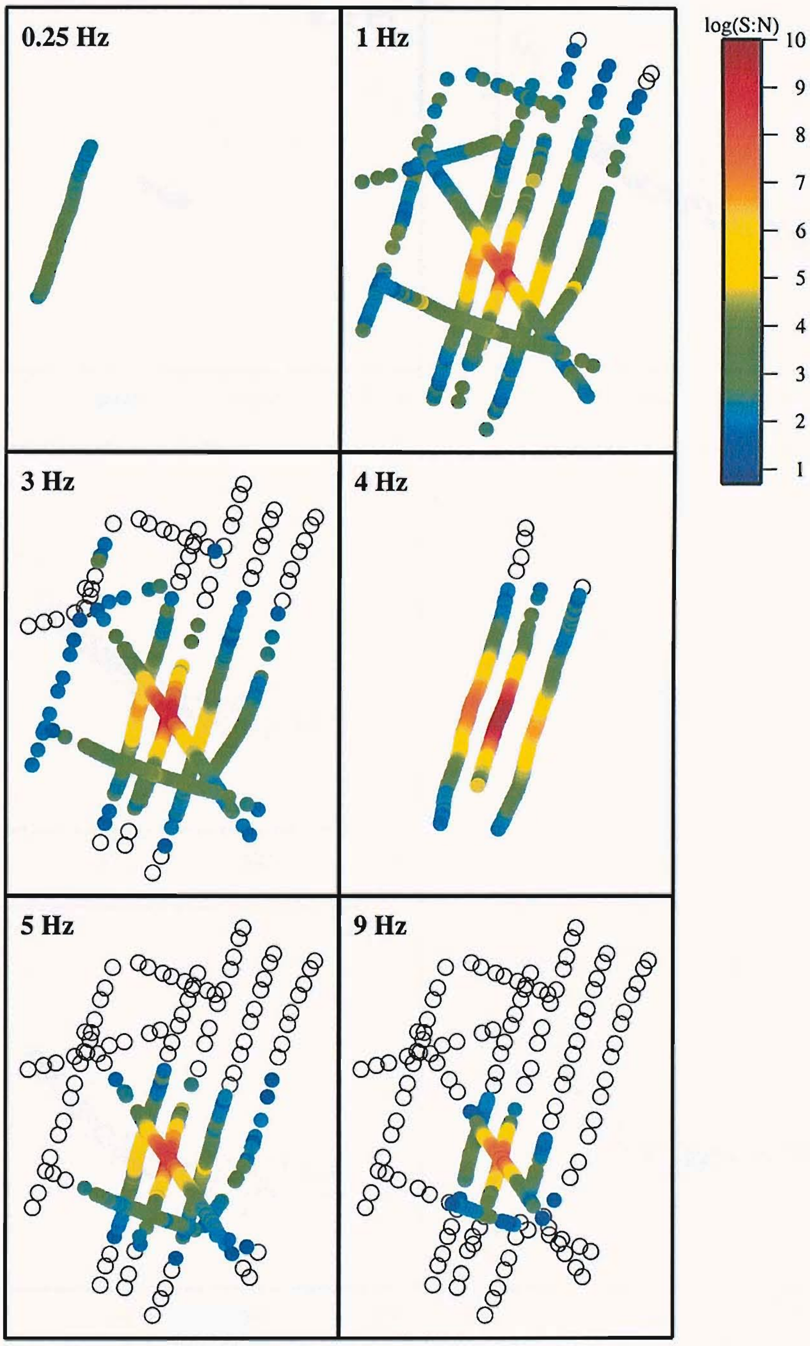

Figure C.7: A plan view of the data coverage obtained by LEMUR16. See the caption of Figure C.1 for more information. Plot region: 32°23'W to 32°11'W and 37°11.5'N to 37°24'N.

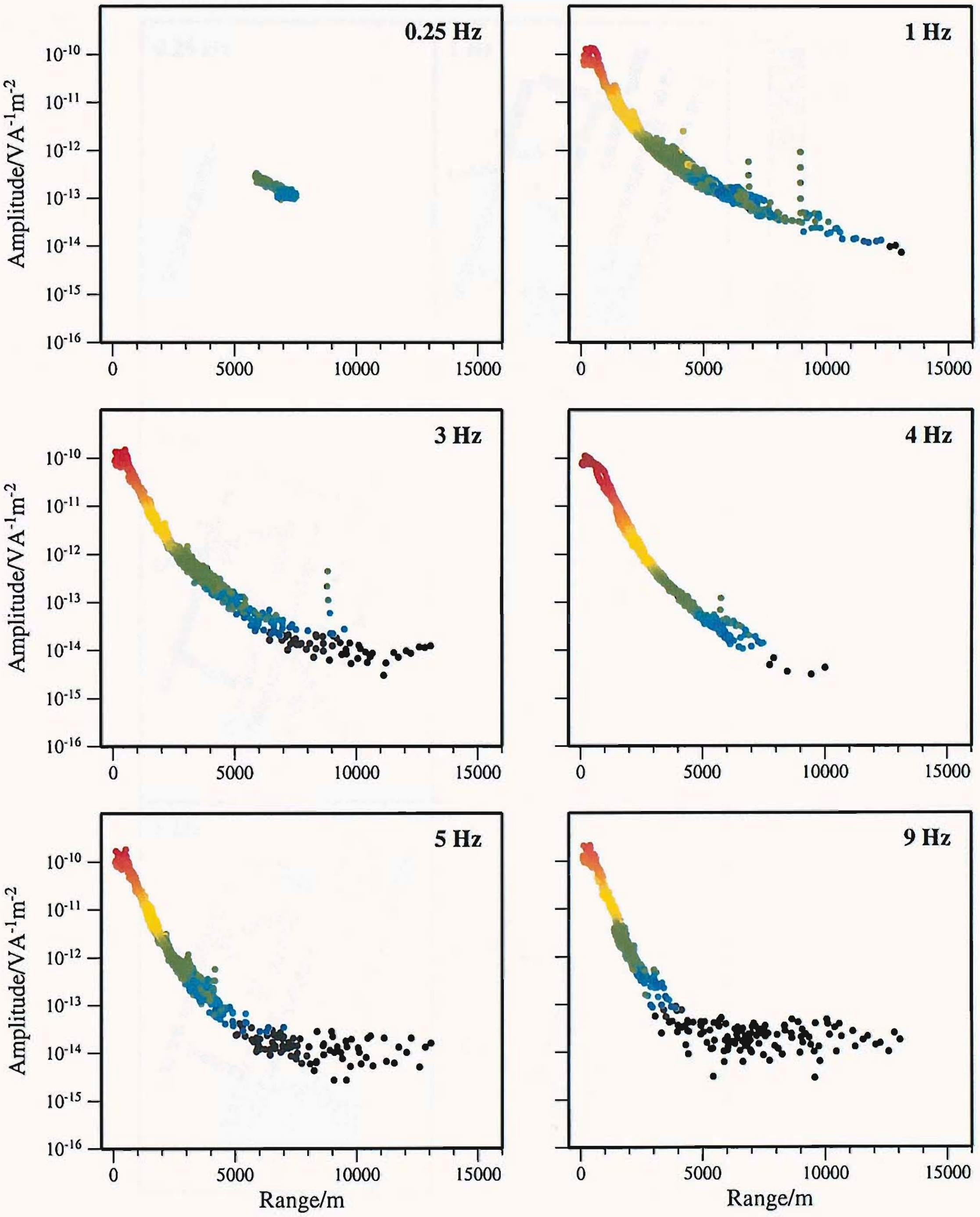

Figure C.8: Plots of PE_{max}amplitude against range for all data in Figure C.7. Data with a signal to noise ratio lower than 5 are plotted in black.

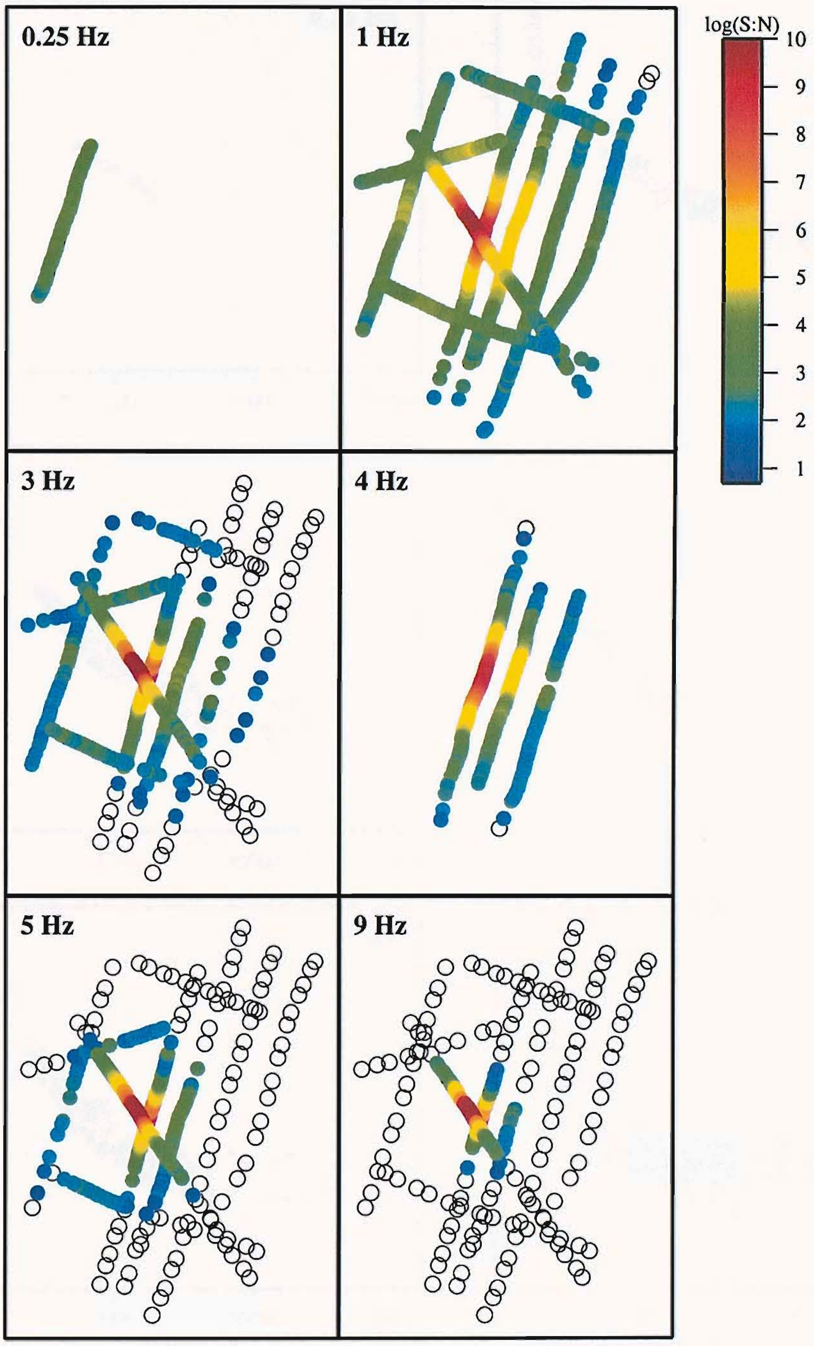

Figure C.9: Plan views of the data coverage obtained by LEMUR18. See the caption of Figure C.1 for more information. Plot region: 32°23'W to 32°11'W and 37°11.5'N to 37°24'N.

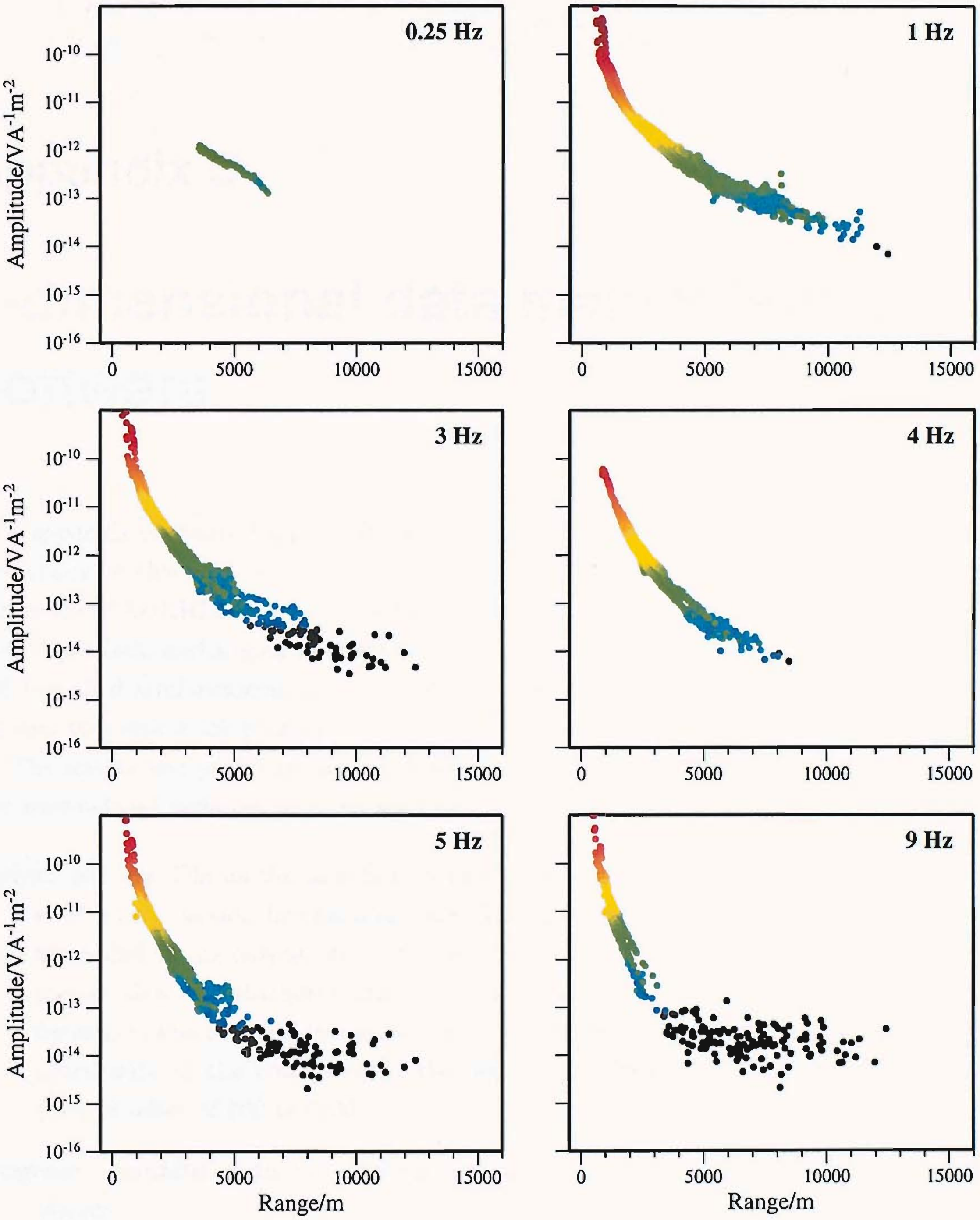

Figure C.10: Plots of PE_{max} amplitude against range for all data in Figure C.9. Data with a signal to noise ratio lower than 5 are plotted in black.

Appendix D

1-dimensional data manipulation software

This appendix contains details of the auxiliary shell scripts and fortran90 programs written specifically for this PhD project to process the full EM datasets generated from data collected during the MADRIGALS cruise (see Chapter 4), in order to model in 1-D. Shell scripts are inter-dependent, exchanging user-defined variables, which allow data subsets to be obtained and modelled semi-automatically. Scripts also generate various plots of the data, allowing the user to monitor job progress.

The scripts and programs are listed below, along with a general description of their job. The user-defined variables required are listed within each script, or program source code.

Script: ***get_occ*** Obtain the user-defined data subset in the form required by the Constable et al. (1987) occam inversion routine. Two columns containing source UTM position are added to the output occam file in order to reconstruct the experimental geometry in plan view for subsequent misfit analysis. Data may be chosen based on transmission frequency, line number, transmitter azimuth and relative position (e.g. only select 1 Hz radial data to the north-west of the receiver, on transmission tow 1, with a source-receiver offset of 900 to 6000 m).

Program: ***combine_data*** Combine datafiles generated by several different invocations of *get_occ*.

Program: ***remove_outlier*** Remove individual datapoints as specified, from the output occam file.

Program: ***get_occ_files*** Generate the other files required by the occam inversion. User can define such options as the type of regularisation applied to the data, and target RMS.

Script: ***run_occ*** Carry out an inversion on the data generated above.

Script: ***rms_search*** Automatically carry out a series of inversions in order to minimise the bias in the generated residuals. The data is initially inverted to a very small target RMS of 0.001. Whilst the inversion is unlikely to be able to reach this RMS, the misfit reached after 60 iterations provides a good lower bound on the possible misfits at which the inversion will converge. From this minimum, the RMS is increased by some increment (generally 0.1) over a specified range (generally up to 1 or 2 above the minimum RMS), with an inversion carried out at each stage. The code then chooses the maximum RMS at which the slope of the residuals is not significantly different from zero, and runs a final inversion at this level. In the absence of an RMS with zero slope on the residuals, the RMS with the minimum slipe is chosen. Finally, results from the process are displayed graphically.

Script: ***constrain_model*** Call *rms_search* several times, each time with data of a lower transmission frequency. After each invocation of *rms_search*, the user may specify a depth to which the subsequent inversions should be constrained to the resistivity profile obtained.

References

Anderson, R. N. & Zoback, M. D. (1982), 'Permeability, underpressures, and convection in the oceanic crust near the costa-rica rift, eastern equatorial pacific', *Journal of Geophysical Research* **87**(B4), 2860–2868.

Archie, G. E. (1942), 'The electrical resistivity log as an aid in determining some reservoir characteristics', *Journal of Petroleum Technology* **5**, 1–8.

Babcock, J. M., Harding, A. J., Kent, G. M. & Orcutt, J. A. (1998), 'An examination of along-axis variation of magma chamber width and crustal structure on the East Pacific Rise between 13^o30N and 12^o20N', *Journal of Geophysical Research* **103**, 30451–30467.

Bannister, P. R. (1984), 'New simplified formulas for ELF subsurface-to-subsurface propagation', *IEEE Journal of Oceanic Engineering* **OE-9**, 154–163.

Barth, G. A. & Mutter, J. C. (1996), 'Variation in oceanic crustal thickness and structure: multichannel seismic reflection results from the northern East Pacific Rise', *Journal of Geophysical Research* **101**, 17951–17975.

Becker, K., Sakai, H., Adamson, A. C., Alexandrovich, J., Alt, J. C., Anderson, R. N., Bideau, D., Gable, R., Herzig, P. M., Houghton, S., Ishizuka, H., Kawahata, H., Kinoshita, H., Langseth, M. G., Lovell, M. A., Malpas, J., Masuda, H., Merrill, R. B., Morin, R. H., Mottl, M. J., Pariso, J. E., Pezard, P., Phillips, J., Sparks, J. & Uhlig, S. (1989), 'Drilling Deep into Young Oceanic Crust, Hole-504b, Costa-Rica Rift', *Reviews of Geophysics* **27**(1), 79–102.

Billings, S. D. (1994), 'Simulated annealing for earthquake location', *Geophysical Journal International* **118**, 680–692.

Bischoff, J. L. & Rosenbauer, J. (1985), 'An empirical equation of state for hydrothermal seawater (3.2 percent NaCl)', *American Journal of Science* **285**, 725–763.

Cannat, M., Briais, A., Deplus, C., Escartin, J., Georgen, J., Lin, J., Mercouriev, S., Meyzen, C., Muller, M., Pouliquen, G., Rabain, A. & da Silva, P. (1999), 'Mid-Atlantic Ridge-Azores hotspot interactions: Along-axis migration of a hotspot-derived event of enhanced magmatism 10 to 4 ma ago.', *Earth and Planetary Science Letters* **173**, 257–269.

Cannat, M., Cann, J. & Maclennan, J. (in prep 2004), Some hard rock constraints on the heat supply to mid-ocean ridges, *in* J. Lin & C. German, eds, 'Thermal regime of ocean ridges and dynamics of hydrothermal circulation', AGU monograph.

Chave, A. D. & Cox, C. S. (1982), 'Controlled electromagnetic sources for measuring electrical conductivity beneath the oceans, 1. Forward problem and model study', *Journal of Geophysical Research* **87**, 5327–5538.

Chen, Y. S. & Morgan, W. J. (1990), 'Rift-valley no rift-valley transition at mid-ocean ridges', *Journal of Geophysical Research* **95**, 17571–17581.

Collier, J. S. & Singh, S. C. (1997), 'Detailed structure of the top of the melt body beneath the East Pacific Rise at 9^o40'N from waveform inversion of seismic reflection data', *Journal of Geophysical Research* **102**, 20287–20304.

Colodner, D. C., Lin, J., Von Damm, K., Buttermore, L., Kozlowski, R., Charlou, J. L., Donval, J. P., Wilson, C. & the Lucky Strike Team (1993), 'Chemistry of Lucky Strike hydrothermal fluids: initial results', *EOS* **74**, 99.

Constable, S. C. & Cox, C. S. (1996), 'Marine controlled source electromagnetic sounding II: The PEGASUS experiment', *Journal of Geophysical Research* **101**, 5519–5530.

Constable, S. C., Parker, R. L. & Constable, C. G. (1987), 'Occam's inversion: a practical algorithm for generating smooth models from electromagnetic data', *Geophysics* **52**, 289–300.

Cooper, M. J., Elderfield, H. & Schultz, A. (2000), 'Diffuse hydrothermal fluids from Lucky Strike hydrothermal vent field: Evidence for a shallow conductively heated system', *Journal of Geophysical Research* **105**(B8), 19369–19375.

Corliss, J. B., Dynond, J., Gordon, L. I., Edmond, J. M., Von Herzen, R. P., Ballard, R. D., Green, K., Williams, D., Bainbridge, A., Crane, K. & van Andel, T. H. (1979), 'Submarine thermal springs on the Galapagos Rift', *Science* **203**, 1073–1083.

Cox, C., Filloux, F. & Larsen, J. (1970), Electromagnetic studies of ocean current and electrical conductivity below the ocean floor, *in* A. Maxwell, ed., 'The Sea', Vol. 4, Interscience, New York, pp. 637–693.

Cox, C., Constable, S., Chave, A. & Webb, S. (1986), 'Controlled-source electromagnetic sounding of the oceanic lithosphere', *Nature* **320**, 52–54.

Crawford, W. C., Webb, S. C. & Hildebrand, J. A. (1991), 'Seafloor compliance observed by long-period pressure and displacement measurements', *Journal of Geophysical Research* **96**, 16151–16160.

de Groot-Hedlin, C. & Constable, S. (1990), 'Occam's inversion to generate smooth, 2-dimensional models from magnetotelluric data', *Geophysics* **55**, 1613–1624.

Detrick, R. S., Buhl, P., Vera, E., Mutter, J., Orcutt, J., Madsen, J. & Brocher, T. (1987), 'Multi-channel seismic imaging of a crustal magma chamber along the East Pacific Rise', *Nature* **326**, 35–42.

Detrick, R., Collins, J. & Swift, S. (1994), 'In situ evidence for the nature of the layer 2/3 boundary in oceanic crust', *Nature* **370**, 288–290.

Detrick, R. S., Needham, H. D. & Renard, V. (1995), 'Gravity anomalies and crustal thickness variations along the Mid-Atlantic ridge between 33°N and 40°N', *Journal of Geophysical Research* **100**, 3767–3787.

Dziak, R., Fox, C., Smith, D., Bohnensteihl, D., Tolstoy, M., Matsumoto, H., Haxel, J., Fornari, D., Shank, T. & Fowler, M. (2003), 'Evidence of a probable magmatic episode at the Lucky Strike segment, Mid-Atlantic Ridge, March 2001', *Geophysical Research Abstracts* **5**.

Edmond, J. M., Measures, C., McDuff, R. E., Chan, L. H., Collier, R., Grant, B., Gordon, L. I. & Corliss, J. B. (1979), 'Ridge crest hydrothermal activity and the balances of major and minor elements in the ocean: The Galapagos data', *Earth and Planetary Science Letters* **46**, 1–18.

Edmonds, H., Michael, P., Baker, E., Connelly, D., Snow, J., Langmuir, C., Dick, H., Muhe, R., German, C. & Graham, D. (2003), 'Discovery of abundant hydrothermal venting on the ultraslow-spreading Gakkel Ridge in the Arctic', *Nature* **421**, 252–256.

Eidesmo, T., Ellingsrud, S., MacGregor, L. M., Constable, S., Sinha, M. C., Johansen, S., Kong, F. N. & Westerdahl, H. (2002), 'Sea Bed Logging (SBL), a new method for remote and direct identification of hydrocarbon filled layers in deepwater areas', *First Break* **20**, 144–152.

Elderfield, H. & Schultz, A. (1996), 'Mid-ocean ridge hydrothermal fluxes and the chemical composition of the ocean', *Annual Review of Earth and Planetary Sciences* **24**, 191–224.

Ellingsrud, S., Eidesmo, T., Johansen, S., Sinha, M. C., MacGregor, L. M. & Constable, S. (2002), 'Remote sensing of hydrocarbon layers using sea-bed logging (SBL): Results of a cruise offshore West Africa', *The Leading Edge* **12**, 972–982.

Ellis, D. V., Schweitzer, J. S. & Ullo, J. J. (1987), 'Nuclear techniques for subsurface geology', *Annual Review of Nuclear and Particle Science* **37**, 213–241.

Escartin, J., Cannat, M., G, P., Rabain, A. & Lin, J. (2001), 'Constraints on the interaction between the Mid-Atlantic Ridge and the Azores hotspot from bathymetry and gravity (36-39°N)', *Journal of Geophysical Research* **106**, 21719–21736.

Evans, R. L., Constable, S. C., Sinha, M. C., Cox, C. S. & Unsworth, M. J. (1991), 'Upper Crustal Resistivity Structure of the East Pacific Rise near 13°N', *Geophysical Research Letters* **18**(10), 1917–1920.

Evans, R. L., Sinha, M. C., Constable, S. C. & Unsworth, M. J. (1994), 'On the electrical nature of the axial melt zone at 13°N on the East Pacific Rise', *Journal of Geophysical Research-Solid Earth* **99**(B1), 577–588.

Everett, M. E. (1990), Active electromagnetics at the mid-ocean ridge, PhD thesis, University of Toronto.

Flosadóttir, A. H. (1990), The response of the oceanic lithosphere to electromagnetic controlled source transmitters modeled using local spectral representation, PhD thesis, UCSD.

Flosadóttir, A. H. & MacGregor, L. M. (2004), 'Induction Sources In the Sea: a model code for oceanic and controlled sources', *Journal of Geophysical Research* **submitted**.

Fornari, D. J., Humphris, S. E. & et al. (1996), 'Near-bottom investigations in the Lucky Strike segment-MAR 37°N using the fiber optic tethered vehicles of the UNOLS national deep submergence facility: ROV Jason, ARGO-II and the DSL-120 kHz sonar', *EOS* **77**, F669.

Fouquet, Y. (1997), 'Where are the large hydrothermal sulphate deposits in the oceans?', *Philosophical transactions of the Royal Society of London* **355**, 437–441.

Fouquet, Y., Charlou, J. L., Costa, I., Donval, J. P., Radford-Knoery, J., Pell, H., Ondras, H., Loureno, N., Segonzac, M. & Tivey, M. (1994), 'A detailed study of the Lucky Strike hydrothermal site and discovery of a new hydrothermal site: Menez Gwen; preliminary results of the DIVA1 cruise (5-29 May, 1994)', *InterRidge News* **3(2)**, 14–17.

Fouquet, Y., Ondreas, H., Charlou, J. L., Donval, J. P., Radfordknoery, J., Costa, I., Lourenco, N. & Tivey, M. K. (1995), 'Atlantic lava lakes and hot vents', *Nature* **377**(6546), 201-201.

Fournier, R. O. (1991), 'The transition from hydrostatic to greater than hydrostatic fluid pressure in presently active continental hydrothermal systems in crystalline rock', *Geophysical Research Letters* **18**, 955–958.

Fox, C. G. (1990), 'Consequences of phase separation on the distribution of hydrothermal fluids at Ashes Vent Field, Axial Volcano, Juan de Fuca Ridge', *Journal of Geophysical Research* **95**, 12923–12926.

Frigo, M. & Johnson, S. G. (1998), FFTW: An adaptive software architecture for the FFT, *in* 'ICASSP conference proceedings', pp. 1381–1384.

German, C. R., Campbell, A. C. & Edmond, J. M. (1991), 'Hydrothermal scavenging at the Mid-Atlantic Ridge - modification of trace-element dissolved fluxes', *Earth and Planetary Science Letters* **107**(1), 101–114.

German, C. R., Klinkhammer, G. P. & Rudnicki, M. D. (1996), 'The Rainbow hydrothermal plume, 36°15'N, MAR', *Geophysical Research Letters* **23**(21), 2979–2982.

German, C., Baker, E., Mevel, C., Tamaki, K. & the FUJI Science Team (1998), 'Hydrothermal acticity along the South West Indian Ridge', *Nature* **395**, 490–493.

Germanovich, L. N. & Lowell, R. P. (1992), 'Percolation theory, thermoelasticity, and discrete hydrothermal venting in the Earth's crust', *Science* **255**, 1564–1567.

Grant, F. S. & West, G. F. (1965), *Interpretation theory in applied geophysics*, McGraw-Hill.

Greer, A. (1999), 'Use of effective medium techniques to integrate seismic and controlled source electromagnetic data', *Lithos Science Report* **1**, 111–114.

Greer, A. A. (2001), Joint interpretation of seismic and electromagnetic results, investigating zero age ocean crust, PhD thesis, University of Cambridge.

Henstock, T. J., Woods, A. W. & White, R. S. (1993), 'The accretion of oceanic crust by episodic sill intrusion', *Journal of Geophysical Research* **98**, 4143–4162.

Humphris, S. E., Fornari, D. J., Scheirer, D. S., German, C. R. & Parsons, L. M. (2002), 'Geotectonic setting of hydrothermal activity on the summit of Lucky Strike Seamount (37°17'N Mid-Atlantic Ridge)', *Geochemistry Geophysics Geosystems* **3**.

Jupp, T. & Schultz, A. (2000), 'A thermodynamic explanation for black smoker temperatures', *Nature* **403**(6772), 880–883.

Keller, G. W. (1988), Rock and mineral properties, *in* M. N. Naibighian, ed., 'Electromagnetic Methods in Applied Geophysics', Vol. 1, Society of Exploration Geophysicists, Tulsa, Okla.

Kelley, D., Karson, J., Blackman, D., Fruh-Green, G., Butterfield, D., Lilley, M., Olson, E., Schrenk, M., Roe, K., Lebon, G. & Rivizzigno, P. (2001), 'An off-axis hydrothermal vent field near the Mid-Atlantic Ridge at 30°N', *Nature* **412**, 145–149.

Kent, G. M., Harding, A. J. & Orcutt, J. A. (1990), 'Evidence for a smaller magma chamber beneath the East Pacific Rise at 9°30N', *Nature* **344**, 650–653.

Kent, G. M., Harding, A. J. & Orcutt, J. A. (1993), 'Distribution of magma beneath the East Pacific Rise between the Clipperton transform and the 9°19N deval from forward modelling of common depth point data', *Journal of Geophysical Research* **98**, 13945–13969.

Klinkhammer, G., Wilson, C., Chin, C. & German, C. (1995), Rare earth element data for hydrothermal fluids and other results from the Lucky Strike hydrothermal field on the MAR at 37°17'N, *in* L. M. Parson, C. L. Walker & D. R. Dixon, eds, 'Hydrothermal Vents and Processes', Vol. 87, Geological Society, pp. 87–96.

Kuo, B. Y. & Forsyth, D. W. (1988), 'Gravity anomalies of the ridge transform system in the South Atlantic between 31 and 34.5°S: upwelling centres and variations in crustal thickness', *Marine Geophysical Researches* **10**, 205–232.

Langmuir, C. H., Charlou, J. L., Colodner, D., Corey, S., Costa, I., Desbruyeres, D., Emerson, T., Fornari, D., Fiala-Medioni, A., Fouquet, Y., Humphris, S., Saldanah, L., Sours-Page, R., Thatcker, M., Tivey, M., Dover, C. V., Von Damm, K. L., Wiese, K. & Wilson, C. (1993), 'Lucky Strike - A newly discovered hydrothermal site on the Azores Platform', *Ridge Events* pp. 3–5.

Langmuir, C., Humphris, S., Fornari, D., VanDover, C., VonDamm, K., Tivey, M. K., Colodner, D., Charlou, J. L., Desonie, D., Wilson, C., Fouquet, Y., Klinkhammer, G. & Bougault, H. (1997), 'Hydrothermal vents near a mantle hot spot: The Lucky Strike vent field at 37 degrees N on the Mid-Atlantic Ridge', *Earth and Planetary Science Letters* **148**(1-2), 69–91.

Lin, J., Purdy, G. M., Schouten, H., Sémpére, J. C. & Zervas, C. (1990), 'Evidence from gravity data for focussed magmatic accretion along the Mid-Atlantic Ridge', *Nature* **344**, 627–632.

Lister, C. R. B. (1972), 'On the thermal balance of a mid-ocean ridge', *Geophysical Journal of the Royal Astronomical Society* **26**, 515–535.

Lister, C. R. B. (1974), 'On the penetration of water in to hot rock', *Geophysical Journal of the Royal Astronomical Society* **39**, 465–509.

Lowell, R. P., Van Cappellen, P. & Germanovich, L. (1993), 'Silica precipitation in fractures and the evolution of permeability in hydrothermal upflow zones', *Science* **260**, 192–194.

MacGregor, L. M. (1997), Electromagnetic investigation of the Reykjanes Ridge near 58°North, PhD thesis, University of Cambridge.

MacGregor, L. M. (1999), 'Marine controlled source electromagnetic sounding: development of a regularised inversion for 2-dimensional resistivity structures', *Lithos Science Report* **1**, 103–109.

MacGregor, L. & Sinha, M. (2000), 'Use of marine controlled-source electromagnetic sounding for sub-basalt exploration', *Geophysical Prospecting* **48**(6), 1091–1106.

MacGregor, L. M., Constable, S. & Sinha, M. C. (1998), 'The RAMESSES experiment - III. Controlled-source electromagnetic sounding of the Reykjanes Ridge at 57°45'N', *Geophysical Journal International* **135**(3), 773–789.

MacGregor, L., Sinha, M. & Constable, S. (2001), 'Electrical resistivity structure of the Valu Fa Ridge, Lau Basin, from marine controlled-source electromagnetic sounding', *Geophysical Journal International* **146**(1), 217–236.

Mackie, R. L. & Madden, T. R. (1993), 'Conjugate direction relaxation solutions for 3-D magnetotelluric modeling', *Geophysics* **58**, 1052–1057.

Mackie, R. L., Smith, J. T. & Madden, T. R. (1994), 'Three dimensional electromagnetic modelling using finite difference equations: the magneto-telluric example', *Radio Science* **29**, 923–935.

Madsen, J. A., Detrick, R. S., Mutter, J. C., Buhl, P. & Orcutt, J. A. (1990), 'A 2- and 3-dimensional analysis of gravity anomalies associated with the East Pacific Rise at 9°N and 13°N', *Journal of Geophysical Research* **95**, 4967–4987.

Maxwell, J. C. (1891), *A treatise on electricity and magnetism*, 3rd edn, Dover Publ. Inc.

McKenzie, D. P. (1967), 'Some remarks on heat flow and gravity anomalies', *Journal of Geophysical Research* **72**, 6261–6273.

Morgan, J. P. & Parmentier, E. M. (1987), 'Mechanisms for the origin of mid-ocean ridge axial topography: implications for the thermal and mechanical structure of accreting plate boundaries', *Journal of Geophysical Research* **92**, 12823–12836.

Morton, J. & Sleep, N. (1985), Seismic reflections from a Lau Basin magma chamber, *in* D. Scholl & T. Vallier, eds, 'Geology and offshore resources of Pacific island arcs - Tonga region', Houston, TX, Circum-Pacific Council for Energy and Mineral Resources.

Navin, D. A., Peirce, C. & Sinha, M. C. (1998), 'The RAMESSES experiment - II. Evidence for accumulated melt beneath slow spreading ridge from wide-angle refraction and multichannel reflection seismic profiles', *Geophysical Journal International* **135**(3), 746–772.

Nobes, D., Law, L. & Edwards, R. (1992), 'Results of a sea-floor electromagnetic survey over a sedimented hydrothermal area on the Juan de Fuca Ridge', *Geophysical Journal Internations* **110**, 333–346.

Parson, L., Murton, B., Searle, R., Booth, D., Evans, J., Field, P., Keeton, J., Laughton, A., McAllister, E., Millard, N., Redbourne, L., Rouse, I., Shor, A., Smiht, D., Spencer, S., Summerhayes, C. & Walker, C. (1993), 'En-echelon axial volcanic ridges at the Reykjanes Ridge - a life-cycle of volcanism and tectonics', *Earth and Planetary Science Letters* **117**, 1993.

Pezard, P. A. (1990), 'Electrical properties of midocean ridge basalt and implications for the structure of the upper oceanic-crust in Hole 504b', *Journal of Geophysical Research* **95**(B6), 9237–9264.

Phipps-Morgan, J. & Chen, Y. J. (1993), 'The genesis of oceanic crust: magma injection, hydrothermal circulation and crustal flow', *Journal of Geophysical Research* **98**, 6283–6297.

Presnall, D. C., Simmons, C. L. & Porath, H. (1972), 'Changes in the electrical conductivity of a synthetic basalt during melting', *Journal of Geophysical Research* **77**, 5665–5672.

Press, W. H., Teukolsky, S. A., Vetterling, W. T. & Flannery, B. P. (1992), *Numerical Recipes in FORTRAN*, 2nd edn, Cambridge University Press.

Scheirer, D. S., Fornari, D. J., Humphris, S. E. & Lerner, S. (2000), 'High-resolution seafloor mapping using the DSL-120 sonar system: Quantitative assessment of sidescan and phase-bathymetry data from the Lucky Strike segment of the Mid-Atlantic Ridge', *Marine Geophysical Researches* **21**(1-2), 121–142.

Schilling, J. G., Zajac, M., Evans, R., Johnston, T., White, W., Devine, J. D., & Kingsley, R. (1983), 'Petrologic and geochemical variations along the Mid-Atlantic Ridge from 29^oN to 73^oN', *American Journal of Science* **283**, 510–586.

Schmeling, H. (1986), 'Numerical models of the influence of partial melt on elastic, anelastic and electrical properties of rocks. Part II: electrical conductivity', *Physics of the Earth and Planetary Interiors* **43**, 123–136.

Seewald, J. S. & Seyfried, W. E. (1990), 'The effect of temperature on metal mobility in subseafloor hydrothermal systems: constraints from basalt alteration experiments', *Earth and Planetary Science Letters* **101**, 388–403.

Shankland, T. J. & Waff, H. S. (1977), 'Partial melting and electrical conductivity anomalies in the upper mantle', *Journal of Geophysical Research* **82**, 5409–5417.

Sinha, M. C. (1999), Madrigals RRS Charles Darwin cruise 120, Cruise report, University of Cambridge.

Sinha, M. C. (2003), 'Modelling in Environmental and Earth System Science', *University of Southampton OA402 course notes* .

Sinha, M. C. & Louden, K. E. (1983), 'The Oceanographers fracture zone. 1. Crustal structure from seismic refraction studies', *Geophysical Journal of the Royal Astronomical Society* **75**(713-736).

Sinha, M. C., Patel, P. D., Unsworth, M. J., Owen, T. R. E. & MacCormack, M. R. G. (1990), 'An active source electromagnetic sounding system for marine use', *Marine Geophysical Researches* **12**(1-2), 59–68.

Sinha, M. C., Constable, S. C., Peirce, C., White, A., Heinson, G., MacGregor, L. M. & Navin, D. A. (1998), 'Magmatic processes at slow spreading ridges: implications of the RAMESSES experiment at 57°45'N on the Mid-Atlantic Ridge', *Geophysical Journal International* **135**(3), 731–745.

Sinha, M. C., Flosadóttir, A. H., MacGregor, L. M., Santos, F. A. M. & Junge, A. (1998a), Applications of 3-dimensional electromagnetic induction by sources in the ocean, First annual report, University of Cambridge.

Smith, B. D. & Ward, S. H. (1974), 'Short note on the computation of polarisation ellipse parameters', *Geophysics* **39**, 867–869.

Smith, W. H. F. & Sandwell, D. T. (1997), 'Global sea floor topography from satellite altimetry and ship depth soundings', *Science* **277**, 1956–1962.

Spudich, P. & Orcutt, J. (1980), 'A new look at the seismic velocity structure of oceanic crust', *Reviews of Geophysics and Space Physics* **18**, 627–645.

Stein, C. A. & Stein, S. (1994), 'Constraints on hydrothermal heat flux through the oceanic lithosphere from global heat flow', *Journal of Geophysical Research* **99**, 3081–3095.

Stratton, J. A. (1941), *Electromagnetic theory*, McGraw-Hill.

Toomey, D. R., Solomon, S. C. & Purdy, G. M. (1994), 'Tomographic imaging of the shallow crustal structure of the East Pacific Rise at 9°30'N', *Journal of Geophysical Research* **99**, 24135–24197.

Turner, I. M., Peirce, C. & Sinha, M. C. (1999), 'Seismic imaging of the axial region of the Valy Fa Ridge, Lau Basin - the accretionary process of an intermediate back-arc spreading ridge', *Geophysical Journal Internations* **138**, 495–519.

Unsworth, M. J. (1991), Electromagnetic exploration of the oceanic crust with controlled sources, PhD thesis, University of Cambridge.

Unsworth, M. J., Travis, B. J. & Chave, A. D. (1993), 'Electromagnetic induction by a finite electric-dipole source over a 2-D Earth', *Geophysics* **58**(2), 198–214.

Von Damm, K. L. (1990), 'Seafloor hydrothermal activity: Black smoker chemistry and chimneys', *Annual Review of Earth and Planetary Sciences* **18**, 173–204.

Von Damm, K. L. (1995), Controls on the chemistry and temporal variability of seafloor hydrothermal fluids, *in* S. E. Humphris, R. A. Zierenberg, L. S. Mullineaux & R. E.

Thompson, eds, 'Geophysical Monograph 91: Seafloor Hydrothermal Systems', American Geophysical Union, pp. 222–247.

Von Damm, K. L. & Bischoff, J. L. (1987), 'Chemistry of hydrothermal solutions from the Southern Juan de Fuca Ridge', *Journal of Geophysical Research* **92**, 11334–11346.

Von Damm, K. L., Bray, A. M., Buttermore, L. G. & Oosting, S. E. (1998), 'The geochemical controls on vent fluids from the Lucky Strike vent field, Mid-Atlantic Ridge', *Earth and Planetary Science Letters* **160**(3-4), 521–536.

Webb, S. & Cox, C. S. (1986), 'Pressure and electrical fluctuations on the deep seafloor: Background noise for seismic detection', *Geophysical Research Letters* **11**, 967–970.

White, R. S., Detrick, R. S., Sinha, M. C. & Cormier, M. H. (1984), 'Anomalous seismic crustal structure of oceanic fracture zones', *Geophysical Journal of the Royal Astronomical Society* **79**, 779–798.

Wiens, D. A. & Stein, S. (1983), 'Age dependence of oceanic intraplate seismicity and implications for lithospheric evolution', *Journal of Geophysical Research* **88**, 6455–6468.

Wilson, C., Charlou, J. L., Ludford, E., Klinkhammer, G., Chin, C., Bougault, H., German, C., Speer, K. & Palmer, M. (1996), 'Hydrothermal anomalies in the Lucky Strike segment on the Mid-Atlantic Ridge (37°17'N)', *Earth and Planetary Science Letters* **142**(3-4), 467–477.

Wyllie, M. R. J., Gregory, A. R. & Gardner, G. H. (1958), 'An experimental investigation of factors affecting elastic wave velocities in porous media', *Geophysics* **23**, 459–493.

Young, P. D. & Cox, C. S. (1981), 'Electromagnetic active source sounding near the East Pacific Rise', *Geophysical Research Letters* **8**(10), 1043–1046.